DEEP AND SURFACE CIRCULATION IN THE NORTHWEST INDIAN OCEAN FROM ARGO, SURFACE DRIFTER, SATELLITE, AND IN SITU PROFILING CURRENT OBSERVATIONS

A Thesis

by

SARAH A. STRYKER

Submitted to the Office of Graduate Studies of
Texas A&M University
in partial fulfillment of the requirements for the degree of

MASTER OF SCIENCE

August 2011

Major Subject: Oceanography

Deep and Surface Circulation in the Northwest Indian Ocean from Argo, Surface Drifter, Satellite, and In Situ Profiling Current Observations

DEEP AND SURFACE CIRCULATION IN THE NORTHWEST INDIAN OCEAN FROM ARGO, SURFACE DRIFTER, SATELLITE, AND IN SITU PROFILING CURRENT OBSERVATIONS

A Thesis

by

SARAH A. STRYKER

Submitted to the Office of Graduate Studies of
Texas A&M University
in partial fulfillment of the requirements for the degree of

MASTER OF SCIENCE

Approved by:

Chair of Committee,	Steven F. DiMarco
Committee Members,	Howard F. Seidel
	Kenneth P. Bowman
	Piers Chapman
Head of Department,	Piers Chapman

August 2011

Major Subject: Oceanography

ABSTRACT

Deep and Surface Circulation in the Northwest Indian Ocean from Argo, Surface Drifter, Satellite and In Situ Profiling Current Observations. (August 2011)

Sarah A. Stryker, B.S., The State University of New York at Fredonia

Chair of Advisory Committee: Dr. Steven F. DiMarco

The physical oceanography in the northwest Indian Ocean is largely controlled by the seasonal monsoon. The seasonal variability in circulation is complex. Many studies have investigated processes in the Persian (Arabian) Gulf and Arabian Sea, but little is understood about the Sea of Oman. This thesis incorporated observations from Argo floats, surface drifters and satellite imagery to study the deep and surface circulation in the northwest Indian Ocean. An assessment of four independent moorings located in the Sea of Oman and Arabian Sea, as well as a model skill comparison of the Simple Ocean Data Assimilation (SODA) model, contributed to understanding the dynamics in this region.

Spatial patterns of surface current velocity produced from surface drifter data from 1995-2009 agreed with previously known surface currents. The Somali Current, East Arabian Current, Equatorial Current, Northeast/Southwest Monsoon Current, Great Whirl and Ras al Hadd Jet were all identified. During the Southwest Monsoon, flow direction was to the east and southeast in the Arabian Sea. The Somali Current flowed northeast along the Somali Coast extending to the East Arabian Current along the Oman

coast. During the Northeast Monsoon, evaporation increased over the Arabian Sea, which resulted in a salinity gradient. This imbalance caused low-salinity surface water from the northeast Indian Ocean to flow into the northwest Indian Ocean as the Northeast Monsoon Current. Current direction reversed with the change of wind direction from the Southwest Monsoon to the Northwest Monsoon. Many characteristics seen at the surface were also identified in the subsurface as deep as 1500m.

The comparison of moored observations to the Argo observations co-located in space and time showed reasonable agreement with the largest salinity difference of 0.23 and largest temperature difference of 0.78˚C. The Murray Ridge mooring had a temperature correlation of 0.97 when compared to Argo observations.

Argo observations were compared with SODA model numerical output from 1992-2001, and, after Argo, were assimilated from 2002-2009. With assimilation of Argo data into the SODA model, the temperature and salinity from the model numerical output improved, with most differences between model numerical output and Argo observations falling within one standard deviation.

DEDICATION

To my wonderful friends and family

ACKNOWLEDGEMENTS

I would like to thank my committee chair, Dr. DiMarco, and my committee members, Dr. Seidel, Dr. Bowman, and Dr. Chapman, for their guidance and support throughout the course of this research. Thanks also go to the Texas A&M Department of Oceanography for graduate support.

The Lighthouse Ocean Research Initiative project in the Oman and Arabian Sea was developed and constructed by Lighthouse R & D Enterprises, Inc. In Oman, the project is coordinated with the Oman Ministry of Agriculture and Fisheries Wealth through the Marine Science and Fisheries Centre. We thank the Oman Ministry of Agriculture and Fisheries Wealth and Lighthouse R & D Enterprises, Inc. for providing access to the data and Lighthouse R & D Enterprises, Inc. for the financial support of this project.

Finally, I would like to thank the data providers. Thanks to UCSD/JCOMMOPS whose data were collected and made freely available by the International Argo Project and the national programs that contribute to it. (http://www.argo.ucsd.edu, http://argo.jcommops.org). Argo is a pilot program of the Global Ocean Observing System. Thanks also to the NOAA Global Drifter Program for surface drifter observations and to NASA for MODIS observations.

TABLE OF CONTENTS

Page

LIST OF FIGURES

Page

Page

Page

Page

LIST OF TABLES

1. INTRODUCTION

The northwest Indian Ocean is a region of complex circulation and atmospheric influence (Schott *et al.*, 2009). The region can be divided into smaller areas, such as the Sea of Oman, Arabian Sea, the Gulf of Aden and the lower latitudes (Equatorial region). The Persian (Arabian) Gulf and Red Sea are marginal seas, which also contribute to the complexity by contributing dense, high-salinity water masses to the Arabian Sea (Figure 1).

The purpose of this study is to provide a general description of the surface and deep circulation and hydrography in the northwest Indian Ocean, with an emphasis on the dynamics of the Sea of Oman and its interaction with the Persian (Arabian) Gulf and Arabian Sea. Several studies have investigated the physical dynamics of the Persian(Arabian) Gulf and Arabian Sea (Johns *et al.*, 2003; Banse, 1997; Kämpf and Sadrinasab, 2006; Morrison, 1997; Swift and Bower, 2003), but relatively little is known about the dynamics in the Sea of Oman (previously known as the Gulf of Oman). The study incorporates a variety of observational data sets and numerical model output (see Section 2 for data descriptions).

The study area for this thesis is the northwest Indian Ocean and defined by the region bounded by 0˚N-35˚N and 40˚E-80˚E (Figure 1). Primary data observations used here were Argo float observations made from January 1, 2002 through December 31, 2009. No in-situ data were available in the Persian (Arabian) Gulf or Red Sea, but the

---

This thesis follows the style of *Journal of Geophysical Research.*

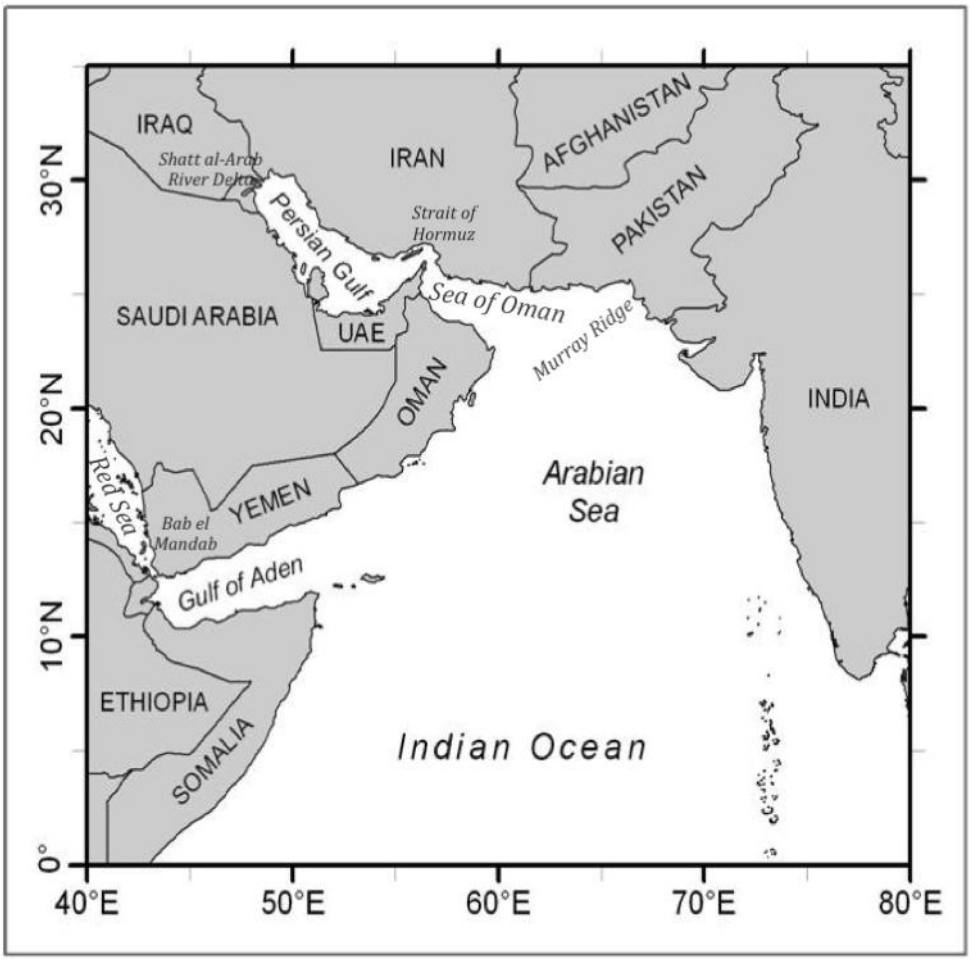

Figure 1. Political map of the study region. Modified from original (Nazarenko, 2009).

exchange between those marginal seas and the study area was investigated since they have a large influence in the regional oceanography. Array for Real-Time Geostrophic Oceanography (Argo) floats were used as a principal observation data set. Observations from surface drifters and satellite observations were used as ancillary data sources. A map of the regional bathymetry is shown in Figure 2. The maximum depth in the northwest Indian Ocean exceeds 5600m. The maximum depth of data collected ranges from 2000m-3000m.

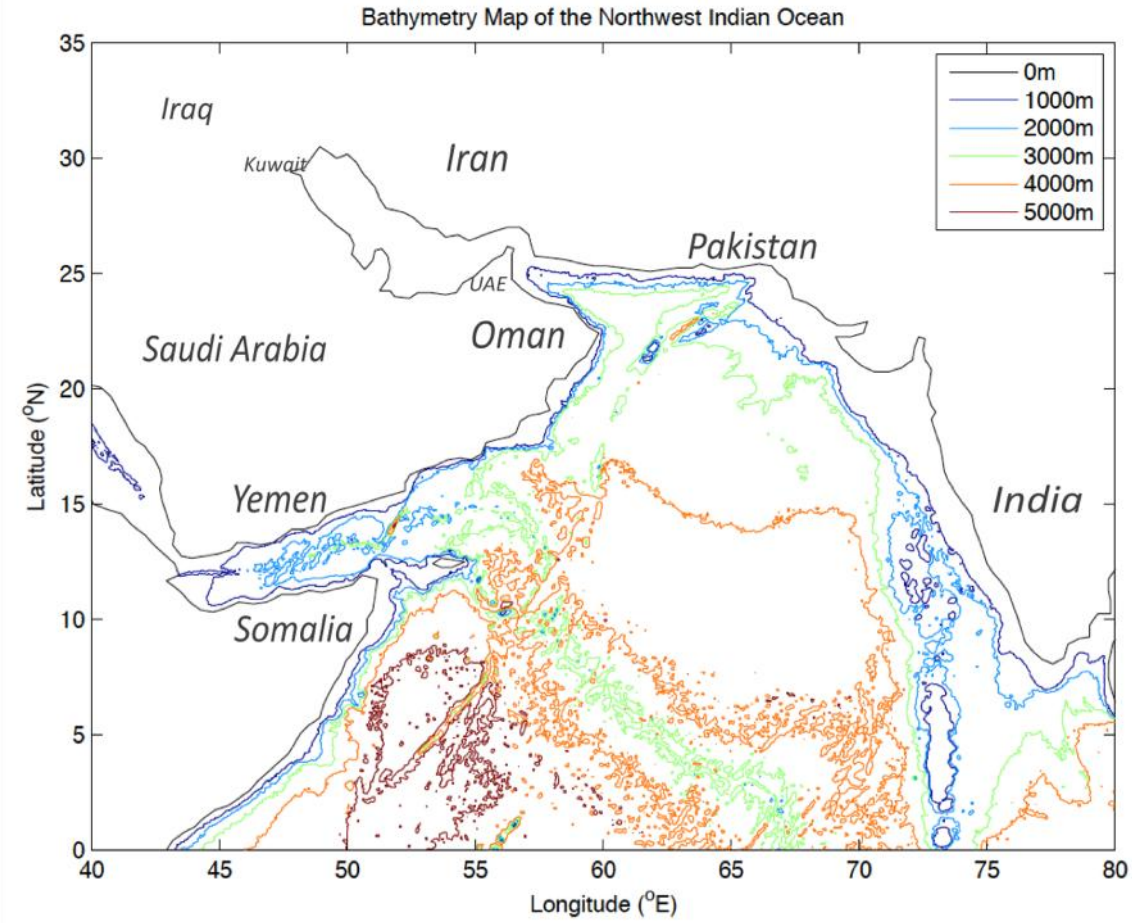

Figure 2. Bathymetry map of the northwest Indian Ocean. ETOPO2v2 data were obtained from NOAA/NGDC (ETOPO2v2 Global Gridded 2-minute Database, 2006). Isobaths are drawn for 0m, 1000m, 2000m, 3000m, 4000m and 5000m.

Emphasis in this project was placed on the physical oceanography of the Sea of Oman, the Arabian Sea and the interaction with the Persian (Arabian) Gulf. In 2005, Lighthouse R&D Enterprises, Inc. (henceforth LH) installed four autonomous moorings with the cooperation of the Oman Ministry of Agriculture and Fisheries Wealth. The moorings are located near Cape Ras al Hadd and Murray Ridge. One key objective in

their installation was to support the ministry in its efforts to develop and manage the Sultanate's highly important fisheries resources.

In 2005, LH, with the full backing of the government of the Sultanate of Oman, installed the first cabled seabed observatory in the region. The Sea of Oman was selected as an ideal test location due to the dynamic nature of the water bodies in the region and the relatively uncharacterized nature of those waters. In country, the project is coordinated alongside the Ministry of Agriculture and Fisheries Wealth through the Marine Science and Fisheries Centre.

1.1 Background

Reviewing the existing knowledge of the regional atmospheric and oceanic characteristics helped to guide the analysis of new observations made during this study. Here, background information regarding the atmospheric influence, oceanography of marginal seas, and oceanography of the Indian Ocean within (and outside) the study area is described.

1.1.1 Atmospheric Meteorology

The regional pattern of wind during each monsoon changes drastically (Weller *et al.*, 1998). Winds over the northwest Indian Ocean are northeasterly in the winter (NE Monsoon) and southwesterly during the summer (SW Monsoon) (Figure 3), which largely influences the circulation (Shi *et al.*, 2000; McCreary and Kundu, 1989). In a study of the atmospheric forcing of the Arabian Sea in 1994 and 1995, Weller *et al.*

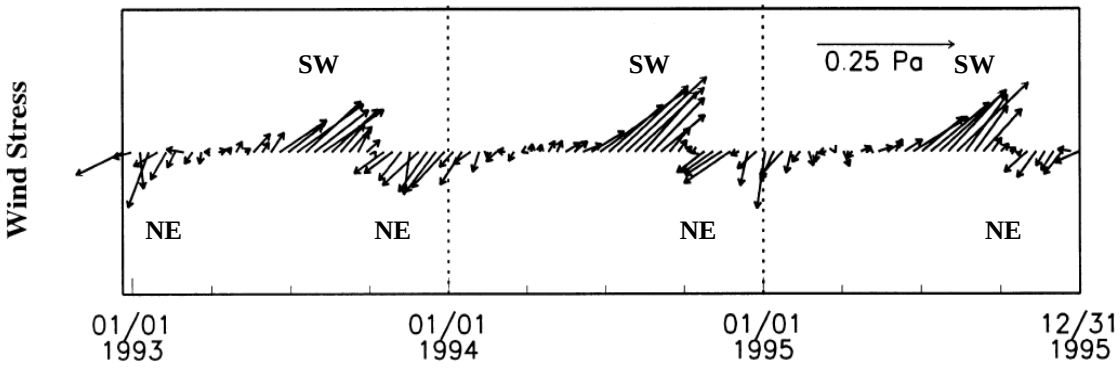

Figure 3. Time-series of the modeled mean wind stress in the northwest Indian Ocean from 1993-1995 using oceanographic convention. Wind stress is in Pascals. The southwest monsoon is labeled with SW and the northeast monsoon is labeled with NE (from Shi *et al.*, 2000).

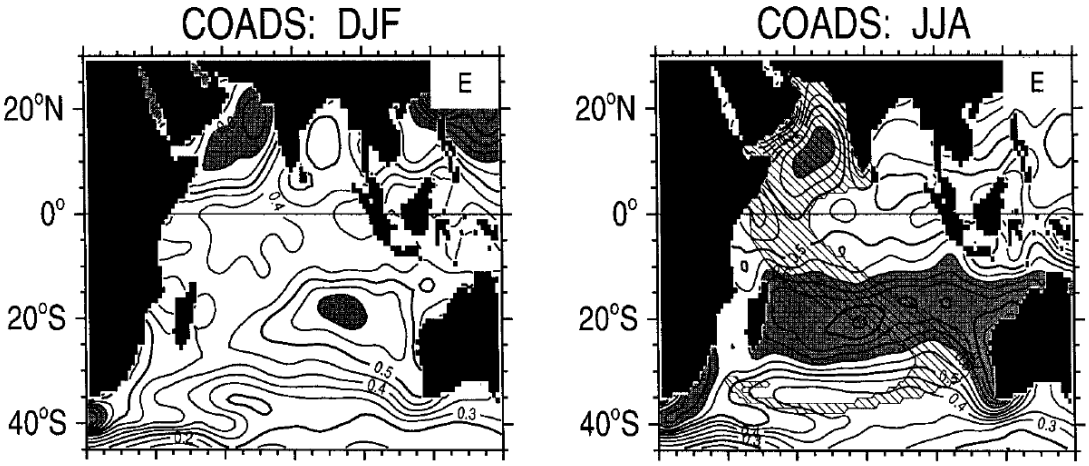

Figure 4. Comprehensive Ocean-Atmospheric Dataset (COADS) evaporation rates (E) for the Indian Ocean during the winter (DJF) and summer (JJA). Contour intervals are 0.05mm and regions with an evaporation rate of more than 0.6mm are shaded in gray. The hatches for JJA are the modeled streamtube for the 10-m airflow that intersects India, which was used to track precipitation over Indian in the source study (from Wajsowicz and Schopf, 2001).

(1998) found that sea surface temperatures (SST) decreased from December through February and June through July. Compared to the NE Monsoon, the SW Monsoon has a lower barometric pressure (~9 mb) and higher humidity over the Arabian Sea. The Wajsowicz and Schopf (2001) model also shows increased evaporation rates over the Arabian Sea, Persian (Arabian) Gulf and Red Sea during the winter (Figure 4).

The spring Intermonsoon (March-May) is the transitional period between the Northeast and Southwest Monsoon. The fall Intermonsoon (September-November) is the transitional period between the Southwest and Northeast Monsoon.

1.1.2 Persian (Arabian) Gulf

The Persian (Arabian) Gulf is a large (241,000 km^2) basin that acts as a reverse estuary (Banse, 1997). The depth is very shallow, averaging 35m, with a maximum depth of 90m (Johns *et al.,* 2003). The Strait of Hormuz connects the Persian (Arabian) Gulf to the Sea of Oman and has a maximum depth of 100m (Pous *et al.*, 2004a).

The Persian (Arabian) Gulf has a major river delta at its northernmost end called the Shatt al-Arab, which has an effect on local water density, but does not greatly impact the southern Persian (Arabian) Gulf or the rest of the northwest Indian Ocean (Pous *et al.*, 2004a). In the winter, evaporation rates increase in the Persian (Arabian) Gulf (Figure 4) from thermal high that forms over the Tibetan Plateau. Increased evaporation results in the formation of a high-salinity, dense water mass called Persian Gulf Water (PGW). PGW forms along the northern coast of the United Arab Emirates (Kämpf and Sadrinasab, 2006), and sinks as it flows out along the southern edge of the Strait of Hormuz (Johns *et al.*, 2003; Chao *et al.*, 1992) and into the Sea of Oman and Arabian

Sea (Banse, 1997; Pous *et al.*, 2004b). Indian Ocean Surface Water (IOSW) flows into the Persian (Arabian) Gulf (Banse, 1997; Pous *et al.*, 2004a) at the northern edge of the strait (Brewer and Dyrssen, 1985; Reynolds, 1993).

When compared with water in the Sea of Oman, PGW is characterized by a slightly elevated temperature of ~1-2° (Banse, 1997). As PGW extends to the southeast along the northern coast of Oman,, mixing occurs, which results in decreased salinity. Salinities greater than 40 exist in the Persian (Arabian) Gulf, but according to Banse (1997), rarely extend beyond the strait. However, a model study (Thoppil and Hogan, 2008) investigating water mass exchange in the Strait of Hormuz showed episodic salinity pulses (salinity increases of up to 2 and lasting 15-30 days) that extend from the Strait of Hormuz into the Sea of Oman, resulting from a highly variable surface layer flow caused by fluctuations in the wind stress forcing. At a depth of 200-350 m, PGW separates the Gulf Deep Water (GDW) from IOSW (Swift and Bower, 2003).

The spatial coverage of PGW along the southern coast of Oman is seasonal (Morrison, 1997). During the NE Monsoon, PGW flows around Cape Ras al Hadd, but continued lateral mixing results in decreased salinity (Wyrtki *et al.*, 1971). During the spring Intermonsoon, Arabian Sea Central Water (ASCW) is present in place of PGW along the southern coast of Oman. ASCW is also characterized by high-salinity (36.6). From the early SW monsoon (June) through the early NE monsoon (December), low-salinity Indian Central Water (ICW) extends northward toward the southern coast of Oman (Morrison, 1997). ICW follows the σ=26.7kg/m^3 isopycnal, and has salinities of 35.6-35.8 along the southern Oman coast (You and Tomczak, 1993).

1.1.3 Red Sea

The Bab el Mandab connects the Red Sea to the Gulf of Aden. The shallowest part of the Bab el Mandab is the Hanish Sill (160m), which regulates all subsurface exchange.

During the winter (December-February), evaporation rates over the Red Sea increase to greater than 0.2mm/hour (Figure 3) (Wajsowicz and Schopf, 2001). Increased evaporation rates combined with the NE Monsoon winds result in the flow of Gulf of Aden Surface Water (GASW) into the Red Sea (Figure 5).

Two water masses (Red Sea Water and Red Sea Deep Water) combine to form Red Sea Outflow Water (RSOW), which flows out of the Red Sea in the subsurface year round (Siddall *et al.,* 2002), though it decreases drastically in the summer (Smeed, 2004). For this study, it is unnecessary to distinguish between Red Sea Water and Red Sea Deep Water, so any subsurface outflow is simply called Red Sea Water (RSW). After RSW sinks, it becomes part of the Indian Ocean intermediate circulation, which can be identified at mid-depth with maximum salinities in the Arabian Sea (Aiki, *et al.*, 2006) and as far south as South Africa (Beal and Bryden, 1999).

During the summer, Red Sea Surface Water (RSSW) flows out at the surface of the Bab el Mandab. Since the Hanish sill is so shallow, Gulf of Aden Intermediate Water (GAIW) does not normally pass through the Bab el Mandab into the Red Sea; however,

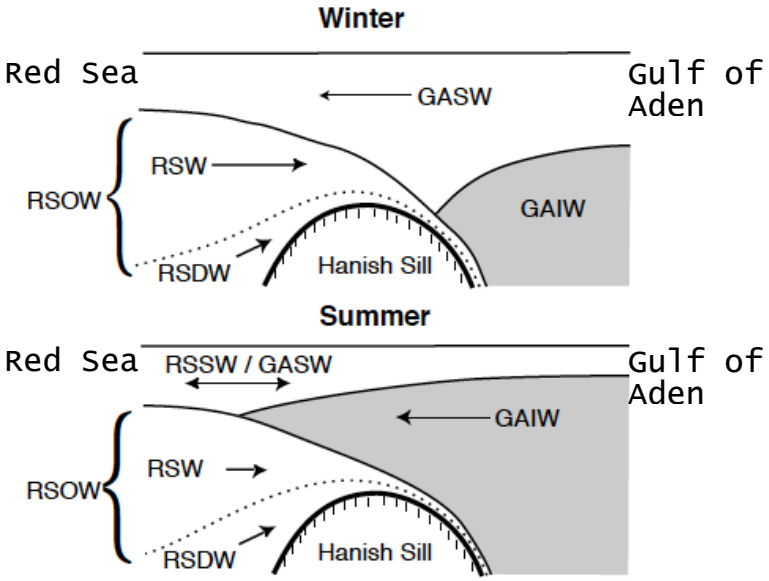

Figure 5. Winter and summer exchange between the Red Sea and the Gulf of Aden. Water masses include Gulf of Aden Surface Water (GASW), Red Sea Water (RSW), Red Sea Deep Water (RSDW), Red Sea Outflow Water (RSOW), Gulf of Aden Intermediate Water (GAIW) and Red Sea Surface Water (RSSW) (from Siddall *et al.*, 2002).

the SW monsoon favors upwelling of GAIW, which allows it to pass over the Hanish sill (Siddall, *et al.*, 2002).

1.1.4 Northwest Indian Ocean

A map of known surface currents in the northwest Indian Ocean during the winter and summer can be viewed in Figure 6. During the summer monsoon, the Somali Current flows northeast along the Somali coast, transporting low-salinity waters (Schott and McCreary, 2001) associated with Indian Central Water (ICW) (Morrison, 1997). Several eddies are formed as the Somali Current separates from the coast (McCreary and Kundu, 1989).

The East Arabian Current (EAC) is an extension of the Somali Current and runs northward along the southern coast of Oman. The EAC is only present during the SW Monsoon and is responsible for upwelling along the coast.

In September, the EAC extends to the Ras al Hadd (RAH) Jet. The RAH Jet is an intense offshore feature, which forms off the eastern tip of Oman at Cape Ras al Hadd and flows east into the Arabian Sea. EAC and RAH Jet velocities maximize in late June and weaken in September (Elliot and Savidge, 1990). Böhm *et al.* (1999) observed that local wind speed and direction are highly correlated with the RAH Jet current velocity and that minimum SST at the RAH Jet occurs when current velocities are maximum. During the summer, the coolest SST (~26˚C) occurs along the Arabian and Somali coast. This is a result of upwelling. When winds reverse in the winter, the Somali Current reverses and SST is minimum (~23˚C) in the northern Arabian Sea (McCreary and Kundu, 1989).

The Oman shelf is steep, reaching a depth of 3,000m only 54 km from shore (slope greater than 0.56) (Figure 2). Murray Ridge extends over 750 km and runs southwest between the Sea of Oman and Arabian Sea. The shallowest points of the ridge are less than 500 m deep. The coasts of Pakistan and Iran that fall between the Strait of Hormuz and Murray Ridge, experience maximum upwelling during the SW monsoon. This is due to the coast's east-west orientation, narrow continental shelf and steep continental slope (Quraishee, 1984).

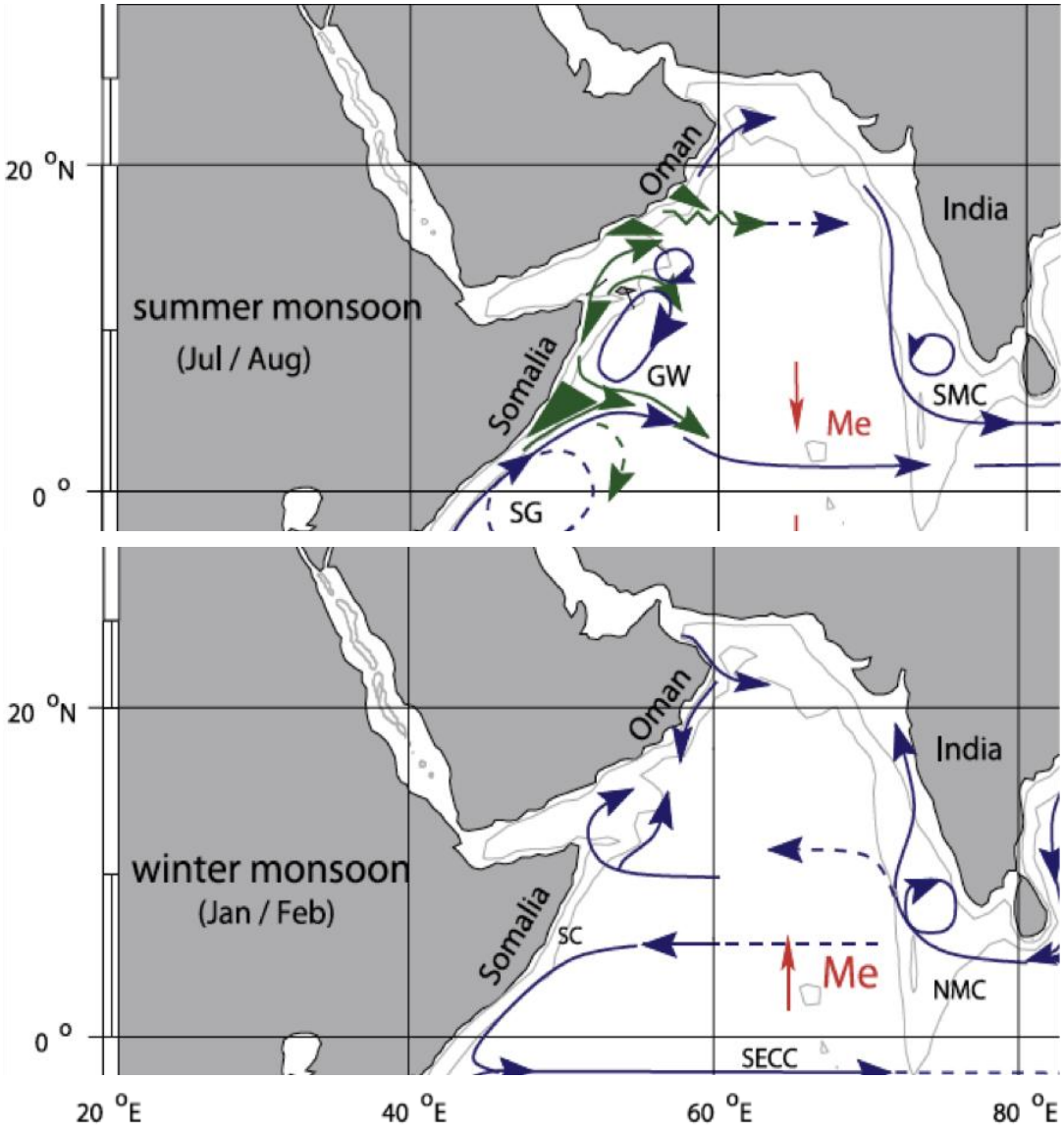

Figure 6. Map of known surface currents during the summer and winter monsoon. The currents in the NW Indian Ocean are the Southwest Monsoon Current (SMC), the Northeast Monsoon Current (NMC), the Somali Current (SC), the Great Whirl (GW) and the Southern Gyre (SG). Other currents that are not labeled include the East Arabian Current (EAC), which is indicated by the blue arrow along the Oman coast during the summer monsoon, and the North Equatorial Current, which is indicated by the blue dashed arrow flowing west along the equator during the winter monsoon. Meridional Ekman transport is indicated by the red arrows labeled Me. Depth contours are in gray, and indicate the 1000m and 3000m isobaths (from Schott *et al.*, 2009).

1.1.5 Southwest Indian Ocean

Chapman *et al.* (2003) and DiMarco *et al.* (2002) studied the deep general circulation of the southwest Indian Ocean (32˚S-0˚, 33˚E-57˚E) using Autonomous Lagrangian Circulation Explorer (ALACE) float trajectory and hydrographic data. In situ observations and satellite imagery show distinct coastal currents (African Coastal, Agulhas, Mozambique and East Madagascar Current) as well as the formation of eddies. Subsurface velocities (800 meters depth) away from the East Madagascar Current were also found to correspond with eddy movement, which was determined from the combination of ALACE float tracks, SSH anomaly maps and Ocean Circulation and Climate Advanced Modelling Project (OCCAM) model numerical output (Chapman *et al.,* 2003).

The East African Coastal Current (EACC) feeds into the Somali Current as it crosses over the equator (Schott *et al.*, 2009). The structure of the EACC was observed in DiMarco *et al*. (2002) as having a width around 200km and maximum subsurface (1000m) velocities near 20 cm/s (Figure 7). Once the EACC passes the equator, part of it feeds into the Somali Current while the rest separates from the coast and flows east along the equator.

1.1.6 Northeast Indian Ocean

The Vinayachandran and Nanjundian (2009) model showed that during the winter monsoon, the Northeast Monsoon Current transports low-salinity surface water from the Bay of Bengal around the southern tip of India, and into the northwest Indian Ocean. During the summer monsoon, high-salinity water from the Arabian Sea spreads

(a) Bathymetry map

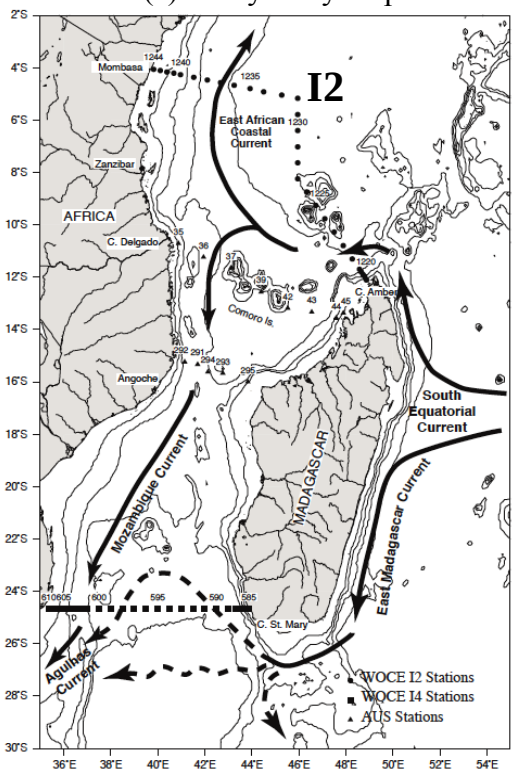

(b) Cross-section of I2

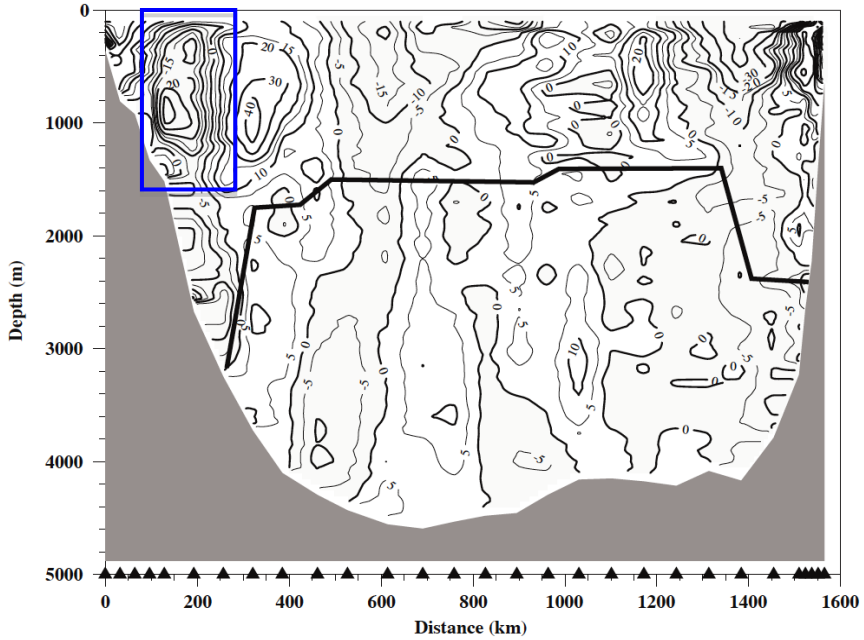

Figure 7. (a) Bathymetry of the Mozambique Channel region showing station positions from WOCE line I2. Regional current regimes are shown schematically. (b) Meridional ADCP current velocities (cm/s) along line I2. (from DiMarco *et al.*, 2002).

to the southeast and enters into the Bay of Bengal by the Southwest Monsoon Current. This forcing is caused by asymmetry in the salinity across the northern Indian Ocean as well as wind forcing.

1.2 Study Objectives and Guiding Questions

For this thesis, the principal objective is to use observations and numerical model numerical output to quantitatively describe the general surface and subsurface circulation and hydrography of the northwest Indian Ocean. Data sets include observations from Argo floats, surface drifters, satellite imagery, and autonomous moorings. Specific questions are used to guide the analysis and to fulfill the study objectives by giving a description of the physical dynamics in the region and their associated forcing parameters:

- What spatial patterns of horizontal current velocities are identified at the surface and subsurface? How do the velocities and current patterns at the surface compare to those in the subsurface? How do these patterns change seasonally?
- What is the seasonal variability of sea surface temperature and sea surface height? Are sea surface changes associated with dynamical features?
- How do the moored data compare to Argo float data?
- What is the relative importance of salinity and temperature to the vertical stratification?
- How does the SODA model compare to the Argo float data? How does the assimilation of Argo data into the SODA model affect the output?

2. DATA AND METHODS

Multiple data sets were used in the study of the circulation and hydrography in the region. Bathymetry data (ETOPO2v2) were obtained from the National Geophysical Data Center (NGDC) with the U.S. National Oceanic and Atmospheric Administration (NOAA).

2.1 Data Sources

Argo float, surface drifter and mooring observations were the three primary data sources used in this project. Standard oceanographic techniques, which will be described in detail in this section, were used in the analysis of each data set as well as in the comparison between data sets. In addition to comparison between data sets, Argo data were compared to numerical model output (SODA- Simple Ocean Data Assimilation) (Carton *et al.*, 2000; Carton and Giese, 2008). All data were processed and analyzed using MATLAB (MathWorks, 2011). Additional data sets include satellite imagery for wind direction and speed, sea surface temperature and sea surface height.

2.1.1 Argo Float Observations

Argo data were downloaded as netCDF files. These data were collected and made freely available by the International Argo Project and the national programs that contribute to it (UCSD Argo, 2011; JCOMMOPS Argo, 2008). Argo is a pilot program of the Global Ocean Observing System. As of May 24, 2011, 3407 Argo floats had been deployed worldwide. 175 floats had trajectories within the defined area from January 2002-December 2009. The temporal distribution of each float can be seen in Figure 8

and Table C-1 in Appendix C. One full float cycle (beginning with descent and ending with resurfacing) lasts 10 days during which the float remains at its cruising depth (predetermined pressure) for nine days. The depths at which data are collected varies by float, but is typically every 5-10m in the upper water column, and every 100-500m in the lower water column.

Argo floats operate in one of two mission operation types. In Simple Mission Operation, the float descends at a rate of 10 cm/s to a predetermined cruising depth (~6 hours depending on final depth). Once the float reaches its cruising depth, it drifts with the current at that depth. After drifting for approximately nine days, the float ascends at 10 cm/s, collecting a temperature, salinity and pressure profile. The float spends six to twelve hours at the surface and transmits the data and its new location to satellites. This completes the 10-day cycle.

In Park and Profile Mission Operation, the float descends to a predetermined cruising depth and drifts for approximately nine days. After nine days, it descends to a greater depth before ascending. Each Argo float is set to follow one mission type. Drifting depth is used to determine subsurface current velocity and profile depth is used to study salinity and temperature stratification. In Simple Mission Operation, drifting depth and profile depth are the same, but in Park and Profile Mission Operation, profile depth is greater than the drifting depth. Spatial distribution of Argo data by profile depth is shown in Figure 9.

158 floats had a cruising depth of 1000m, 1500m and 2000m. Approximately 64% of the 158 floats used in the region had a cruising depth of 1000 meters. Floats with

a cruising depth of 1500m made up 8% of the floats used. Around 28% had a cruising depth of 2000 meters.

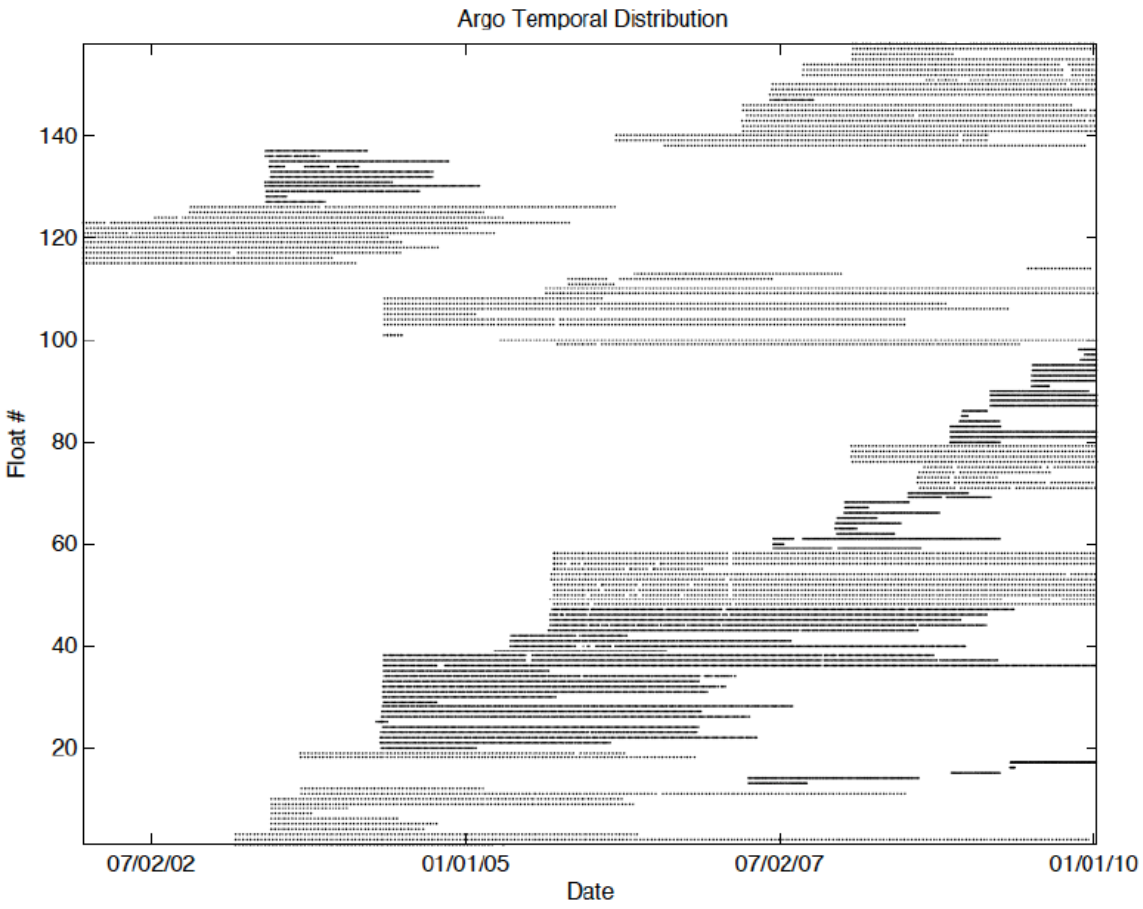

Figure 8. Temporal distribution of Argo data from January 1, 2002 through December 31, 2009 within the defined study region. Float # assignments can be found in Table C-1 in Appendix C. Each dot along the time series represents a completed cycle.

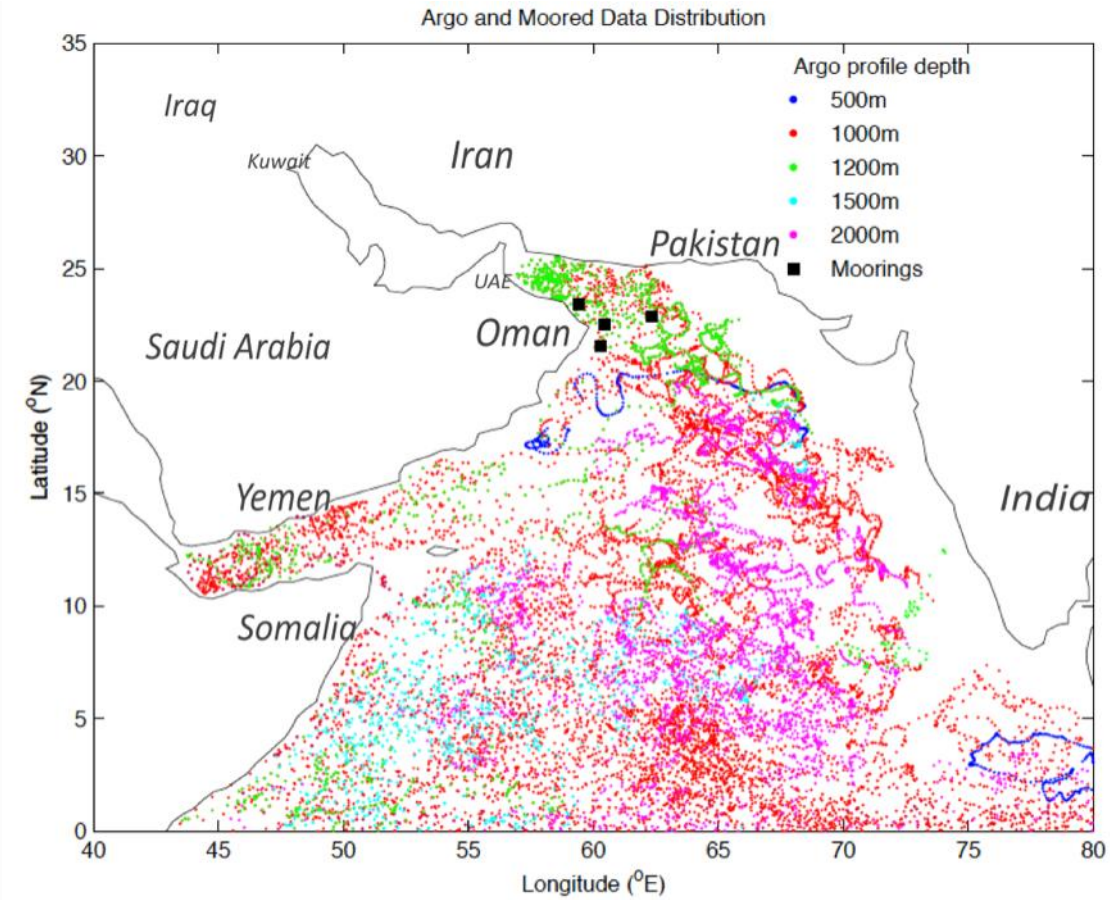

Figure 9. Map of the spatial distribution of Argo data and four independent moorings. The dots represent each Argo profile, with each color representing a defined profile depth. The black boxes represent the location of each mooring.

2.1.2 Satellite Imagery

Sea surface temperatures (11 micron in day) were obtained from the Giovanni Ocean Color Time-Series Online Visualization and Analysis Moderate Resolution Imaging Spectroradiometer (MODIS)- Aqua Monthly Global 9-km Products can be found at http://modis.gsfc.nasa.gov (Frazier, 2011). Sea surface heights (SSH) were

obtained from the Colorado Center for Astrodynamics Research (CCAR) Global Near Real-Time Sea Surface Anomaly Data Viewer (CCAR, 2009).

2.1.3 Surface Drifters

The Global Drifter Array expanded to the Indian Ocean in 1994 as part of World Ocean Circulation Experiment (WOCE) and the Atlantic Climate Change Program (ACCP). The array spanned the tropical and South Atlantic Ocean by 2004 (Lumpkin and Garzoli, 2005).

Monthly and annual mean near-surface temperatures and mean surface velocities from the Global Drifter Array were obtained from the Drifter-Derived Climatology of the Atlantic Oceanographic and Meteorological Laboratory (AOML) of the NOAA as developed by Rick Lumpkin (NOAA/AOML). The data were downloaded as NetCDF files from http://www.aoml.noaa.gov/phod/dac/drifter_climatology.html. The properties provided in the files were longitude, latitude, north/south velocity, east/west velocity, sea surface temperature, Ekman-removed north/south velocity, Ekman-removed east/west velocity and the number of drifter-days per square degree. Climatology includes data from March 1995 through March 2009.

2.1.4 Moorings

The ocean observing system installed by LH consists of four autonomous moorings positioned off Cape Ras al Hadd and Murray Ridge. At each mooring, data are collected at three or four depths with an Anderaa Recording Current Meter (RCM) 11. Sampling frequency is one hour for all four moorings (DiMarco *et al.*, 2008). The depth

of each instrument for each mooring is provided in Table 1. The Ras al Hadd (RH) moorings measure temperature, salinity (conductivity), pressure and velocity, as well as dissolved oxygen and turbidity at select depths. The Murray Ridge mooring measures temperature pressure and velocity. The instruments are located at four depths for most deployments on each mooring, with the deepest instrument around 3000 meters.

2.1.5 SODA Climate Model

Multiple data sources are used in constructing the SODA climate model, which is based on Los Alamos National Laboratory Parallel Ocean Program (POP). Assimilated data include hydrographic profile data (from ship measurements), ocean station data, moored temperature and salinity time-series, surface temperature and surface salinity observations since 1870. The data assimilation corrects forecasts by looking at difference between the forecast and the actual observations. The model grid is curvilinear and has a horizontal spatial resolution of 600 x 900 (latitude x longitude), with higher resolution (0.25°) at the equator. Vertically, the model has 40 layers, with 15 layers present in the upper 200 meters (Carton and Giese, 2008).

SODA 2.1.6 output was chosen because it covers the study period, has adequate vertical and horizontal resolution, and includes the most accurate wind data in the assimilation.

2.2 Processing and Analysis Techniques

In many of the data sets, preliminary processing was performed by the data providers before the data set was made available. Once each data set was obtained, additional processing was performed as needed.

Many data were processed and analyzed by season. Spring is defined as March-May, summer is defined as June-August, fall is defined as September-November, and winter is defined as December-February.

Table 1. Depth of each instrument for Ras al Hadd North, Ras al Hadd Middle, Ras al Hadd South, and Murray Ridge moorings. TT stands for the top instrument, MT for the mid-top instrument, MB for the mid-bottom instrument, and BB for the bottom instrument.

Ras Al Hadd North Instrument Depth (m)				
Instrument	03/04/05-05/29/06	05/29/06-01/28/07	01/28/07-11/22/07	11/22/07-12/31/09
TT	X	641.87	251.94	656.21
MT	1150.81	1160.02	1165.94	1177.66
MB	2082.79	2076.73	2085.80	2085.80
BB	3004.67	3000.28	3011.53	3017.39

Ras Al Hadd Middle Instrument Depth (m)				
Instrument	03/03/05-05/28/06	05/28/06-01/26/07	01/26/07-11/23/07	11/23/07-12/31/09
TT	X	638.63	237.60	644.49
MT	1157.91	1148.36	1148.40	1163.04
MB	2041.32	2074.09	2068.23	2074.09
BB	3005.20	2999.81	2993.95	2999.81

Ras Al Hadd South Instrument Depth (m)				
Instrument	03/02/05-05/26/05	05/26/06-01/24/07	01/24/07-11/24/07	11/24/07-12/31/09
TT	X	691.36	298.96	688.90
MT	1199.40	1201.10	1202.21	1202.21
MB	X	2120.96	2126.23	2120.04
BB	3055.85	3046.68	3062.03	3049.68

Murray Ridge Instrument Depth (m)				
Instrument	01/03/05-05/27/06	05/27/06-01/27/07	01/27/07-11/25/07	11/25/07-12/31/09
TT	542.64	517.95	536.47	524.12
MT	1039.09	1026.70	1039.09	1026.71
MB	1957.85	1947.71	1966.31	X
BB	2890.59	2875.53	2887.85	2875.53

2.2.1 Argo Data Processing and Analysis

Real-time Argo floats undergo a general Quality Assurance/Quality Control (QA/QC) process before the data are made available (Schmid *et al.*, 2007); however, subsequent processing was required for the analyses conducted in this thesis. Based on climatology of the physical parameters in the region (Wyrtki *et al.*, 1971), unrealistic salinity and temperature values were identified and excluded.

The trajectory of each float was also plotted to determine whether latitude and longitude data were unrealistic or were on land. When a coordinate was determined to be unreliable, the entire profile associated with that location was removed. In some cases, pressure data were flagged as bad or missing data in the initial QA/QC process. When no pressure data were provided, the temperature and salinity from that depth were also removed.

All flagged data were replaced with the mean value of nearby profiles. Density was calculated from the salinity and temperature of each profile. Salinity, temperature and density profiles and time-series were plotted for each float. A visual inspection of each plot was used to verify data integrity.

Velocities were calculated using reported time and location at each station (Δgreat arc length/Δtime) and separated into north/south and east/west components. At a given depth, velocities greater than 3 standard deviations of all velocities at that depth were excluded, which accounted for less than 1% of the data. To construct velocity fields in the subsurface, the drifting depth of each Argo float was determined (1000m,

1500m and 2000m). East/west velocity was plotted against north/south velocity to verify that all outliers were removed (Figure 10).

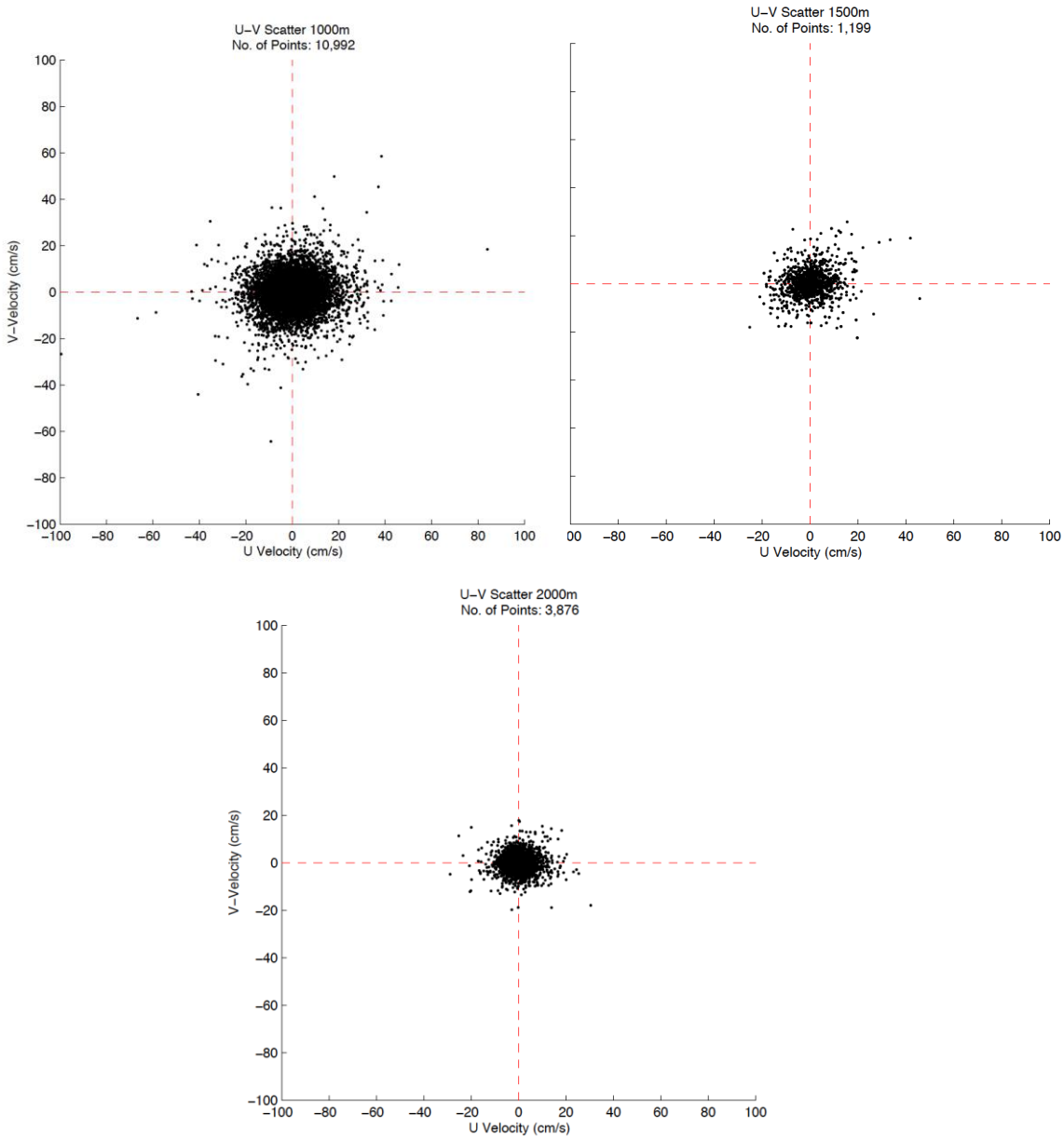

Figure 10. Scatter plots of U Velocity versus V Velocity (cm/s) at 1000m, 1500m and 2000m depth.

Because there is so much spatial and temporal variability in the study area, a velocity map was created at each depth with mean velocity for each season. Velocity data in each 2° by 2° box were averaged when at least three velocity vectors were present. For boxes with less than three velocity vectors, no mean velocity was plotted. The box was then shifted by 1°, i.e., 50% overlap of 2˚x2˚ boxes, and the same process was performed. Using this technique, every two velocity vectors are independent. This method of averaging gave the best representation of known current velocities and patterns. Variance ellipses were also calculated for each 2˚x2˚ box. Each variance ellipse estimate includes calculating the mean of north/south and east/west velocity, the ellipse orientation (indicated by the mathematical angle), and the magnitude of the major and minor axes (Emery and Thomson, 1997). The variance ellipses were plotted over mean velocities on the same map to determine the whether or not the mean was a reliable representation of the velocity in each location.

Temperature-salinity (T-S) diagrams with superimposed isopycnal lines were generated to identify the presence or absence of water masses of the region. The T-S diagram was divided into six regions within the northwest Indian Ocean: the Arabian Sea (5˚N-20˚N, 54˚E-70˚E), the Somali Current (0˚-10˚N, 42˚E-52˚E), the East Arabian Current (17˚N-22˚N, 53˚E-60˚E), the Gulf of Aden (10˚N-16˚N, 42˚E-53˚E), the Sea of Oman (22˚N-26˚N, 56˚E-60˚E) and the Northeast/Southwest Monsoon Currents (3˚N-15˚N, 67˚E-80˚E) (Figure 11). Each region was selected based on previous knowledge of its unique characteristics.

Because of the dense water mass formation in the Red Sea and Persian (Arabian) Gulf, it is hypothesized that salinity stratification dominates in the northwest Indian Ocean. The T-S diagram was used for a qualitative analysis of the relative importance of

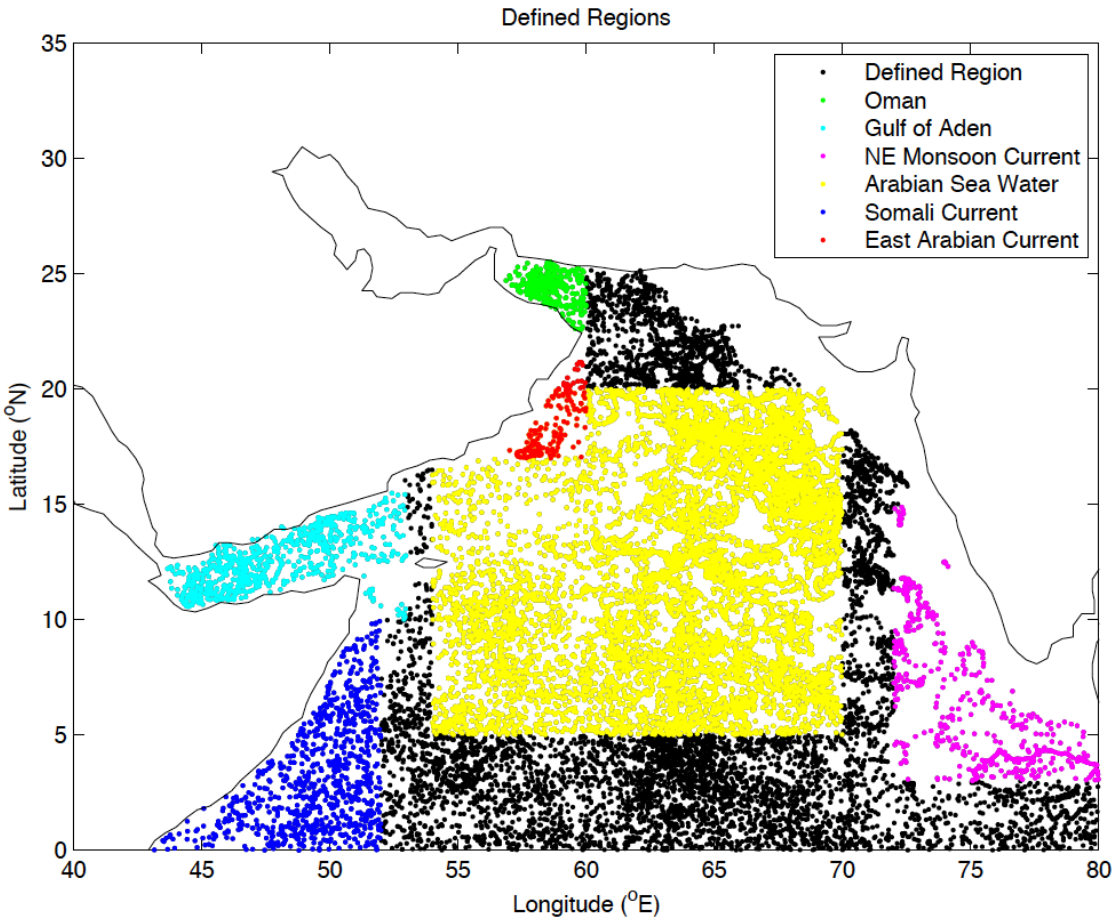

Figure 11. Map of the northwest Indian Ocean, with regions defined for hydrographic analysis. Arabian Sea Water is yellow and defined as 5°-20°N, 54°-70°E. The Somali Current is dark blue and defined as 0°-10°N, 42°-52°E. The East Arabian Current is red and defined as 17°-22°N, 53°-60°E. The Gulf of Aden is light blue and defined as 10°-16°N, 42°-53°E. The Sea of Oman is green and defined as 22°-26°N, 56°-60°E. The Northeast/Southwest Monsoon Currents are pink and defined as 3°-15°N, 72°-80°E.

salinity and temperature to vertical stratification. The importance was quantified using the formula for the density ratio found in McDougall (1987):

$$Rp = [\alpha(dT/dp)]/[\beta(dS/dp)]$$

T: temperature (°C)

S: salinity

p: pressure (Decibars, dbar)

α: thermal expansion ($\alpha=(-1/\rho)(\partial\rho/\partial T)$) ($°C^{-1}$)

β: saline contraction ($\beta=(1/\rho)(\partial\rho/\partial S)$)

ρ: density (kg/m^3)

2.2.2 Surface Drifter Data Processing and Analysis

The satellite-tracked drifting buoys undergo an initial QA/QC process. Errors in the data result primarily from instrumental noise and instrument-satellite communication. Surface drifters record current velocity, temperature, pressure, wind speed, ocean color and salinity (Lumpkin and Pazos, 2006). The assembly of the climatology is described in detail at http://www.aoml.noaa.gov/phod/dac/drifter_climatology.html (Lumpkin and Garraffo, 2005) and summarized here.

During preliminary processing, velocity data were corrected for slip (horizontal motion that differs from lateral current motion) by interpolating daily wind estimates onto the drifter position. The Ekman component was also removed from the velocities using wind stress estimates and the local Coriolis parameter. Lumpkin (2003) developed a methodology to correct for aliased time-mean values, which can result when the

presence of strong seasonal variations are neglected. The methodology decomposes the drifter observations into time-mean, seasonal and eddy components (Lumpkin, 2003). The climatology was originally developed for the tropical Atlantic since such strong seasonal variability is present, but can be applied to any drifter that may experience strong seasonal variability and risk aliased time-mean values (Lumpkin and Garraffo, 2005). Lumpkin and Garraffo (2005) further developed the decomposition methodology using SST observations and the Miami Isopycnic Coordinate Ocean Model (MICOM) model. The time-mean, annual and semiannual components of velocity and SST were used to give monthly averages.

Once the data were received, maps for annual, seasonal and monthly sea surface temperatures were plotted. Surface velocity was also plotted by month and by season. All maps were produced based on the surface drifter observations from 1995-2009.

2.2.3 Mooring Analysis

All moored data were received by Lighthouse R&D Enterprises, Inc., and processed by Texas A&M University. All processing included QA/QC procedures (DiMarco *et al*., 2008) to acquire a quality data set to be used in the analysis. Basic statistics were performed on the following data and saved as separate files for each instrument: current speed, depth, direction, east-west velocity, north-south velocity, dissolved oxygen, salinity, pressure, turbidity and temperature. Additional processing included the production of spectra for salinity, temperature, and current velocity smoothed with a 512 pt Kaiser-Bessel window and having 50% overlap.

Once the data were received for this thesis, the time-series of each deployment were combined to give one continuous time-series. Time-series plots of pressure, salinity, temperature, north/south velocity and east/west velocity were produced to identify outliers. The time-series plots were also used as an initial tool for pattern identification. The mean, standard deviation, maximum value and minimum value were calculated for temperature and salinity at each instrument.

2.2.4 Satellite Data Analysis

Average monthly SST maps were produced from July 2002-December 2008 for 0˚-35˚N and 40˚E-80˚E. Giovanni Ocean Color Time-Series Online Visualization and Analysis MODIS- Aqua Monthly Global 9-km Products (http://reason.gsfc.nasa.gov/OPS/Giovanni/ocean.aqua.shtml) allows the user to customize the SST map. The "Plot Type" chosen was "Lat-Lon Map, Time-averaged." This plot type averaged the data values for each data grid for the specified time range (the first day of the month through the last day of the month). The average was weighted by the data providers to account for uneven grid spacing. In the latitude dimension, the average is weighted by the difference between the sine of the latitude at the northern edge of the grid box and the sine of the latitude at the southern edge of the grid box. The edges of the grid box are the mid point between adjacent grid points. A more detailed description can be found at http://disc.sci.gsfc.nasa.gov/giovanni/giovanni_analysis_functions.shtml#latlon_ave. The scaling of the satellite-produced SST maps is the same as the SST scaling from surface drifters.

In addition to monthly SST maps, mean sea surface temperature maps were produced from September 2002-2008 for a smaller region centered around Cape Ras al Hadd. The region includes the Strait of Hormuz, Sea of Oman, and a portion of the Arabian Sea (16˚N-28˚N, 55˚E-66˚E). To investigate the SST spatial variability during the formation of the RAH Jet, September SST plots have a higher resolution than SST plots of the full region.

SSH anomaly maps were produced as GIF files for the 15th of each month between January 2000 and December 2009 for the entire study area. SSH anomalies are the difference between the satellite-observed sea surface height and the mean sea surface height. The Colorado Center for Astrodynamics Research (CCAR) Global Near Real-Time Sea Surface Anomaly Data Viewer (http://Argo.colorado.edu/~realtime/gsfc_ global-real-time_ssh/) also allows the user to customize their map. The "Geographical Region of Interest" input option was latitude from 0°-35°N and longitude from 40°E-80°E. For the "Bathymetry" all data in water deeper than 0m were plotted. The SSH anomaly values displayed range from -30 cm to 30 cm with a 5 cm interval.

SSH anomaly maps were also produced for the SST map dates shown in Böhm *et al.* (1999) to observe the progression of the Ras al Hadd Jet in 1995 and its affect on SSH as well as SST. Latitude was from 21°-24°N and longitude was from 59°E-62°E. All data in water deeper than 0m were plotted. To investigate the small SSH changes associated with the progression of the RAH Jet, a smaller SSH range and interval was chosen. The SSH values displayed range from -14 cm to 14 cm with a 2 cm interval.

In the SSH and SST results, a map may be referenced as representative of patterns seen for a particular month or season. A SSH Anomaly map for every month can be found in Appendix A. A SST map for every month can be found in Appendix B.

2.2.5 Comparison of Argo and Moored Data

The purpose of comparing moored data to Argo data was to lend credibility to the moored observations. Moored data had been collected for five years. Instruments were replaced with newly calibrated, laboratory-tested and deck-tested instruments approximately every 12 months. Since no in-situ measurements from an additional data source have been compared to the moored data, Argo float data can provide an assessment of moored sensor performance.

To begin the comparison, all Argo profiles within 50 kilometers of each mooring were identified (Figure 12). A map of the location of each mooring and the Argo profiles within 50 kilometers of that mooring was plotted. A T-S diagram with superimposed isopycnals was created for each Ras al Hadd mooring and the Argo profiles that were within the defined range for each. Because no salinity measurements were available from the Murray Ridge mooring site, these data were excluded from the comparison for water density. In addition to the verification of the moored data, physical water mass properties were compared between each mooring around Cape Ras al Hadd.

Since few Argo measurements occur within 50km of each mooring from 2005-2009, a monthly average of temperature and salinity was compared. The date (month/year) of each Argo profile was determined. If three or more profiles occurred

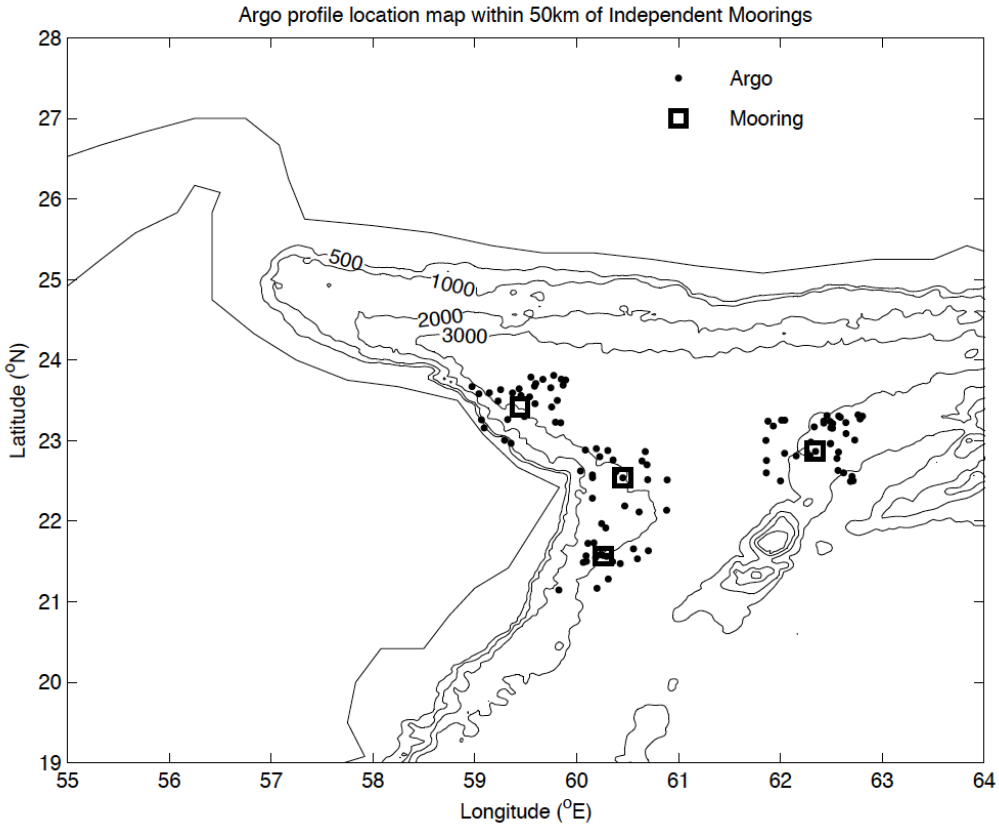

Figure 12. Map showing the locations of each mooring and the Argo profiles that fell within 50 km of each mooring.

during a given month, the temperatures were averaged and plotted against the average moored temperature for the same date (month/year). The same averaging process was also performed for salinity measurements in each data set. The standard deviation of Argo values subtracted from mooring values gave the standard deviation of the difference. The standard deviation of the difference was used to determine the acceptable error. For Murray Ridge, average Argo temperature was plotted against average moored temperature and a correlation was calculated.

2.2.6 Comparison of Argo Data and Numerical Model Numerical Output

SODA output is available beginning in 1871. The SODA model includes Argo data in its assimilation beginning in January 2002. To avoid bias, Argo data were compared to model numerical output from January 1992-December 2001. A T-S diagram with superimposed isopycnals was generated from model numerical output. The plot was divided into the same six regions as the T-S diagram generated from Argo data. This allowed the comparison of model numerical output to Argo data for each small region as well as the entire northwest Indian Ocean. A T-S diagram was also produced from model numerical output from January 2002-December 2008. The 1992-2001 (pre-Argo) T-S plot was compared to the 2002-2008 (with Argo) T-S plot to determine the effect of Argo observations on hydrographic fields in the numerical model. Model numerical output from 2009 was not yet complete so it could not be included in this comparison. Argo observations were subtracted from model numerical output. The standard deviation of the differences provided the amount of acceptable error.

Horizontal velocity fields from SODA model numerical output were generated at 1000m, 1500m, and 2000m depth for each month and season. The monthly velocity plots had a spatial resolution of 0.5 degrees occurring at 0.25 and 0.75 within each degree. Seasonal plots were averaged into 1° boxes. This was done to directly compare model numerical output to seasonal velocity fields estimated from Argo floats on the same spatial grid. The seasonal velocity plots produced from model numerical output were averaged in the same way as the Argo seasonal velocity plots, i.e., by averaging all velocities within a 2˚x2˚box, and shifting the box 1˚ at a time. Since each 2˚x2˚ box

contained 16 velocity output measurements (4 per 1˚x1˚ box), a resulting velocity output exists at every degree. Alternating velocity vectors are independent. Velocity plots were produced for model numerical output from 1992-2001. Velocities are not assimilated into the model at any point. Vector correlations (Crosby *et al*., 1993), scalar correlations and the statistical significance of the scalar correlations were calculated.

3. RESULTS

Results are divided into five subsections: velocity, sea surface height, hydrography, results of the mooring comparison and results of the model comparison.

3.1 Velocity

Velocity was determined primarily using data from Argo and surface drifters. Surface current velocity was calculated from surface drifter observations and subsurface current velocity was calculated from Argo observations. Velocity ranges from all measurements will be described for 1000m, 1500m and 2000m. Mean seasonal velocities will also be described.

3.1.1 Overview of Velocity

The initial analysis of velocity included all the Argo data from 2002-2009 (Figure 10). The maximum velocity at 1000m depth is 103.0 cm/s. The variance had a major axis of 7.9, a minor axis of 6.3 and an orientation of 10.4˚. The maximum velocity at 1500m depth is 46.2 cm/s. The variance had a major axis of 9.2, a minor axis of 6.2 and an orientation of -0.8˚. The maximum velocity at 2000m depth is 35.3 cm/s. The variance had a major axis of 4.0, a minor axis of 3.1 and an orientation of -3.5˚.

3.1.2 Spring Mean Velocity

Along the Somali Coast, the current flows to the northeast with a maximum mean surface velocity of 67.7 cm/s (Figure 13a). From 50°E to 65°E, surface flow is to the west between 3°N and 6°N, and to the east between 8°N and 10°N. Between those two regions, anticyclonic circulation is present. Anticyclonic eddies are also present near

the southern coast of Oman off Cape Ras al Hadd, and around 10˚N and 70˚E near the western coast of India. In the Gulf of Aden, mean surface velocities are to the west.

At 1000m (Figure 13b), the maximum mean velocities flow southeast from the Gulf of Aden (24.7 cm/s). An anticyclonic eddy is present near the Somali coast and in the Sea of Oman. A cyclonic eddy is observed in the Gulf of Aden. There were no obvious circulation patterns in the rest of the region at 1000m, and for the entire region at 1500m (Figure 13c) and 2000m (Figure 13d).

All velocities associated with the presence of eddies have a large variance. This is especially true for the eddies at 1000m depth near the Oman coast (Figure 13b). Large variance is also seen south of India from 0˚-5˚N and 75˚E-80˚E at 1000m (Figure 13b), and along the Somali coast at 1500m (Figure 13c).

3.1.3 Summer Velocity Patterns

Mean surface velocities in the summer are the largest along the southern Somali coast (up to 179.5 cm/s). The flow direction in the Arabian Sea is primarily to the east and southeast, though along the western coastlines of Somalia and Oman, flow is to the northeast. There are increased mean velocities flowing to the northeast along the southern coast of Oman (up to 52.3 cm/s). Anticyclonic circulation forms along the Somali coast as the flow separates from the coast. Anticyclonic circulation is also present in the Gulf of Aden. Mean velocities along the coast of India flow to the southeast and range from 17.0-51.2 cm/s. (Figure 14a).

At 1000m, current patterns along the Somali coast are similar to those at the surface. Maximum velocities occur along the coast of Somalia (up to 26.1 cm/s) and

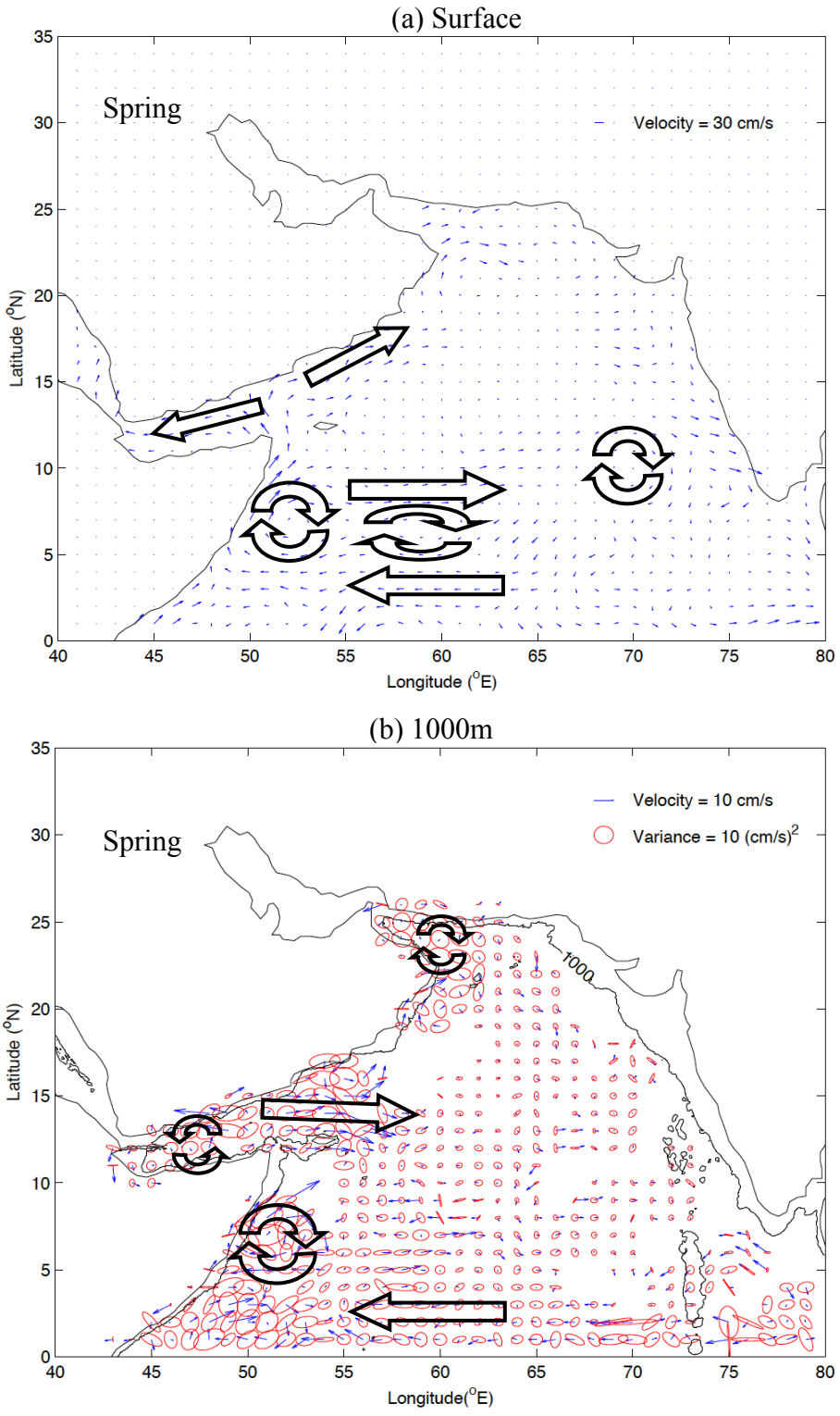

Figure 13. (a) Mean spring surface velocity. (b) Mean spring velocity at 1000m with 1000m isobath and variance ellipses.

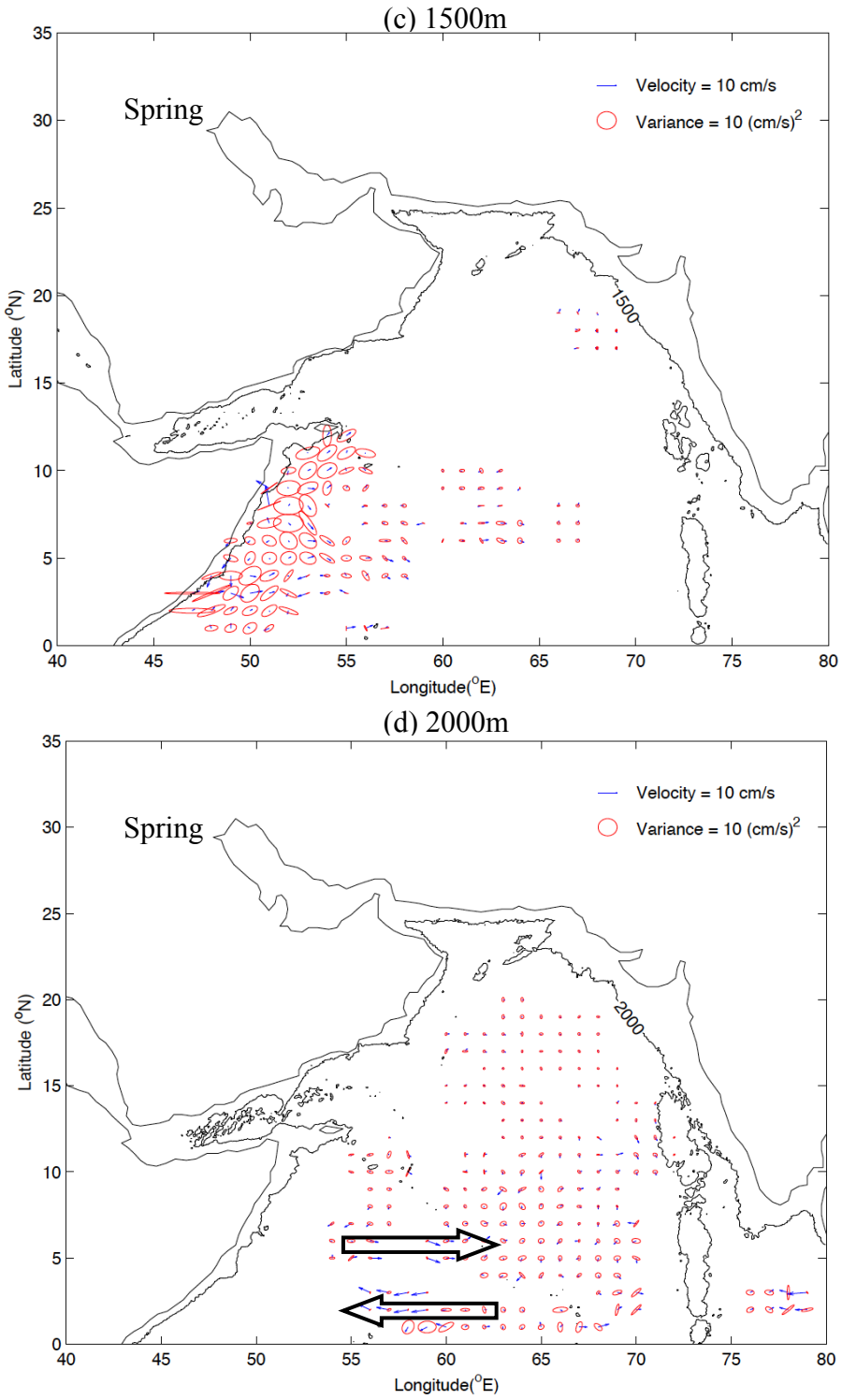

Figure 13 continued. (c) Mean spring velocity at 1500m with 1500m isobath and variance ellipses. (d) Mean spring velocity at 2000m with 2000m isobath and variance ellipses.

anticyclonic eddies form as the northeast current separates from the coast (Figures 13b and 14). Large variance is seen in velocities in the Gulf of Aden and in the Sea of Oman, but the trend in the Sea of Oman is to flow east. For most of the region at 1000m, flow is to the east and southeast. Along the equator, flow direction is uniformly to the east (east of 53°E). Though flow direction is uniform, speed decreases between 60°E and 70°E (Figure 14b). Data are sparse at 1500m, but an eastward flow direction exists along the equator between 50°E and 55°E (Figure 14c). Less data are available at 2000m than 1000m, but eastward/southeastward flow direction exists from 4˚N to 21˚N and 62˚E to 72˚E with decreased velocities (< 10 cm/s). Unlike the surface, 1000m and 1500m, direction is not uniform along the equator at 2000m (Figure 14d).

3.1.4 Fall Mean Velocity

During the fall (September-November), eddies are present at the surface and subsurface (Figures 15 and 16). Maximum mean surface velocities (up to 140 cm/s) occur along the southern coast of Somalia. The current flows to the northeast along Somalia and the southern coast of Oman. Flow along the Somali coast separates from the coast at several locations at the surface, forming anticyclonic circulation. Three adjacent anticyclonic eddies are aligned parallel to the Somali/Oman coast, with three cyclonic eddies to the southeast, also parallel to the coast. Flow between the group of anticyclonic eddies and the group of cyclonic eddies is to the southwest, parallel to the Somali and Oman coasts. Around 6˚N, the southwest current surface curves left, flowing east along the equator with a mean speed of 46.1 cm/s (Figure 16a). Flow is also to the east along the equator at 1000m (Figure 16b) and 2000m (Figure 16d). In the Gulf of

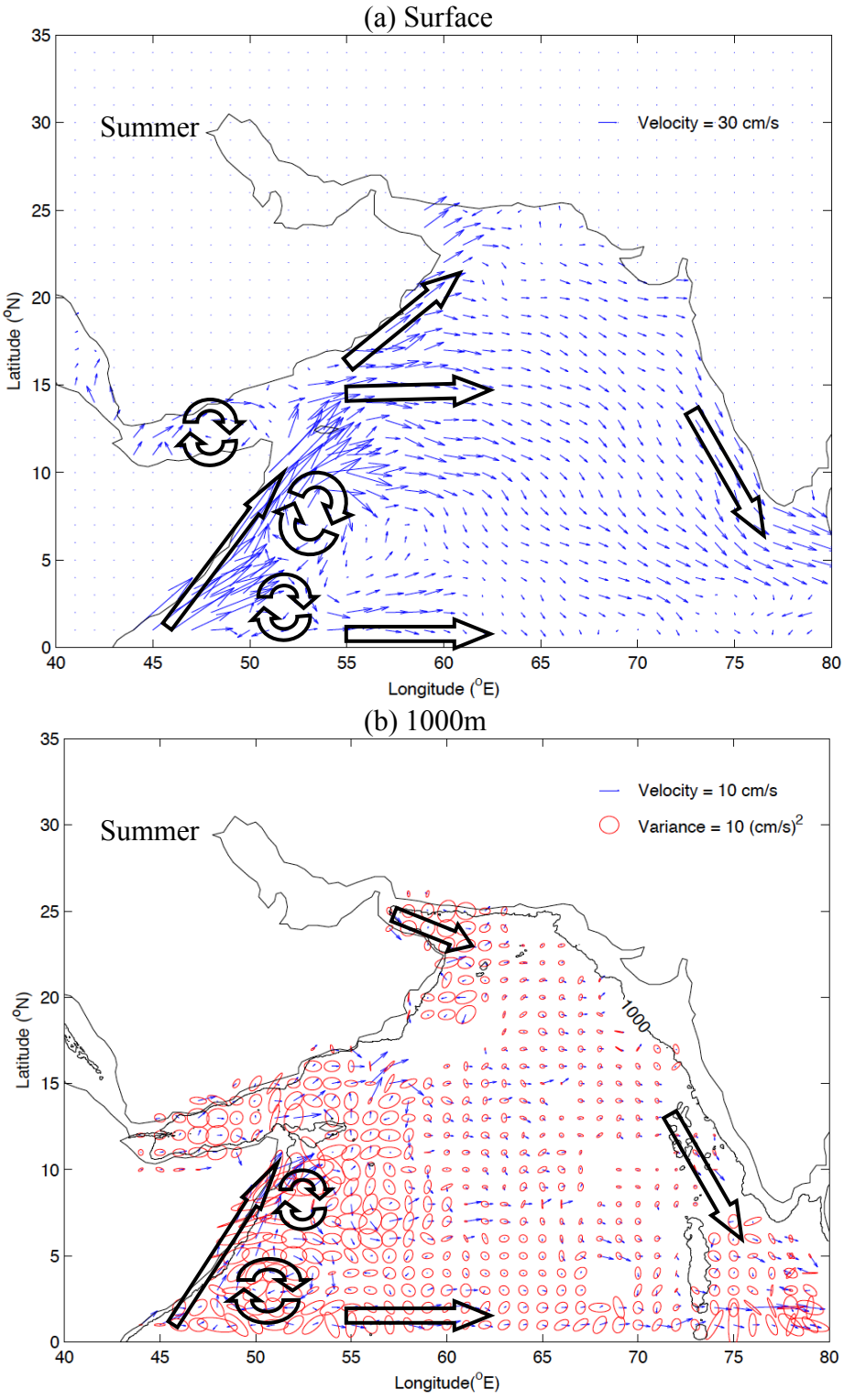

Figure 14. (a) Mean summer surface velocity. (b) Mean summer velocity at 1000m with 1000m isobath and variance ellipses.

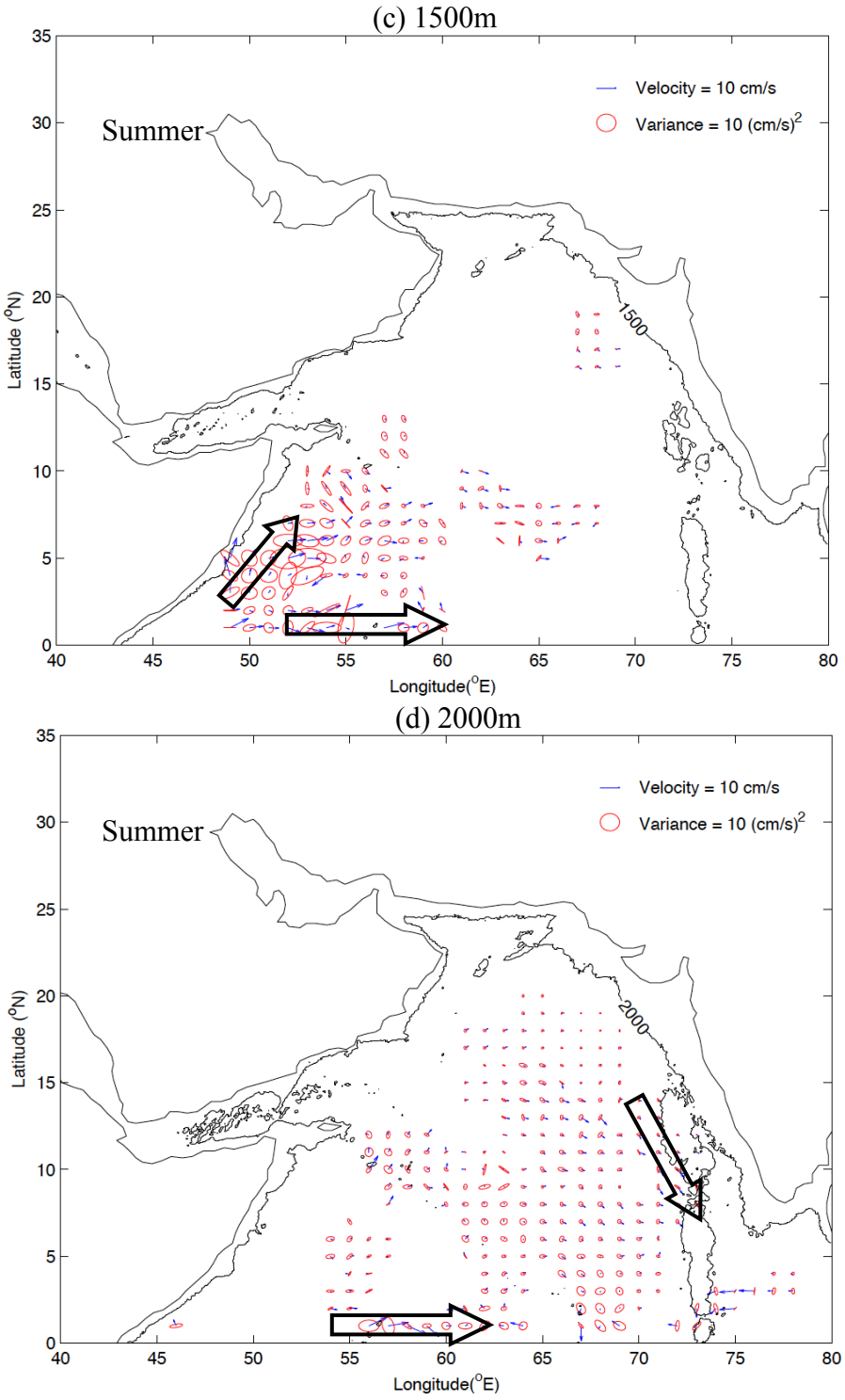

Figure 14 continued. (c) Mean summer velocity at 1500m with 1500m isobath and variance ellipses. (d) Mean summer velocity at 2000m with 2000m isobath and variance ellipses.

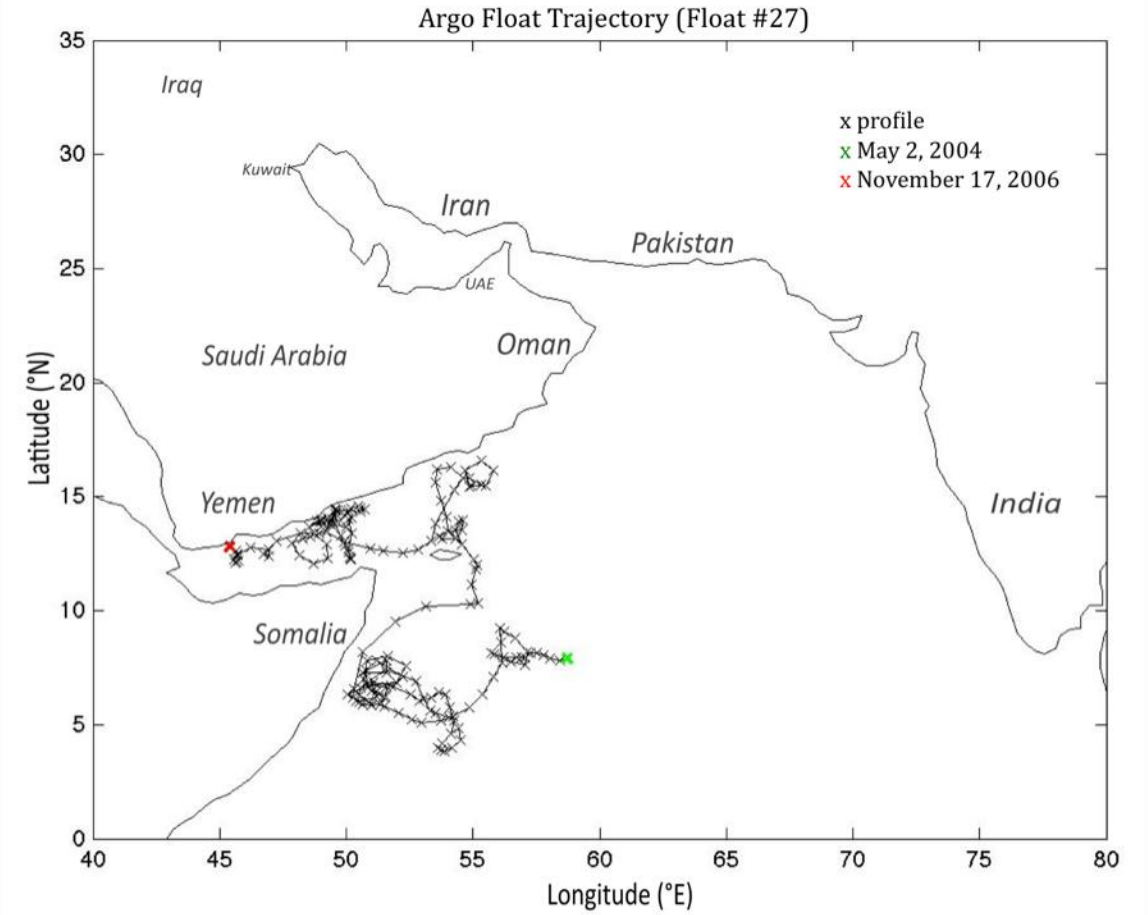

Figure 15. Trajectory for Float #27 (2900342), which begins May 2, 2004 and ends November 17, 2006. Drifting depth is 1000m.

Aden, the surface current is to the west with a maximum velocity of around 62 cm/s (Figure 16a).

At 1000m, a cyclonic eddy is present in the Sea of Oman. An anticyclonic eddy is seen near the Somali coast. Velocities associated with the eddy circulation have large variance (Figure 16b). An anticyclonic eddy is present at 1500m (Figures 15 and 16c) at the same location near the Somali coast, but has smaller velocities. Variance is not as large at this depth (Figure 16c).

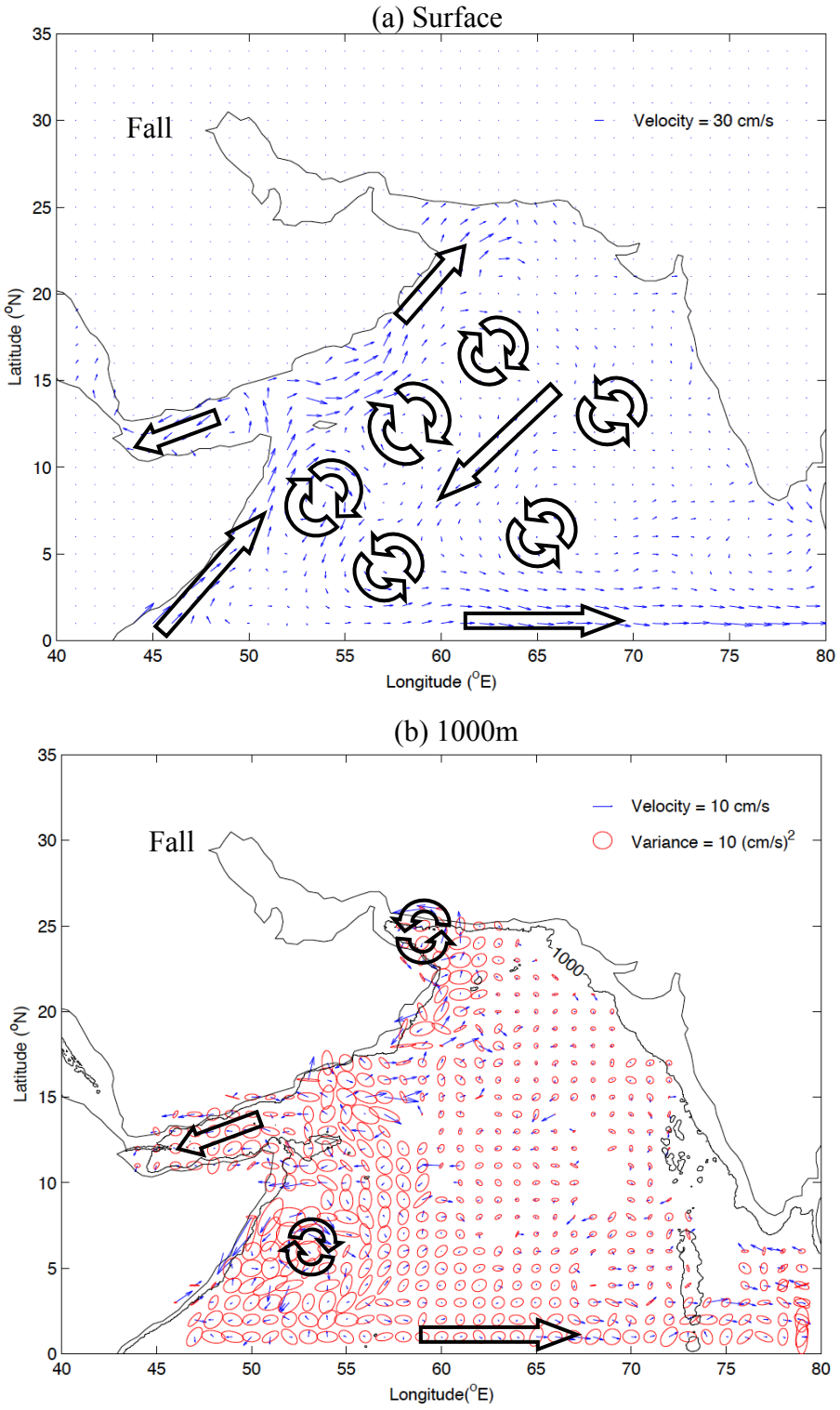

Figure 16. (a) Mean fall surface velocity. (b) Mean fall velocity at 1000m with 1000m isobath and variance ellipses.

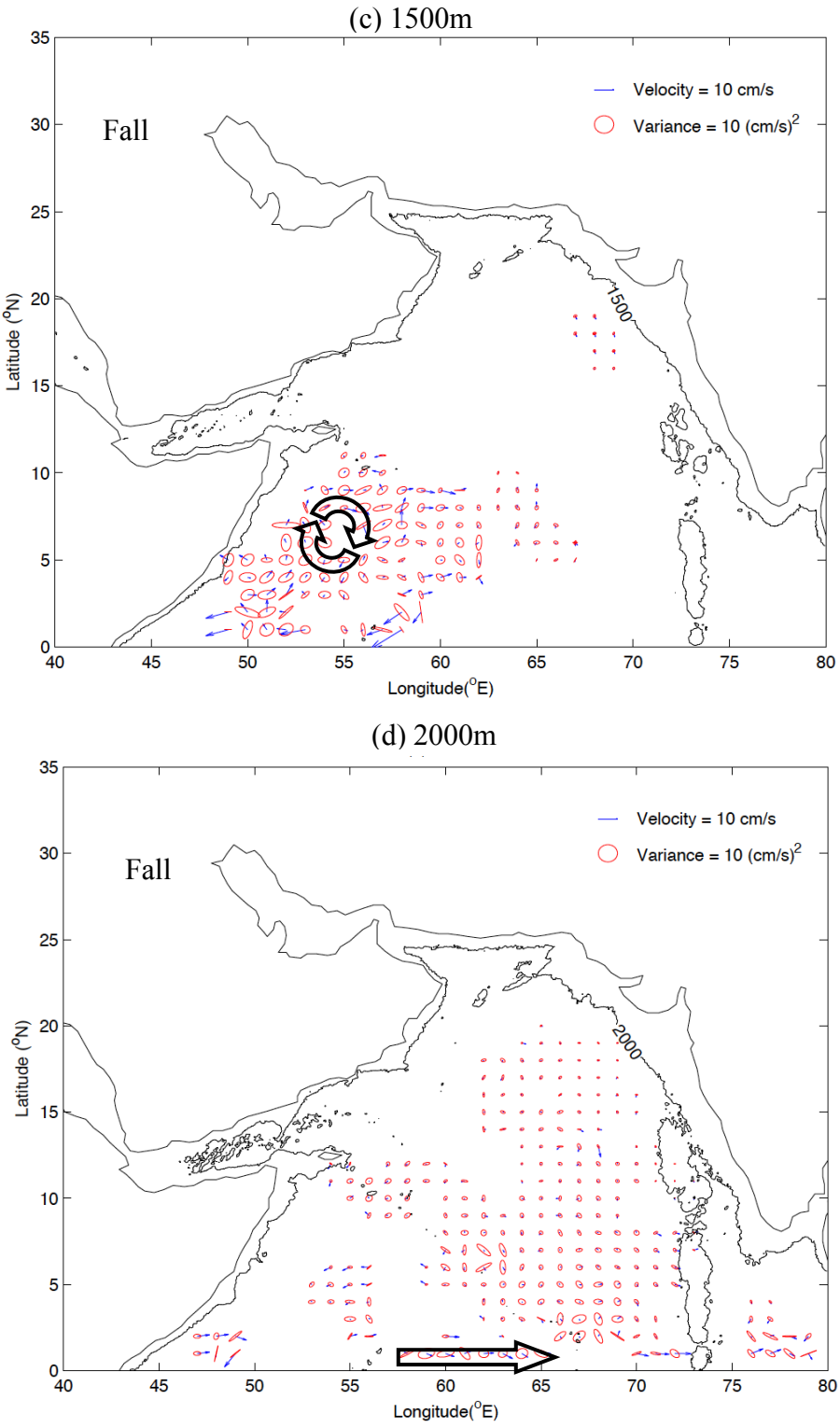

Figure 16 continued. (c) Mean fall velocity at 1500m with 1500m isobath and variance ellipses. (d) Mean fall velocity at 2000m with 2000m isobath and variance ellipses.

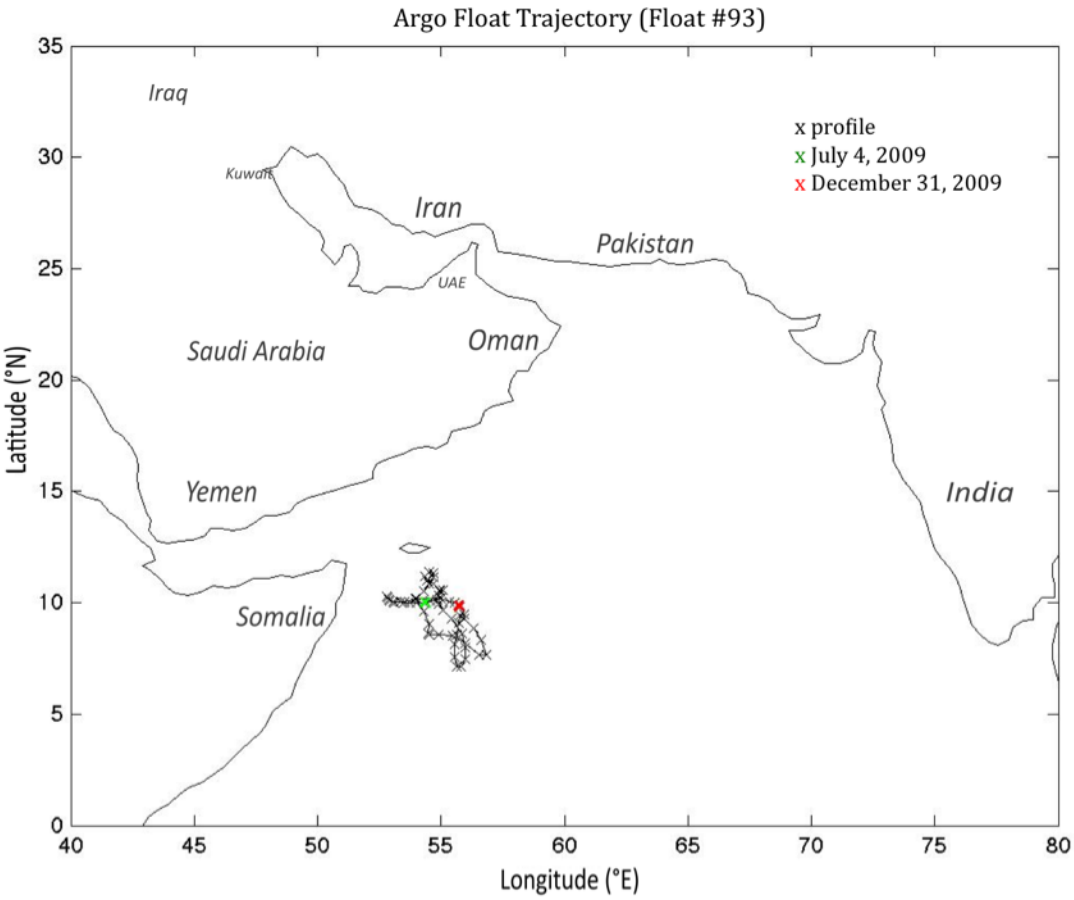

Figure 17. Trajectory for Float #93 (2901149), which began July 4, 2009 and ended December 31, 2009. Drifting depth is 1500m.

3.1.5 Winter Mean Velocity

In the winter (December-February), an anticyclonic eddy is still present at 1500m near the Horn of Somalia (Figure 17). Maximum mean surface velocities occur along the coast of Somalia, flowing to the southwest. The largest mean velocity is 97.3 cm/s, which occurs at 2°N and 46°E. An anticyclonic circulation is present near the tip of India, around 8°N and 75°E. Flow is westward along the equator from 0°-5N with a mean velocity of around 28.5 cm/s (Figure 18a). Flow is also to the west along the

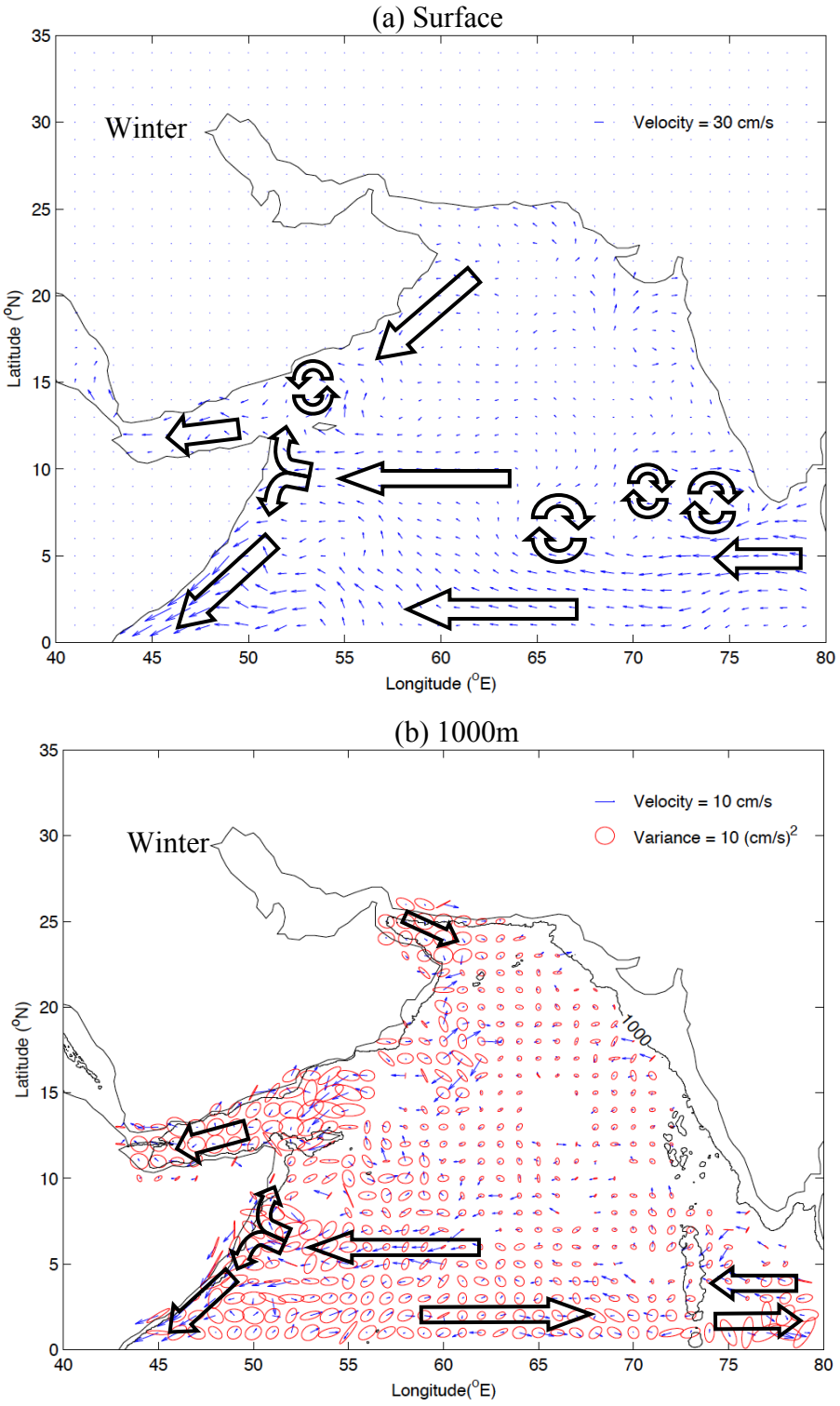

Figure 18. (a) Mean winter surface velocity. (b) Mean winter velocity at 1000m with 1000m isobath and variance ellipses.

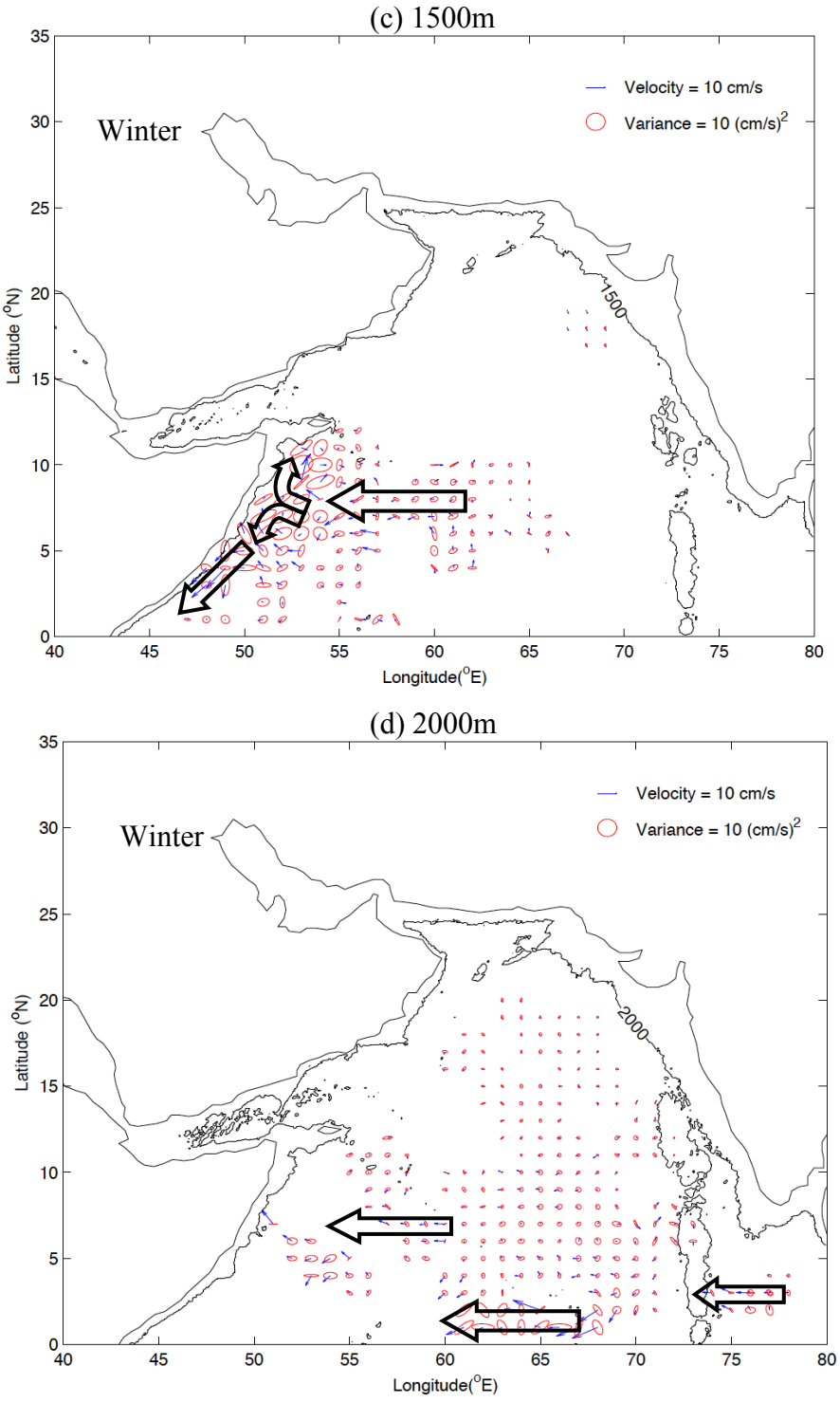

Figure 18 continued. (c) Mean winter velocity at 1500m with 1500m isobath and variance ellipses. (d) Mean winter velocity at 2000m with 2000m isobath and variance ellipses.

equator at 2000m (Figure 18d). In the Gulf of Aden, the surface current is to the west with mean velocities ranging from 8.3-40.2 cm/s (Figure 18a).

Between 8˚N to 12˚N and 51˚E to 63˚E, the surface current is to the west and diverges near at the coast of Somalia (Figure 18a). A similar pattern is present in the subsurface at 1000m (Figure 18b). From 5˚N to 7˚N, the current direction at 1000m is to the west and diverges as it reaches the Somali coast. Less data are available at 1500m depth, but a flow divergence is present at the Somali coast around 5°N. The direction of the flow before and after the divergence is unclear (Figure 18c).

At 1000m depth, anticyclonic circulation is present in the Gulf of Aden. Large variance is associated with velocities in the Gulf of Aden and Sea of Oman (Figure 18b).

3.2 Sea Surface Height

Particular patterns over the entire northwest Indian Ocean are present most clearly during the summer and winter seasons.

In the winter, a SSH anomaly of up to 25 cm exists along the coast of Somalia and the southern coast of Oman. In January, a band of raised SSH around 5-10 cm above sea level was seen stretching west from the tip of India along 5°N (Figure 19). This continues into February and March. Even though this increased elevation was present each year from 2000-2009, the maximum height varied.

In the summer, SSH decreases along the Somali and Oman coasts, reaching values of -30 cm in July and August of the eastern tip of Somalia (Figure 20a). Offshore and parallel to the Somali and Oman coasts, high SSH values are observed with values

usually reaching 30 cm above sea level in August (Figure 20b). Spring and fall SSH showed high variability from year to year (see Appendix A).

The remaining SSH results will be focused on the maps produced to observe the progression of the Ras al Hadd Jet in 1995. On May 20, a negative SSH was observed off Cape Ras al Hadd, with the smallest SSH around -8 cm (Figure 21a). One month

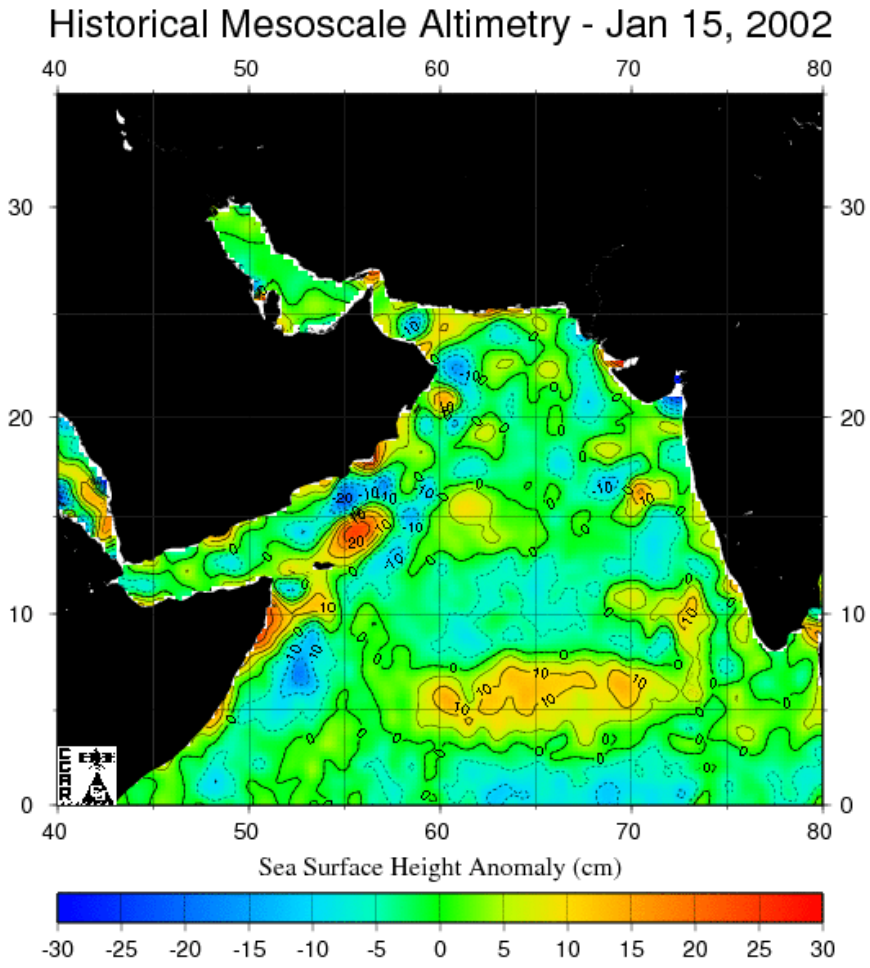

Figure 19. Sea surface height from January 15, 2002. This map is representative of Winter SSH from 2002-2009 (CCAR, 2009).

(a) July 15, 2008

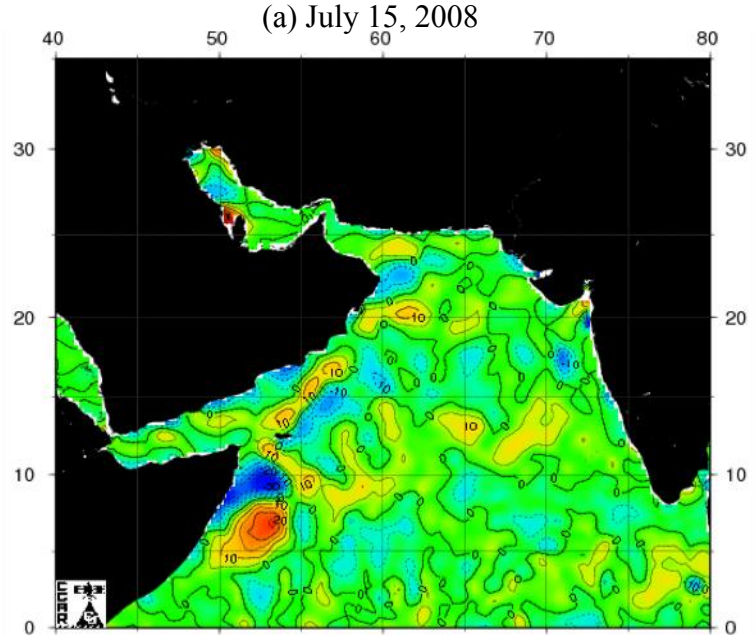

(b) August 15, 2008

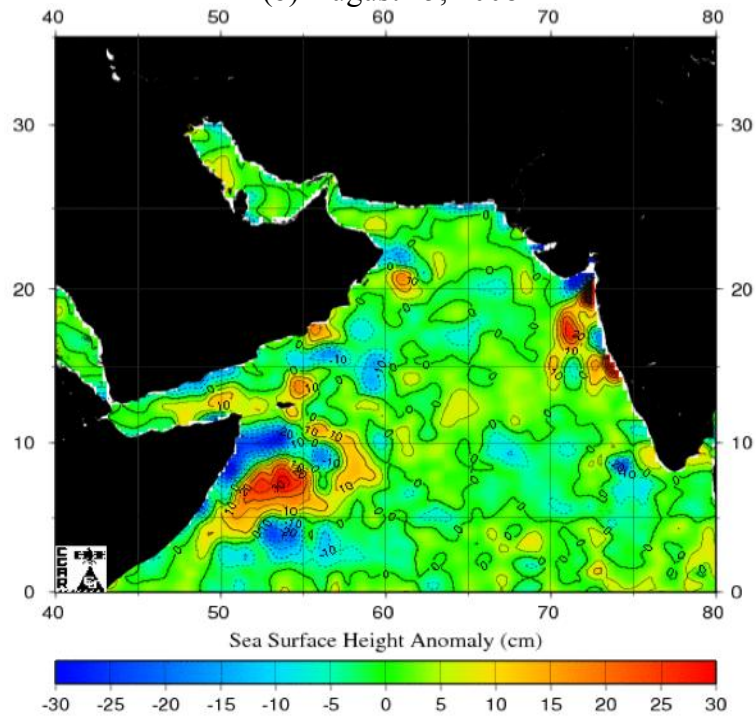

Figure 20. (a) Sea surface height from July 15, 2008. (b) Sea surface height from August 15, 2008. These maps are representative of July and August SSH showing the largest SSH anomalies along the Somali coast from 2002-2009 (CCAR, 2009).

later on June 21, a negative SSH (-4 cm) was observed along the southern coast of Oman, but SSH increased to the east of Cape Ras al Hadd, reaching an elevation greater than 8 cm (Figure 21b). Maps produced for July 12 (Figure 21c) and July 18 (Figure 21d) showed three cells of elevated SSH. One cell occurred along the northern coast of Oman, a second offshore from the southern coast of Oman, and the third existed to the east of Cape Ras al Hadd. All three cells had a maximum SSH around 8 cm. The regions surrounding the three cells had a negative anomaly with a minimum around -8 cm. The region between each of the three high-SSH cells had no height anomaly. Figure 23 also suggests the formation of high and low pressure cells near Cape Ras al Hadd with evidence of eddy-formation.

By August, a high SSH anomaly (8-10 cm) remains off the northern coast of Oman and to the east of Cape Ras al Hadd with SSH of around 8 cm (Figure 21e). The increased SSH off Cape Ras al Hadd continues into September, having maximum a maximum SSH anomaly greater than 9 cm on September 14 (Figure 21f). By September 19, the SSH decreased to 8 cm (Figure 21g). The concentrated area of increased SSH no longer exists by the end of October, but spreads to the south between 60°E-61°E (Figure 21h). Eddy formation is present over three years at 1000m (Figure 22).

3.3 Hydrography

Hydrography of the northwest Indian Ocean is separated into two sections: surface hydrography and subsurface hydrography. Surface drifters and satellite imagery provide surface hydrographic measurements (temperature). Subsurface hydrography

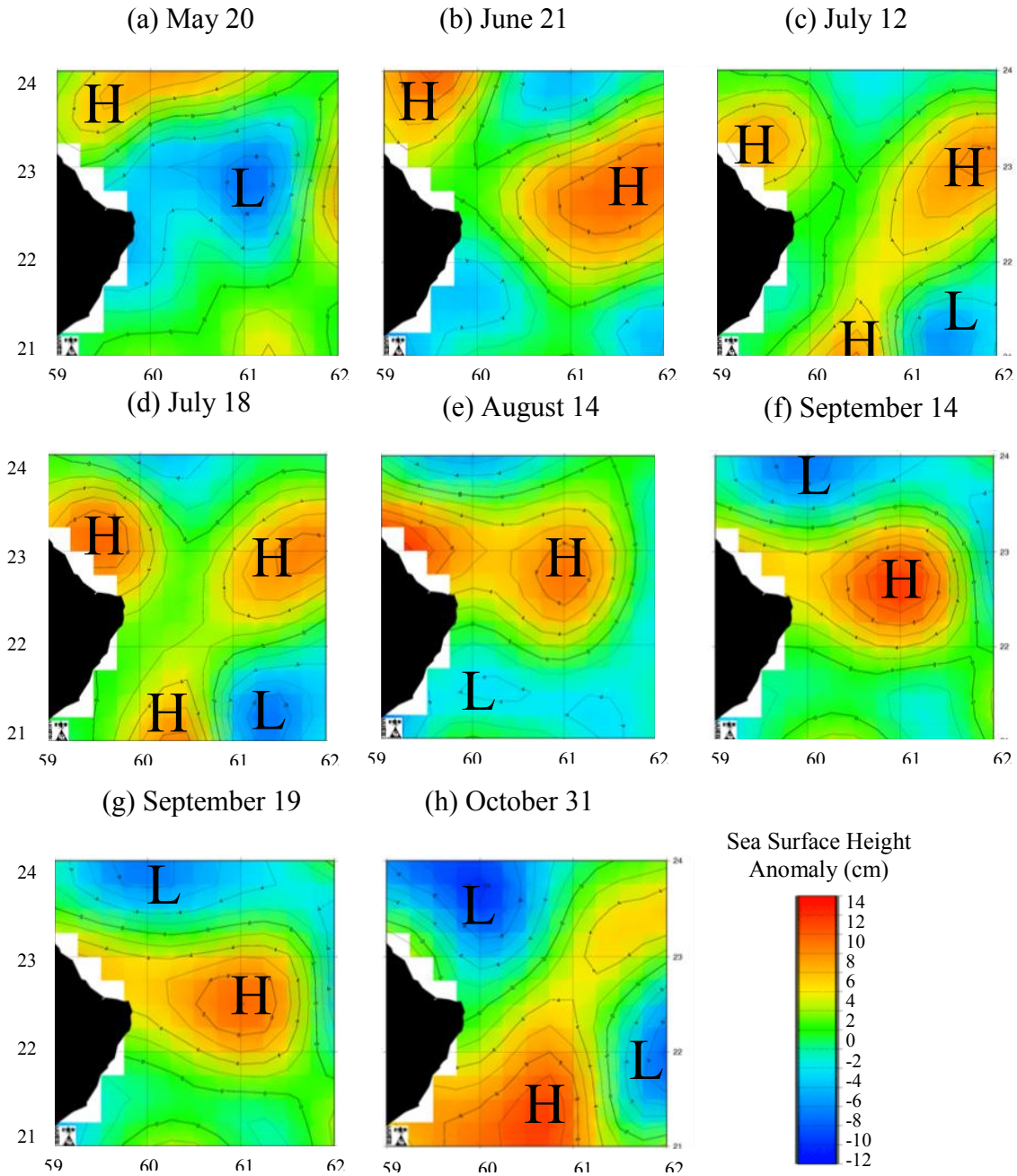

Figure 21. Progression of Ras al Hadd Jet sea surface height from May through October based on sea surface temperature dates found in Böhm *et al.* (1999). Maps were generated by Colorado Center for Astrodynamics Research (CCAR) Global Near Real-Time Sea Surface Anomaly Data Viewer (CCAR, 2009).

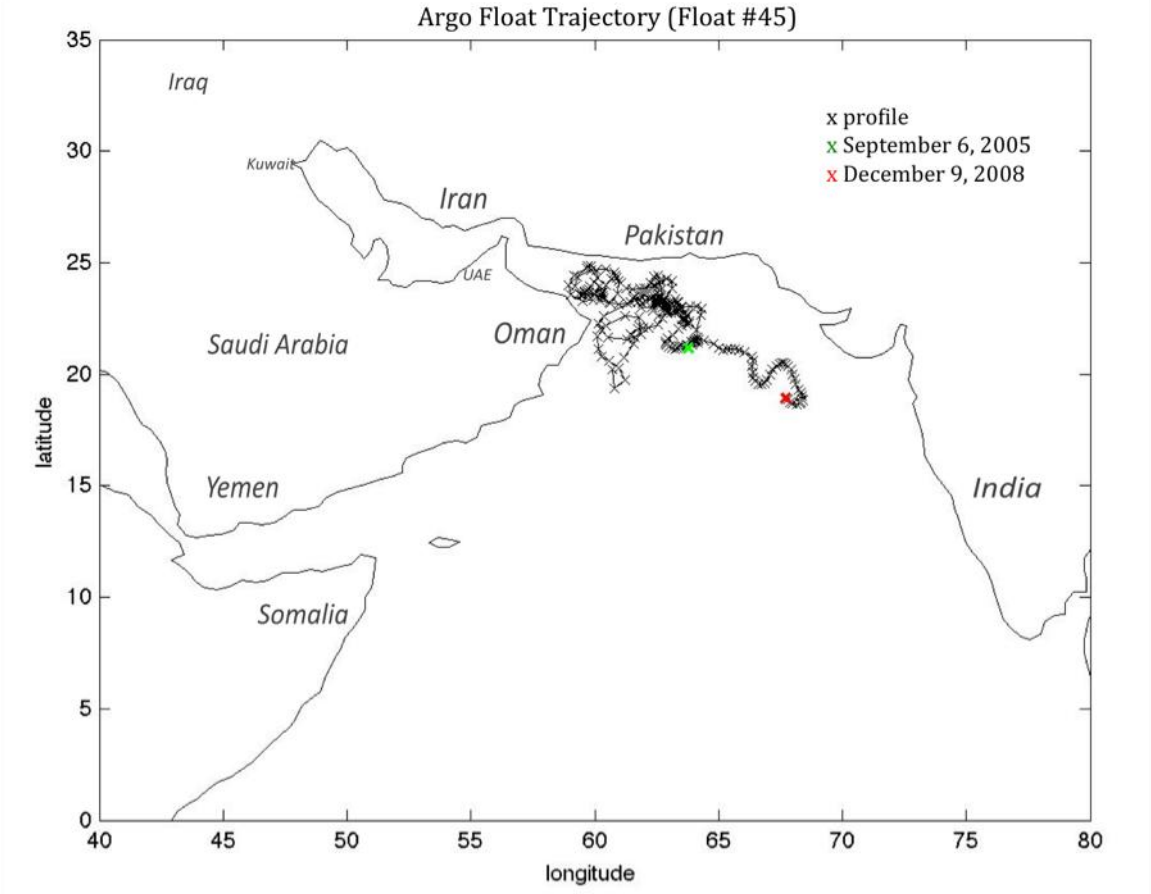

Figure 22. Trajectory for Float #45 (2900554), which began September 6, 2005 and ended December 9, 2008. Drifting depth is 1000m.

(salinity and temperature) will include the deep and near surface information provided by Argo data. Moored data also contribute to the subsurface hydrography.

3.3.1 Surface Temperature

Surface hydrography is estimated from the data of surface drifters and satellite imagery. No data are available in the Persian (Arabian) Gulf from surface drifters. Spring satellite SST in the Arabian Sea and Sea of Oman ranges from 23-32˚C. In March, a stronger north-south gradient of temperatures can be seen (Figure 23a). In

April and May, the mean temperature increases, with temperatures ranging from 26-32˚C (Figure 23b). Similar temperature ranges can be seen in the surface drifter SST. Surface drifter SST shows cooler temperatures in May in the northern Sea of Oman, ranging from 22-23˚C (Figure 24).

During the month of June, most of the Arabian Sea, Sea of Oman, Gulf of Aden, and marginal seas have SST ranging from 30-33˚C with the coolest temperatures occurring along the coast of Somalia (down to 23˚C) (Figure 25a). Through July and August, the cool SST along the Somali coast extends to the north and east with SST from 23-27˚C covering around half of the Arabian Sea surface. SST remains greater than

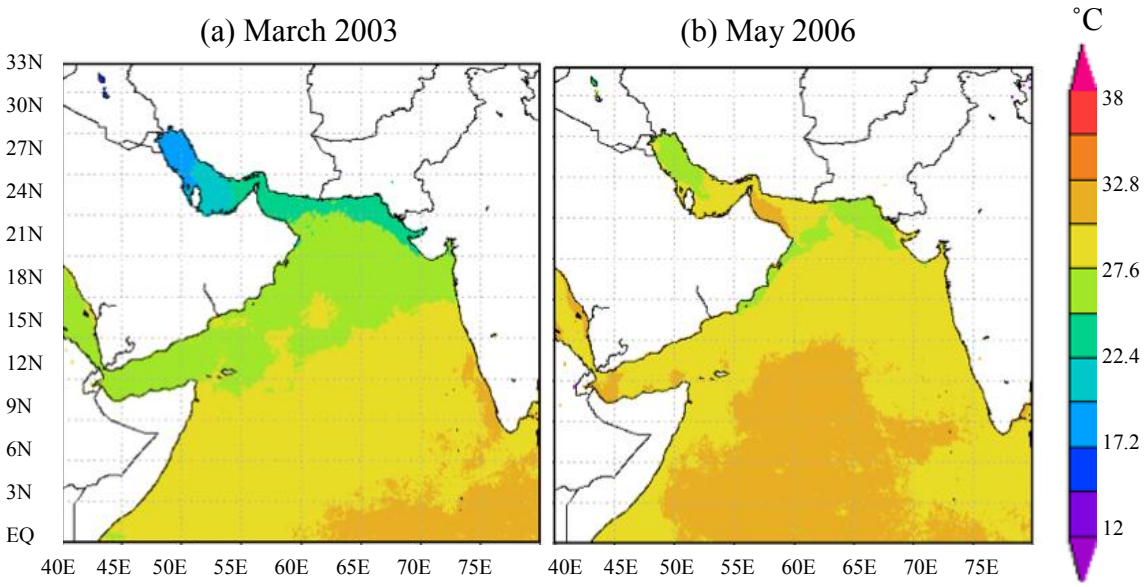

Figure 23. Sea surface temperature maps generated by NASA'S Giovanni (Kempler, 2011). (a) SST map for March 2003, representative of all March SST maps from 2003-2008. (b) SST map for May 2006 representative of all May SST maps from 2003-2008.

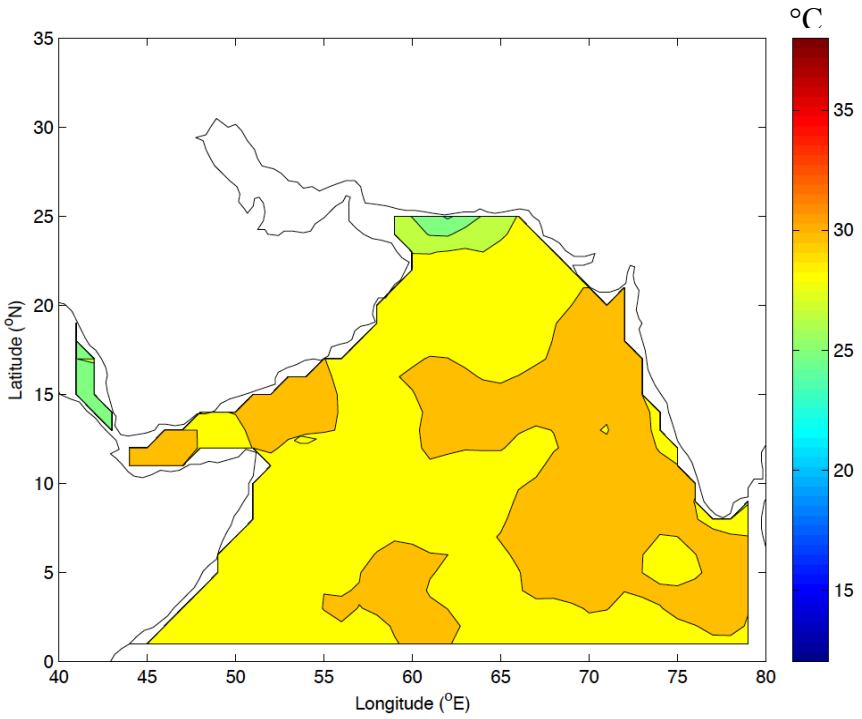

Figure 24. May mean sea surface temperature from surface drifter climatology.

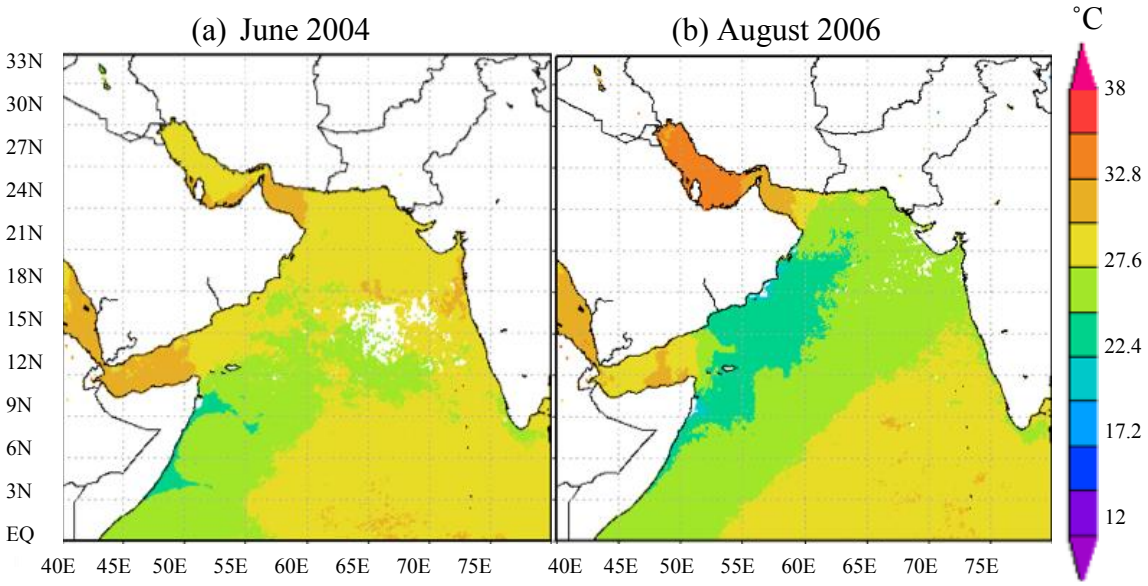

Figure 25. Sea surface temperature maps generated by NASA'S Giovanni (Kempler, 2011). (a) SST map for June 2004, representative of all June SST maps from 2003-2008. (b) SST map for August 2006 representative of July and August SST maps from 2002-2008.

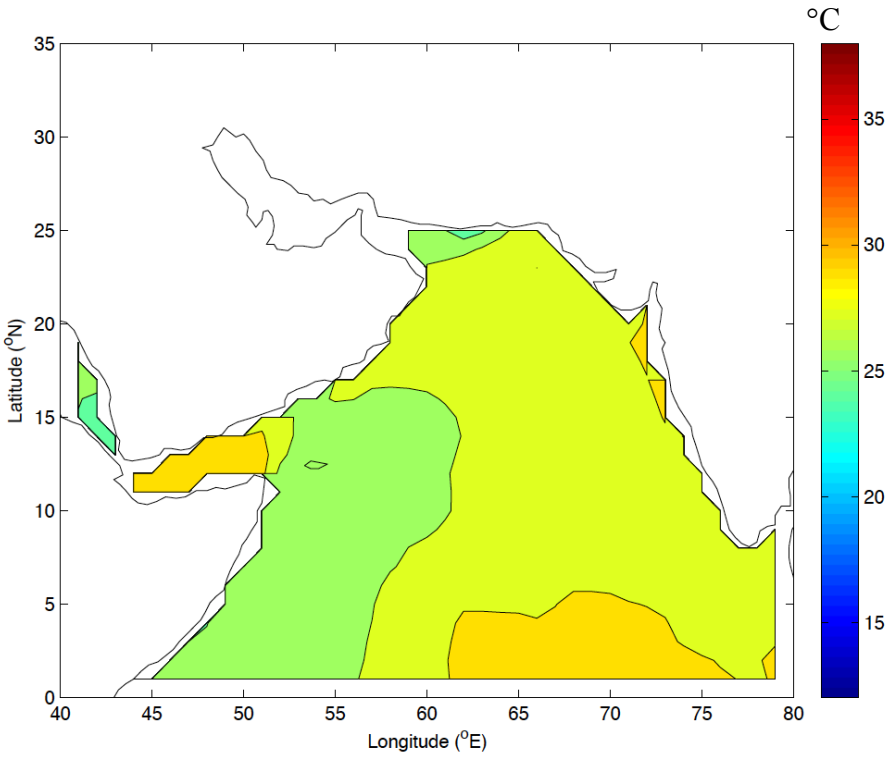

Figure 26. July mean sea surface temperature from surface drifter climatology.

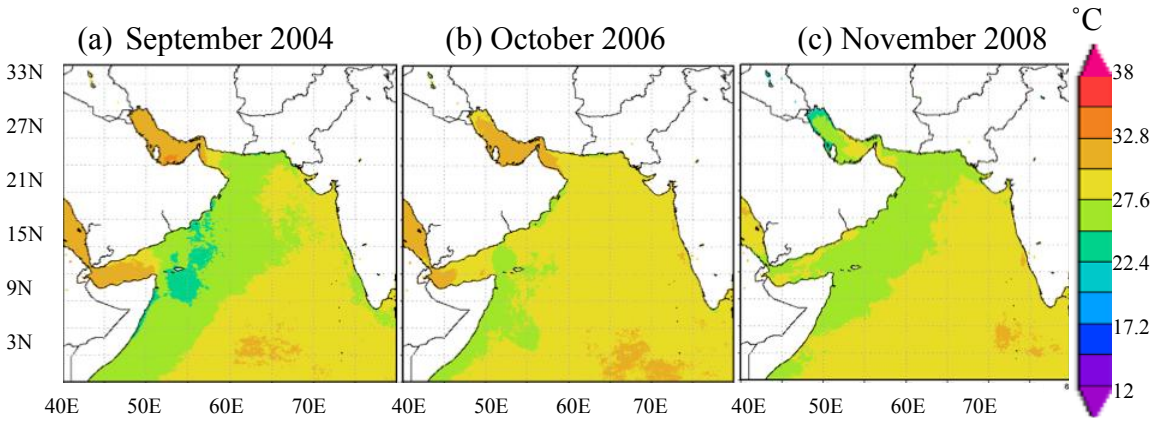

Figure 27. (a) SST map for September 2004, representative of all September SST maps from 2002-2008. (b) SST map for October 2006 representative of October SST maps from 2002-2008. (c) SST map for November 2008 showing minimum temperatures in the northern Persian (Arabian) Gulf.

30˚C in the shallow marginal seas (Red Sea and Persian (Arabian) Gulf), Gulf of Aden, and the western region of the Sea of Oman (Figure 25b). SST from the drifter climatology is similar to the large-scale spatial and temporal distribution of SST from satellite imagery. Drifter SST climatology shows cool temperatures between 23-27˚C occurring in the northern Sea of Oman along the coast of Iran and Pakistan (Figure 26). Satellite imagery shows cooling along this coast, but with SST between 25-27˚C (Figure 25b).

In September, cooler temperatures from 23-27˚C occur along the Somali and Oman coasts, but do not extend to the east as far as in the summer (Figure 27a). By October, the temperature range is similar to what is observed in June, with SST ranging from 30-33˚C (Figure 27b). The coolest SST still exist along the Somali coast, but are still significantly warmer than the temperatures seen in that region during the summer. In the Persian (Arabian) Gulf, SST decreases in the north with temperatures between 23-25˚C (Figure 27c).

Winter SST in the Arabian Sea ranges from 23-31˚C with the coolest temperatures occurring at the northernmost region of the Arabian Sea and the Sea of Oman. SST in the Persian (Arabian) Gulf increases quickly with distance away from the northern coast (Shatt al-Arab River Delta) with temperatures of 18-22˚C representing most of the Persian (Arabian) Gulf surface. The lowest temperatures are near 13˚C (Figure 28). The drifter climatology for winter shows SST ranging from 23-29˚C in the Arabian Sea and Sea of Oman (Figure 29).

SST maps were produced for September from 16˚N-28˚N and 55˚E-66˚E near Cape Ras al Hadd, which have a higher spatial resolution than the maps of the full region. Changes on temperature of 1.1°C can be identified with the higher resolution. SST in the Persian (Arabian) Gulf exceeds 33˚C, which decreases to 30-31˚C in the Strait of Hormuz. SST continues to decrease reach 27-28˚C as it enters the Arabian Sea from the Sea of Oman. Coolest temperatures occur along the southern coast of Oman. SST of around 26˚C extends to the east at Cape Ras al Hadd. Along the southern Oman coast temperatures are much cooler, with minimum temperatures between 22˚C-23˚C (Figure 30).

3.3.2 Subsurface Hydrography

The temperature from the surface to 2000m has a range from 1.14°C-33.46˚C (Figure 31). Salinity ranges from 31.49-39.44. Because salinity and temperature are not uniform in all areas of the northwest Indian Ocean, each of the six regions was analyzed separately.

Arabian Sea Water makes up the largest portion of the northwest Indian Ocean. For all ASW, the temperature ranges from 1.14°C-31.81˚C. For temperatures less than 27˚C (greater depth), salinity ranges mainly from 34.33-37.0 with a few scattered measurements with higher salinity, which occur near the Gulf of Aden. Near the surface when ASW temperature is greater than 28˚C, salinity has a broader range of 33.71-37.20. The lower salinity values occur in the eastern Arabian Sea. ASW covers a broad range of density from 21-27.6 kg/m^3.

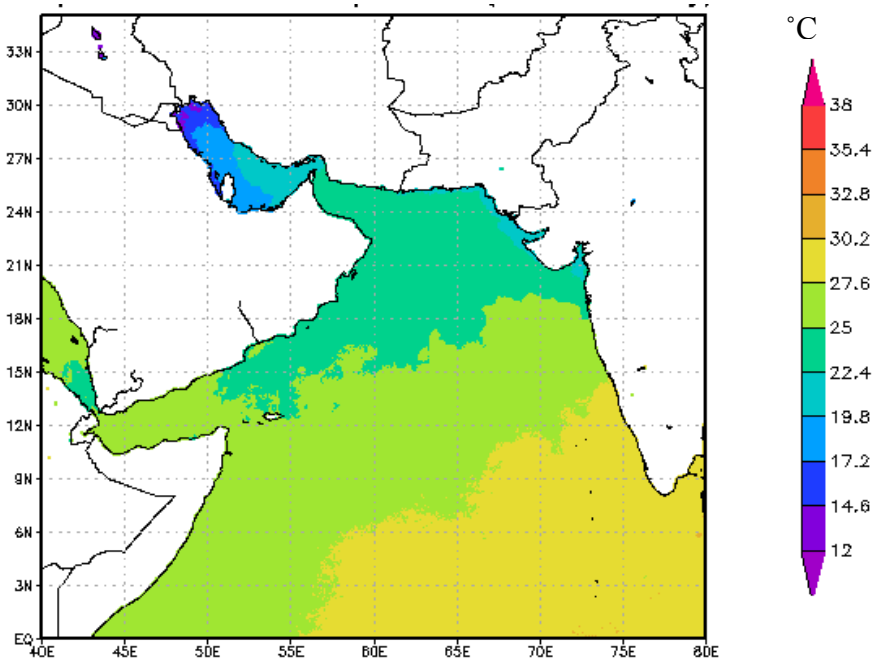

Figure 28. SST map for February 2008 showing cool temperatures occurring in the northern Arabian Sea and Sea of Oman. This map also shows cold temperatures around 13˚C occurring in the northern Persian (Arabian) Gulf.

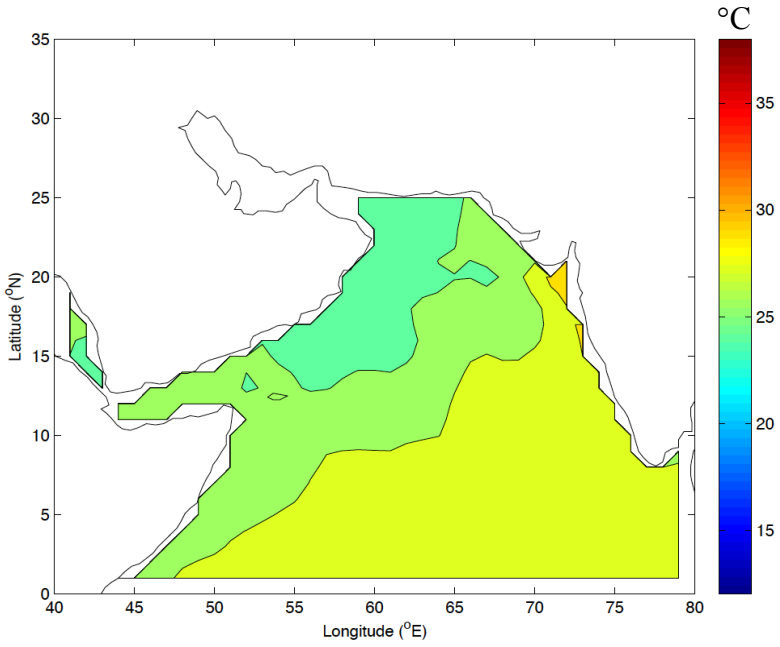

Figure 29. January mean sea surface temperature from surface drifter climatology.

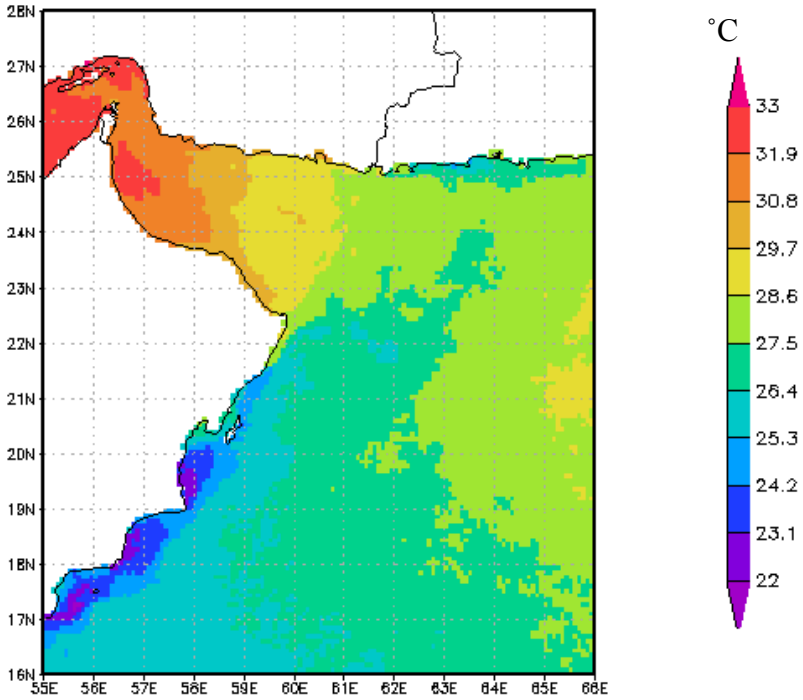

Figure 30. SST map for September 2005 showing 1.1˚C resolution temperature measurements near Cape Ras al Hadd.

The region along the coast of Somalia (defined as Somali Current) has a similar temperature range to Arabian Sea Water (1.38°C-30.64˚C). The Somali coast has a narrower salinity range and a lower mean salinity than Arabian Sea Water.

The East Arabian Current also has a similar temperature range as the Arabian Sea, but unlike the Somali Current, the East Arabian Current has a higher mean salinity than the Arabian Sea Main Water.

The Gulf of Aden has a temperature range of 2.94°C-32.03˚C and a salinity range of 34.82-39.44. While density covers a broad range from 22-27.5 kg/m^3, several measurements fall along a density of 27.3-27.4 kg/m^3. The Sea of Oman measurements have high salinities ranging from 35.18-38.09. Similar to the Gulf of Aden, the total

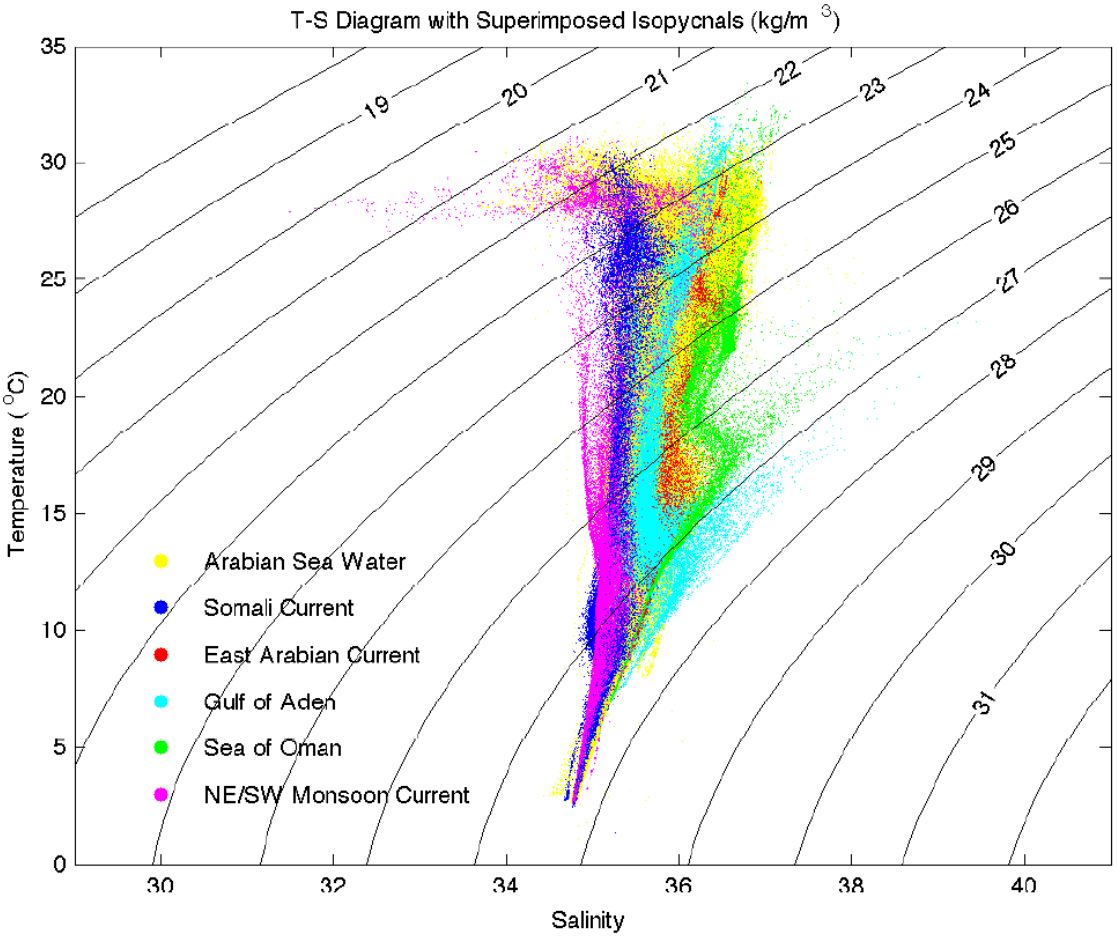

Figure 31. Temperature-salinity diagram of the northwest Indian Ocean with superimposed ispycnals generated from Argo data. Regions are bounded by the latitudes and longitudes described in Figure 11.

density covers a broad range from 22-27.6 kg/m^3, but several measurements fall along the 26.6 kg/m^3 isopycnal.

The Northwest/Southeast Monsoon Current is defined as the region along the west coast of India. Two distinct physical characteristics can be seen in the measurements from this region. One group of measurements has a broad range in salinity from 31.49-36.79 but a narrow range in temperature from 27.0°C-31.12˚C (near

the surface). The low salinity surface measurements were taken during the winter. The other group of measurements has a narrow salinity range from 34.43-36.62 and a broad temperature range from 2.58°C-27.0˚C (deeper in the water column) (Figure 31).

3.4 Mooring Comparison

In addition to the use of Argo float, surface drifter and satellite data, moored data were also analyzed. Argo data within a 50 km radius of each mooring were compared with the moored data.

When Argo data were compared with RHN, the T-S diagram shows an offset in salinity at 262m and 634m, with a mean mooring salinity 0.42 greater than mean Argo salinity (Figure 32a). The offset is not present in RHM (Figure 32b) and RHS (Figure 32c). Persian Gulf Water is present at all three moorings with a density around 26.6 kg/m^3. Salinity values of Persian Gulf Water decrease from RHN to RHM and from RHM to RHS. The decrease from RHN to RHM is primarily due to mixing along the northern coast of Oman. Beyond RHM, the extent of Persian Gulf Water is seasonal, as described in Morrison (1997). In the winter, Persian Gulf Water reaches RHS, but mixing causes a decrease in salinity. Temperature also decreases with depth. During the summer, Indian Center Water flows north to RHS, which also contributes low-salinity water mass characteristics.

Moored and Argo data sets were further compared using the mean monthly temperature and mean monthly salinity. Near RHN (Figure 33a), mean monthly salinity at 634m was from 35.32-35.37 for moored data and 35.34-35.36 for Argo data. At 1162m, moored salinity was from 35.50-35.51 while the Argo salinity was from 35.27-

(a)

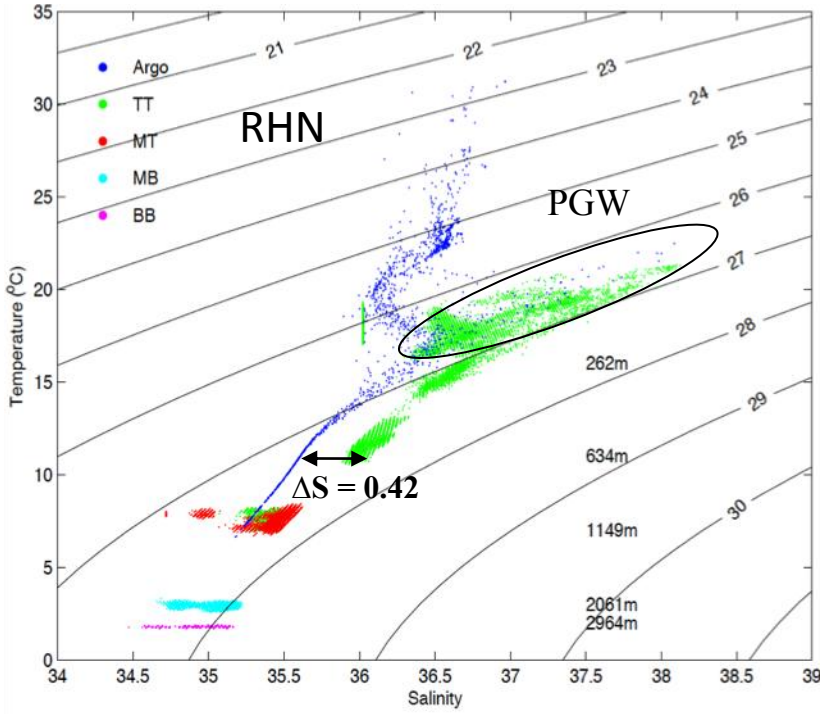

(b)

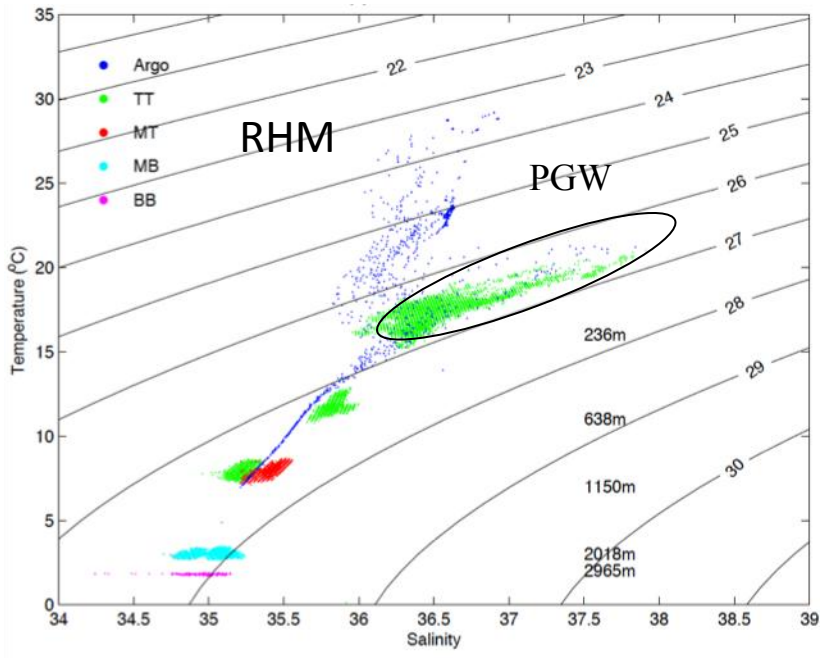

Figure 32. Temperature-salinity diagram with superimposed isopycnals (kg/m) for each mooring and Argo profiles within 50km of each mooring. (a) Measurements for Ras al Hadd North. (b) Measurements for Ras al Hadd Middle.

(c)

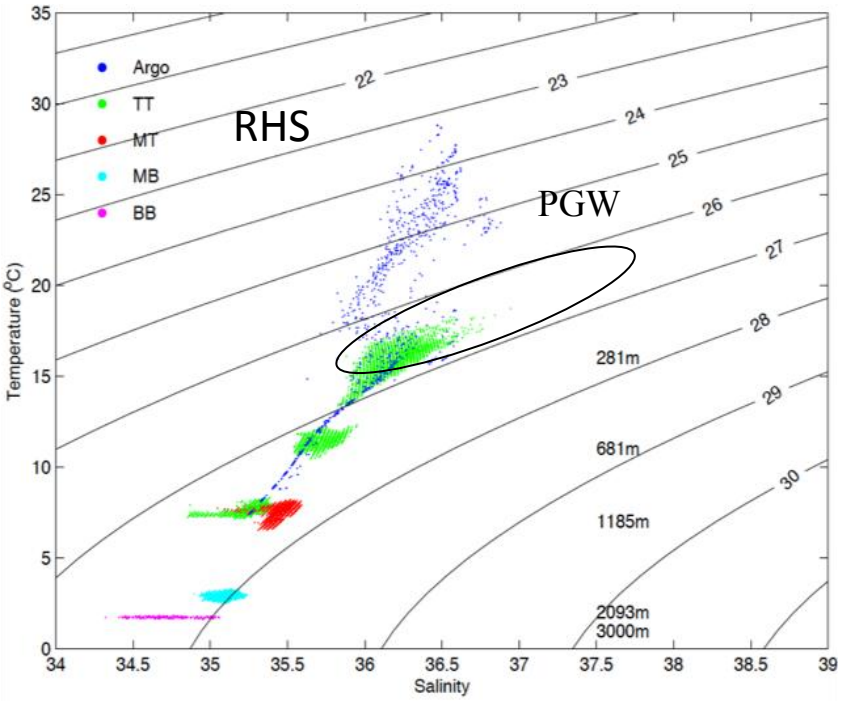

Figure 32 continued. (c) Measurements for Ras al Hadd South.

35.28. The standard deviation of the difference was 0.13. While the measurements at 634m had a maximum disagreement of 0.03, the differences in the measurements around 1162m were 0.22-0.23, which are greater than the standard deviation of the difference.

Mean monthly temperatures (Figure 33b) at 634m fell between 8.23˚C and 8.46˚C for Argo measurements, but moored measurements were between 7.57˚C and 7.72˚C. At 1162m, moored temperatures were between 7.77˚C and 7.91˚C. Argo temperatures were around 7.51˚C to 7.62˚C. The standard deviation of the difference was 0.53˚C. At 1162m, the greatest disagreement was 0.78°C, which is greater than the standard deviation of the difference.

(a)

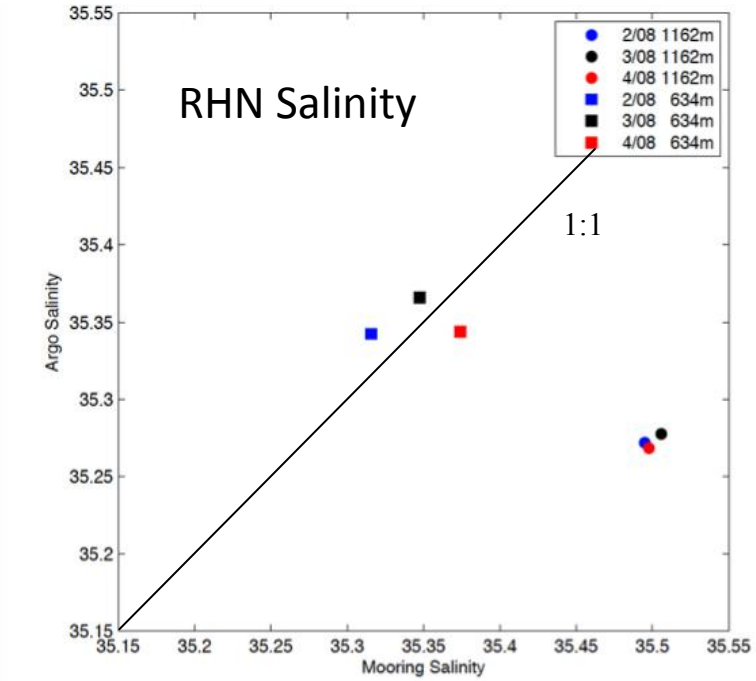

(b)

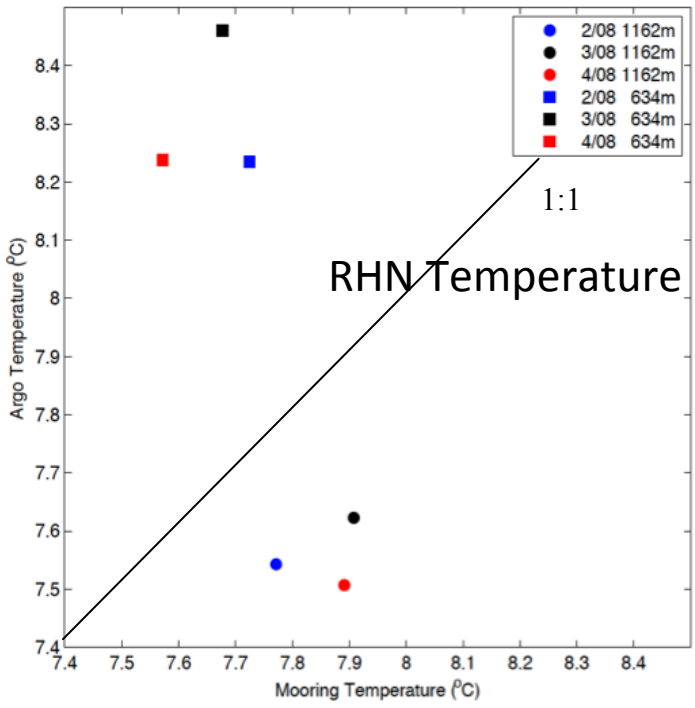

Figure 33. Ras al Hadd North (a) Moored salinity and Argo salinity measurements at 634m and 1162m for February 2008, March 2008 and April 2008. (b) Moored temperature and Argo temperature measurements at 634m and 1162m for February 2008, March 2008 and April 2008.

(a)

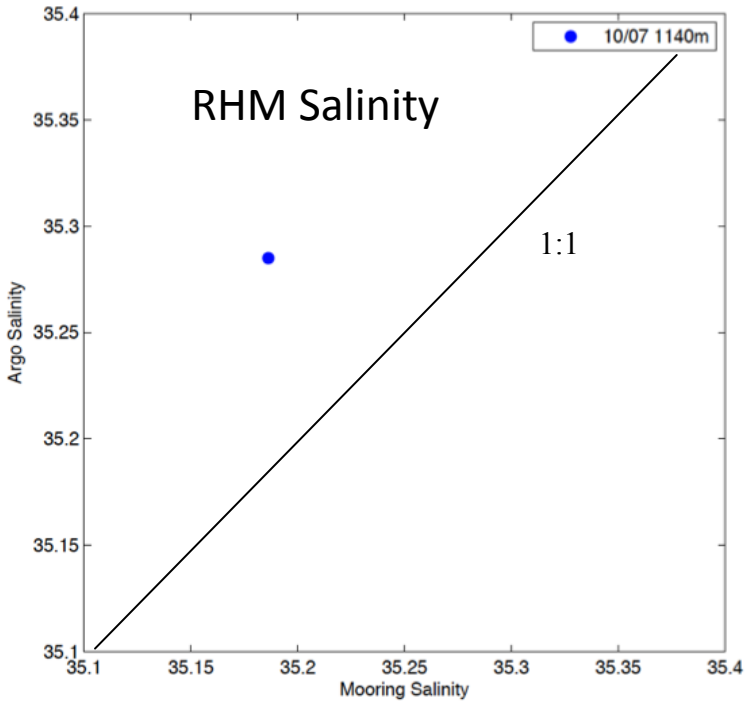

(b)

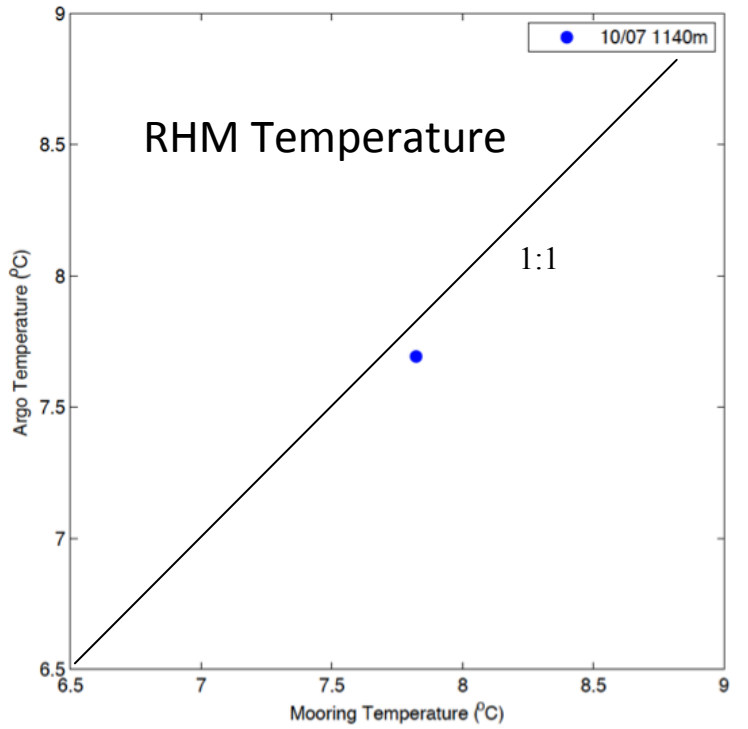

Figure 34. Ras al Hadd Middle (a) Moored salinity and Argo salinity measurement at 1140m for October 2007. (b) Moored temperature and Argo temperature measurement at 1140m for October 2007.

(a)

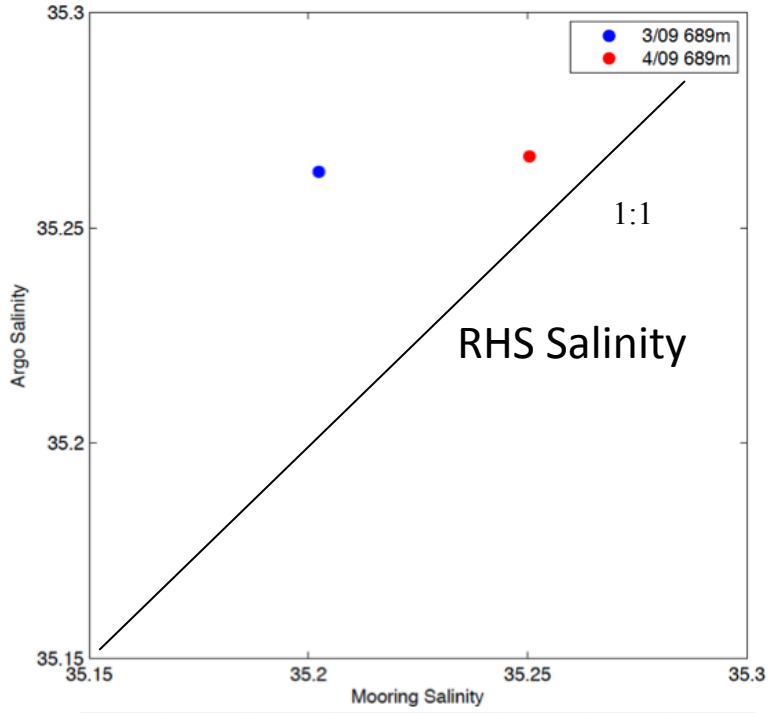

(b)

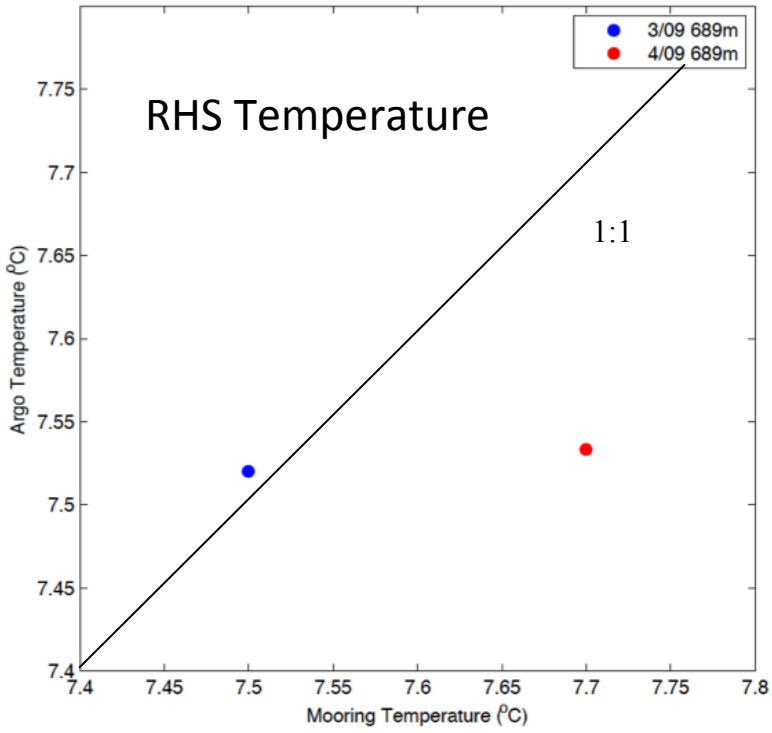

Figure 35. Ras al Hadd South (a) Moored salinity and Argo salinity measurements at 689m for March 2009 and April 2009. (b) Moored temperature and Argo temperature measurements at 689m for March 2009 and April 2009.

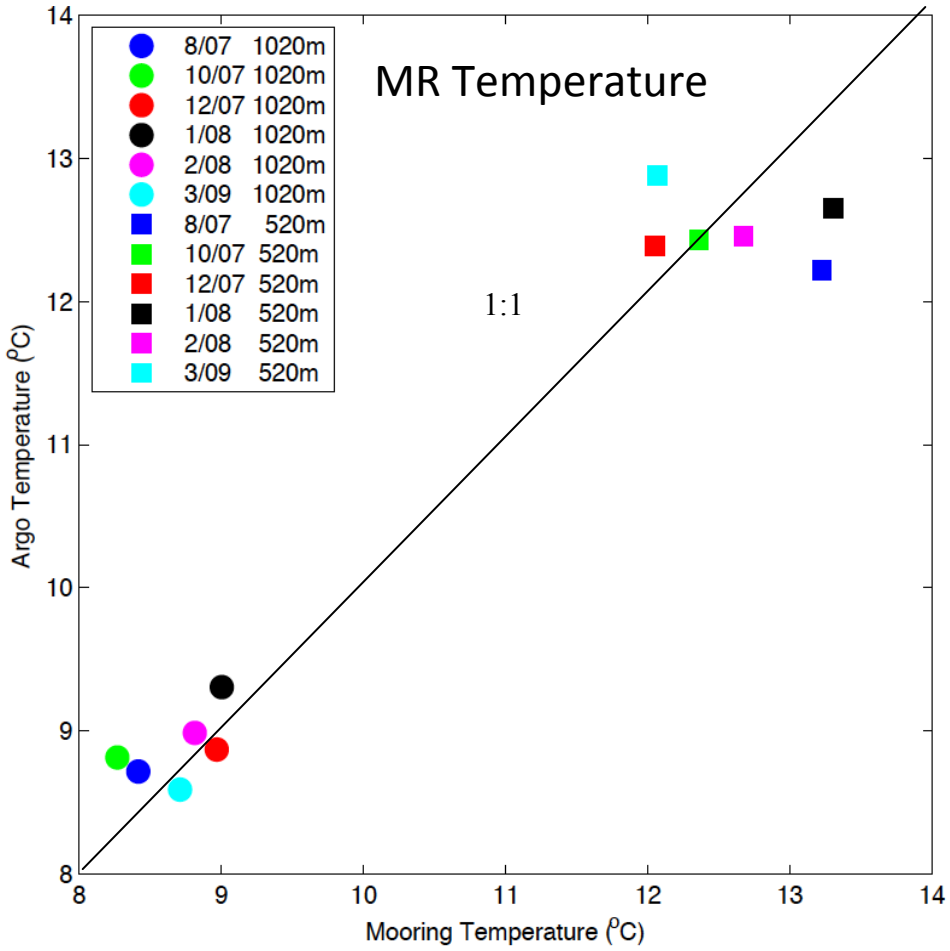

Figure 36. Murray Ridge moored temperature and Argo temperature measurements at 520m and 1020m for August 2007, October 2007, December 2007, January 2008, February 2008 and March 2009.

Near RHM, there was one month where mooring and Argo data shared at least three measurements. Near 1140m, mean Argo salinity was 35.28 and moored salinity was 35.19 (Figure 34a). Argo mean temperature was 7.69˚C and moored temperature measured 7.82˚C (Figure 34b). The standard deviation could not be calculated since there was only one month of overlapping measurements.

Near RHS, two months gave sufficient measurements to compare the two data sets. Moored salinity measurements were 35.20 and 35.25. Argo salinity measurements for both months were 35.26-35.27 (Figure 35a). The standard deviation of the difference was 0.03. Moored temperature measurements were 7.50˚C-7.70˚C. Argo temperatures were 7.52˚C-7.53˚C (Figure 35b). The standard deviation of the difference was 0.13°C. The difference in measurements in March is greater than the standard deviation of the difference for both temperature and salinity.

Most of the measurements at RHN, RHM and RHS fell within the standard deviation of the difference for each mooring location. In some cases, measurements did not agree. A possible reason for this is the vertical and horizontal spatial resolution in the Argo data.

At Murray Ridge, there were no salinity measurements so a T-S diagram could not be used in the analysis, but the mean monthly temperature of Argo and moored measurements were still compared. When plotting the mean monthly temperatures at 520m and 1020m, the data produced a correlation coefficient of 0.97 (Figure 36).

3.5 SODA Model Comparison

3.5.1 Currents and Velocity

When visually comparing model numerical output to Argo and surface drifter velocity data (Figures 12, 13, 15 and 17), similarities can be seen in the current patterns.

In the spring at the surface, the model numerical output (Figure 37a) and drifter data (Figure 13a) both show a westward flow from 3°N-5°N. In the model, the current

(a) Surface

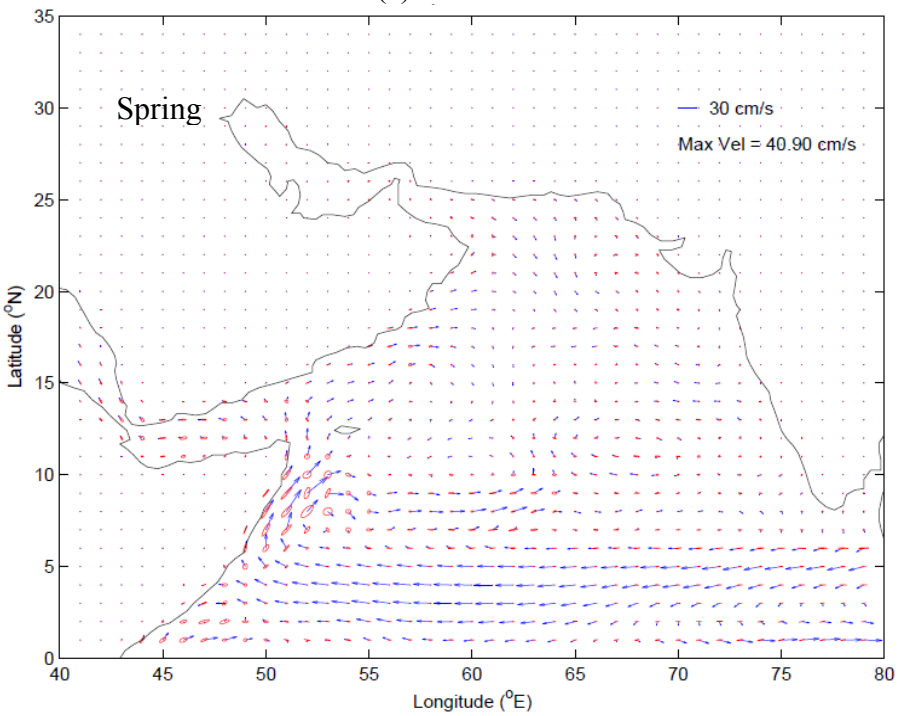

(b) 1000m

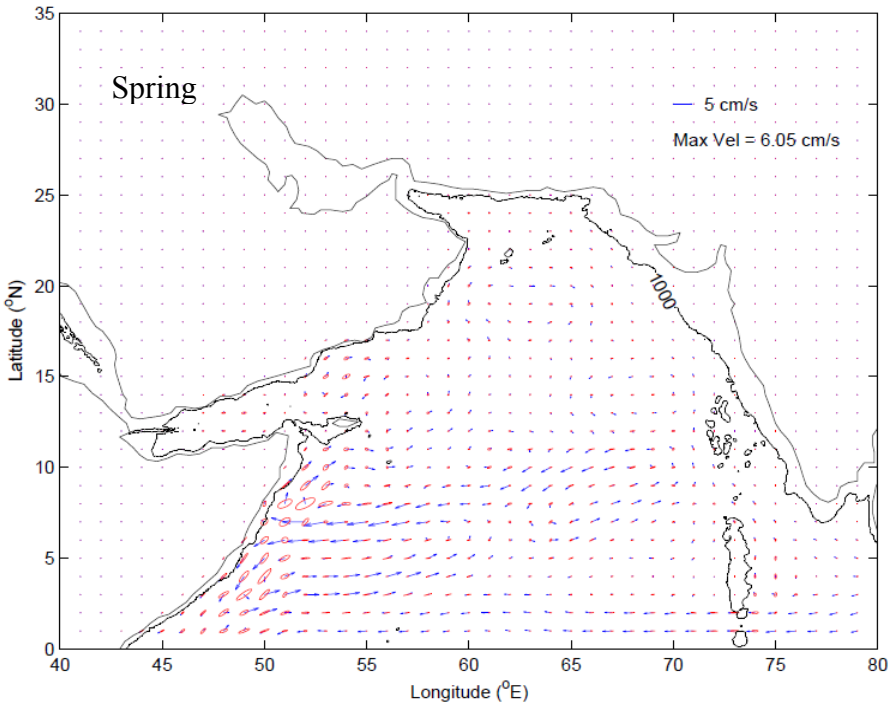

Figure 37. (a) Spring surface velocity from SODA numerical model output. (b) Spring velocity from SODA numerical model output at 1000m.

(c) 1500m

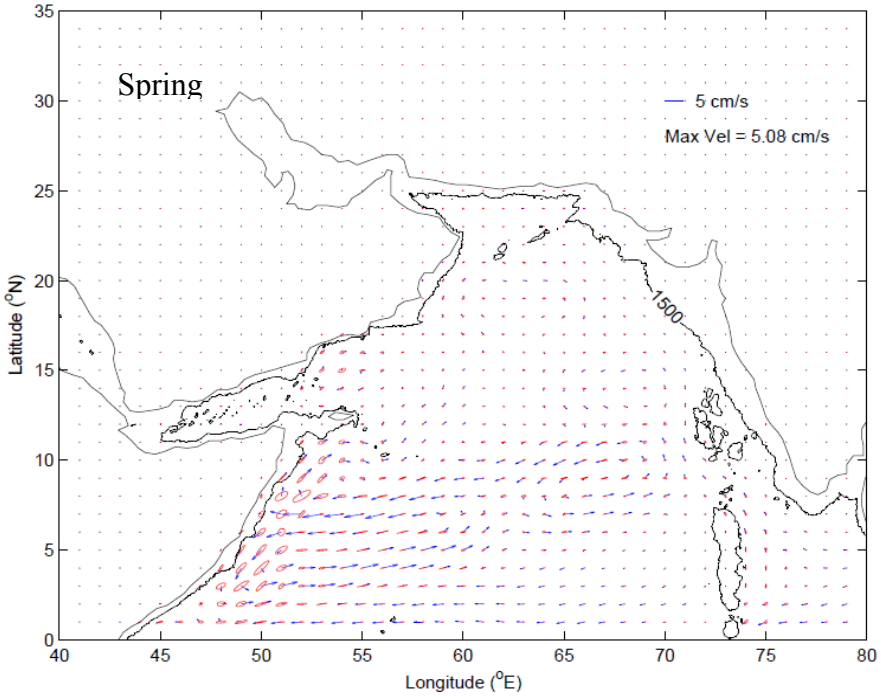

(d) 2000m

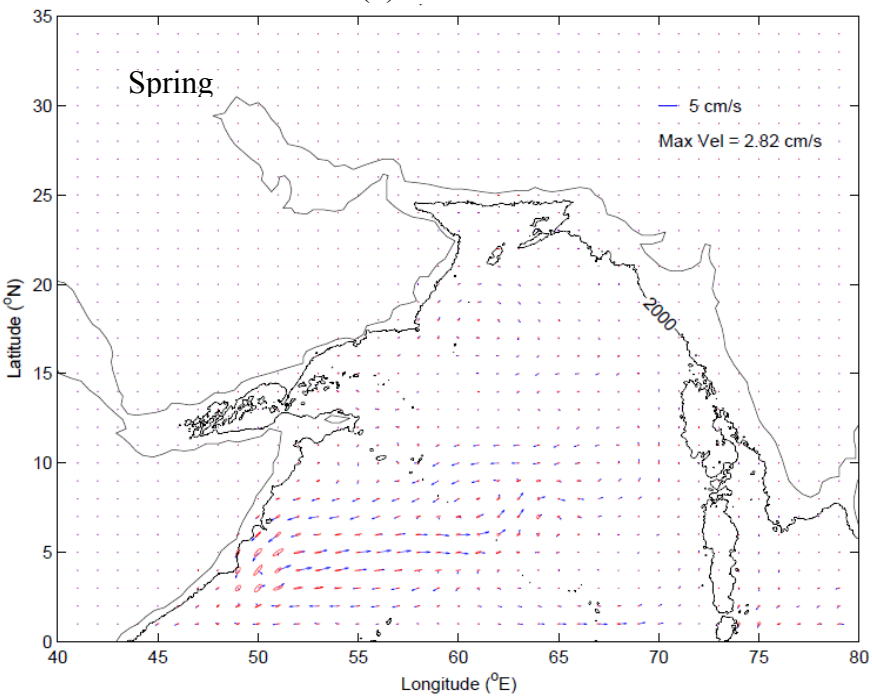

Figure 37 continued. (c) Spring velocity from SODA numerical model output at 1500m. (d) Spring velocity from SODA numerical model output at 2000m.

(a) Surface

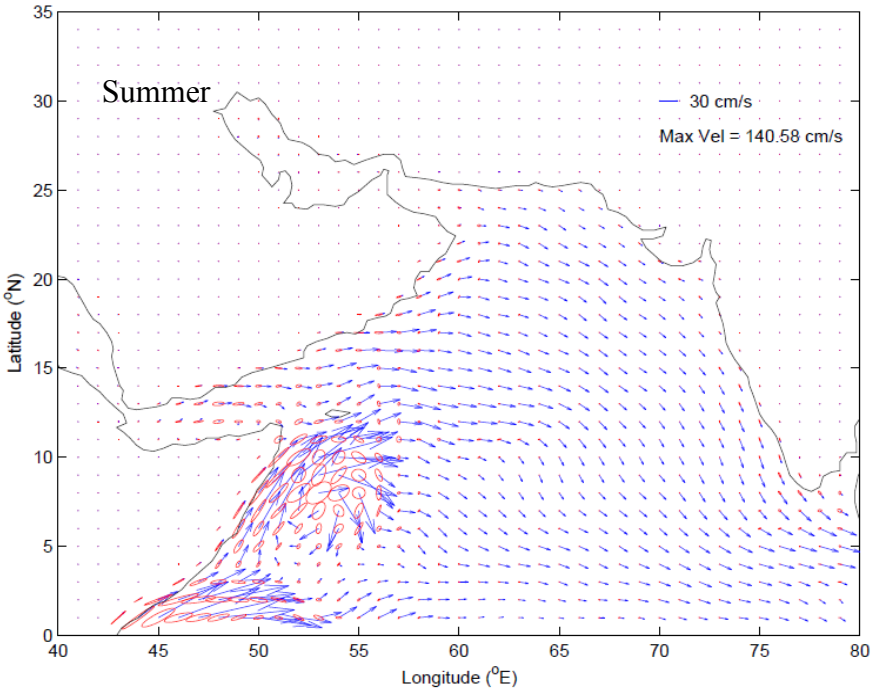

(b) 1000m

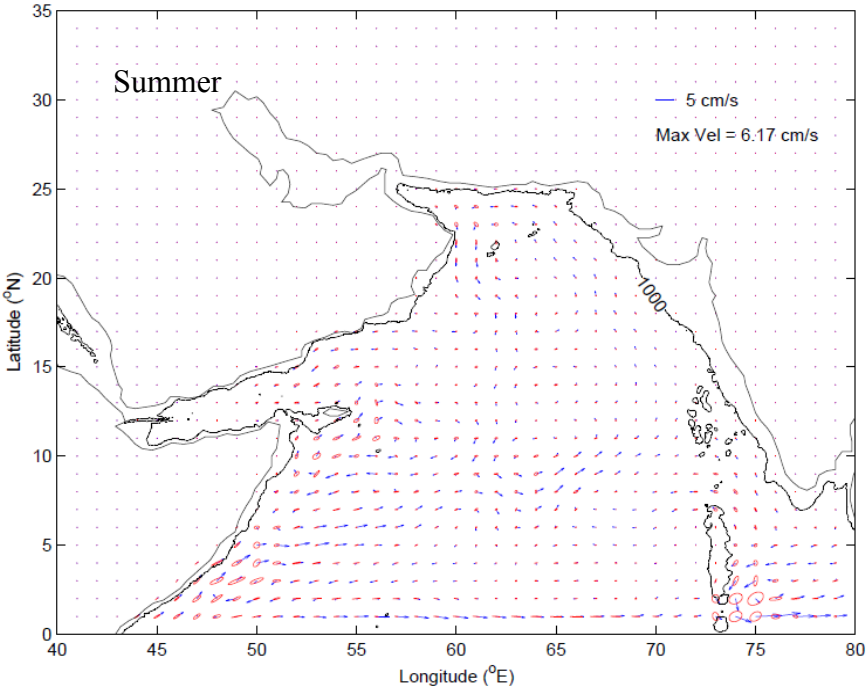

Figure 38. (a) Summer surface velocity from SODA numerical model output. (b) Summer velocity from SODA numerical model output at 1000m.

(c) 1500m

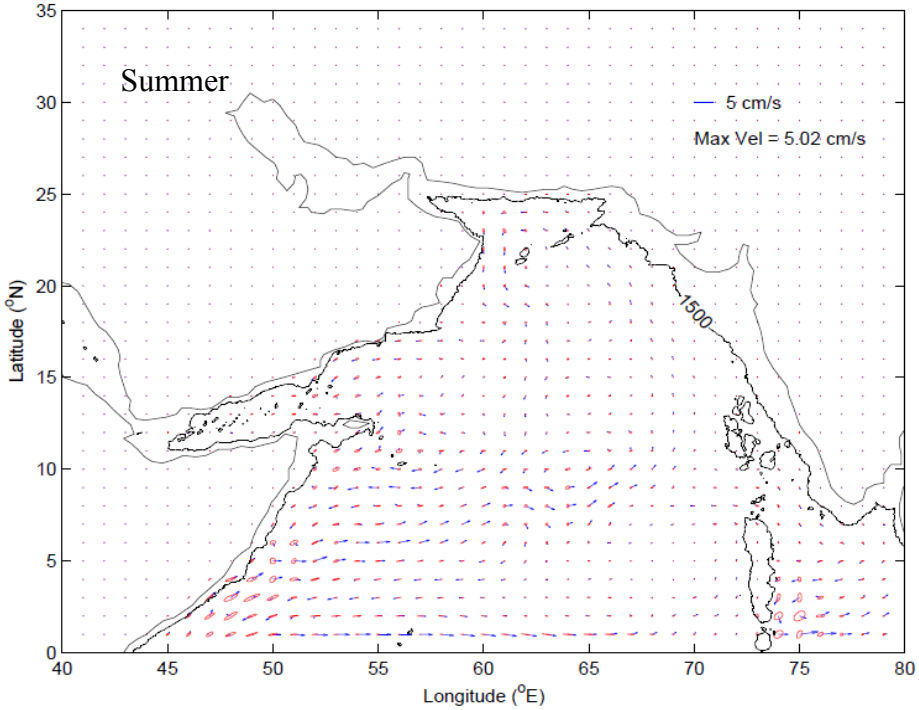

(d) 2000m

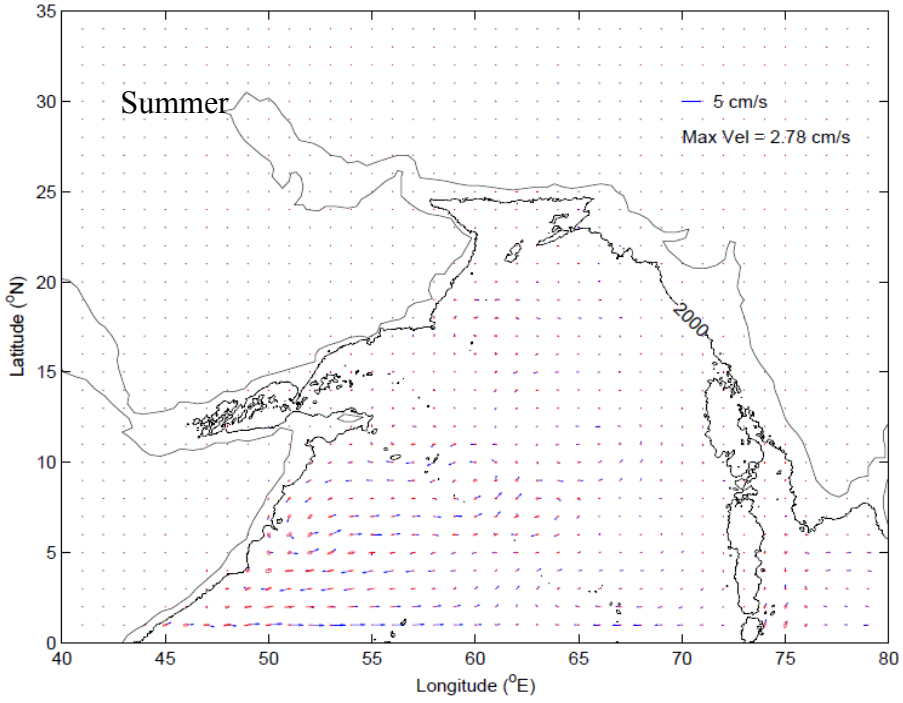

Figure 38 continued. (c) Summer velocity from SODA numerical model output at 1500m. (d) Summer velocity from SODA numerical model output at 2000m.

extends across the entire width of the region, but in the data the westward flow only exists west of 65°E. As the current reaches the Somali coast it separates from the coast, flowing north along the coastline. This current diverges around 10°N with a portion bending offshore and flowing to the east, and the rest continuing to flow north. The northward portion then diverges as it passes the Horn of Somalia, with half flowing west through the Gulf of Aden, and the other half continuing northeast along the Oman coast. Another similarity between the data and model is an eastward current that forms near 70°E between 0°-2°N. In the model, this flow is opposite to the flow just north of it. In the data, there is little consistency in the flow just north of it.

At 1000m, flow is westward along the equator in the model (Figure 37b) and Argo data (Figure 13b). There is also westward flow along 6˚N that diverges at the Somali coast. The recirculation cell that is present between 48˚E-55˚E and 3˚N-6˚N also appears in the model numerical output, but in the model it extends to 61˚E. The recirculation cell is present at 1500m (Figure 37c) and 2000m (Figure 37d) in the model, but not in the data (Figure 13c and 12d).

The best qualitative agreement is the comparison of mean summer surface currents (Figure 38a). The highest velocities are observed along the Somali coast flowing to the northeast. A high-velocity anticyclonic eddy forms as flow separates from the coast (Great Whirl) near the Horn of Somalia. Flow is primarily to the east in the Gulf of Aden. The remaining surface flow is to the east/southeast, except along the southern coast of Oman where flow is to the northeast. In the subsurface, the intense velocities along the Somali coast are not present in model numerical output (Figure 38b

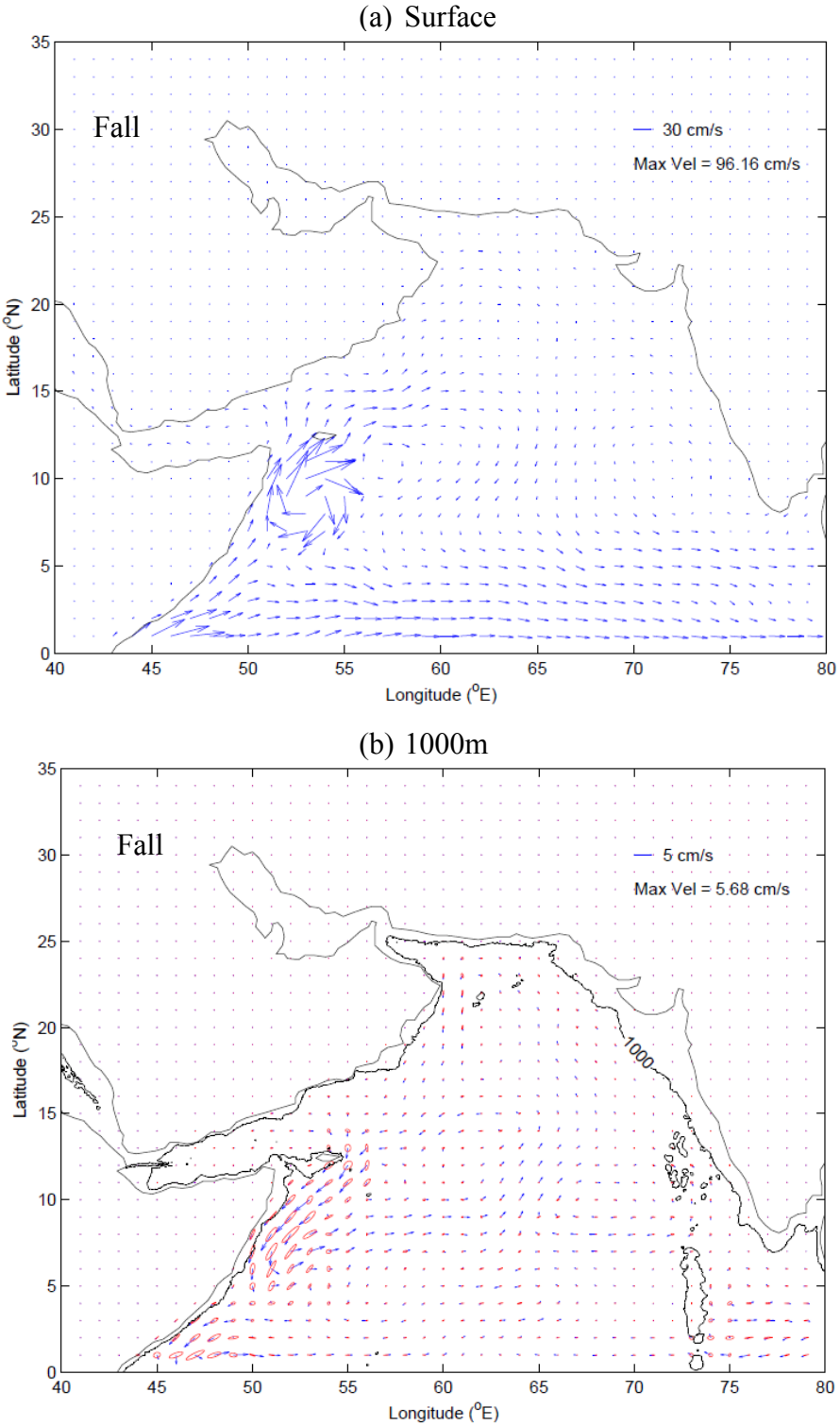

Figure 39. (a) Fall surface velocity from SODA numerical model numerical output. (b) Fall velocity from SODA numerical model output at 1000m.

(c) 1500m

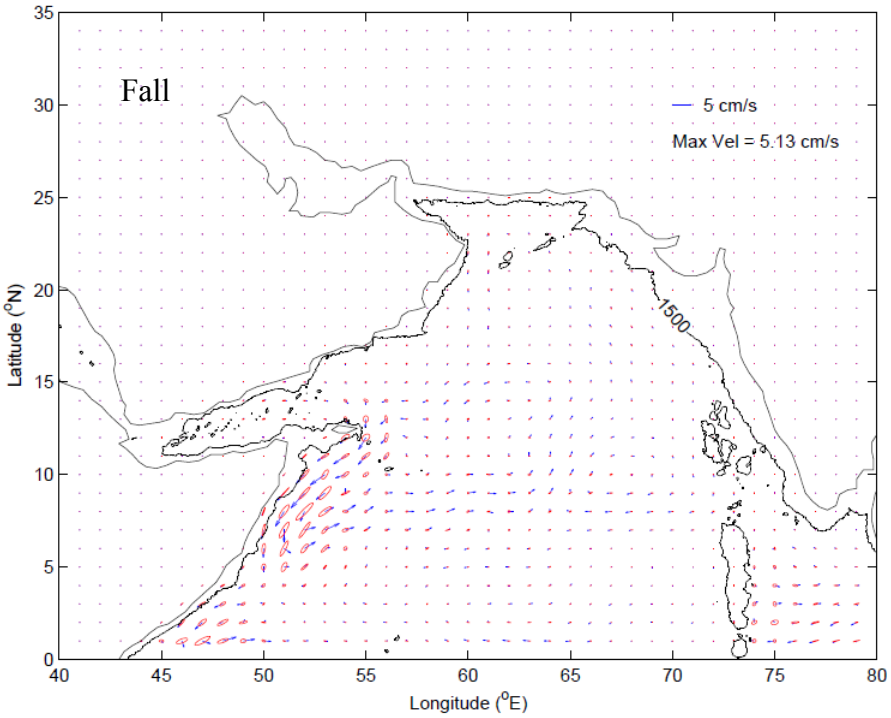

(d) 2000m

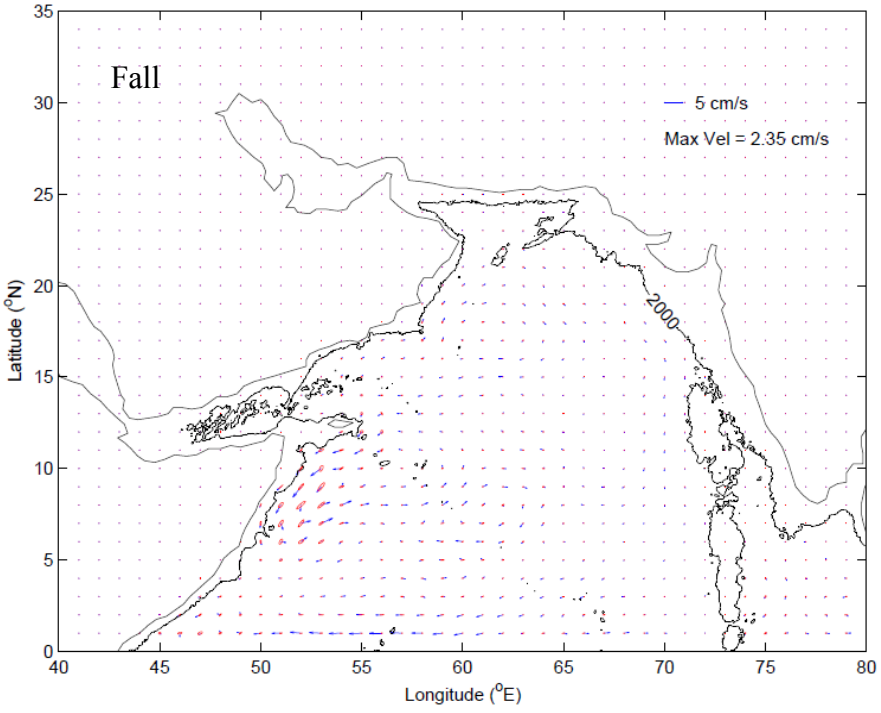

Figure 39 continued. (c) Fall velocity from SODA numerical model output at 1500m. (d) Fall velocity from SODA numerical model output at 2000m.

and 37c), but are still observed in the data at 1000m. All model numerical output shows an eastward flow between 5°N-6°N, west of 60°N. This is also observed in the Argo velocities (Figure 14b and 13c). There is no data at 2000m (Figure 14d) in that region for comparison.

In the fall at the surface (Figure 39a), flow is to the northeast along the coast of Somalia. The Great Whirl is present in both the model and data (Figure 16a) as flow separates from the coast forming an anticyclonic eddy. A southwest flow is present parallel to the Somali and Oman coasts, which bends to the east between 0˚ and 5˚N, and continues east along the equator. In the model at 1000m (Figure 39b), 1500m (Figure 39c) and 2000m (Figure 39d), flow along the Somali coast near the Horn of Somalia is to the southwest and separates from the coast between 5˚N and 8˚N, redirecting to the northwest. At 1000m (Figure 16b), velocity data show a southwest flow along the coast of Somalia, but the current does not bend offshore as it does in the model. Not enough data exists at 1500m and 2000m to see if the pattern exists at those depths (Figures 15c and 15d).

Winter surface currents from model numerical output (Figure 40a) agree reasonably well with surface drifter climatology (Figure 18a). Flow enters from the northeast Indian Ocean and flows west along the equator. As it reaches the Somali coast, it bends to the south. Some of the current does not extend all the way to Somalia, but bends northward, flowing northwest along the coast of India (Northeast Monsoon Current). This flow has a stronger presence in the model numerical output than in the data. In both model numerical output and data, a cyclonic eddy is seen just east of the

(a) Surface

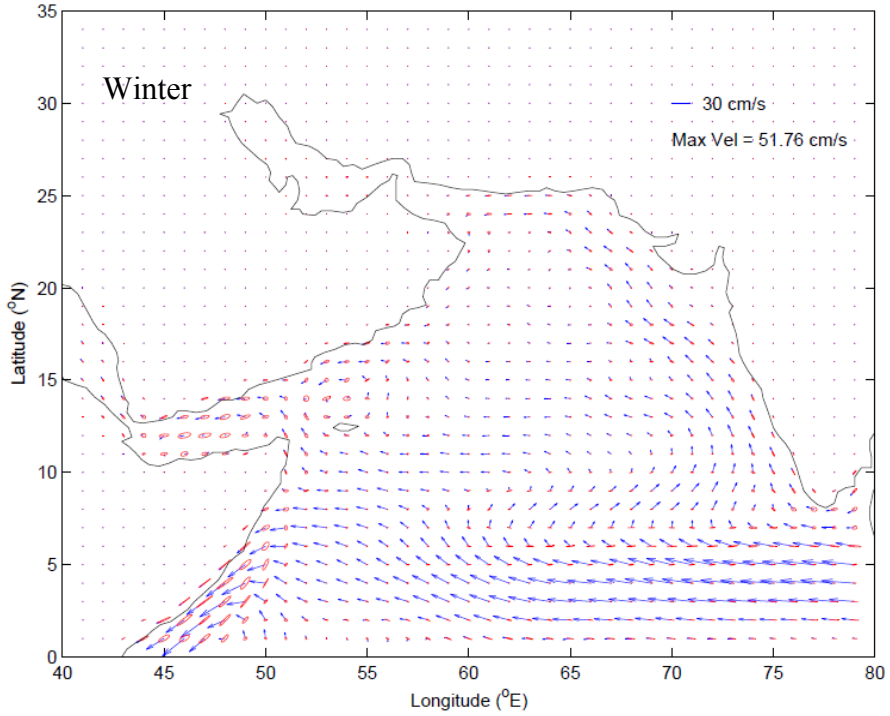

(b) 1000m

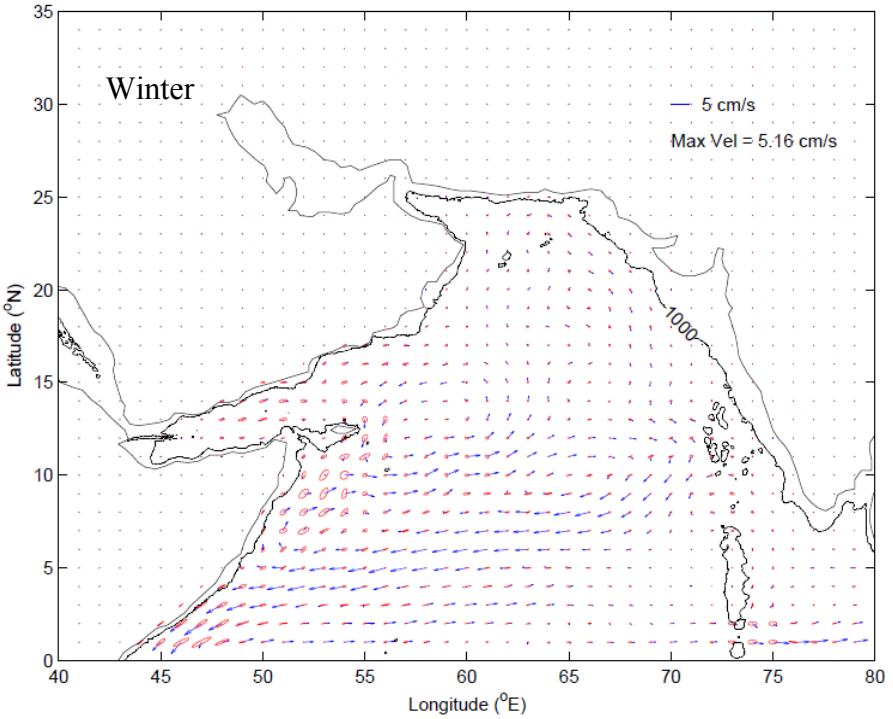

Figure 40. (a) Winter surface velocity from SODA numerical model output. (b) Winter velocity from SODA numerical model output at 1000m.

(c) 1500m

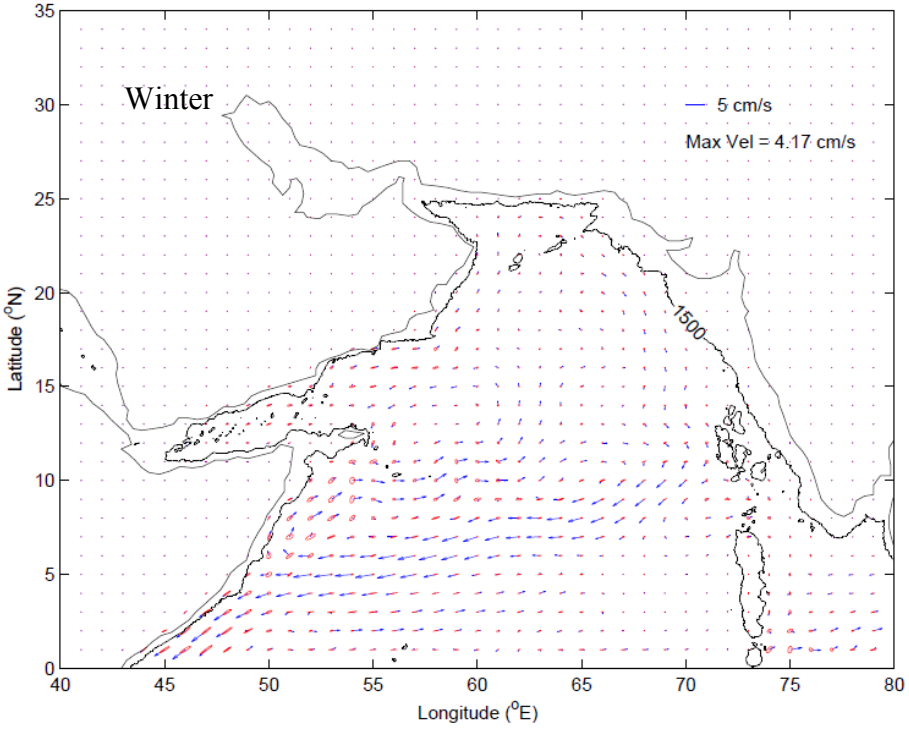

(d) 2000m

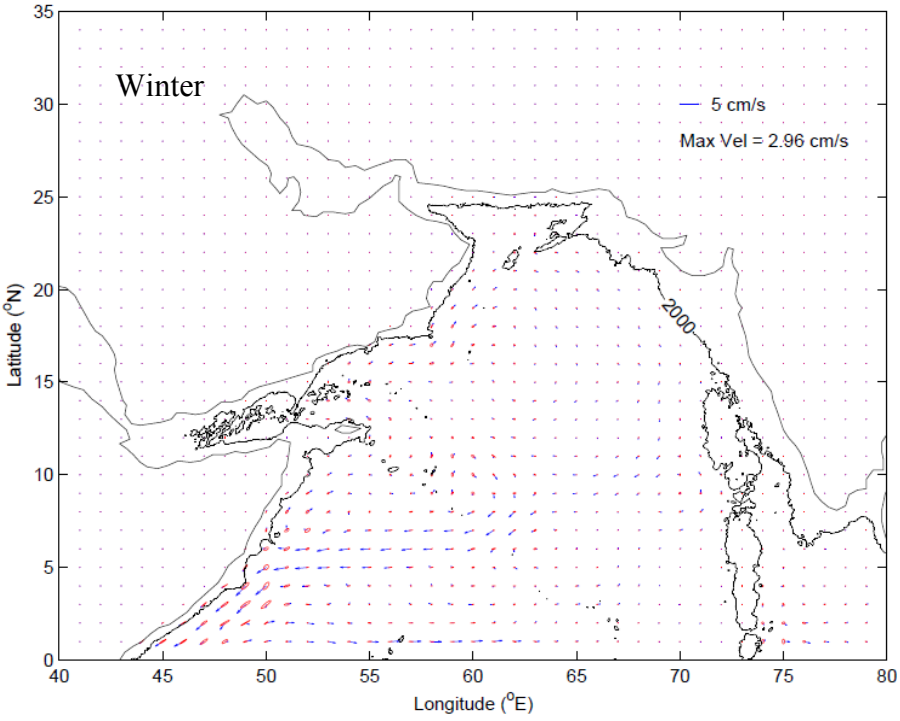

Figure 40 continued. (c) Winter velocity from SODA numerical model output at 1500m. (d) Winter velocity from SODA numerical model output at 2000m.

Gulf of Aden, and a westward flow is present around 10°N west of 65°E. At 1000m (Figure 18b), 1500m (Figure 18c) and 2000m (Figure 18d) the data shows a current flowing west near 5°N, which diverges as it reaches the Somali coast. The model shows this flow as just part of a large anticyclonic circulation cell from 50°E-70°E and 5°N-12°N (Figure 40b, 39c and 39d). The portion that flows north after diverging separates from the coast and flows east/northeast until 68°E-70°E. It then bends to the southwest and continues to flow until reaching the Somali coast. An anticylonic circulation cell can also be seen at 2000m (Figure 40d) in the model numerical output, but only extending to 62°E. Flow along the equator is to the east in the subsurface.

Since a visual comparison between model numerical output and data is only qualitative, statistical methods are required to determine their quantitative comparison. When the model numerical output was statistically compared to Argo data for subsurface velocities, the correlation was weak, and in all cases, not significantly different than zero. Surface velocities showed a stronger correlation than subsurface velocities. Velocities are not assimilated into the model. This could be a reason why current velocities did not agree. The addition of high-salinity water from the Red Sea and Persian Gulf are also not assimilated into the model. Their assimilation would give a more accurate density field in those regions and improve the subsurface velocity fields. In several cases, similar patterns could be seen between the velocity plots generated from surface drifter or Argo data and the velocity plots generated from model output. There appeared to be an offset in many of these patterns. If the offsets were corrected,

Table 2. Vector correlation, scalar correlation and scalar correlation significance of velocity between SODA model numerical output and data from Argo floats and surface drifters.

Velocity Correlation between SODA Model numerical output and Argo Float and Surface Drifter Data				
Season	Depth	Vector Correlation	Scalar Correlation	Scalar Correlation Significance
Spring	Surface	0.7110	0.3989	4.7684×10^{-7}
	1000m	0.2071	0.2209	0.1971
	1500m	0.2467	0.1927	0.3995
	2000m	0.3165	0.3991	0.5202
Summer	Surface	1.0057	0.7233	0.0000
	1000m	0.1007	0.1484	0.7056
	1500m	0.2364	0.2984	0.1308
	2000m	0.1829	0.2893	0.6466
Fall	Surface	0.7519	0.5350	0.0000
	1000m	0.0165	0.1736	0.8747
	1500m	0.0407	0.1227	0.4092
	2000m	0.0114	0.2221	0.3349
Winter	Surface	0.7827	0.6096	0.0000
	1000m	0.2375	0.1869	0.6027
	1500m	0.5823	0.3030	0.3235
	2000m	0.0958	0.1848	0.4737

the correlation coefficients for both vector correlation and scalar correlation would probably increase.

At the surface, both vector and scalar correlation were stronger than in the subsurface. The scalar correlation was significant in all cases. The highest scalar correlation values are seen at the surface in the summer and winter, with summer having a correlation value of 0.7233 and winter having a correlation value of 0.6096. The results of all of the vector correlations, scalar correlations and the significance of the scalar correlations at the surface, and in the subsurface can be seen in Table2.

3.5.2 Hydrography

To begin the comparison of temperature and salinity between model numerical output and Argo data (Figure 31), a temperature-salinity diagram was produced for model numerical output from 1992-2001 (Figure 41) and 2002-2008 (Figure 42). The mean temperature and salinity for the Argo data and model numerical output are shown in Table 3. The standard deviation of salinity and temperature for the model and data, and the standard deviation of the difference are shown in Table 4.

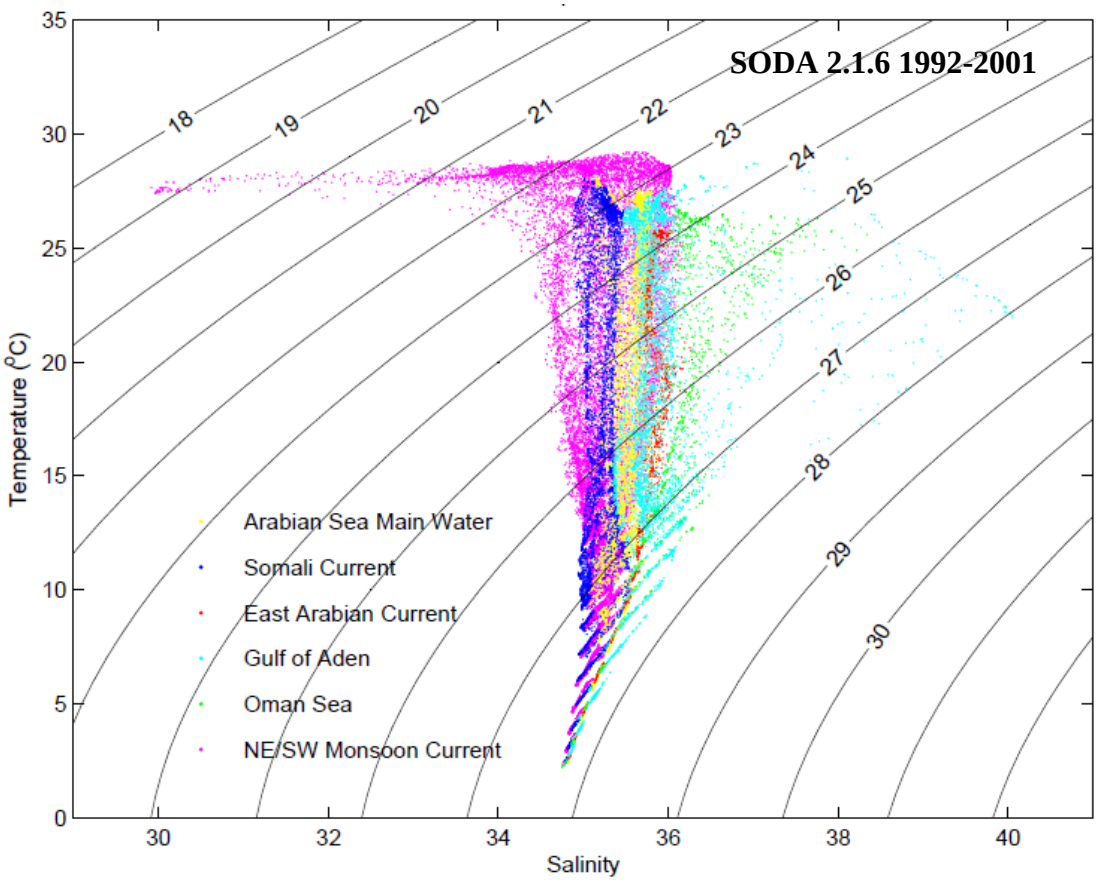

Figure 41. Temperature-salinity diagram with superimposed isopycnals (kg/m^3) from SODA model numerical output from 1992-2001, prior to the assimilation of Argo data.

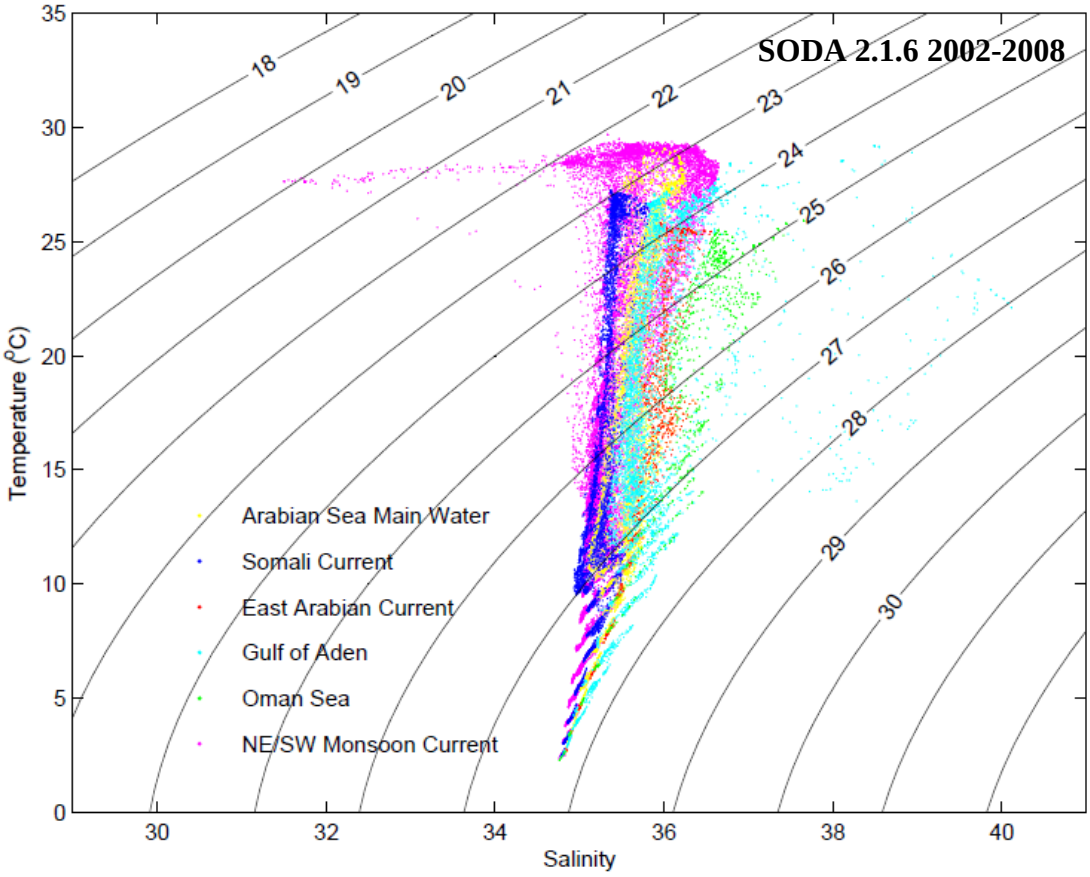

Figure 42. Temperature-salinity diagram with superimposed isopycnals (kg/m^3) from SODA model numerical output from 2002-2008, after the assimilation of Argo data.

After Argo data were assimilated into the model, all salinity measurements increased. The standard deviation of the difference for salinity using model numerical output from 1992-2001 was 0.08. Arabian Sea Water, the East Arabian Current and the Sea of Oman salinity differences all fell outside the acceptable error. After Argo was assimilated into the model, the standard deviation of the difference for salinity using model numerical output from 2002-2008 was 0.13. Arabian Sea Water, the Somali Current, the East Arabian Current, the Gulf of Aden and the Sea of Oman all fell within

the acceptable error. The difference between model numerical output and Argo data for salinity in the NE/SW Monsoon Current worsened after the assimilation of Argo, falling outside the acceptable error for model numerical output from 2002-2008.

When comparing Argo temperature data to model output prior to the assimilation of Argo data, only Arabian Sea Water and the Sea of Oman mean temperatures fell within one standard deviation. After the assimilation of Argo data, all regions fell within one standard deviation, with the exception of the East Arabian Current. When comparing salinity data and model output prior to the assimilation of Argo data, the Somali Current, Gulf of Aden and NE/SW Monsoon Current all fell within one standard deviation. After the assimilation of Argo data, all regions fell within one standard deviation, with the exception of the NE/SW Monsoon Current. Reasons for the change in the model from 1992-2001 and 2002-2008 could be interannual variability in the region or the improvement of the model with the assimilation of additional data sources.

Table 3. Mean temperature and salinity from Argo floats and SODA model numerical output before and after the assimilation of Argo data.

Mean Temperature (˚C)					
	Argo	Model 1992-2001	Difference 1992-2001	Model 2002-2008	Difference 2002-2008
Arabian Sea Water	16.02	16.02	0	16.23	0.21
Somali Current	14.90	15.43	0.53	15.52	0.62
East Arabian Current	17.30	16.41	0.89	16.47	0.83
Gulf of Aden	17.91	16.64	1.27	16.50	1.41
Sea of Oman	18.63	18.61	0.02	18.38	0.25
NE/SW Monsoon Current	15.36	15.90	0.54	16.36	1.00
Mean Salinity					
Arabian Sea Water	35.62	36.46	0.16	35.58	0.04
Somali Current	35.22	35.21	0.01	35.29	0.07
East Arabian Current	35.91	35.70	0.21	35.80	0.11
Gulf of Aden	35.87	35.82	0.05	35.87	0
Sea of Oman	36.27	36.15	0.12	36.25	0.02
NE/SW Monsoon Current	35.14	35.15	0.01	35.40	0.26

Table 4. Standard deviation of Argo data, numerical model output from 1992-2001, numerical model output from 2002-2008, and standard deviation of the differences.

Standard Deviations of Salinity and Temperature (˚C)					
	Argo	Model 1992-2001	Difference 1992-2001	Model 2002-2008	Difference 2002-2008
Salinity	0.44	0.40	0.08	0.37	0.13
Temperature (°C)	1.49	0.88	0.1	0.86	1.15

4. DISCUSSION

The discussion is divided into two sections. The first section will discuss the seasonal currents in the northwest Indian Ocean based on the results and previous work. The second section will discuss vertical stratification.

4.1 Seasonal Currents

Seasonal velocity, salinity and temperature were used to analyze the seasonal changes in currents in the northwest Indian Ocean. Surface drifter velocity data are consistent with known circulation patterns in the northwest Indian Ocean. The seasonal monsoon drives the surface and subsurface circulation patterns and hydrography in the northwest Indian Ocean. This is evident from the seasonal change in current direction, and the seasonal exchange of deep and surface water with marginal seas and the northeast Indian Ocean. Seasonal changes in evaporation also contribute to the surface salinity. Since the physical characteristics are determined by controls associated with changing seasons, the results of the data will be discussed by season.

4.1.1 Summer

The primary control during the summer is the Southwest Monsoon, which drives surface and subsurface currents (Figure 14). The Somali Current velocities are strongest in August. As the Somali Current separates from the coast near the Horn of Somalia, a large high-velocity anticyclonic eddy is formed (Figures 13a and 14), known as the Great Whirl. The Great Whirl is present as deep as 1000m and has a high SSH anomaly associated with it (Figure 20). In addition to the affect of the Coriolis force acting on the Somali Current as some of the flow bends offshore to the right, bathymetry plays a large

role in the formation of the Great Whirl. At the Horn of Somalia, bathymetry decreases rapidly reaching a water depth of less than 1000m (Figure 2). While some of the Somali Current separates from the coast, another portion extends northward, and continues to flow northeast along the southern coast of Oman. This extension is the East Arabian Current, and is only present during the summer (Figure 14a) and early fall (Figure 16a). The Somali Current and East Arabian Current lead to upwelling along the southern coasts of Somalia and Oman. Evidence of upwelling along these coastal regions includes negative sea surface heights (Figure 20) and cool sea surface temperatures. As the monsoon strengthens through August, temperatures along both coasts become cooler and extend further away from the coast (Figure 25). Water builds up as it continues to move offshore causing a high SSH anomaly parallel to the Somali and Oman coasts (Figures 19). The upwelling region along the Somali coast has the coolest SST for the entire northwest Indian Ocean, which consistent with observation made by McCreary and Kundu (1989); however, satellite and drifter observations showed a minimum temperature near 23˚C while McCreary and Kundu (1989) observed the coolest temperatures near 26˚C (Figures 24). The reason for this difference is unknown.

Before the Somali Current passes into the northern hemisphere, it begins partially as the East African Coastal Current (Figure 6 and 7). The EACC divides into two main paths as it passes over the equator. One path feeds into the Somali Current. The other path separates from the coast and continues to flow east/southeast along 0° (Figure 14a).

The Somali Current and eastward flow along the equator extend to 1500m in the subsurface, though velocities decrease (Figure 14b). The subsurface flow of the Somali

Current and East Arabian Current brings low-salinity Indian Central Water northward near Cape Ras al Hadd (Figures 31c).

In the northern Sea of Oman, upwelling occurs along the coasts of Iran and Pakistan. This is evident by cooler sea surface temperatures along the coast in the northern Sea of Oman (Figure 26). Another current associated with the summer is the Southwest Monsoon Current. Velocities are identified at the surface and subsurface (Figures 8a, 8b and 8d), flowing southeast along the coast of India and entering the northeast Indian Ocean.

4.1.2 Winter

In the winter, evaporation plays a large role in the surface circulation and salinity balance. The Northeast Monsoon also affects surface circulation. Driven by the monsoon, the Somali Current reverses at the surface (Figure 18a) and in the subsurface at 1000m (Figure 18b) and 1500m (Figure 18c). SST agree with McCreary and Kundu (1989) with minimum temperatures in the northern Arabian Sea near 23°C (Figures 27 and 28).

Evaporation increases drastically, especially affecting marginal seas. In the Red Sea and Persian (Arabian) Gulf, evaporation rates exceed 0.2mm/hour (Waisowicz and Schopf, 2001), resulting in the formation of the dense, high-salinity Persian Gulf Water and Red Sea Outflow Water. The dense water masses sink and flow out in the subsurface while surface water from the Sea of Oman and Gulf of Aden (Figure 18a) flow in.

High salinity values from the Red Sea can be identified in the subsurface in Figure 31 as Arabian Sea Water. The Red Sea Water mass can also be identified with salinity values near 40. With distance from the Bab el Mandab, Red Sea Water salinity and temperature decrease as it sinks and mixes laterally.

In addition to the effects of evaporation on exchange between the Persian (Arabian) Gulf and the Sea of Oman, local winds affect the oceanography. During the Northeast Monsoon, local winds over the Sea of Oman come from the northwest. These local winds have a larger impact on the regional oceanography than the Northeast Monsoon winds. As with Red Sea Water, Persian Gulf Water begins with high salinity values as it passes through the Strait of Hormuz. As PGW continues to flow along the northern coast of Oman, it sinks and mixes with fresher water in the Sea of Oman. Persian Gulf Water is observed flowing southeast along the northern coast of Oman at 1000m (Figures 17b and 30). In the winter, PGW can extend south of Cape Ras al Hadd, though significant mixing occurs (Figure 32).

Evaporation increases over the Arabian Sea creating high surface salinity in the northwest Indian Ocean. This creates a salinity imbalance between the northwest and northeast Indian Ocean. The salinity imbalance combined with the Northeast Monsoon causes low-salinity surface water from the northeast Indian Ocean to flow into the northwest Indian Ocean (Figure 18a). Part of this flow continues west along the equator as the North Equatorial Current. Another part flows to the north along the coast of India as the Northeast Monsoon Current. Low salinity measurements were observed along the Indian coast during the winter (Figure 31). Between 5˚N-10˚N, several anticyclonic

eddies are present (Figure 18a). Since anticyclones are high-pressure cells, the region also shows an increase in SSH (Figure 19).

4.1.3 Spring and Fall

Spring and fall are intermonsoonal periods, which results in high variability of current speed and direction as the wind transitions between monsoons. Circulation associated with the spring Intermonsoon is first seen in April. Fall Intermonsoon circulation is first seen in October and remains highly variable through November. Eddies form along the Somali and Oman coasts, in the Sea of Oman and in the Gulf of Aden. Several subsurface averaged velocities in these regions have a large variance associated with them. This is expected during the intermonsoon seasons when flow is irregular and un-uniform.

4.1.4 Ras al Hadd Jet

Prior to fall Intermonsoon circulation, velocities along the southern Oman coast continue to flow north with velocities increasing through August. The analysis of sea surface height agreed with the temperatures observed for selected days during the study by Böhm *et al.* (1999). Sea surface height off Cape Ras al Hadd continues to increase with increased current velocity. In September (Figure 21f), a SSH anomaly of nearly 10cm can be seen. Intensity decreases rapidly and by the end of October, no evidence of the Ras al Hadd Jet formation is present (Figure 31h).

Satellite imagery also shows sea surface temperature associated with the Ras al Hadd Jet in September. Figure 30 shows that temperatures are less than 23°C along the Oman coast, and are associated with upwelling from the EAC. Cool temperatures from

upwelling along the Oman coast extend to the northeast of Cape Ras al Hadd. As the EAC continues to the northeast, the cool surface water is transported and separates from the coast with the RAH Jet. The low SST off Cape Ras al Hadd extends as far as the RAH Jet, and can be used as a tool to measure the progression of the RAH Jet.

4.2 Vertical Stratification

Surface stratification is controlled by salinity, especially during the winter. Figure 31 shows a broad range of salinity at the surface, which crosses over several density isopycnals. The density ratio from McDougall (1987) showed that one unit of change in salinity has a greater affect on the density than one unit of change in temperature. Since temperature only varies by a few degrees, the density near the surface is changing as a result of salinity changes. This is especially evident in the Northeast Monsoon Current.

While surface stratification is controlled by salinity, subsurface stratification is primarily controlled by temperature. Below a temperature of 27˚, salinity changes very little outside of Persian Gulf Water and Red Sea Water. Since temperature changes more drastically than salinity in the subsurface, and density continues to increase with decreasing temperature, subsurface stratification is controlled by temperature.

5. SUMMARY AND FUTURE WORK

5.1 Summary

Surface and subsurface currents are driven by the seasonal monsoon. Surface currents agree with currents known to exist in the northwest Indian Ocean. In some cases, such as the Somali Current, the current extends to the subsurface. The identified surface and subsurface current velocities, and in some cases, current widths, were quantified. In the Sea of Oman and Gulf of Aden, surface flow direction is often opposite of subsurface flow direction because of exchange between the marginal seas and the northwest Indian Ocean. When wind direction changes with the monsoon, current directions also change.

Sea surface temperature and sea surface height vary the most along the Somali and Oman coasts. During the Southwest Monsoon, temperatures along the Somali and Oman coasts decrease from upwelling. Sea surface height also decreases right along the coast, but a positive SSH anomaly occurs offshore parallel to the coast.

Sea surface height near Cape Ras al Hadd varies with the progression of the Ras al Hadd Jet. Positive SSH anomalies associated with eddy formation near the Ras al Hadd Jet were evident as well as the extension of cooler SST off Cape Ras al Hadd.

When investigating the importance of salinity and temperature in vertical stratification, salinity had a larger impact on density changes near the surface while temperature had a larger impact on density changes in the subsurface. Salinity's role in surface stratification was especially strong during the winter with inflow of fresh water

from the northeast Indian Ocean with the Northeast Monsoon Current. Even though temperature varied by a few degrees, the density ratio from McDougall (1977) showed that one unit of salinity change has a greater affect than one unit of temperature on density changes. In the subsurface, salinity is relatively constant while temperature continues to decrease with depth.

When comparing the moored data to Argo float data, both salinity and temperature measurements agreed well. About half of the salinity and temperature measurements fell within one standard deviation of the difference between Argo and moored mean values. Disagreements could possibly due to the low vertical resolution of Argo observations between 1000m and 2000m. When Murray Ridge temperature data were compared with nearby Argo temperature data, a correlation of 0.97 was calculated.

When comparing Argo observations to SODA model numerical output prior to the assimilation of Argo (1992-2001), many salinity and temperatures were similar, but fell outside the range of acceptable error. With the assimilation of Argo observations (2002-2008), overall salinity increased. Both salinity and temperature comparisons improved in the model from 2002-2008, with most measurement differences falling within the acceptable range of error. While it appears that the SODA model improves with the assimilation of Argo data, a longer time series is needed to confirm this. Disagreements in the data and model could be due to interannual variability. Since there is no Argo data from 1992-2001, a comparison of the model with and without Argo assimilation for the same time period cannot be done.

5.2 Future Work

While there is a better understanding of the dynamics in the Sea of Oman and the Persian (Arabian) Gulf exchange, the cabled observatory (installed in 2005) and the autonomous moorings will add to the understanding of Persian Gulf Water exchange and the dynamics near Cape Ras al Hadd. The incorporation of a longer time-series from those observing systems will give insight to low frequency events and characteristics, as well as high frequency seasonal events.

REFERENCES

Aiki, H., K. Takahashi, and T. Yamagata (2006), The Red Sea outflow regulated by the Indian Monsoon, *Continental Shelf Research, 26,* 1448-1468, doi:10.1016/j.csr.2006.02.017.

Banse, K. (1997), Irregular flow of Persian Gulf Water to the Arabian Sea, *Journal of Marine Research, 55,* 1049-1067.

Beal, L. M. and H. L. Bryden (1999), The velocity and vorticity structure of the Agulhas Current at 32°S, *Journal of Geophysical Research, 40*, 5151-5176.

Böhm, E., J. M. Morrison, V. Manghnani, H. Kim, and C. N. Flagg (1999), The Ras al Hadd Jet: Remotely sensed and acoustic Doppler profiler observations in 1994-1995, *Deep-Sea Research II, 46,* 1531-1549.

Brewer, P. G. and D. Dyrssen (1985), Chemical oceanography of the Persian (Arabian) Gulf, *Progress in Oceanography, 14,* 41-55.

Carton, J. A., G. Chepurin, X. Cao and B. Giese (2000), A simple ocean data assimilation analysis of the global upper ocean 1950-95. Part I: Methodology, *Journal of Physical Oceanography, 30,* 294-309.

Carton, J. A. and B. S. Giese (2008), A reanalysis of ocean climate using simple ocean data assimilation (SODA), *Monthly Weather Review, 136,* 2999-3017, doi:10.1175/2007MWR1978.1.

CCAR (unpublished data, 2009) available from CCAR Real-Time Altimeter Data Group (http://argo.colorado.edu/~realtime/gsfc_global-real-time_ssh/).

Chao, S., T. W. Kao, and K. R. Al-Hajri (1992), A numerical investigation of circulation in the Arabian Gulf, *Journal of Geophysical Research, 97,* 11219-11236, doi:10.1029/92JC00841.

Chapman, P., S. F. DiMarco, R. E. Davis, and A. C. Coward (2003), Flow at intermediate depths around Madagascar based on ALACE float trajectories, *Deep-Sea Research II, 50,* 1957-1986, doi:10.1016/S0967-0645(03)00040-7.

Crosby, D. S., L. C. Breaker, and W. H. Gemmill (1993), A proposed definition for vector correlation in geophysics: theory and application, *Journal of Atmospheric and Oceanic Technology, 10,* 355-367.

DiMarco, S. F., P. Chapman, W. D. Nowlin, P. Hacker, K. Donohue, M. Luther, G. Johnson, and J. Toole (2002), Volume transport and property distributions of the Mozambique Channel, *Deep-Sea Research II, 49,* 1481-1511, doi:10.1016/S0967-0645(01)00159-X.

DiMarco, S. F., A. E. Jochens, C. J. Jang, L. Belabbassi, and M. K. Howard (2008), Final report: physical oceanography in the Gulf of Oman: data processing, analysis and synthesis of cabled and moored data, pp 1-15.

Elliot, A. J. and G. Savidge (1990), Some features of the upwelling off Oman, *Journal of Marine Research, 48,* 319-333.

Emery, W. J. and R. E. Thomson (2004), Objective analysis, in *Data Analysis Methods in Physical Oceanography*, 2nd ed., edited by W. J. Emery and R. E. Thomson, pp. 309-319, Elsevier B. V., Amsterdam, The Netherlands.

ETOPO2v2 Global Gridded 2-minute Database (unpublished data, 2006) available from National Geophysical Data Center, National Oceanic and Atmospheric Administration, U.S. Dept. of Commerce (http://www.ngdc.noaa.gov/mgg/global/etopo2.html).

Frazier, S. (unpublished data, 2011) available from MODIS (http://modis.gsfc.nasa.gov/).

JCOMMOPS Argo (unpublished data, 2008) available from Joint WMO-IOC Technical Commission for Oceanography and Marine Meteorology in situ Observing Platform Support Centre (http://argo.jcommops.org).

Johns, W. E., F. Yao, D. B. Olson, S. A. Josey, J. P. Grist, and D. A. Smeed (2003), Observations of seasonal exchange through the Straits of Hormuz and the inferred heat and freshwater budgets of the Persian (Arabian) Gulf, *Journal of Geophysical Research, 108*(21), 1-17, doi:10.1029/2003JC001881.

Kämpf, J. and M. Sadrinasab (2006), The circulation of the Persian (Arabian) Gulf: a numerical study, *Ocean Science, 2*, 27-41.

Kempler, S. (unpublished data, 2011) available from NASA (http://giovanni.gsfc.nasa.gov).

Lumpkin, R. (2003), Decomposition of surface drifter observations in the Atlantic Ocean, *Geophysical Research Letters, 30*(6), 2-4, doi:10.1029/2003GL017519.

Lumpkin, R. and M. Pazos (2006), Measuring surface currents with surface velocity program drifters: the instrument, its data, and some recent results, in *Lagrangian Analysis and Prediction of Coastal and Ocean Dynamics (LAPCOD),* Chapter II 39-67, edited by by A. Griffa, A. D. Kirwan, A. J. Mariano, T. Ozgokmen, and T. Rossby., Cambridge University Press, Cambridge, New York.

Lumpkin, R. and Z. Garraffo (2005), Evaluating the decomposition of Tropical Atlantic drifter observations, *Journal of Atmospheric and Oceanic Technology, 22,* 1403-1415.

Lumpkin, R. and S. Garzoli (2005), Near-surface circulation in the Tropical Atlantic Ocean, *Deep-Sea Research I, 52*, 495-518, doi:10.1016/j.dsr.2004.09.001.

MathWorks (unpublished data, 2011) MATLAB available from www.mathworks.com.

McCreary, J. P. and P. K. Kundu (1989), A numerical investigation of sea surface temperature variability in the Arabian Sea, *Journal of Geophysical Research, 94,* 16097-16114, doi:10.1029/JC094iC11p16097.

McDougall, T. J. (1987), Neutral surfaces, *Journal of Physical Oceanography, 17,* 1950-1964.

Morrison, J. (1997), Inter-monsoonal changes in the T-S properties of the near-surface waters of the northern Arabian Sea, *Geophysical Research Letters, 24*, 2553-2556.

Nazarenko, N. (unpublished data, 2009) available from APRS (http:aprsworld.net/gisdata/world/).

Pous, S. P., X. Carton, and P. Lazure (2004a), Hydrology and circulation in the Strait of Hormuz and the Gulf of Oman- Results from the GOGP99 Experiment: 1. Strait of Hormuz, *Journal of Geophysical Research, 109*(C12037), 1-15, doi:10.1029/2003JC002145.

Pous, S. P., X. Carton, and P. Lazure (2004b), Hydrology and circulation in the Strait of Hormuz and the Gulf of Oman- Results from the GOGP99 Experiment: 2. Gulf of Oman, *Journal of Geophysical Research, 109*(C12038), 1-22, doi:10.1029/2003JC002146.

Quraishee, G. S. (1984), Circulation in the north Arabian Sea at Murray Ridge during S.W. Monsoon, *Deep-Sea Research Part A- Oceanographic Research Papers, 31,* 651-664.

Reynolds, R. M. (1993), Physical oceanography of the Gulf, Strait of Hormuz, and the Gulf of Oman- results from the *Mt Mitchell* expedition, *Marine Pollution Bulletin, 27,* 35-59.

Schmid, C., R. L. Molinari, R. Sabina, Y. Daneshzadeh, X. Xia, E. Forteza, and H. Yang (2007), The real-time data management system for Argo profiling float observations, *Journal of Atmospheric and Oceanic Technology, 24,* 1608-1628.

Schott, F. A. and J. P. McCreary (2001), The monsoon circulation of the Indian Ocean, *Progress in Oceanography, 51,* 1-123.

Schott, F. A., S. Xie, and J. P. McCreary (2009), Indian Ocean circulation and climate variability, *Reviews of Geophysics, 47,* 1-46, doi:10.1029/2007RG000245.

Shi, W., J. M. Morrison, E. Böhm, V. Manghnani (2000), The Oman upwelling zone during 1993, 1994, 1995, *Deep-Sea Research II, 42,* 1227-1247.

Siddall, M., D. A. Smeed, S. Matthiesen, and E. J. Rohling (2002), Modelling the seasonal cycle of the exchange flow in Bab El Mandab (Red Sea), *Deep-Sea Research, 49,* 1551-1569.

Smeed, D. A. (2004), Exchange through the Bab el Mandab, *Deep-Sea Research II, 51,* 455-474, doi:10.1016/j.dsr2.2003.11.002.

Swift, S. A. and A. S. Bower (2003), Formation and circulation of dense water in the Persian/Arabian Gulf, *Journal of Geophysical Research, 108,* 1-15, doi:10.1029/2002JC001360.

Thoppil, P. G. and P. J. Hogan (2008), On the mechanisms of episodic salinity outflow events in the Strait of Hormuz, *Journal of Physical Oceanography, 39,* 1340-1359, doi:10.1175/2008JPO3941.1.

UCSD Argo (unpublished data, 2011) available from the University of California at San Diego (http://www.argo.ucsd.edu).

Vinayachandran, P. N. and R. S. Nanjundiah (2009), Indian Ocean sea surface salinity variations in a coupled model, *Climate Dynamics, 33*, 245-263, doi:10.1007/s00382-008-0511-6.0

Wajsowicz, R. C. and P. S. Schopf (2001), Oceanic influences on the seasonal cycle in evaporation over the Indian Ocean, *Journal of Climate, 14,* 1199-1226.

Weller, R. A., M. F. Baumgartner, S. A. Josey, A. S. Fischer, and J. C. Kindle (1998), Atmospheric forcing in the Arabian Sea during 1994-1995: observations and comparisons with climatology and models, *Deep-Sea Research II, 45,* 1961-1999.

Wyrtki, K., E. B. Bennett, and D. J. Rochford (1971), *Oceanographic Atlas of the International Indian Ocean Expedition*, National Science Foundation, Washington, D.C.

You, Y. and M. Tomczak (1993), Thermocline circulation and ventilation in the Indian Ocean derived from water mass analysis, *Deep-Sea Research 1*, *40*, 13-56.

APPENDIX A

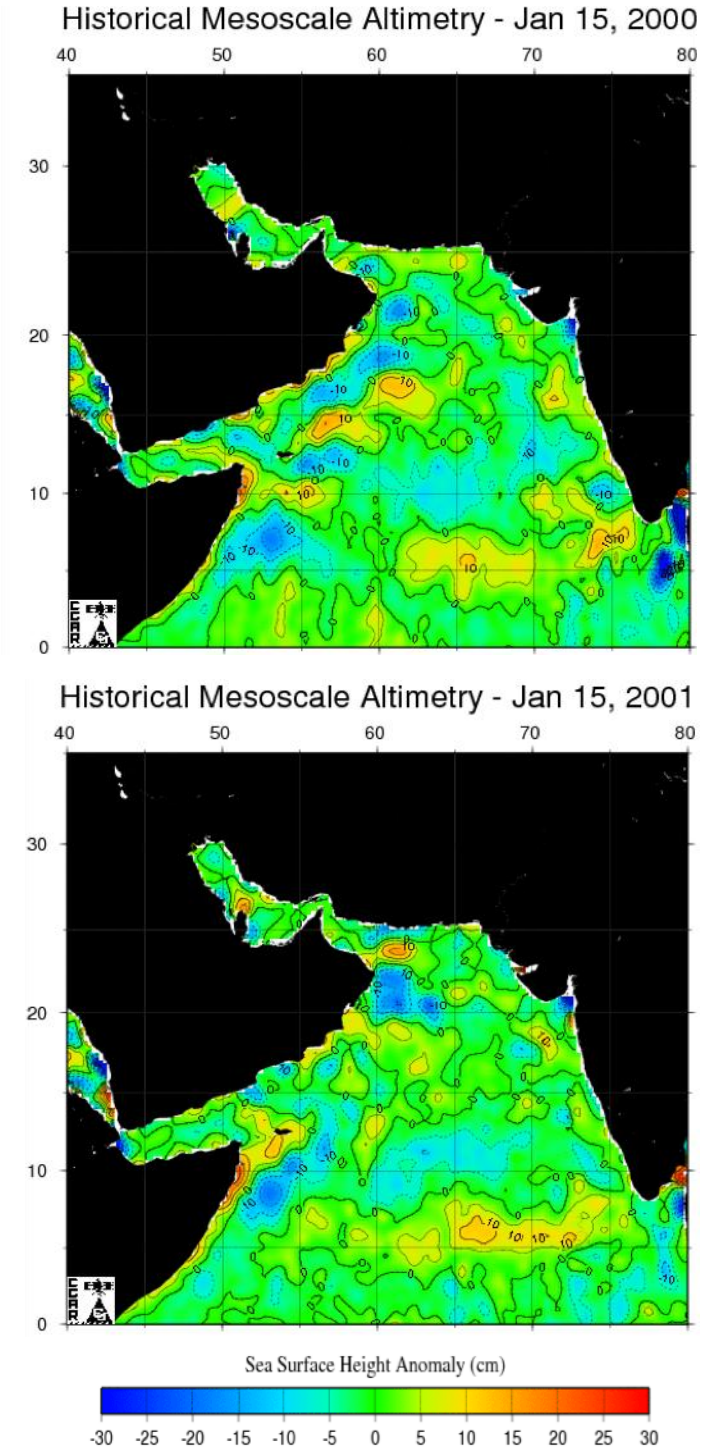

Figure A-1. Historical and real-time mesoscale altimetry maps for January 15, 2000-2009 (CCAR, 2009).

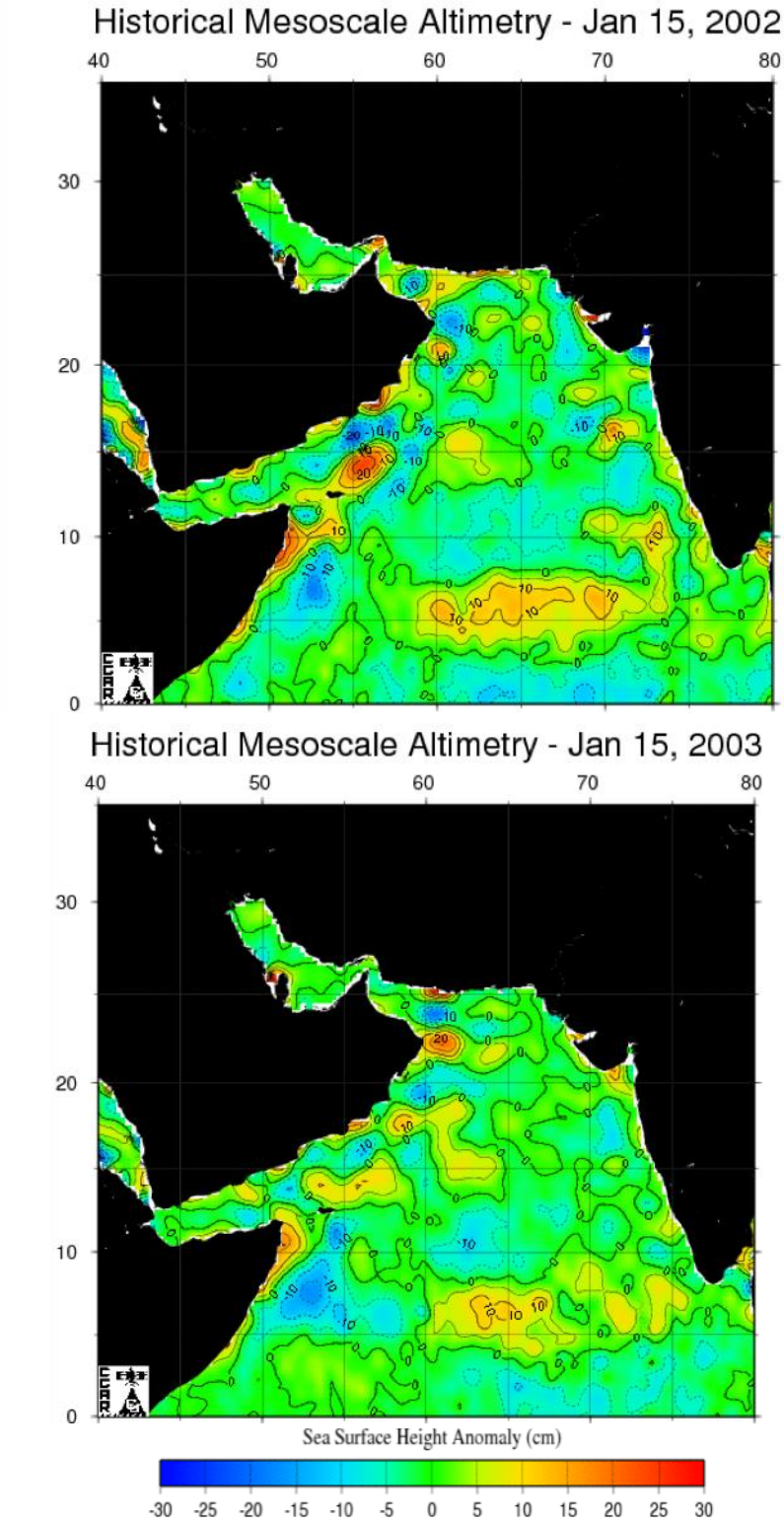

Figure A-1 continued.

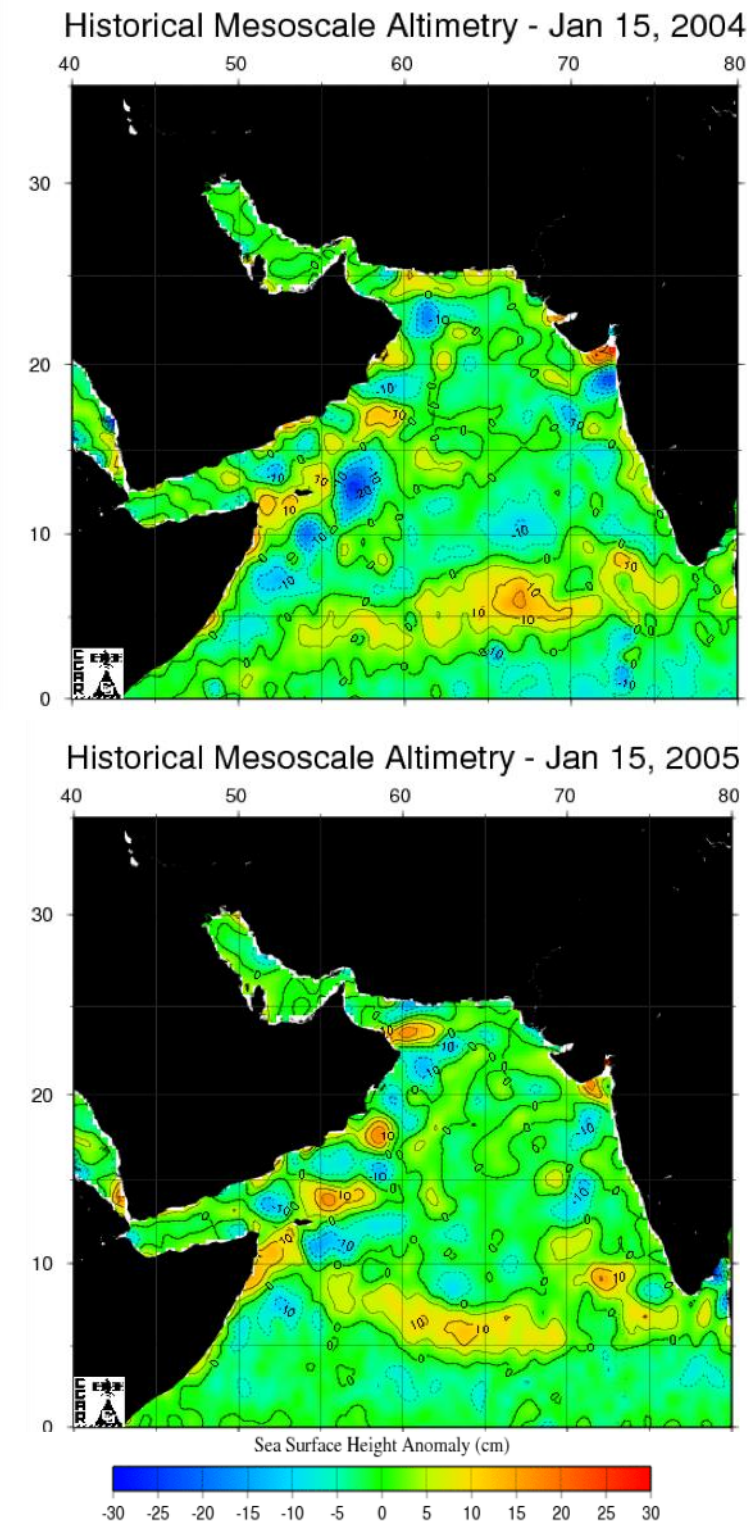

Figure A-1 continued.

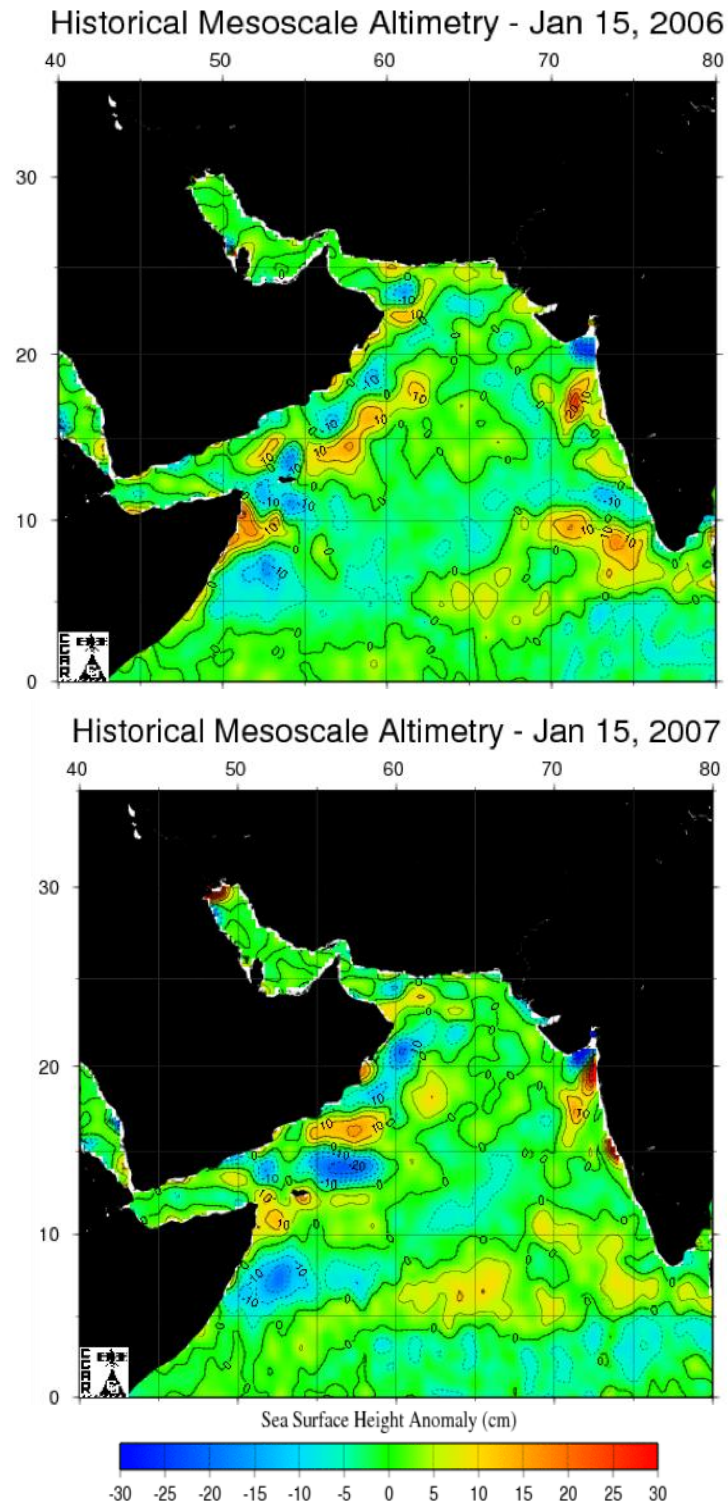

Figure A-1 continued.

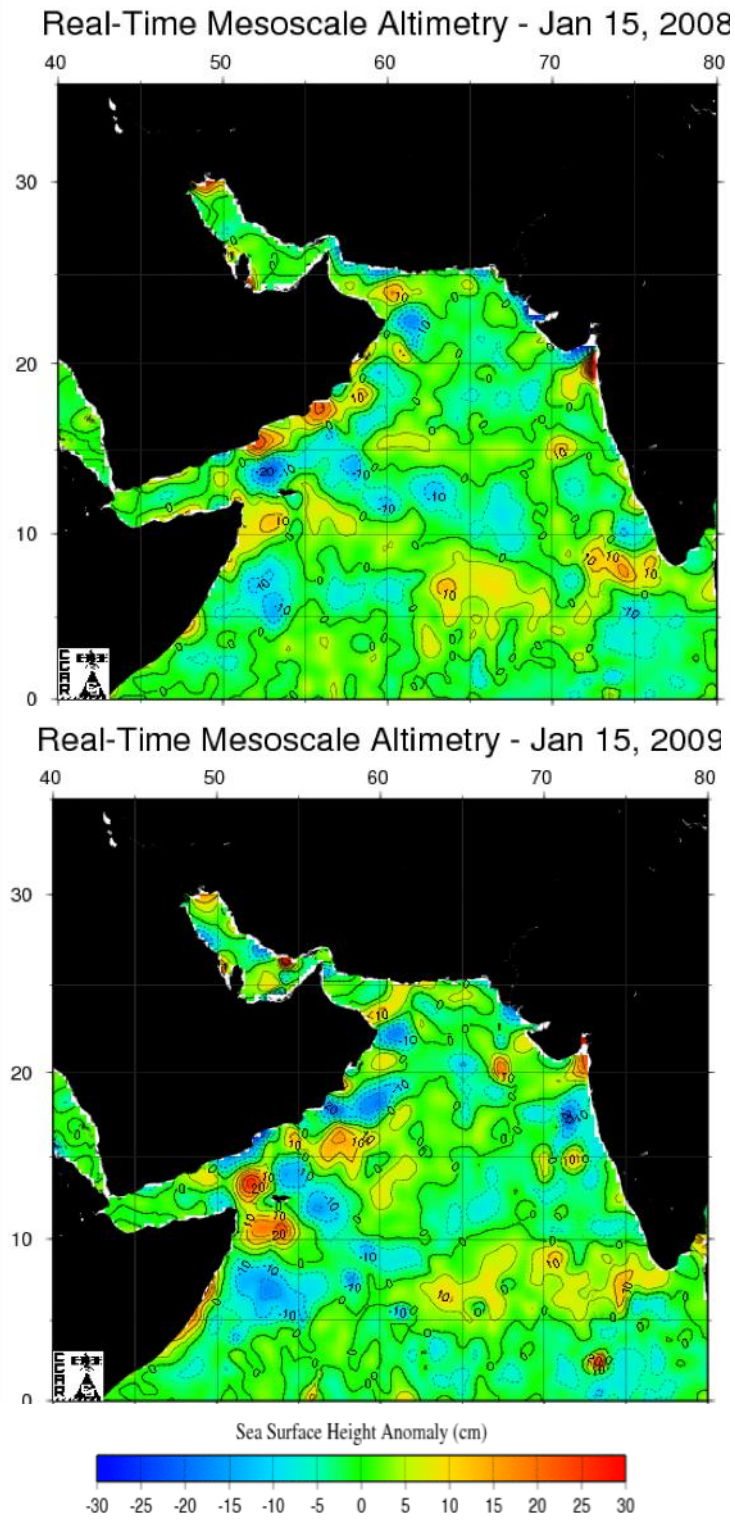

Figure A-1 continued.

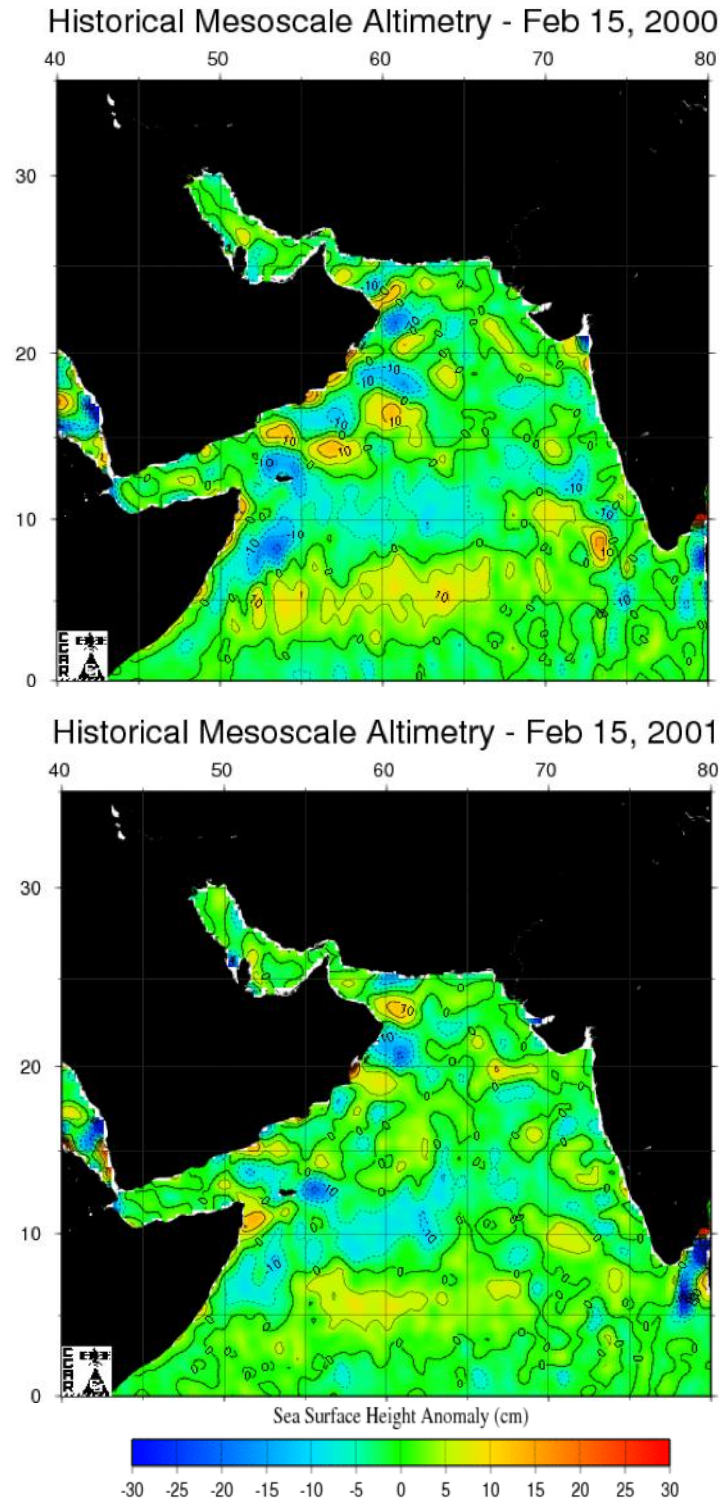

Figure A-2. Historical and real-time mesoscale altimetry maps for February 15, 2000-2009 (CCAR, 2009).

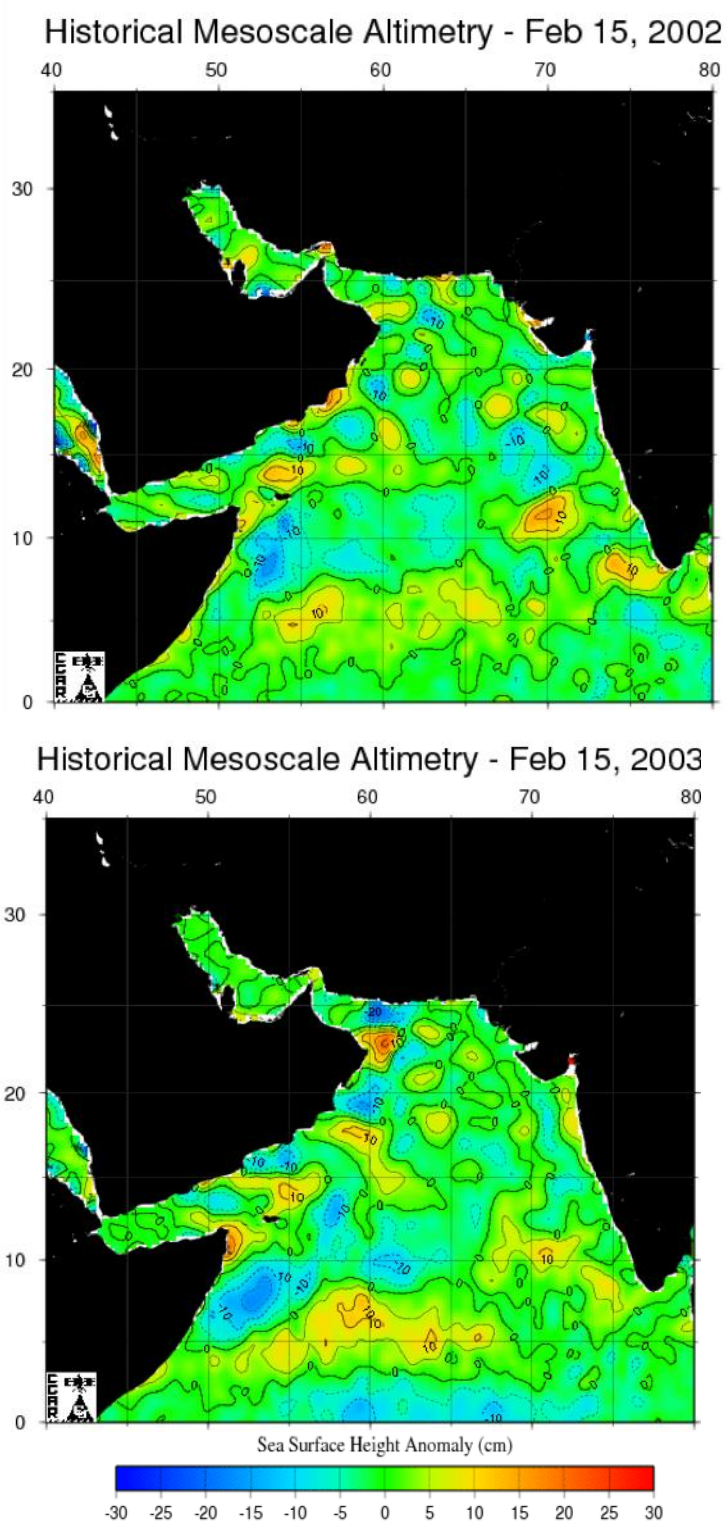

Figure A-2 continued.

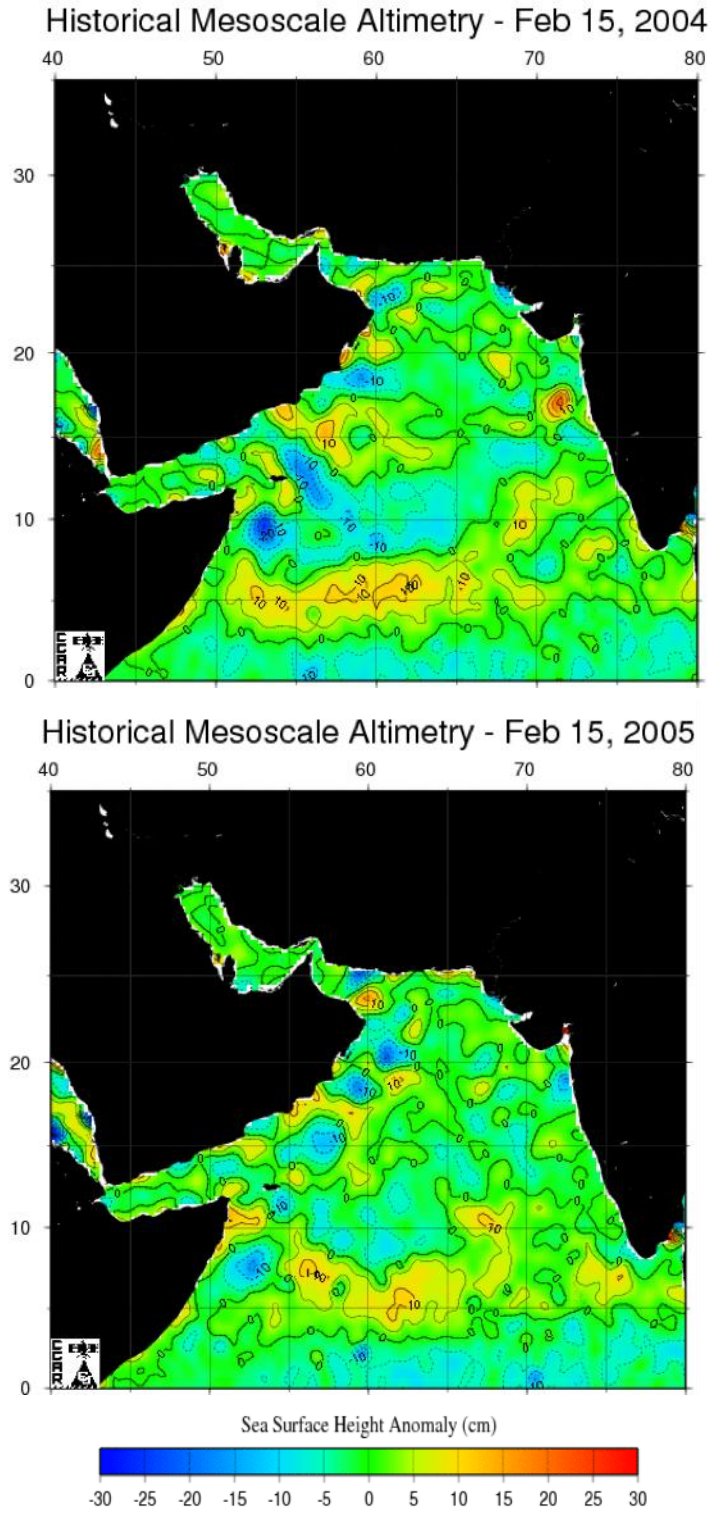

Figure A-2 continued.

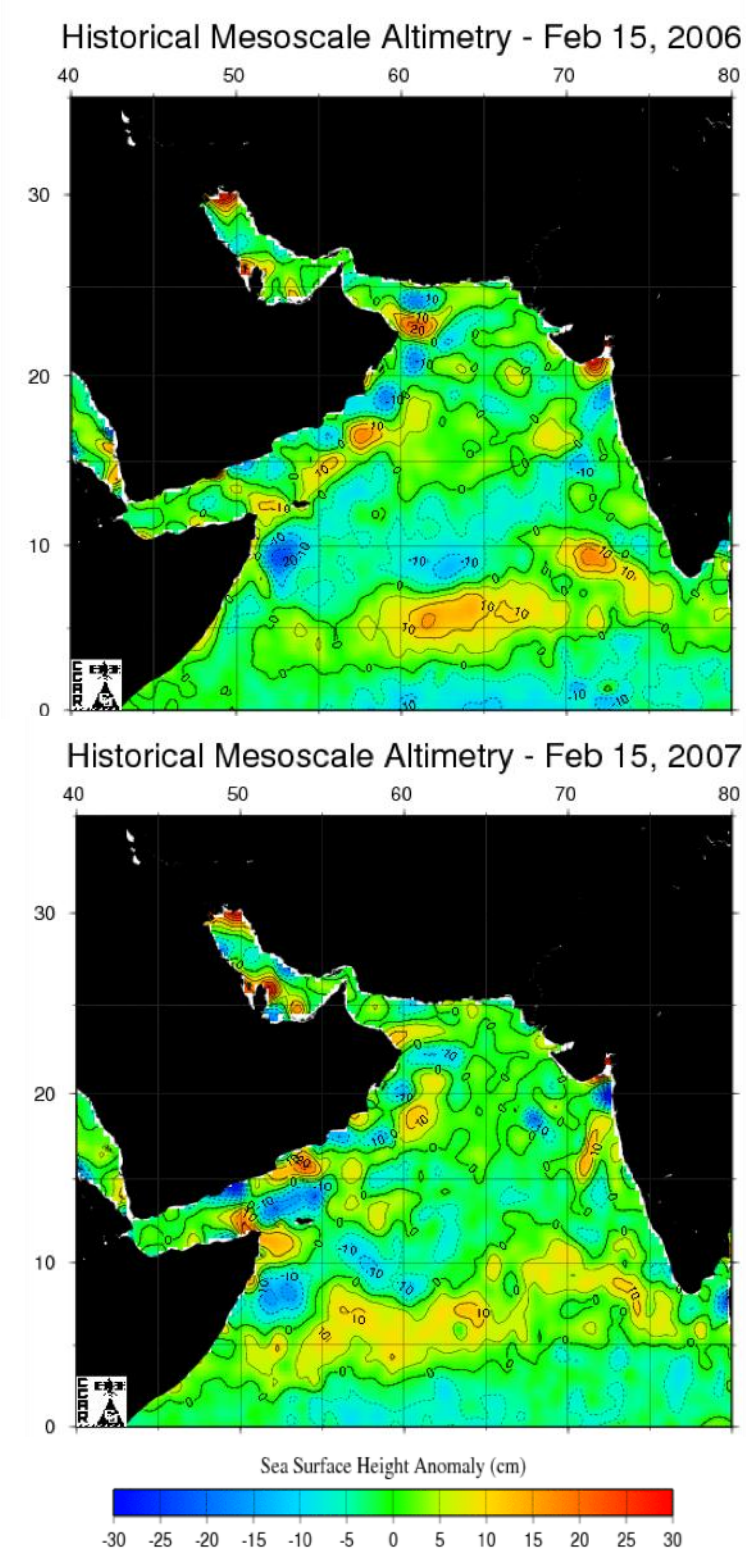

Figure A-2 continued.

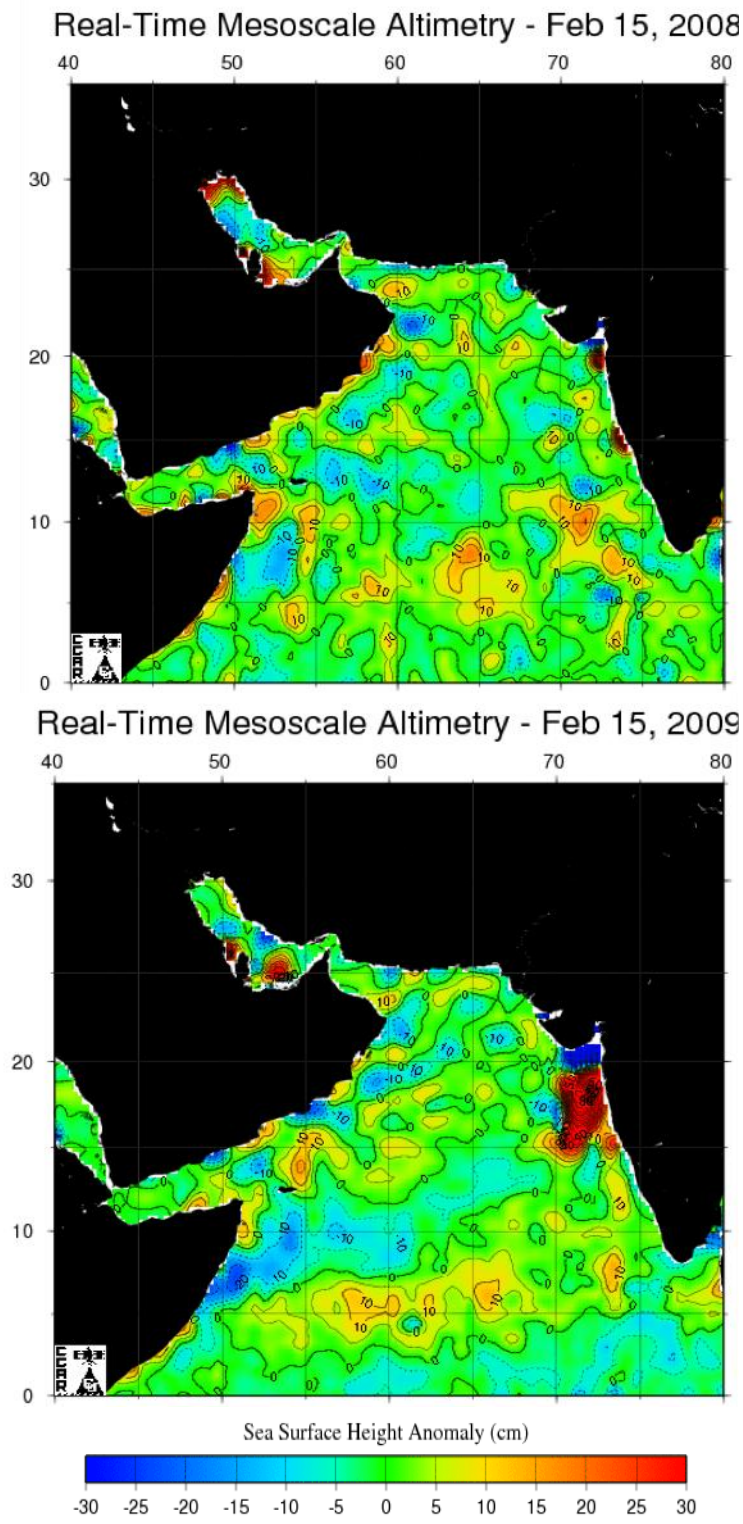

Figure A-2 continued.

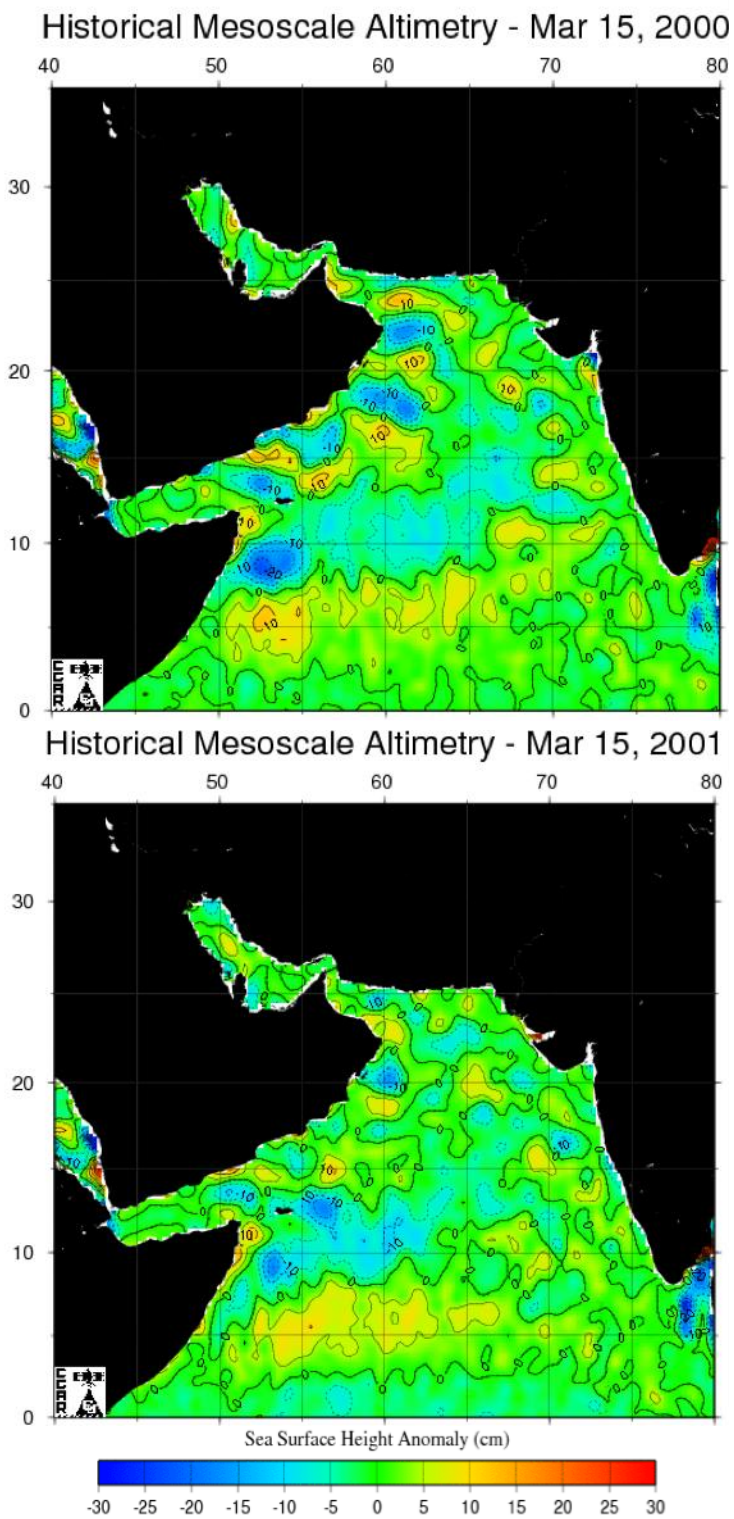

Figure A-3. Historical and real-time mesoscale altimetry maps for March 15, 2000-2009 (CCAR, 2009).

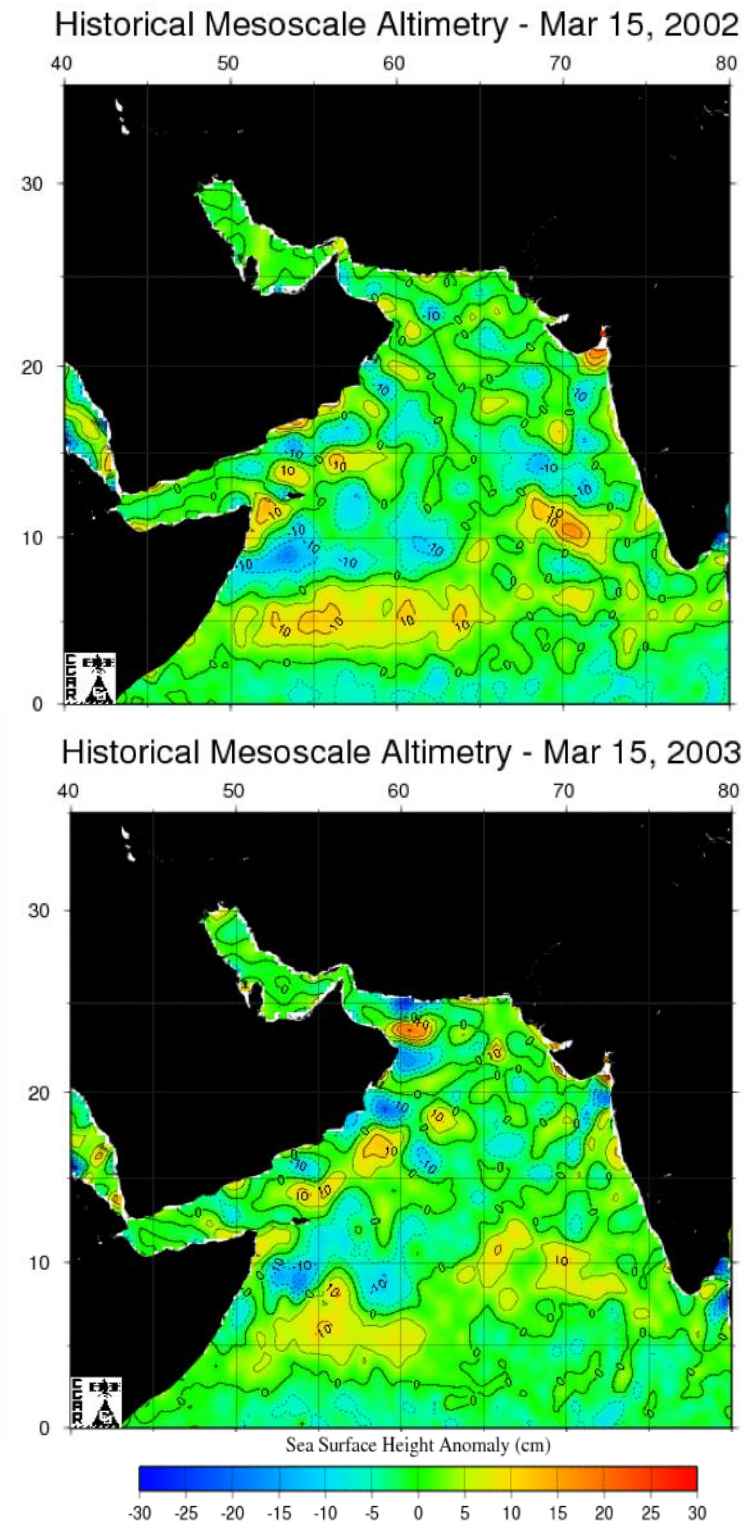

Figure A-3 continued.

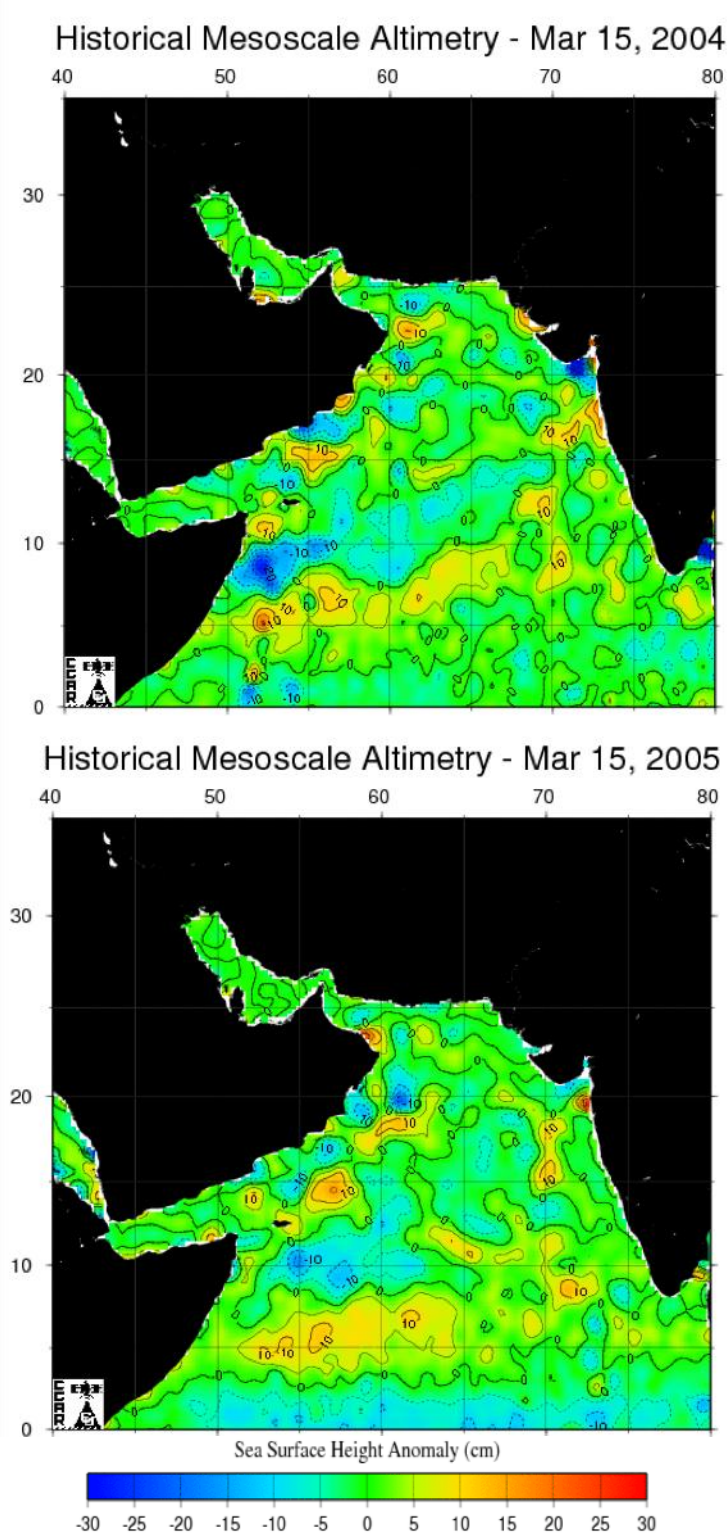

Figure A-3 continued.

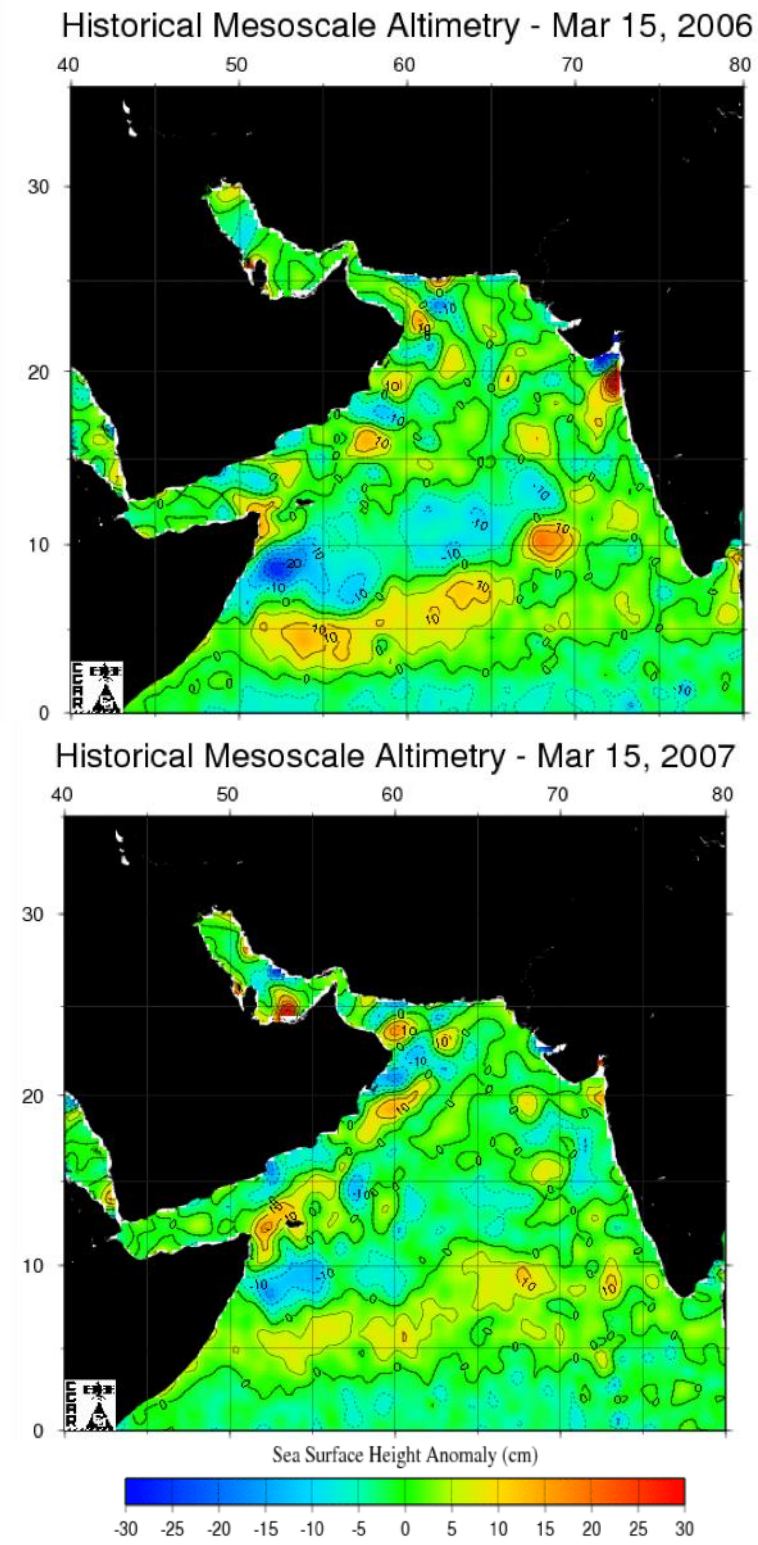

Figure A-3 continued.

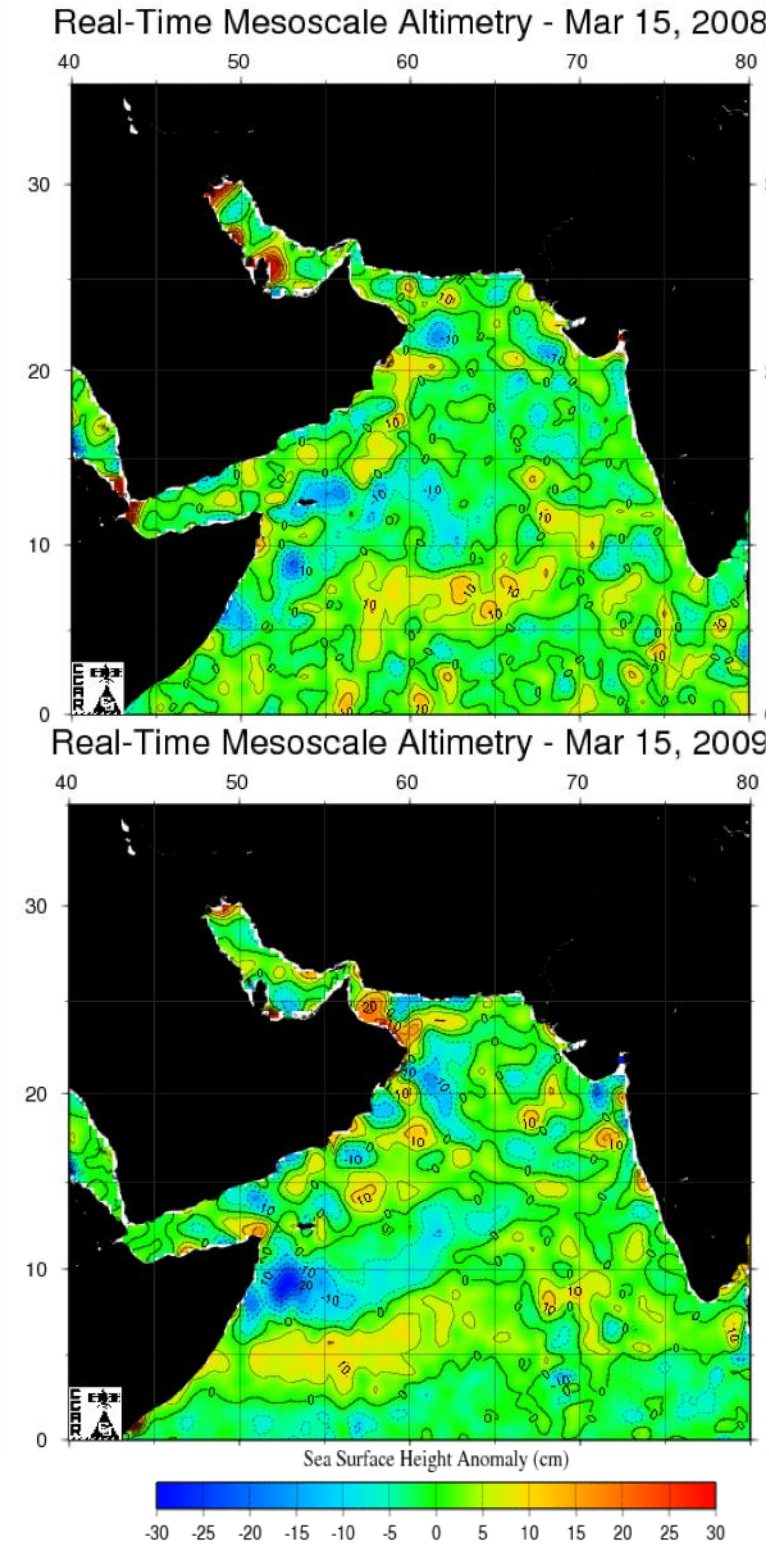

Figure A-3 continued.

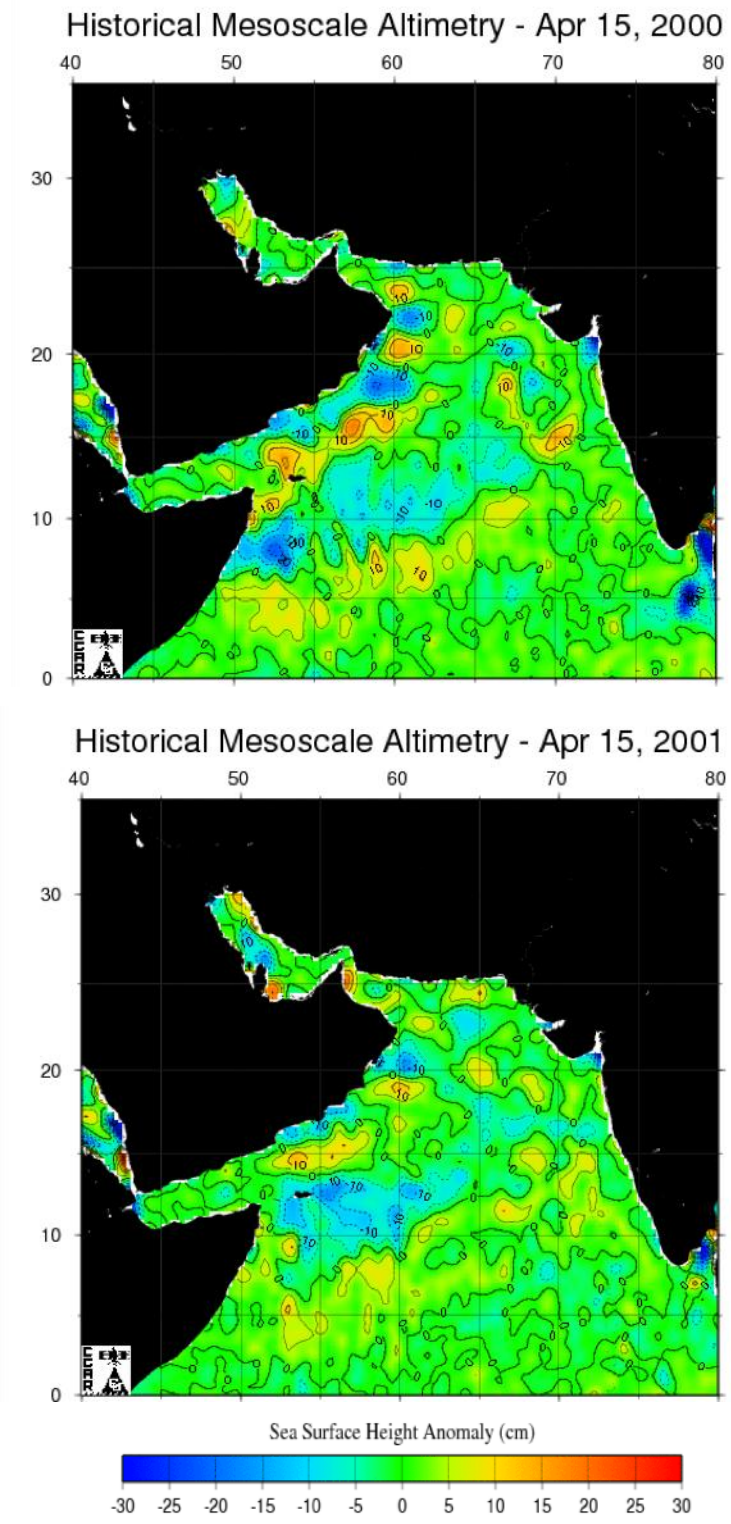

Figure A-4. Historical and real-time mesoscale altimetry maps for April 15, 2000-2009 (CCAR, 2009).

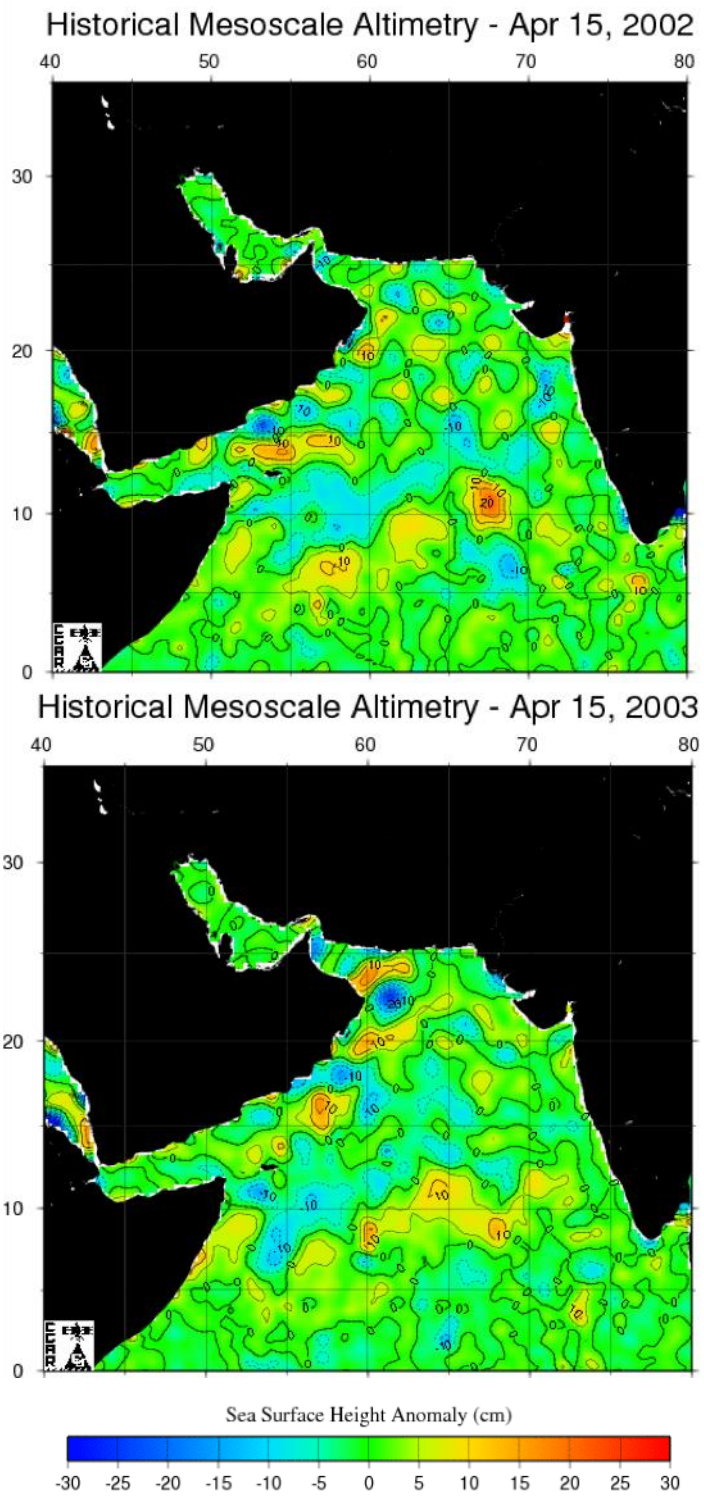

Figure A-4 continued.

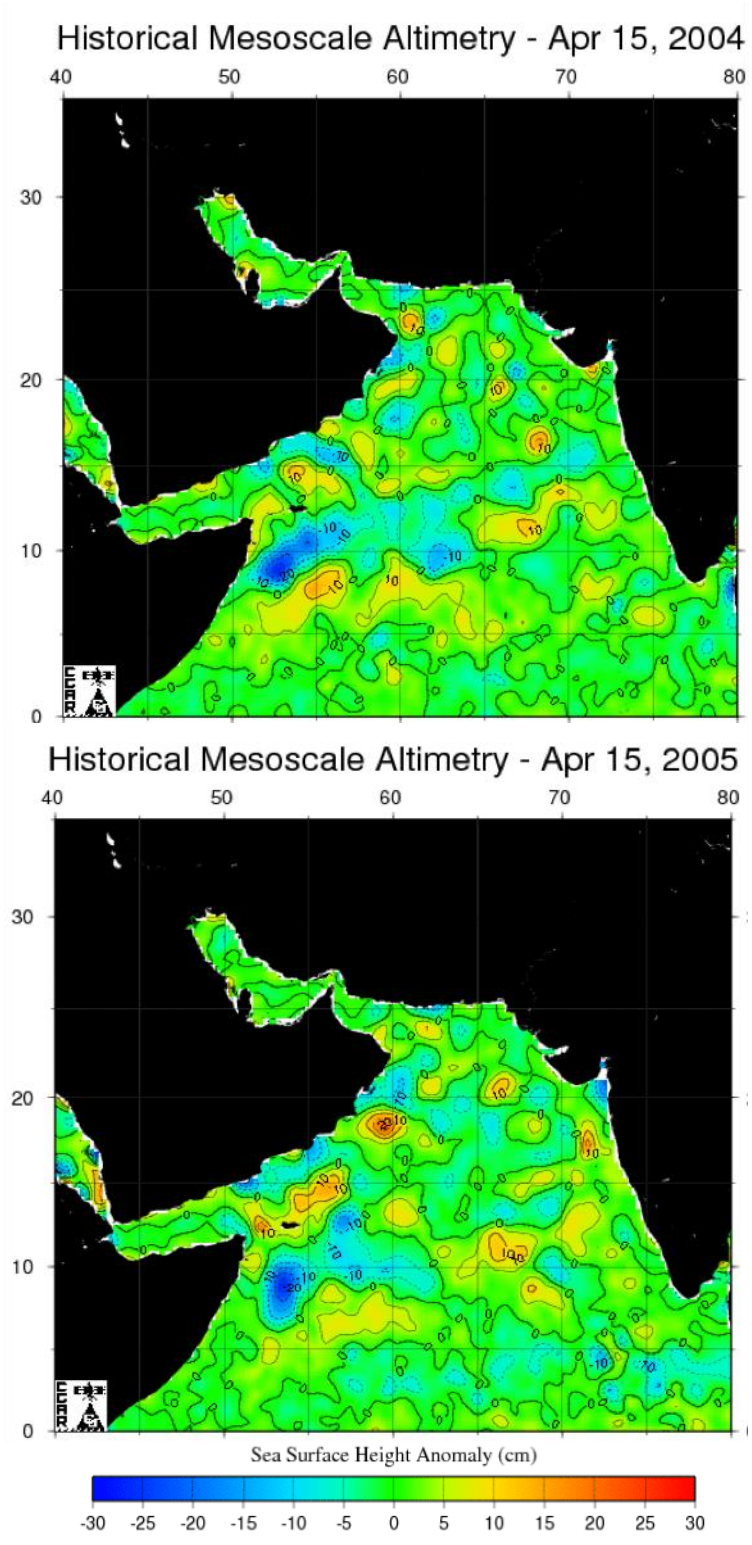

Figure A-4 continued.

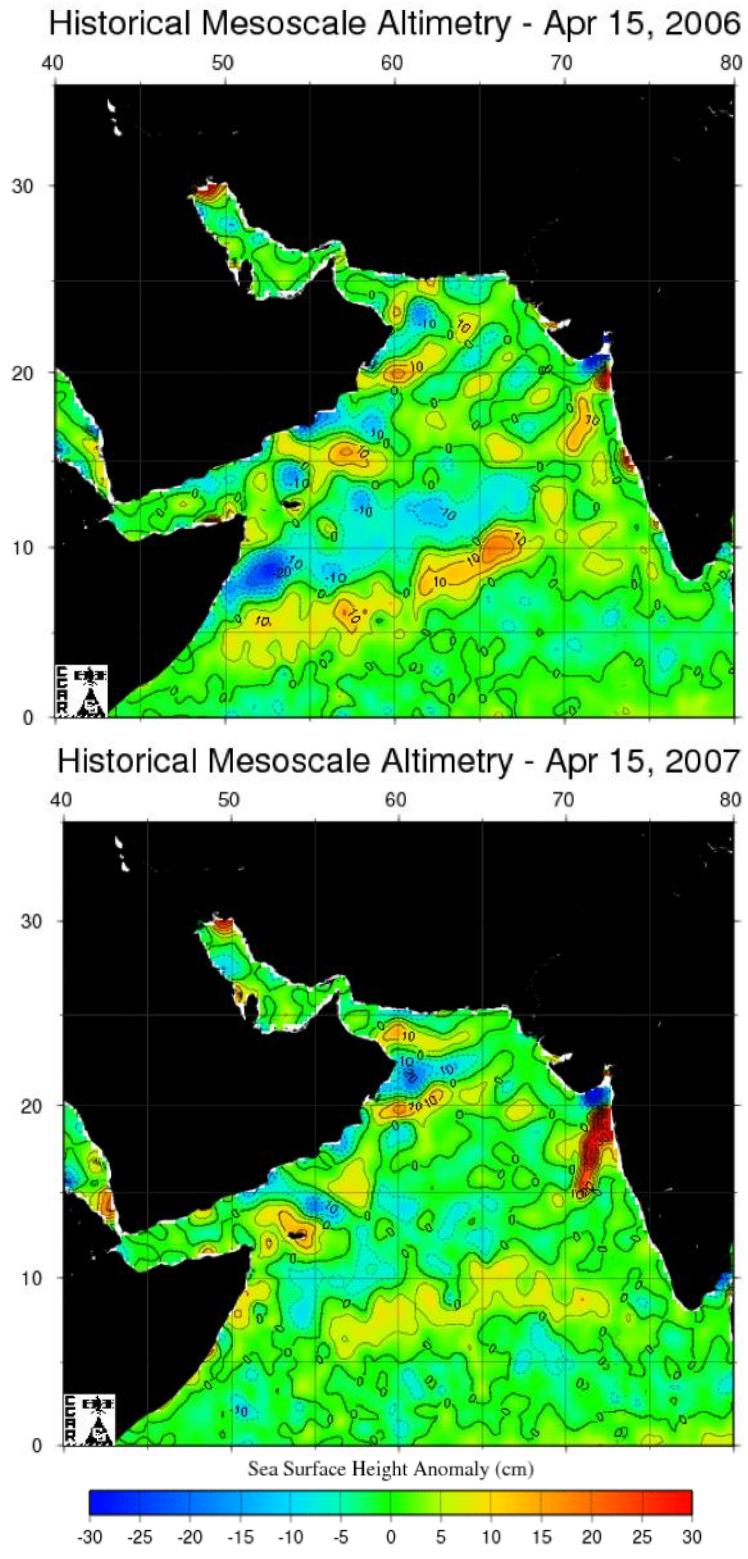

Figure A-4 continued.

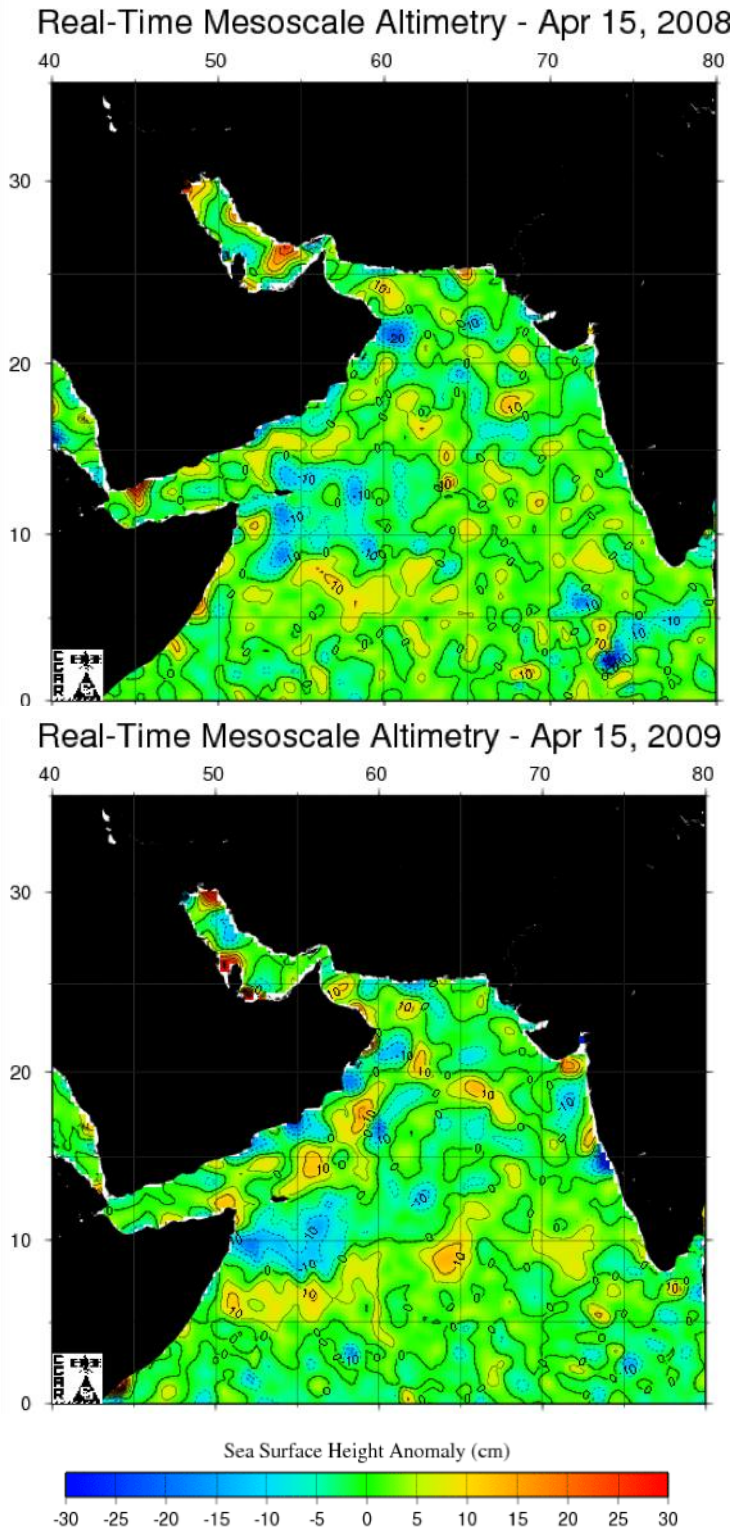

Figure A-4 continued.

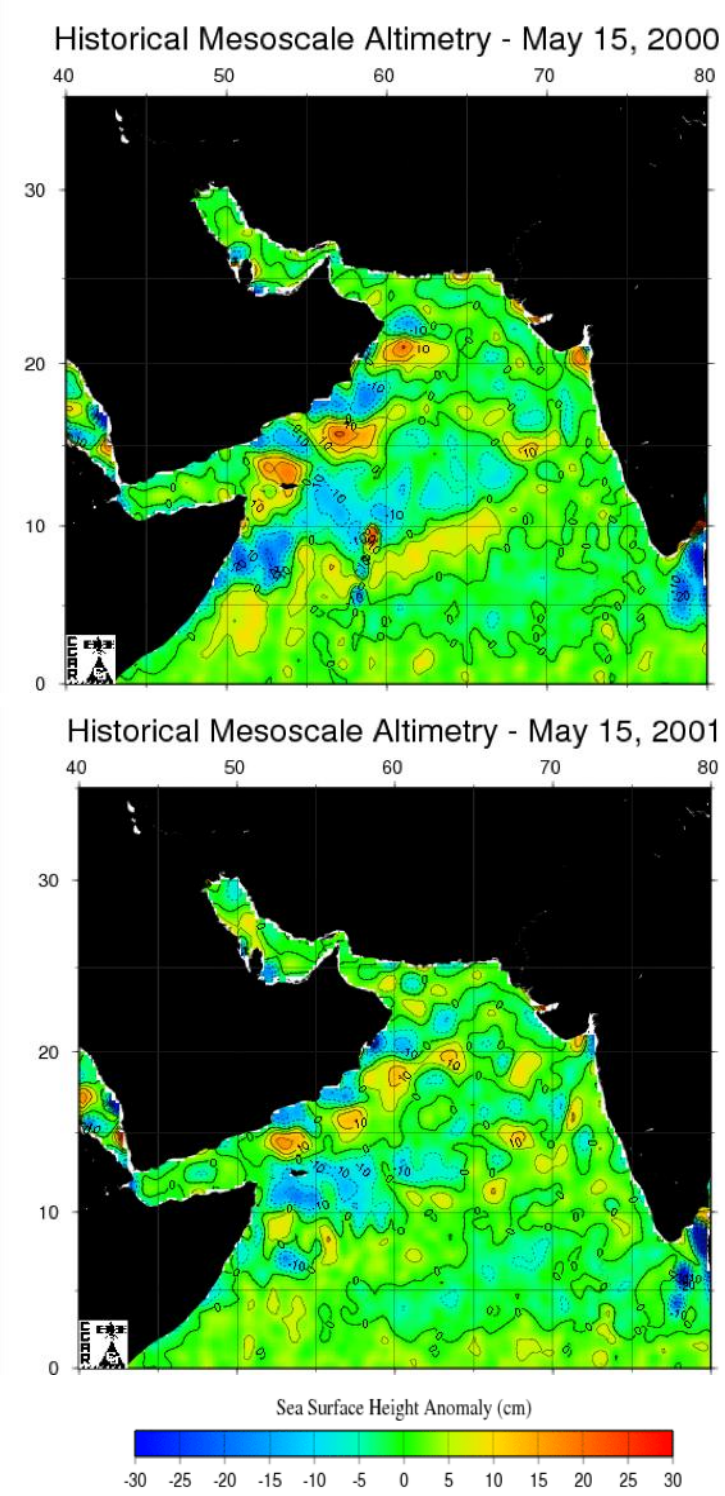

Figure A-5. Historical and real-time mesoscale altimetry maps for May 15, 2000-2009 (CCAR, 2009).

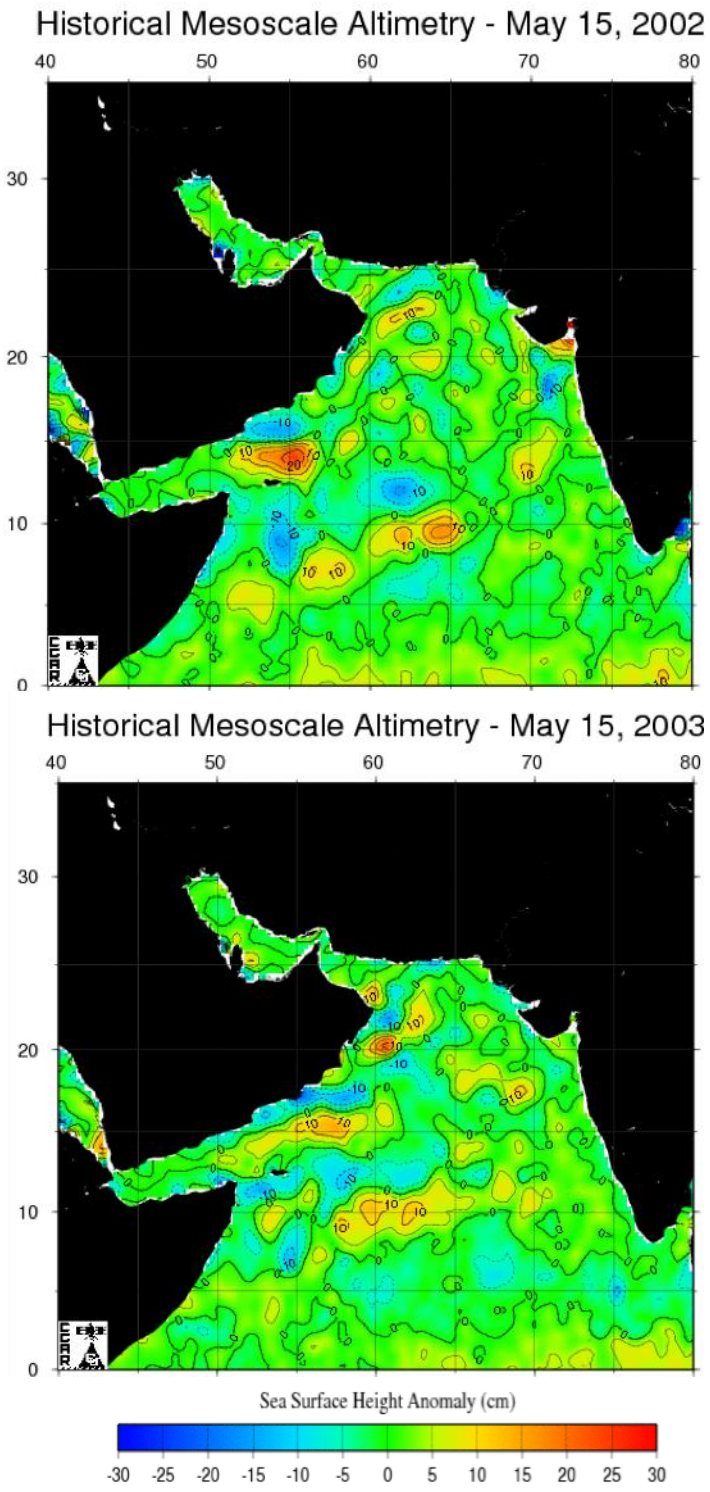

Figure A-5 continued.

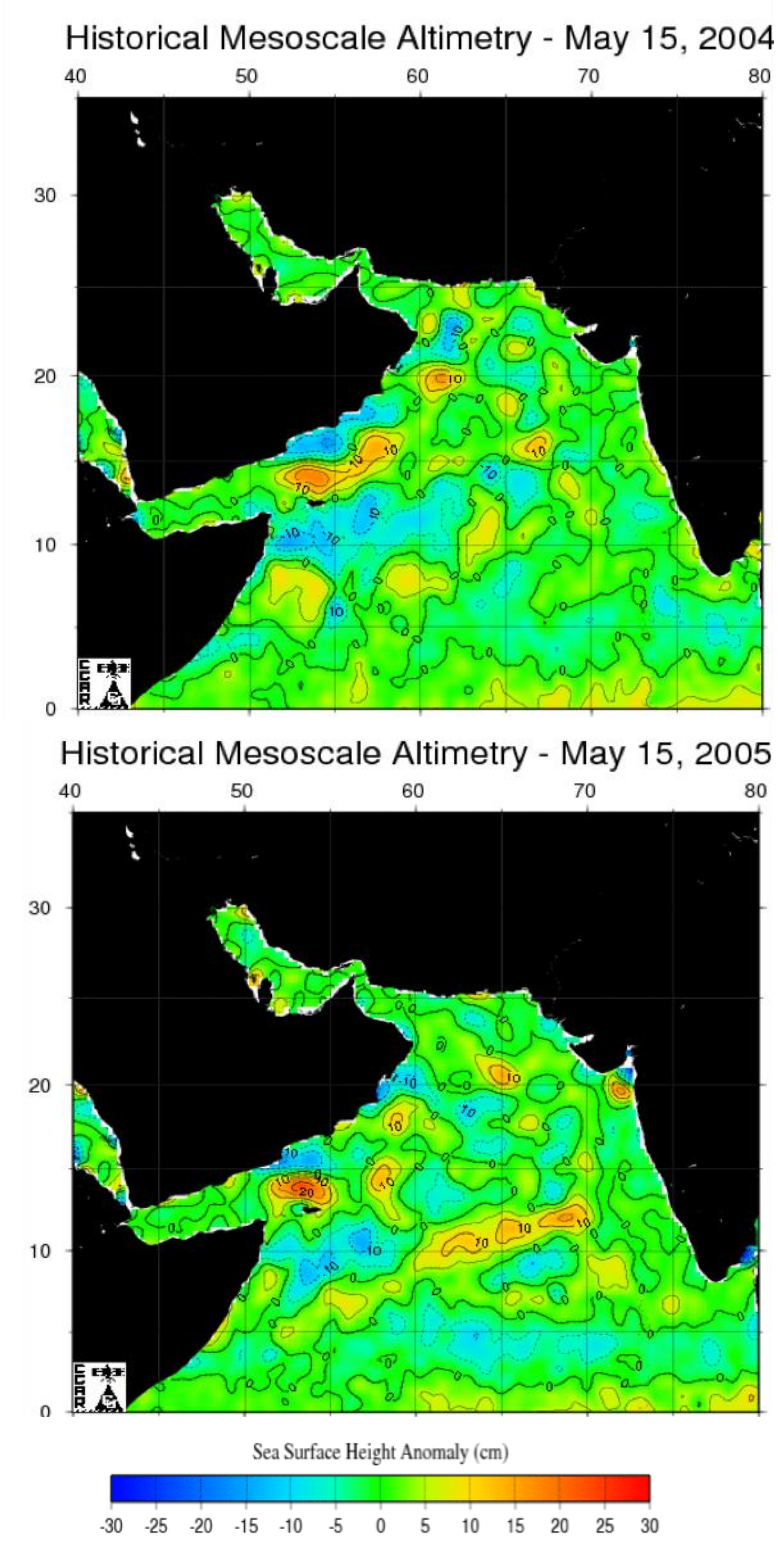

Figure A-5 continued.

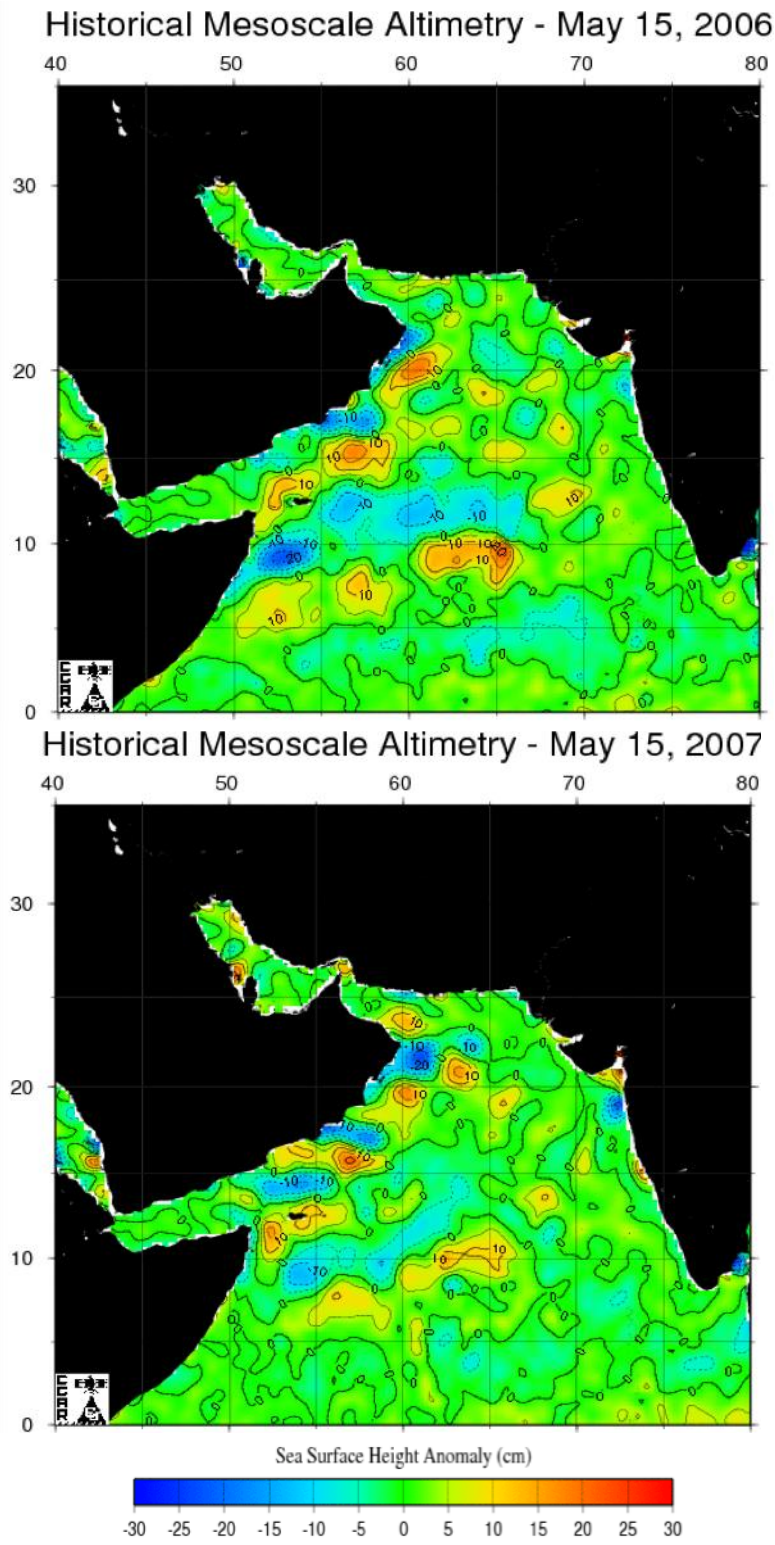

Figure A-5 continued.

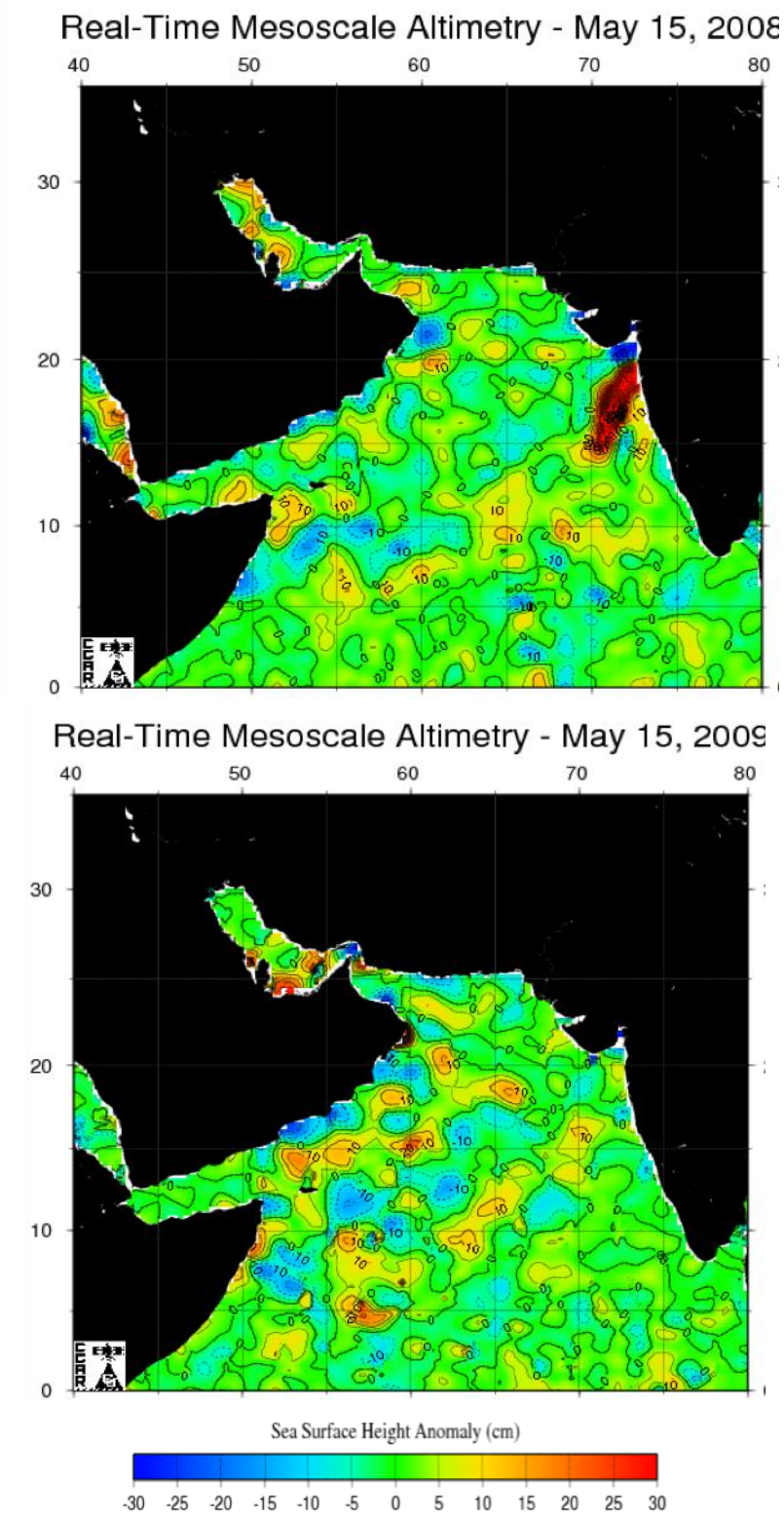

Figure A-5 continued.

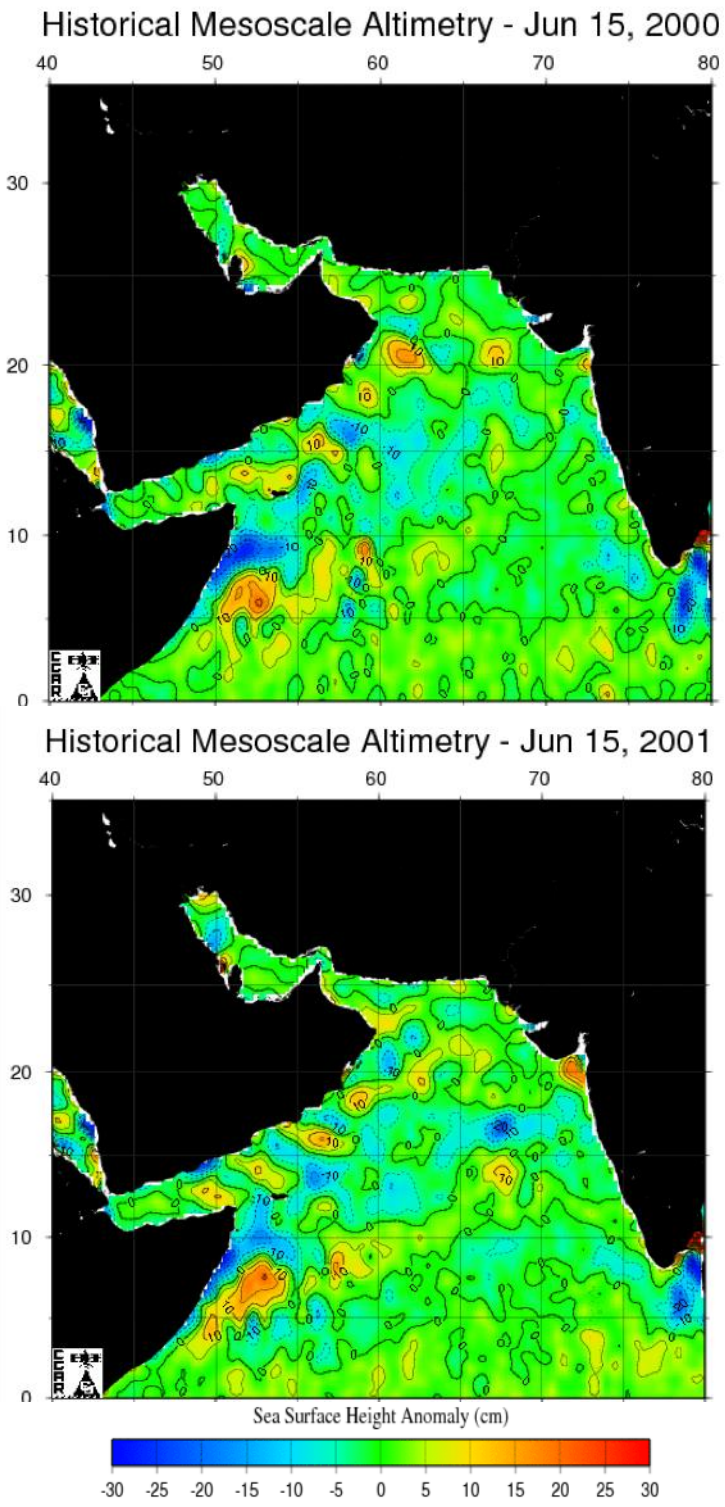

Figure A-6. Historical and real-time mesoscale altimetry maps for June 15, 2000-2009 (CCAR, 2009).

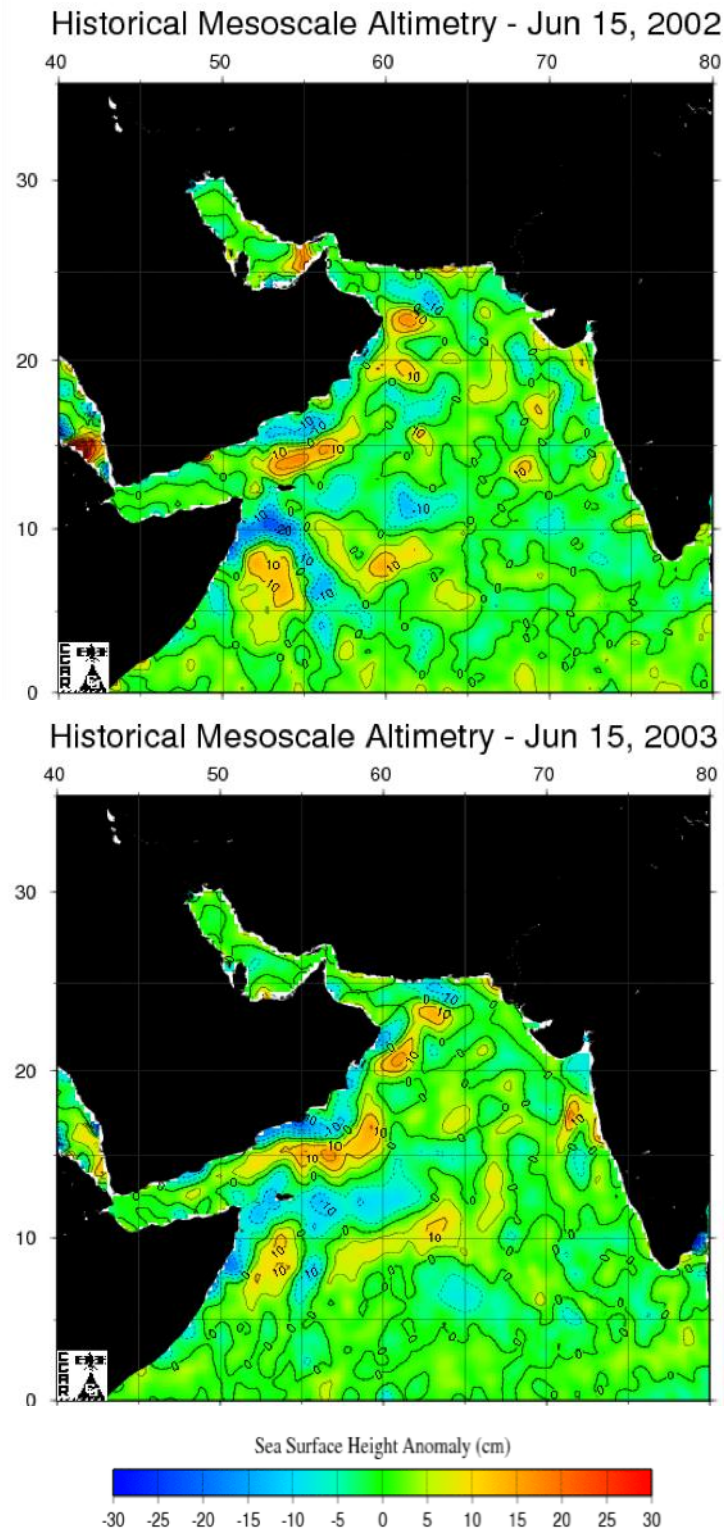

Figure A-6 continued.

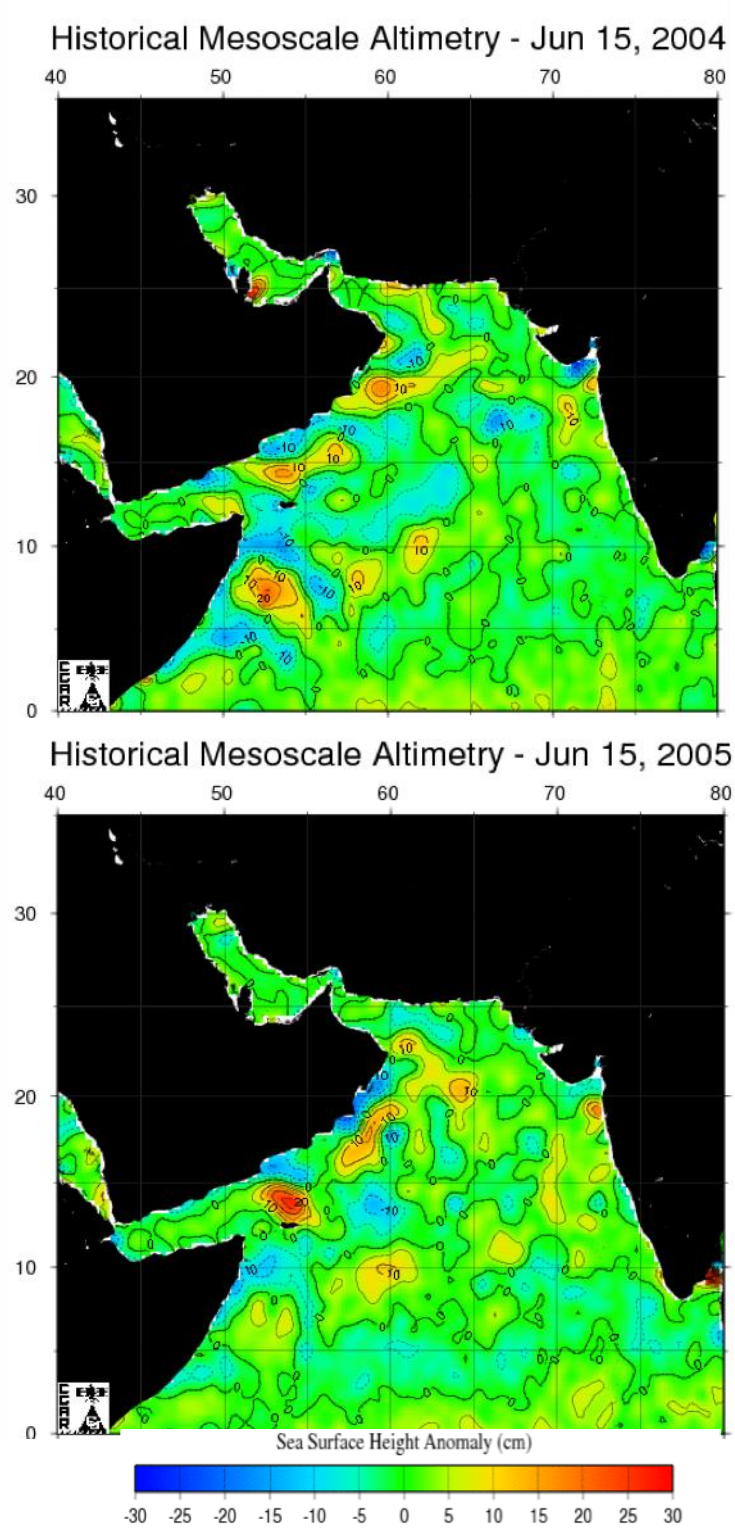

Figure A-6 continued.

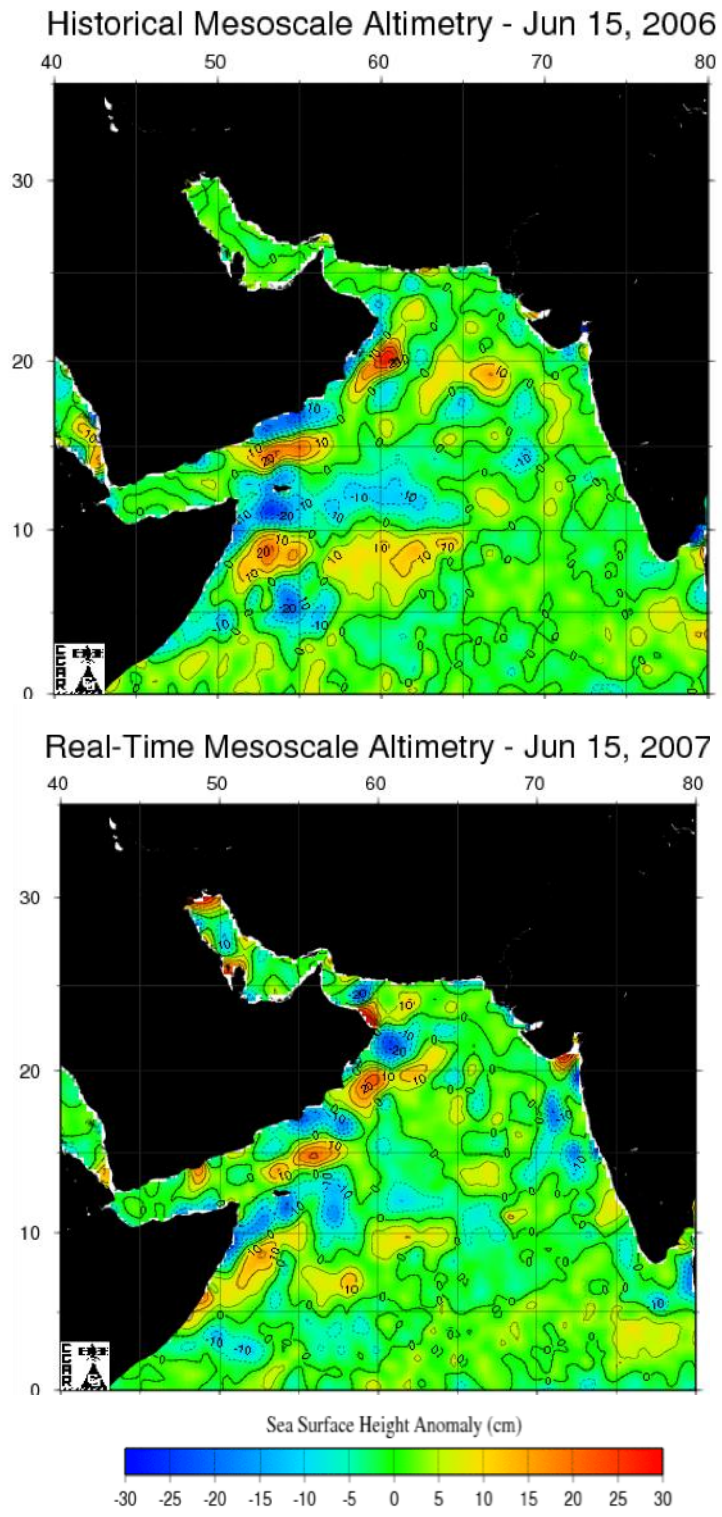

Figure A-6 continued.

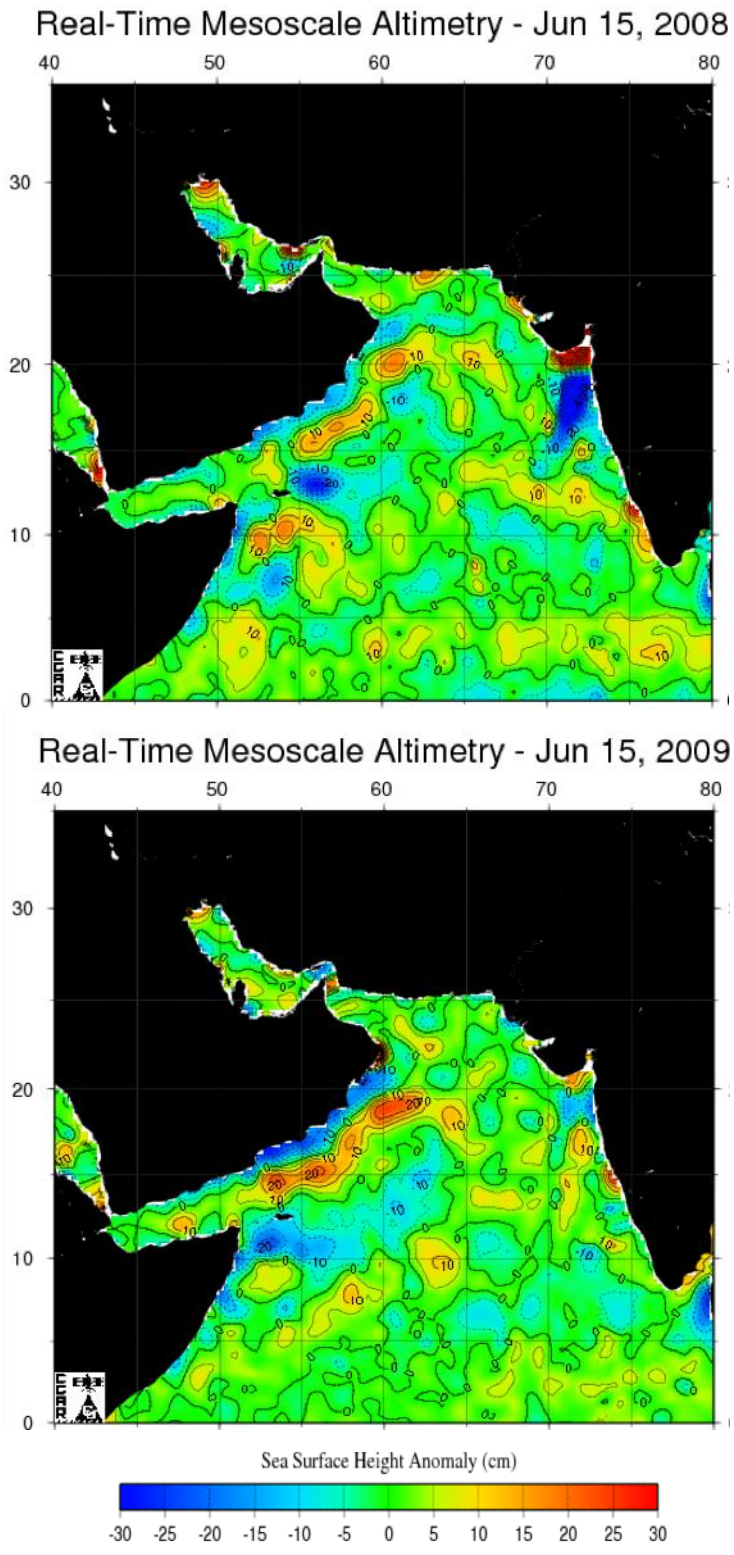

Figure A-6 continued.

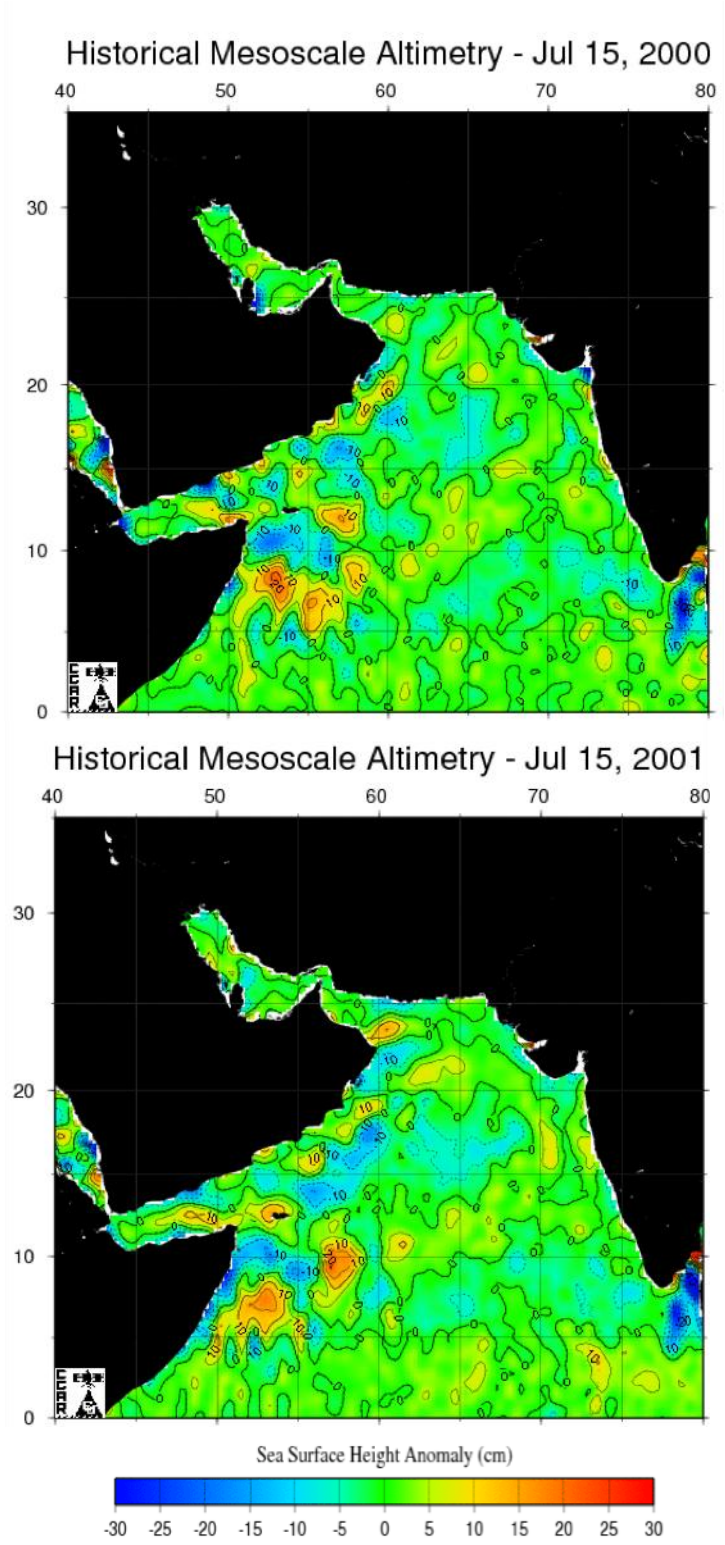

Figure A-7. Historical and real-time mesoscale altimetry maps for July 15, 2000-2009 (CCAR, 2009).

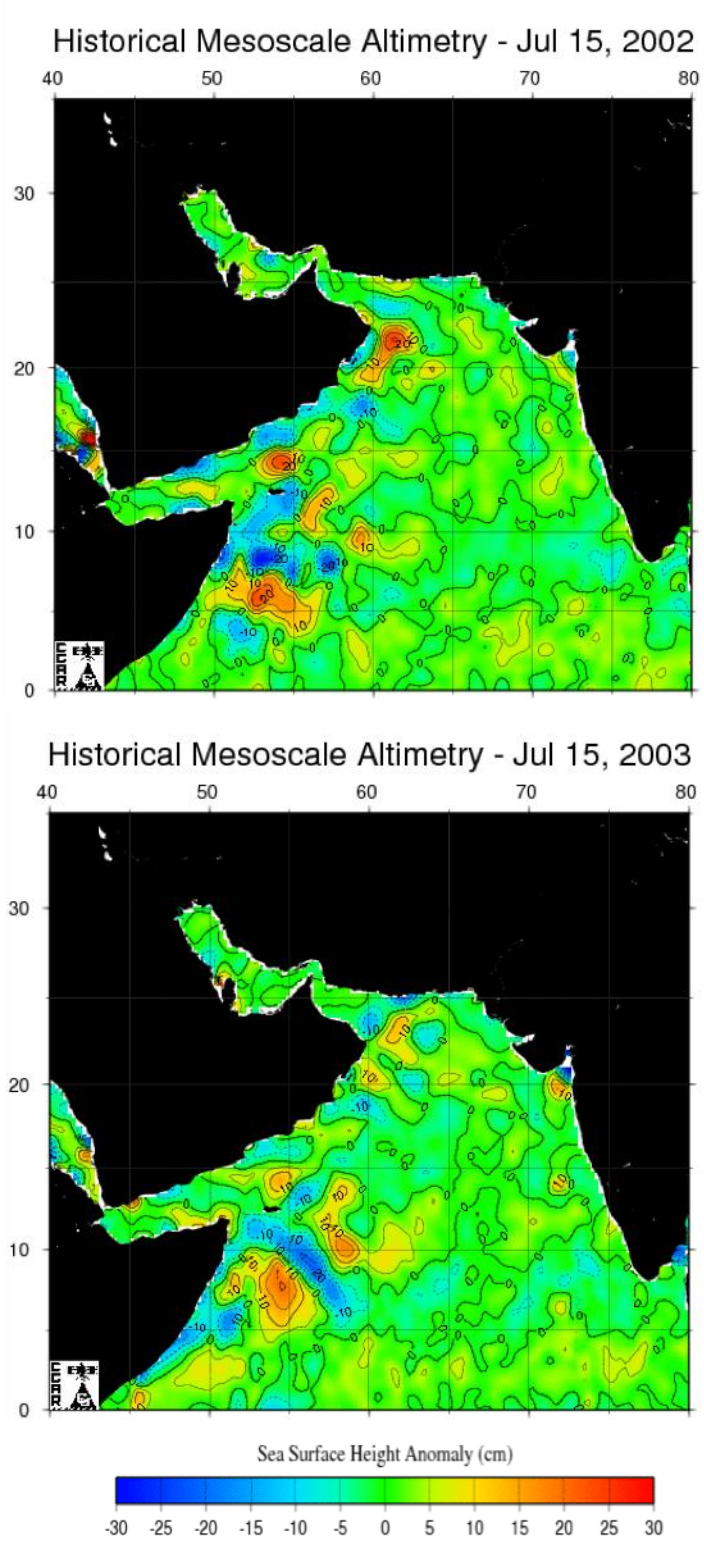

Figure A-7 continued.

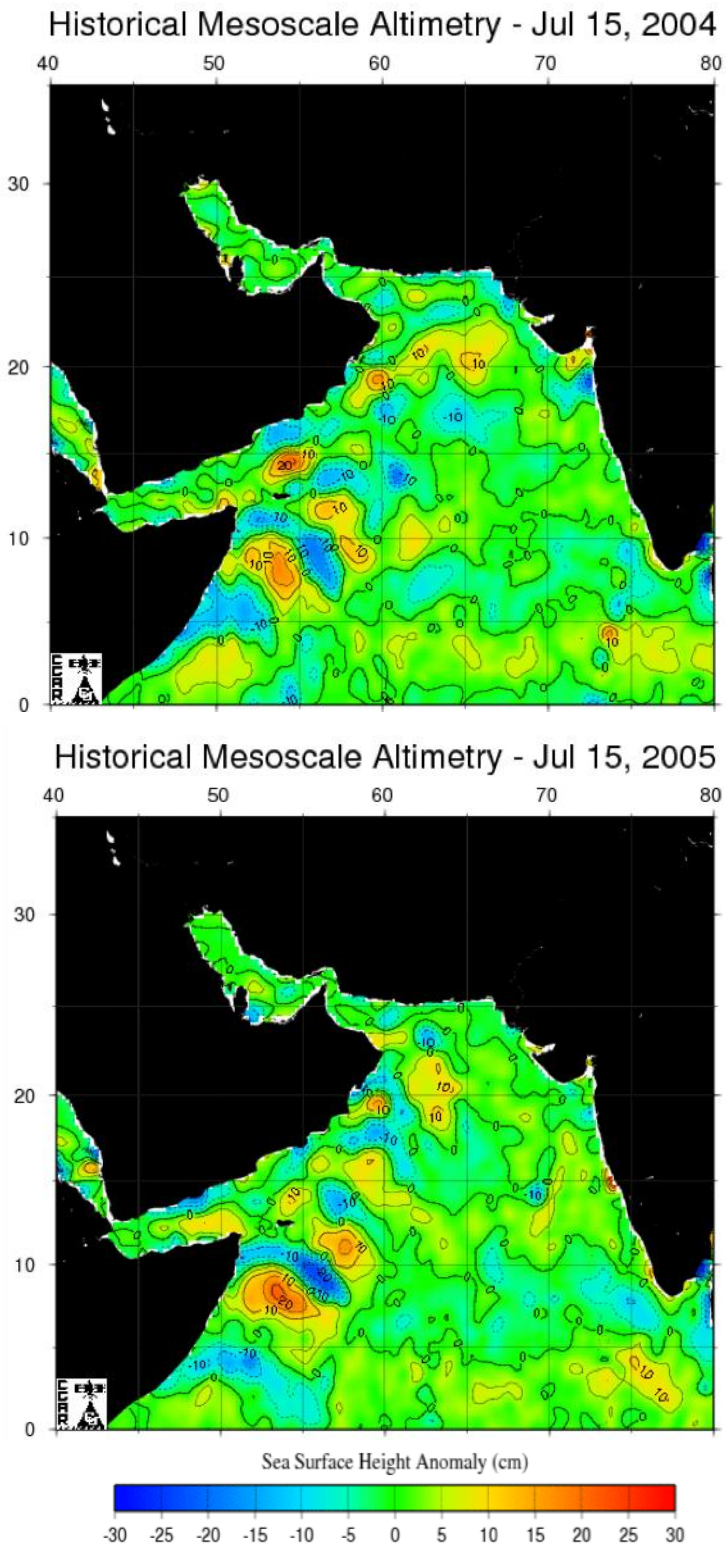

Figure A-7 continued.

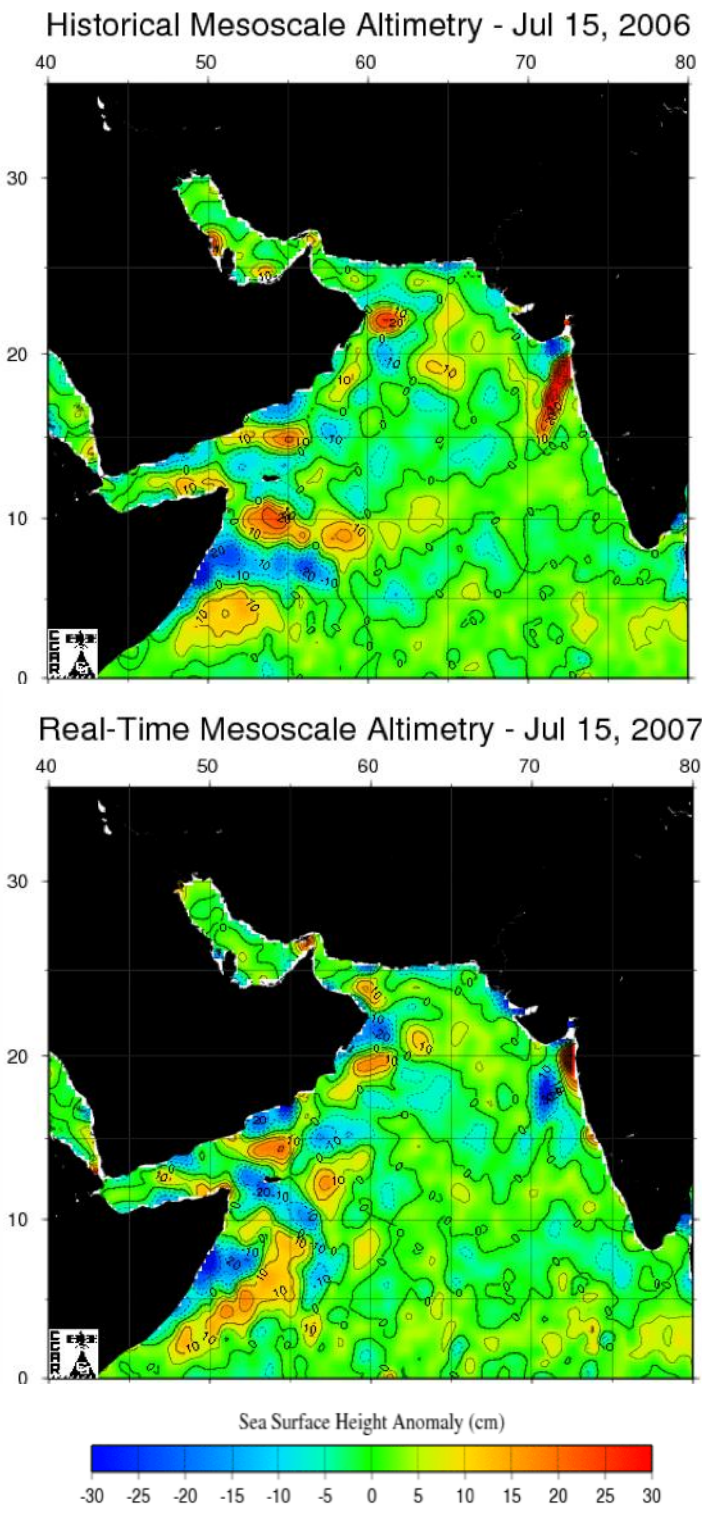

Figure A-7 continued.

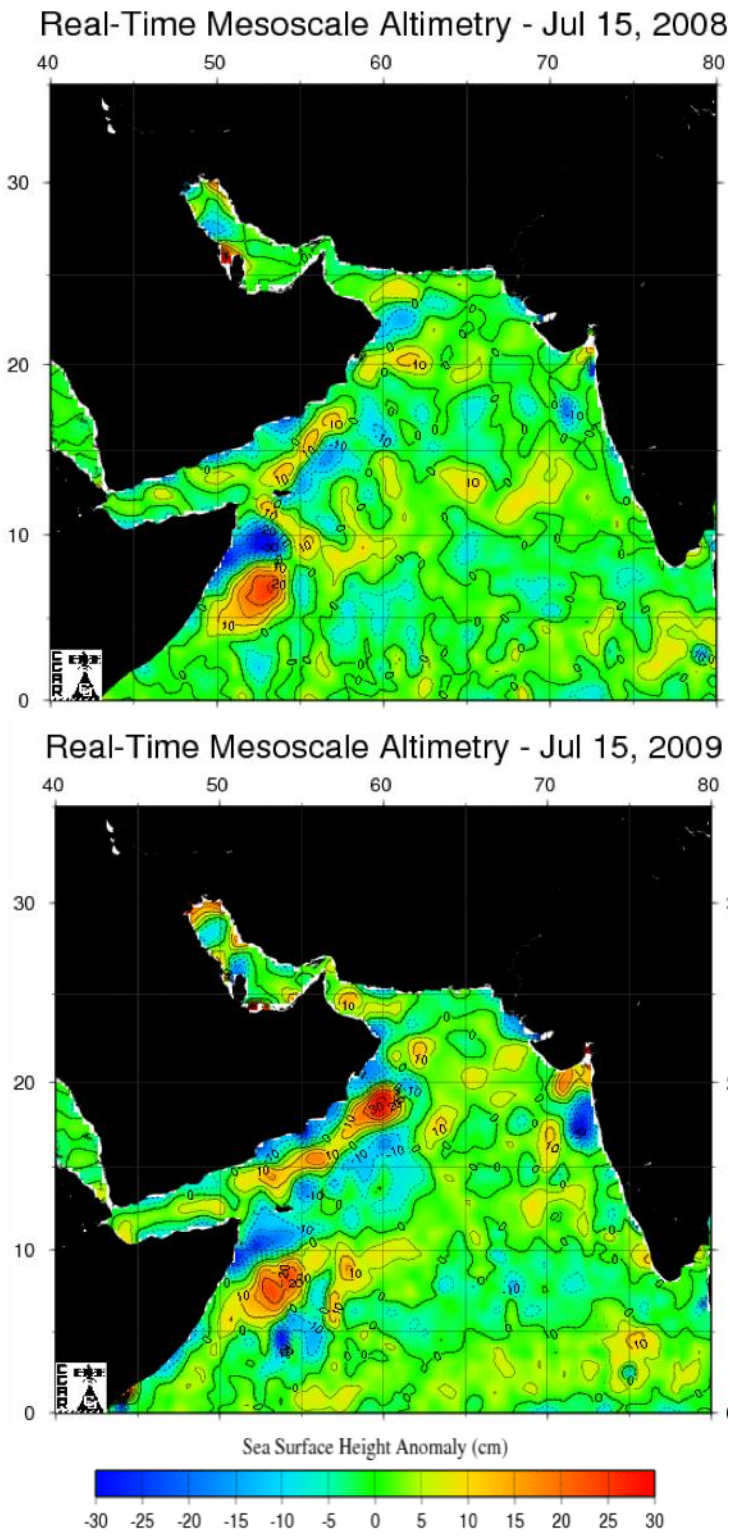

Figure A-7 continued.

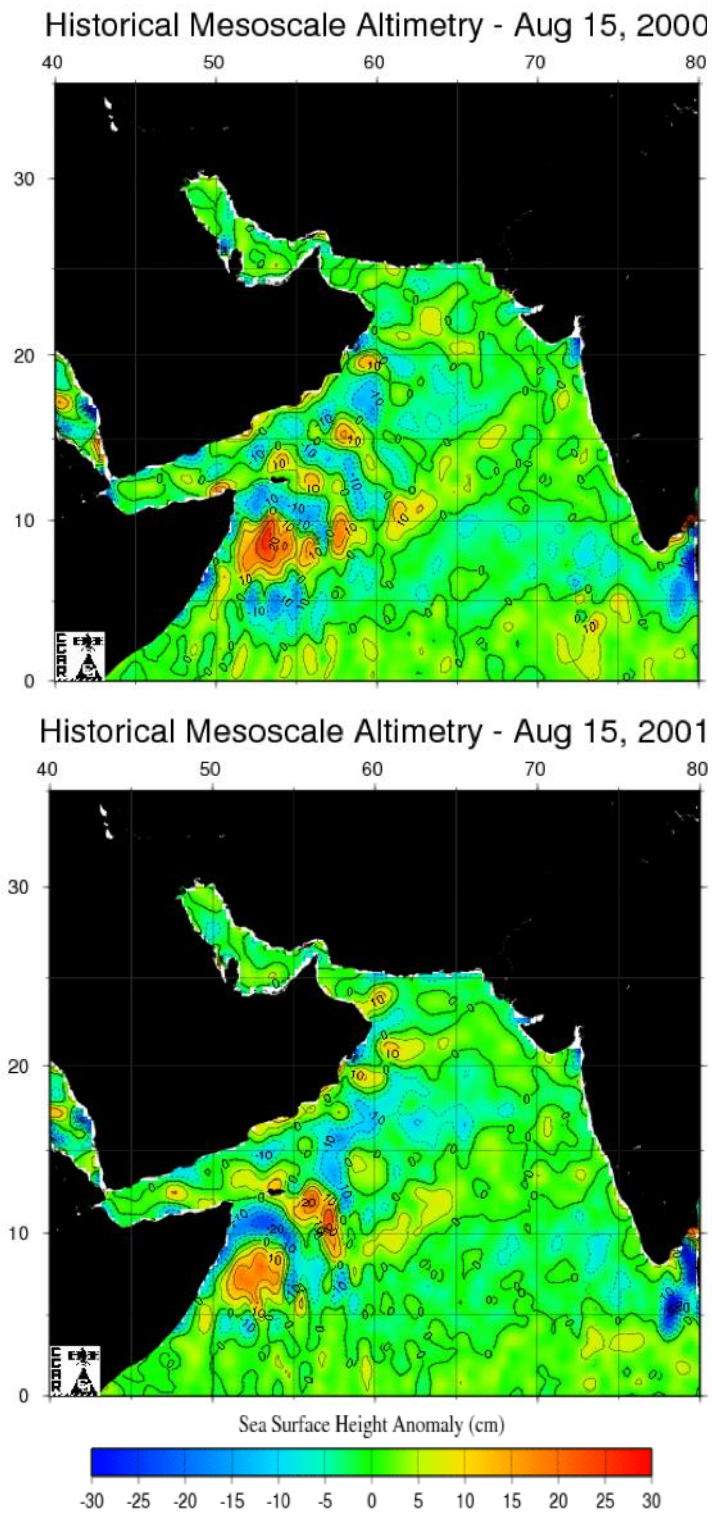

Figure A-8. Historical and real-time mesoscale altimetry maps for August 15, 2000-2009 (CCAR, 2009).

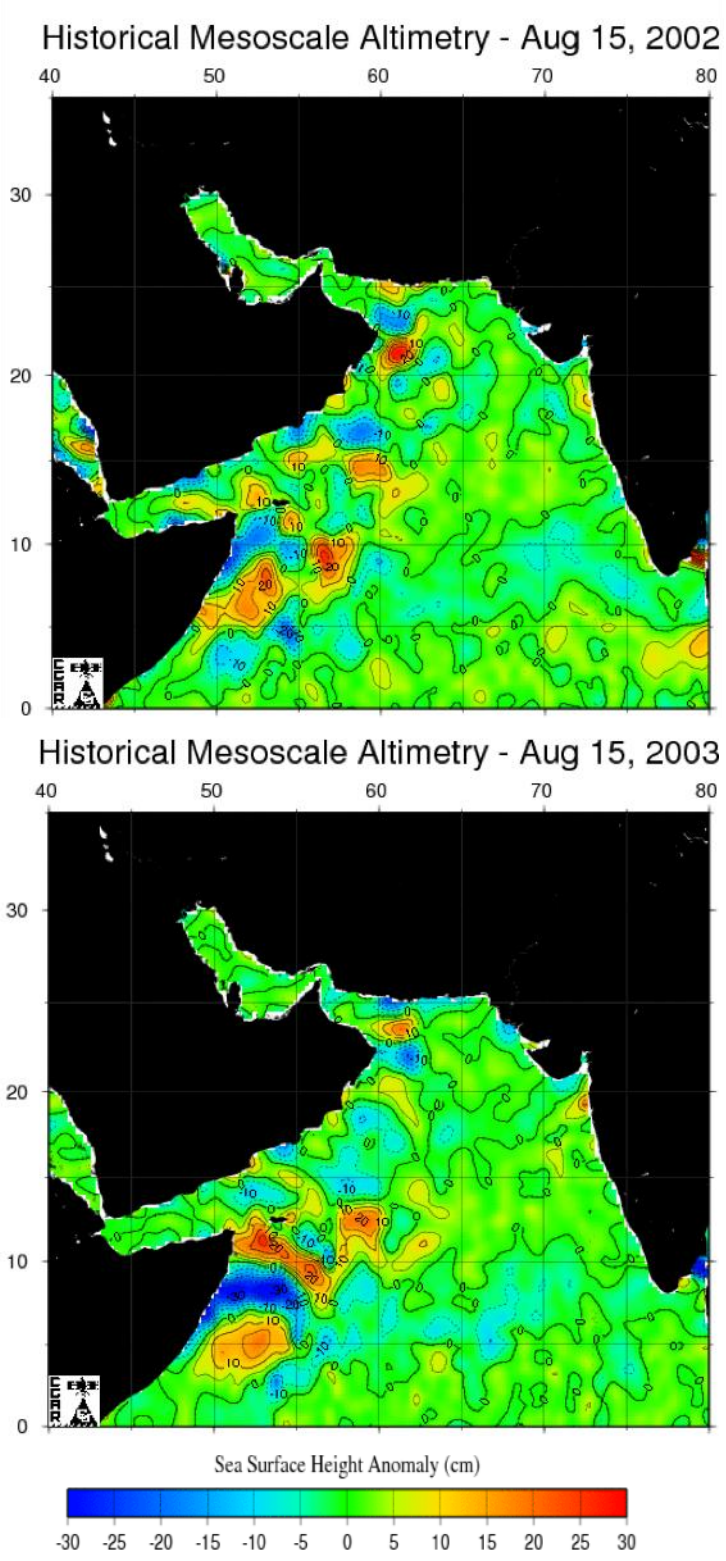

Figure A-8 continued.

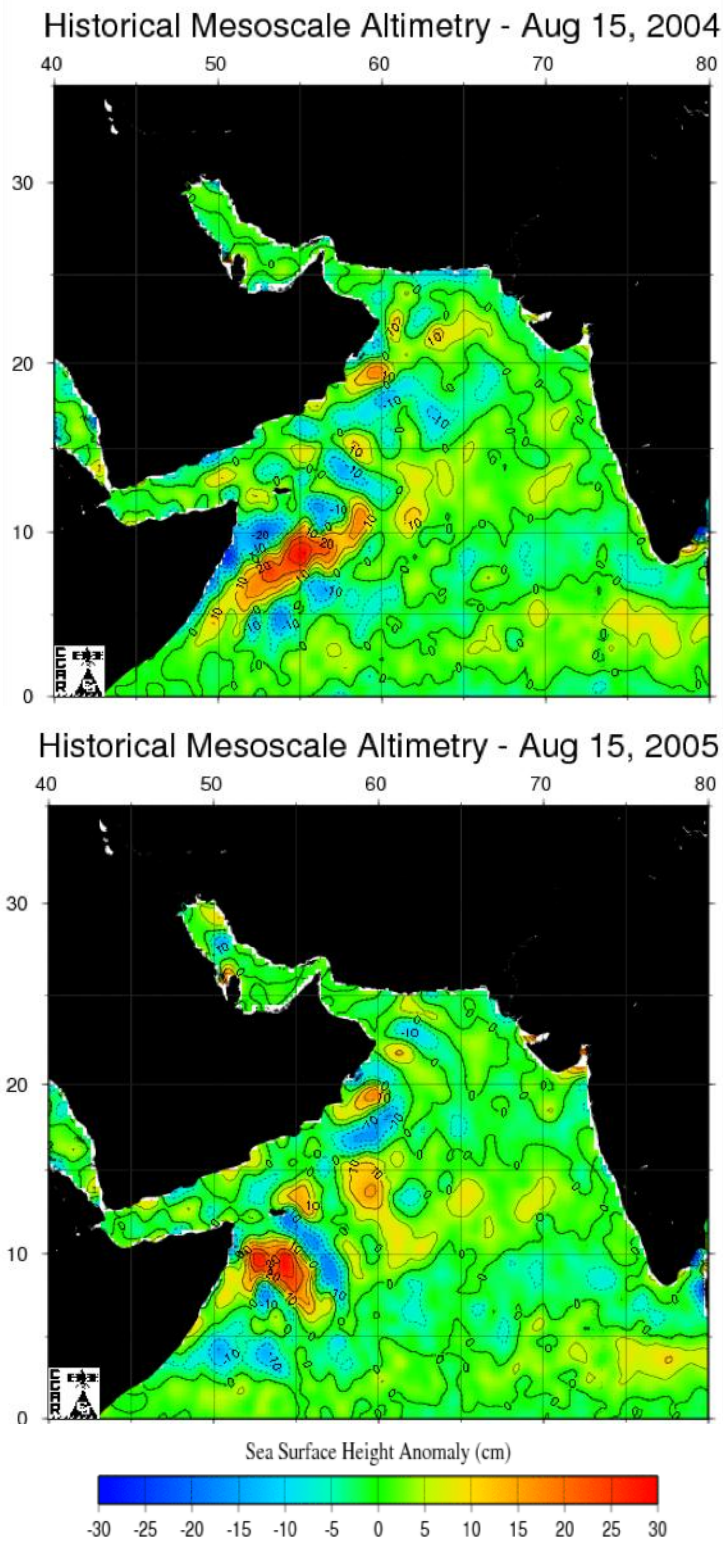

Figure A-8 continued.

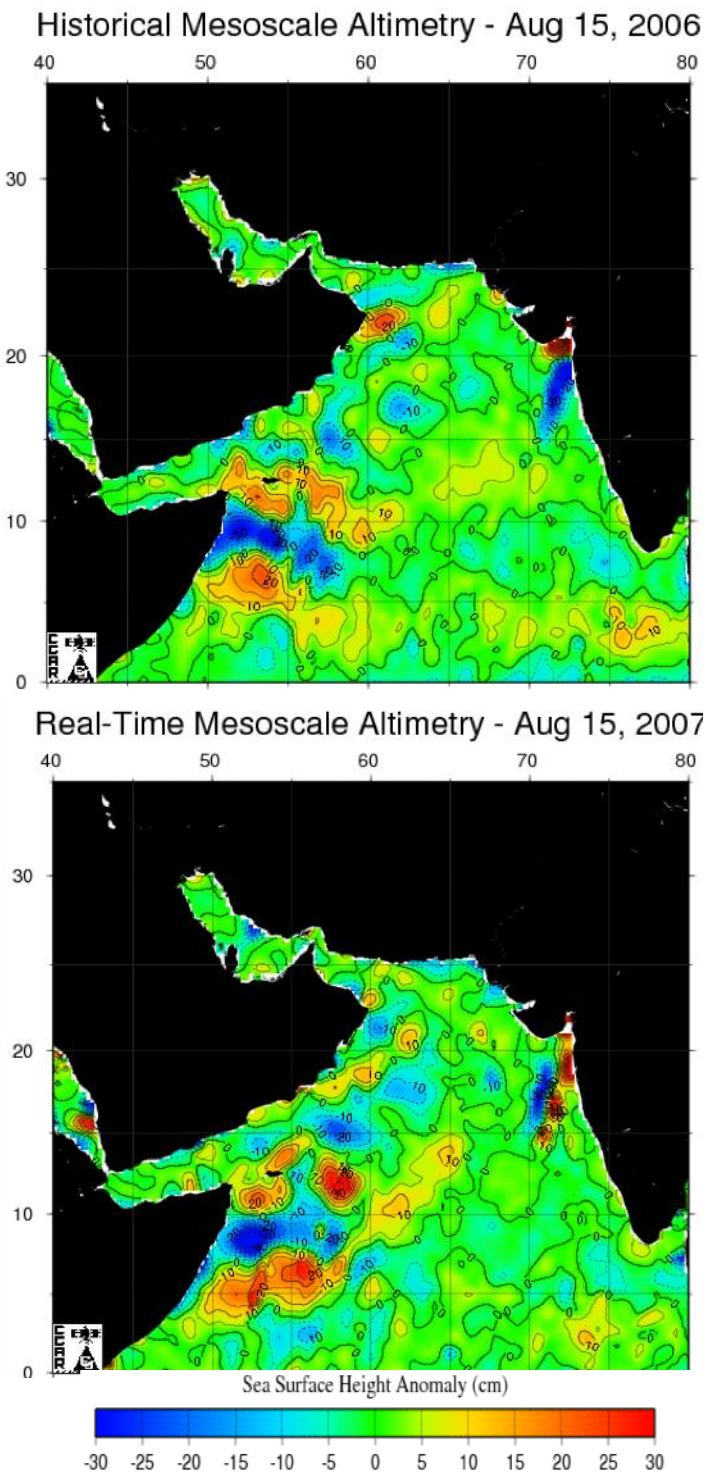

Figure A-8 continued.

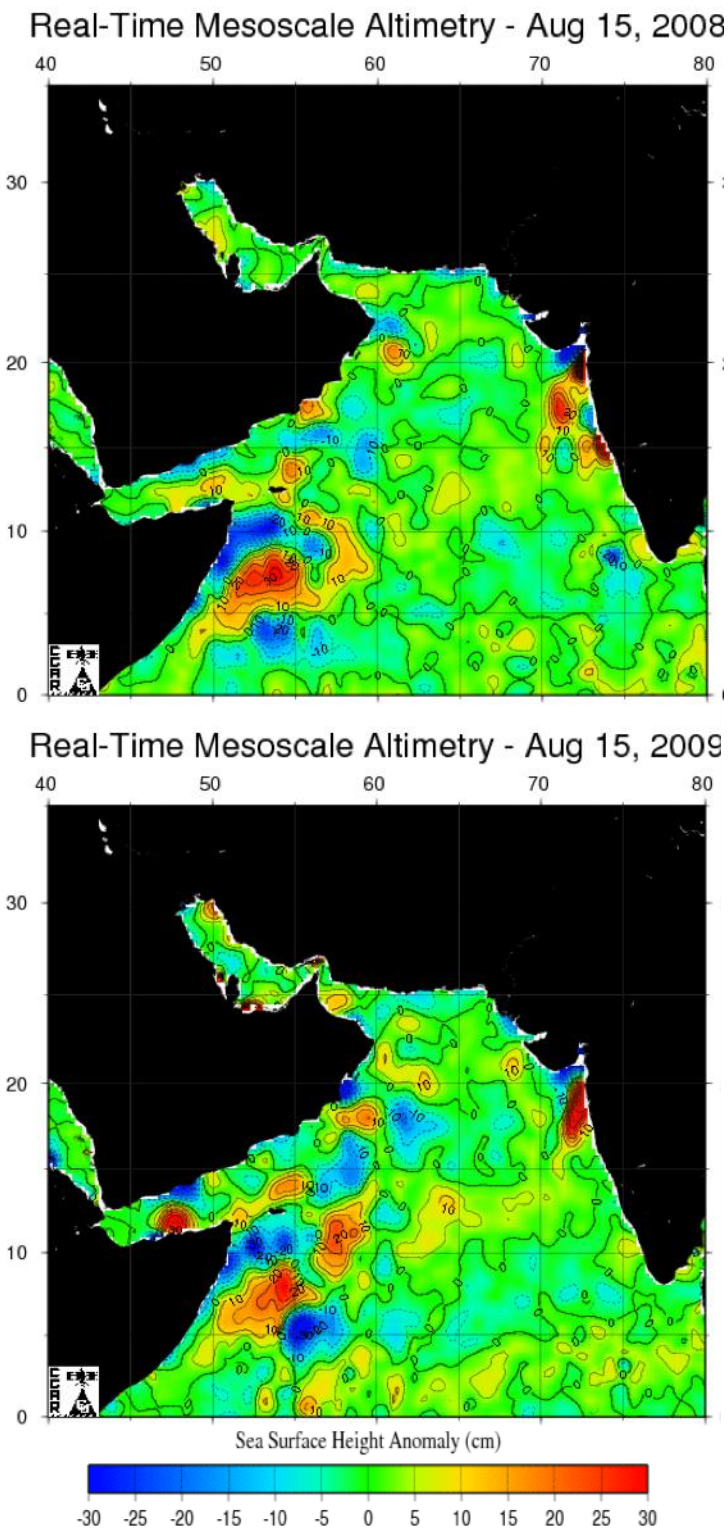

Figure A-8 continued.

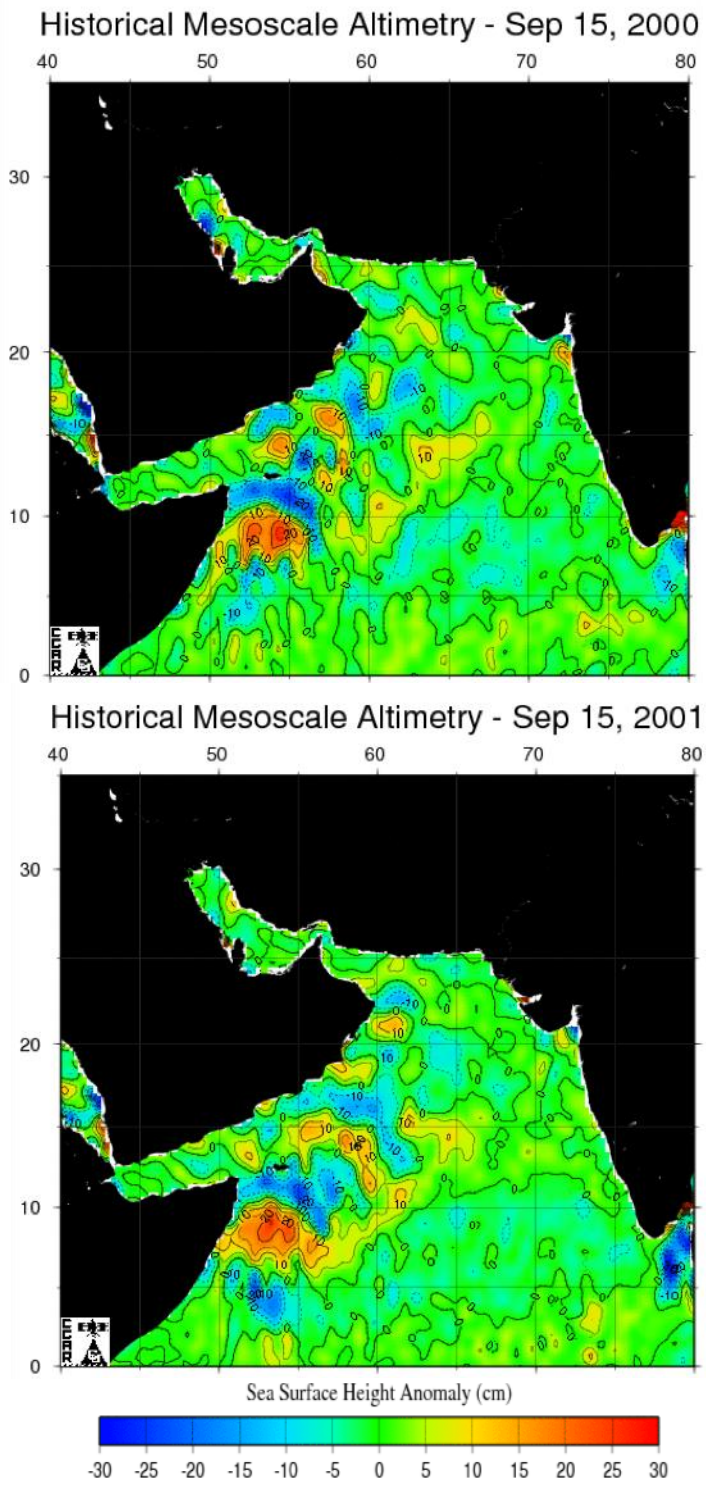

Figure A-9. Historical and real-time mesoscale altimetry maps for September 15, 2000-2009 (CCAR, 2009).

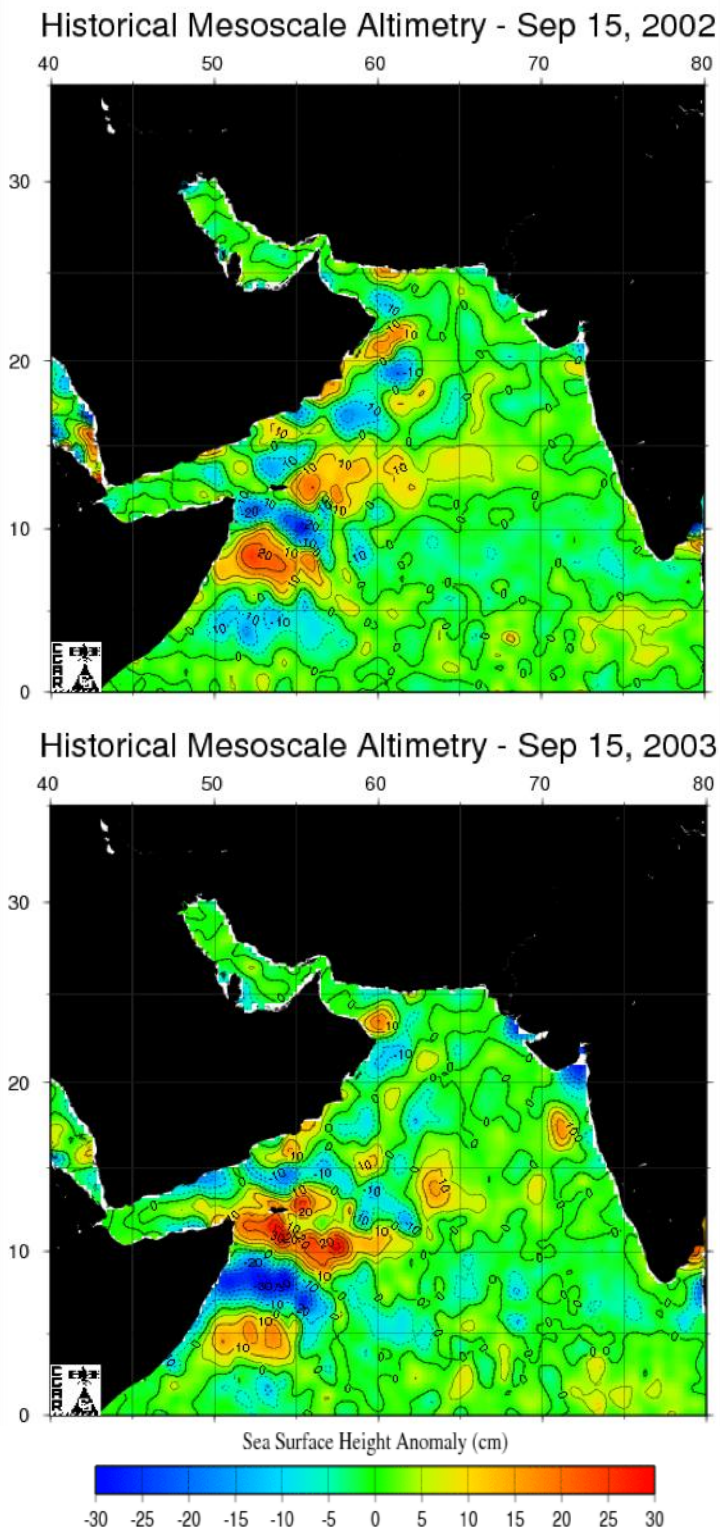

Figure A-9 continued.

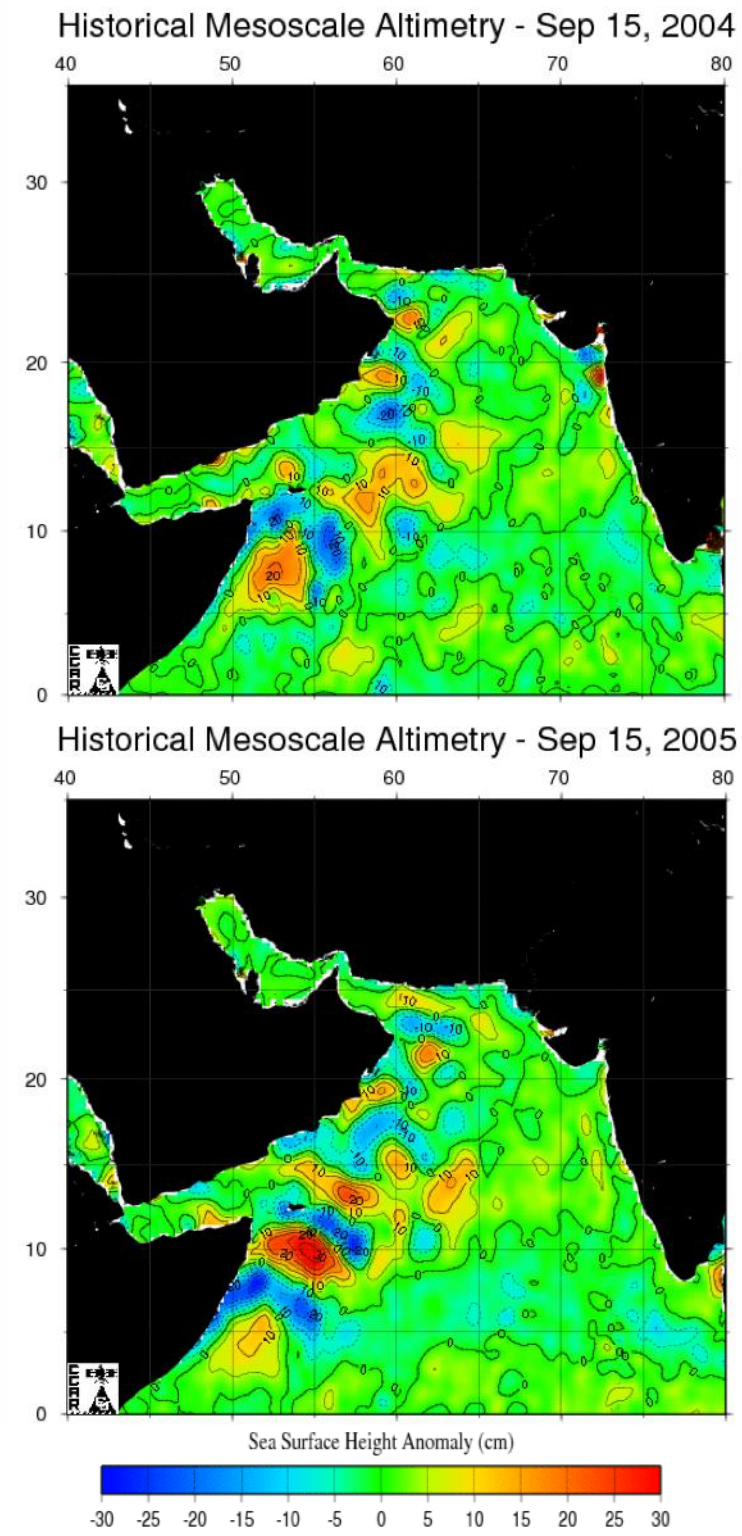

Figure A-9 continued.

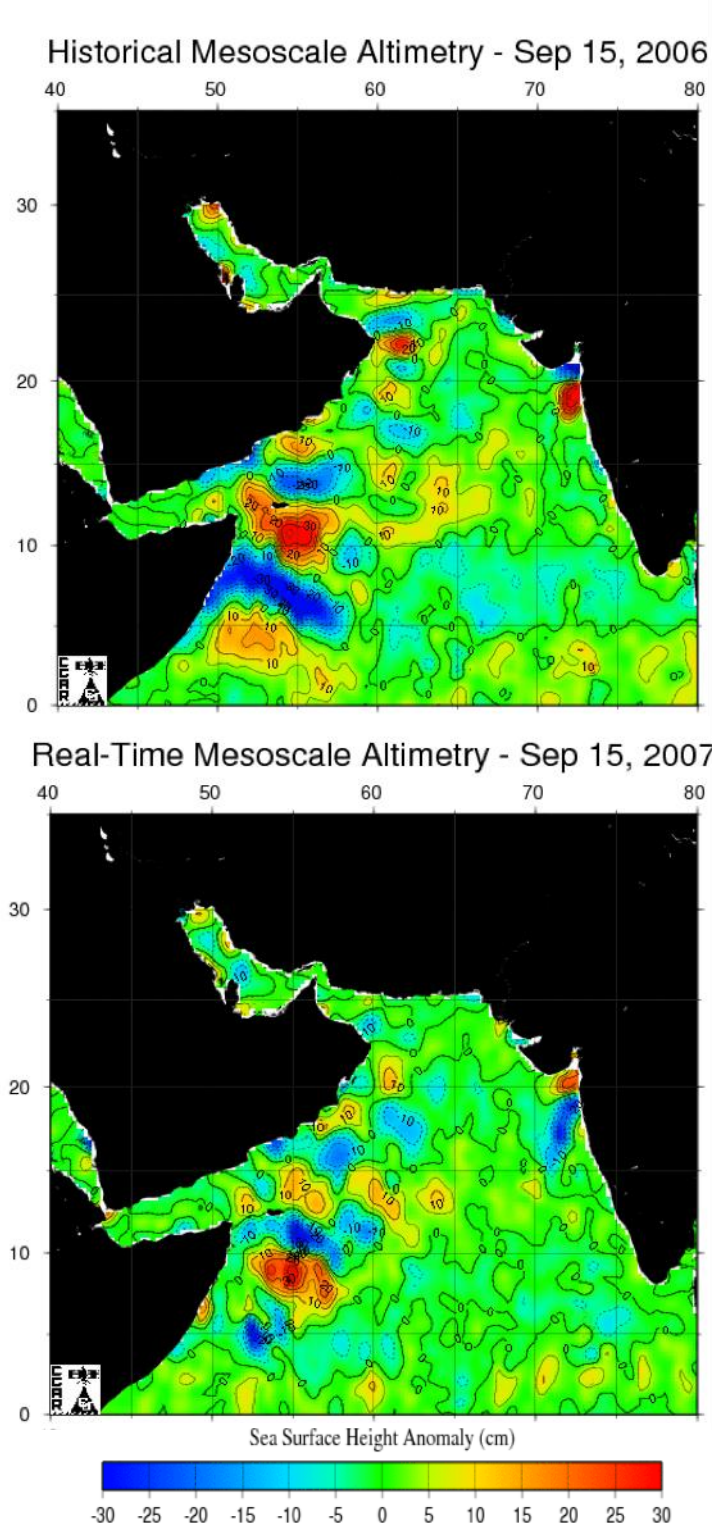

Figure A-9 continued.

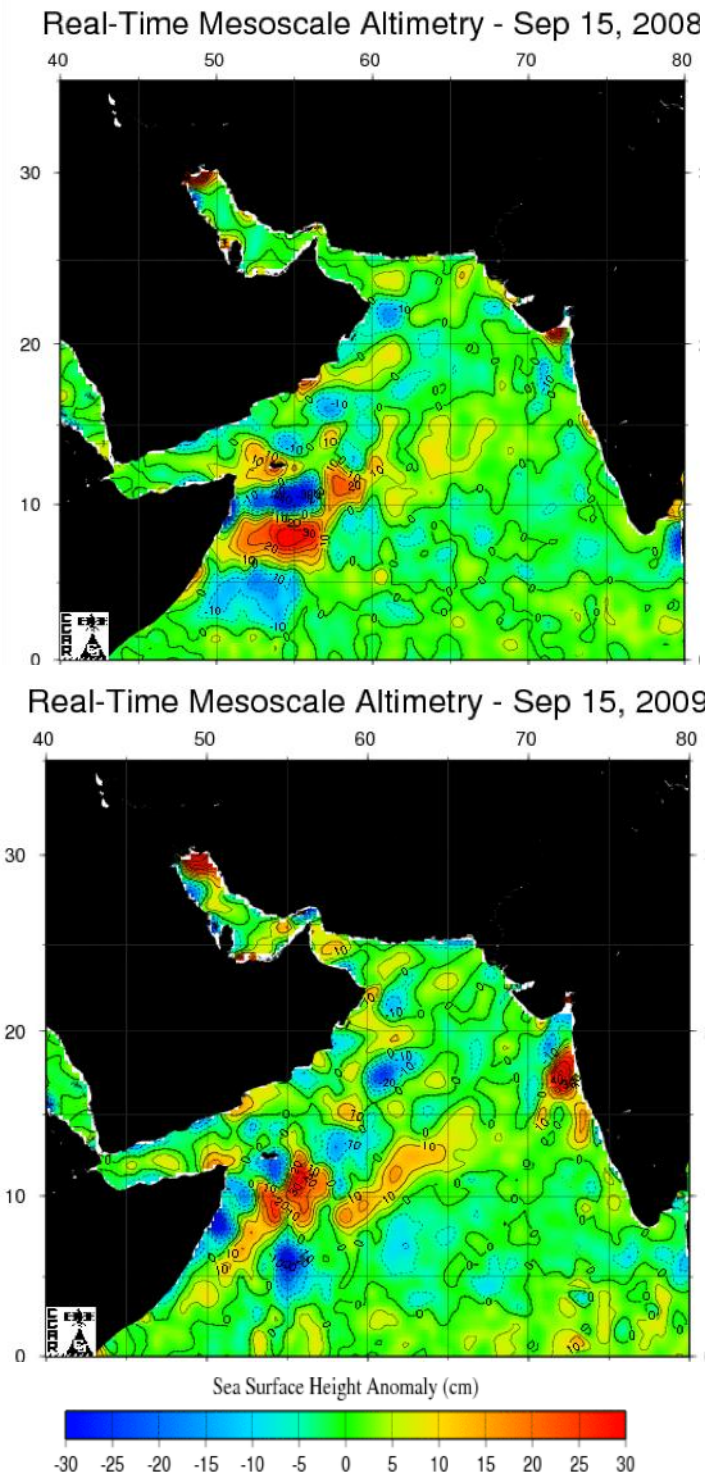

Figure A-9 continued.

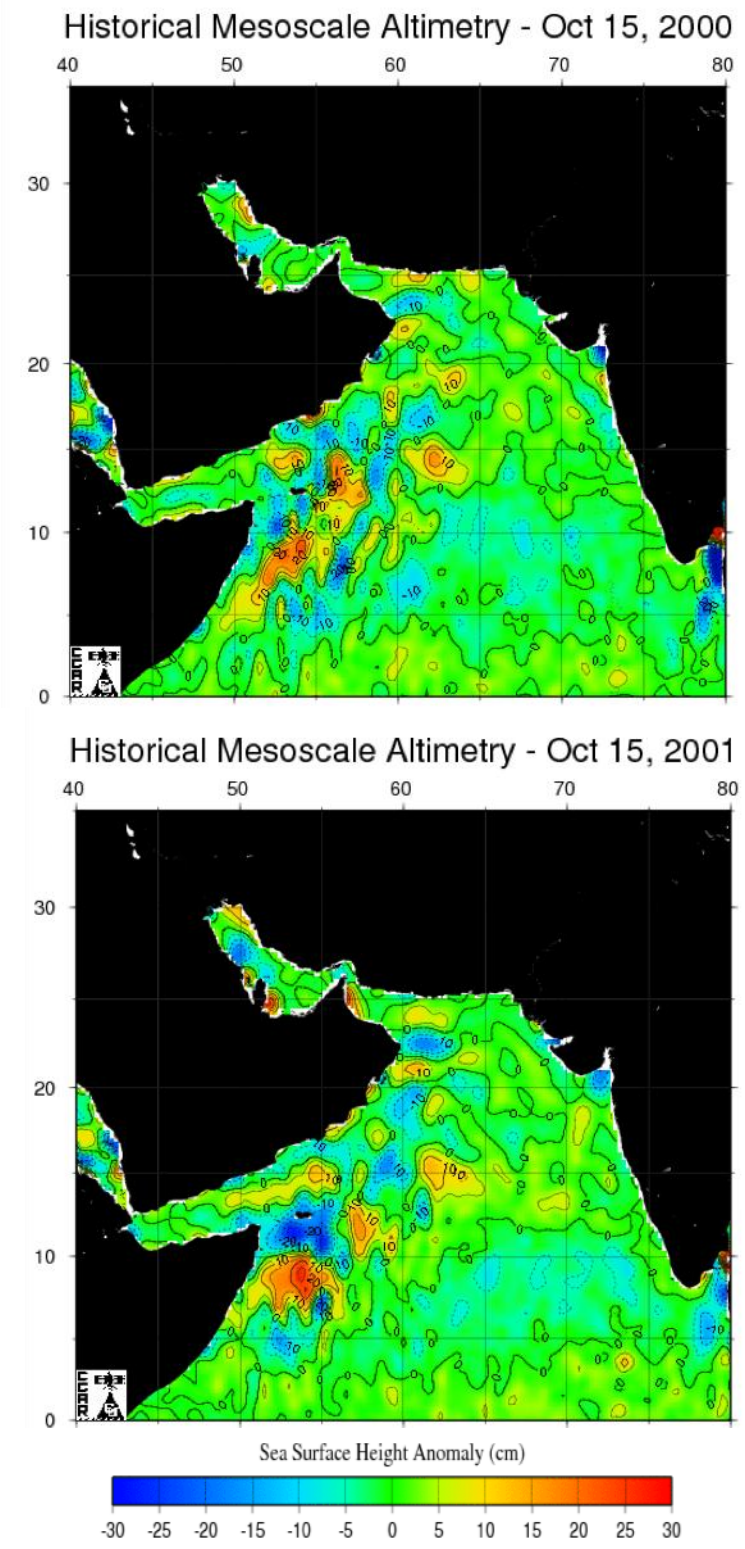

Figure A-10. Historical and real-time mesoscale altimetry maps for October 15, 2000-2009 (CCAR, 2009).

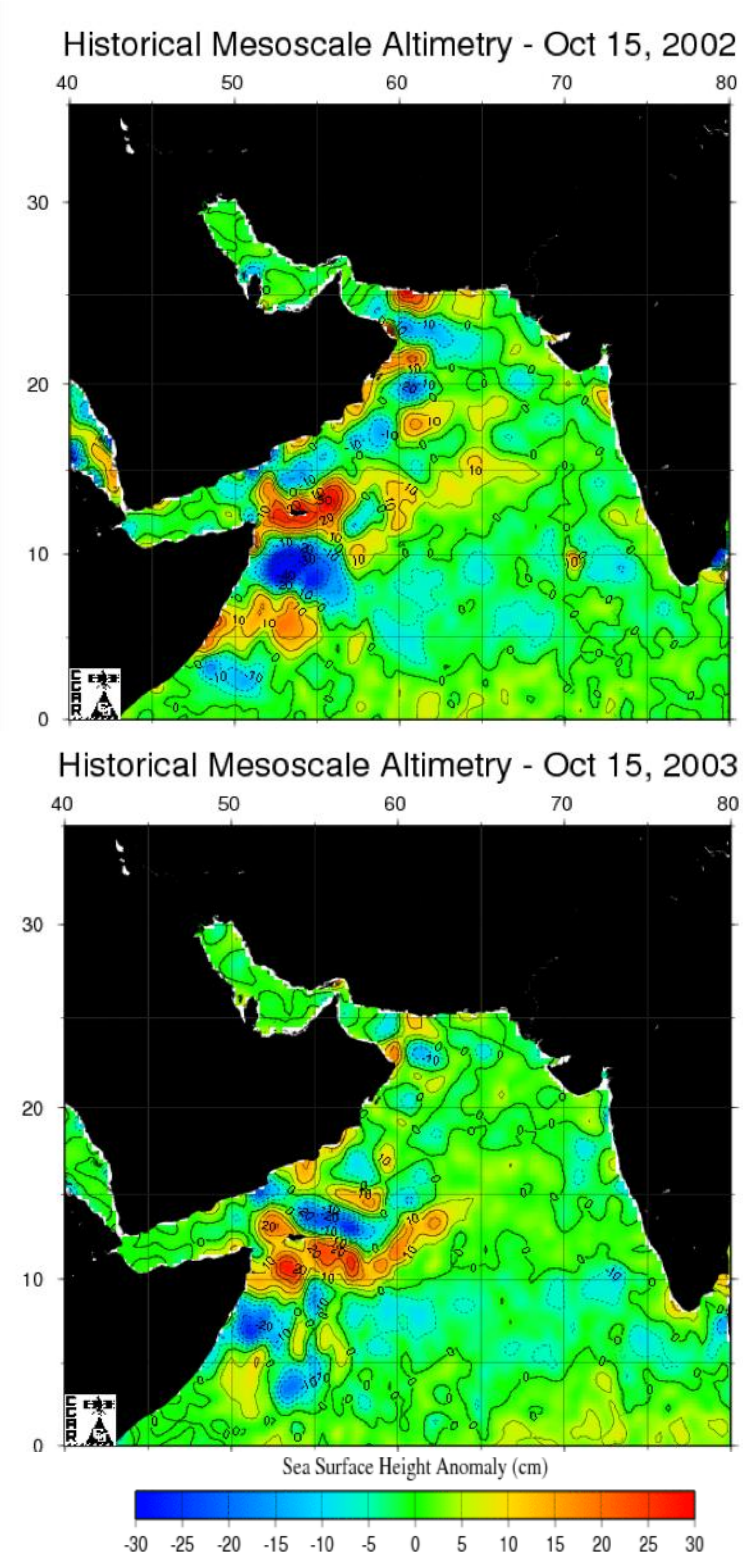

Figure A-10 continued.

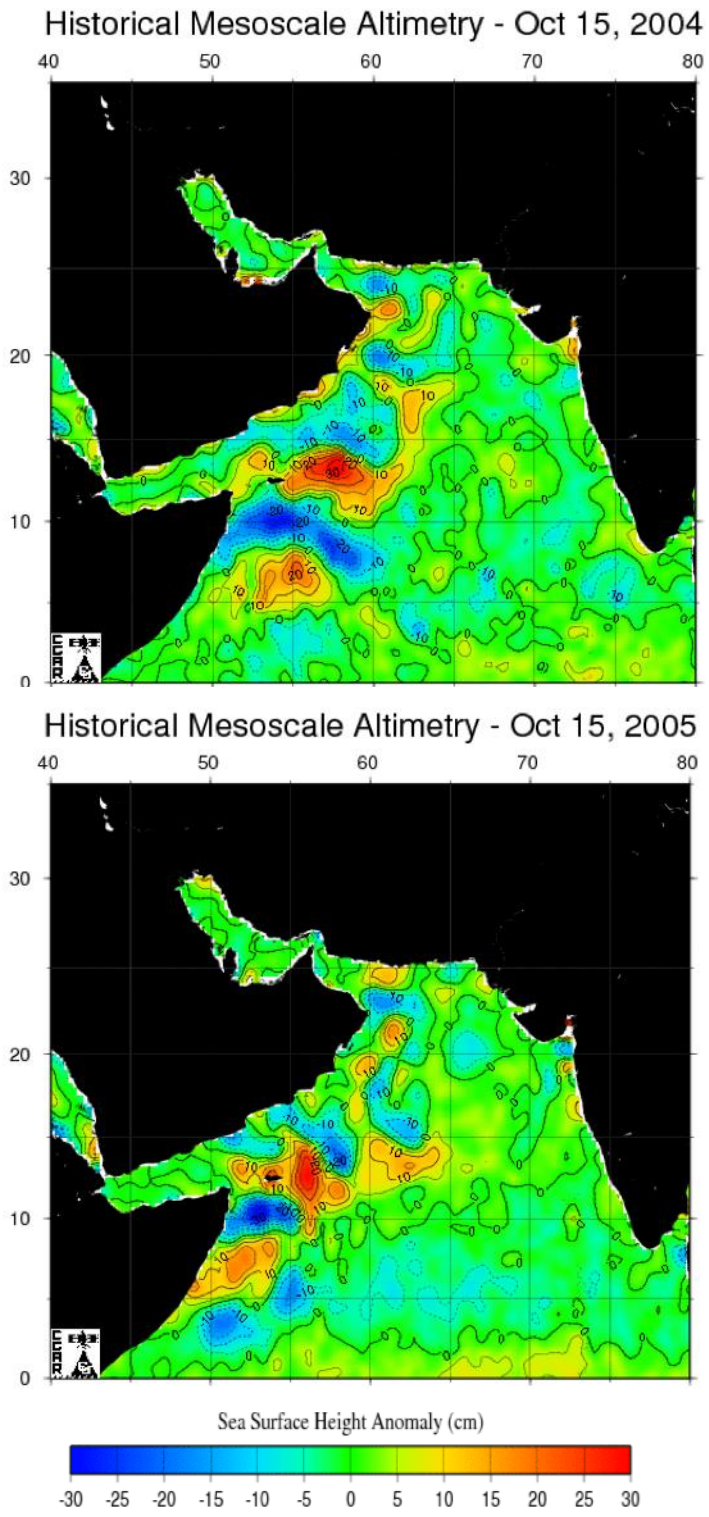

Figure A-10 continued.

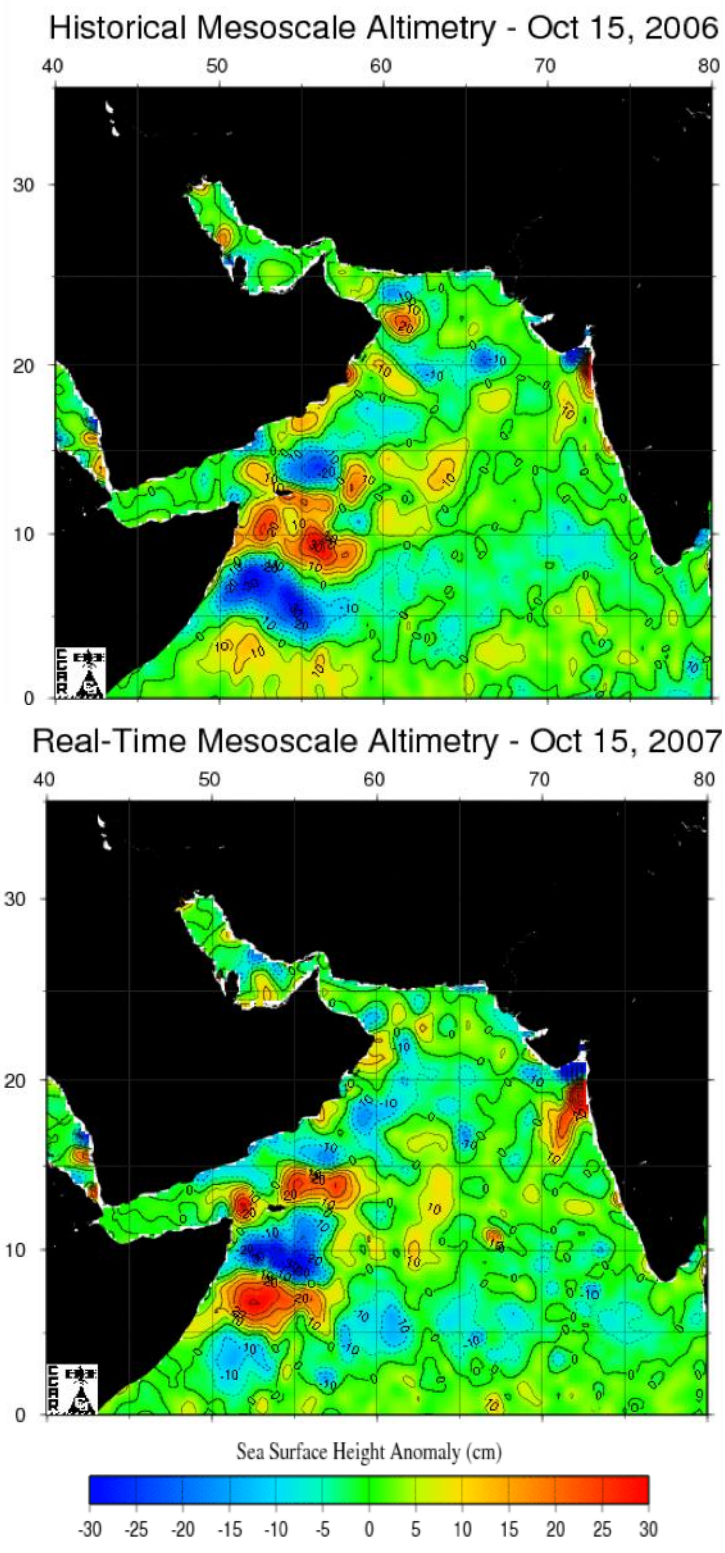

Figure A-10 continued.

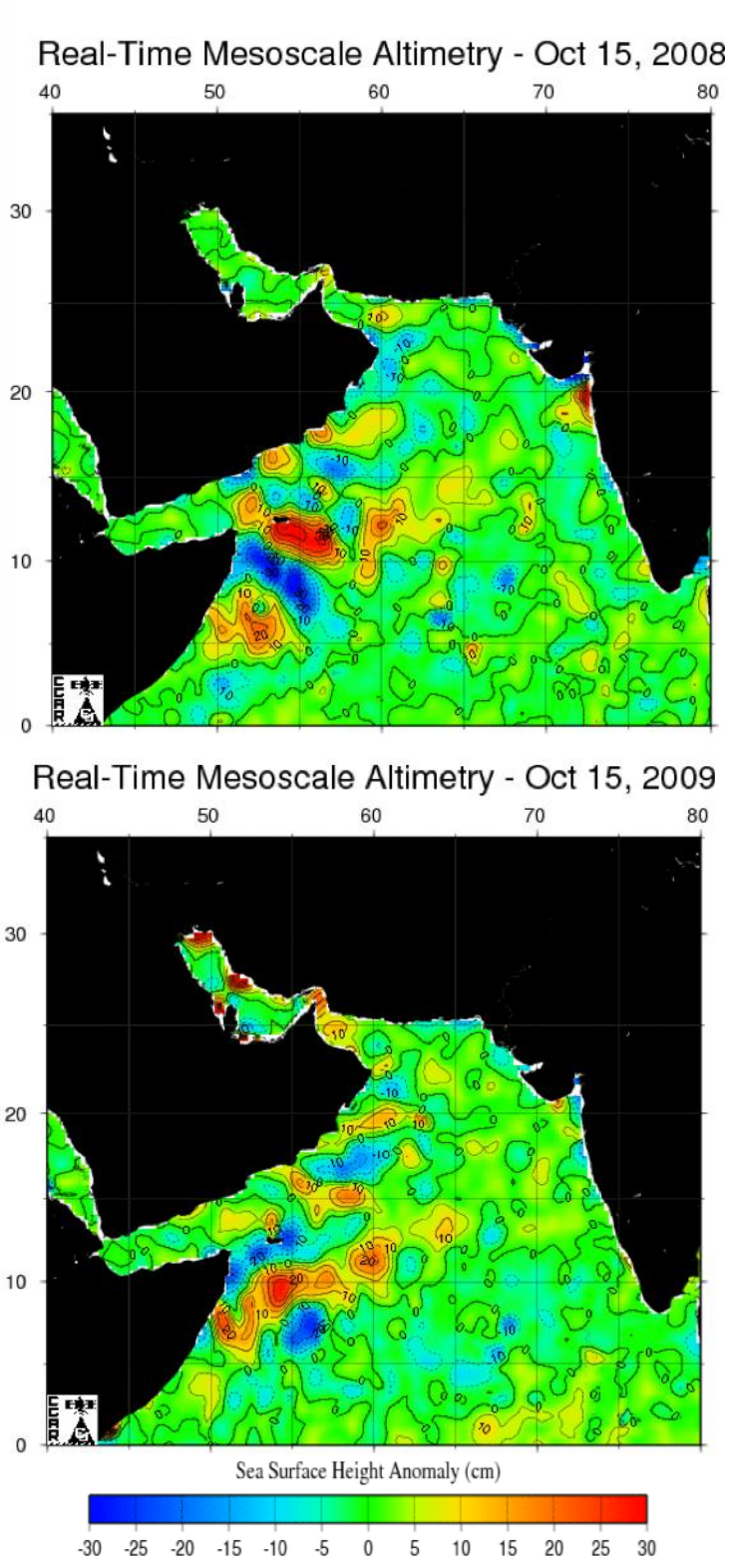

Figure A-10 continued.

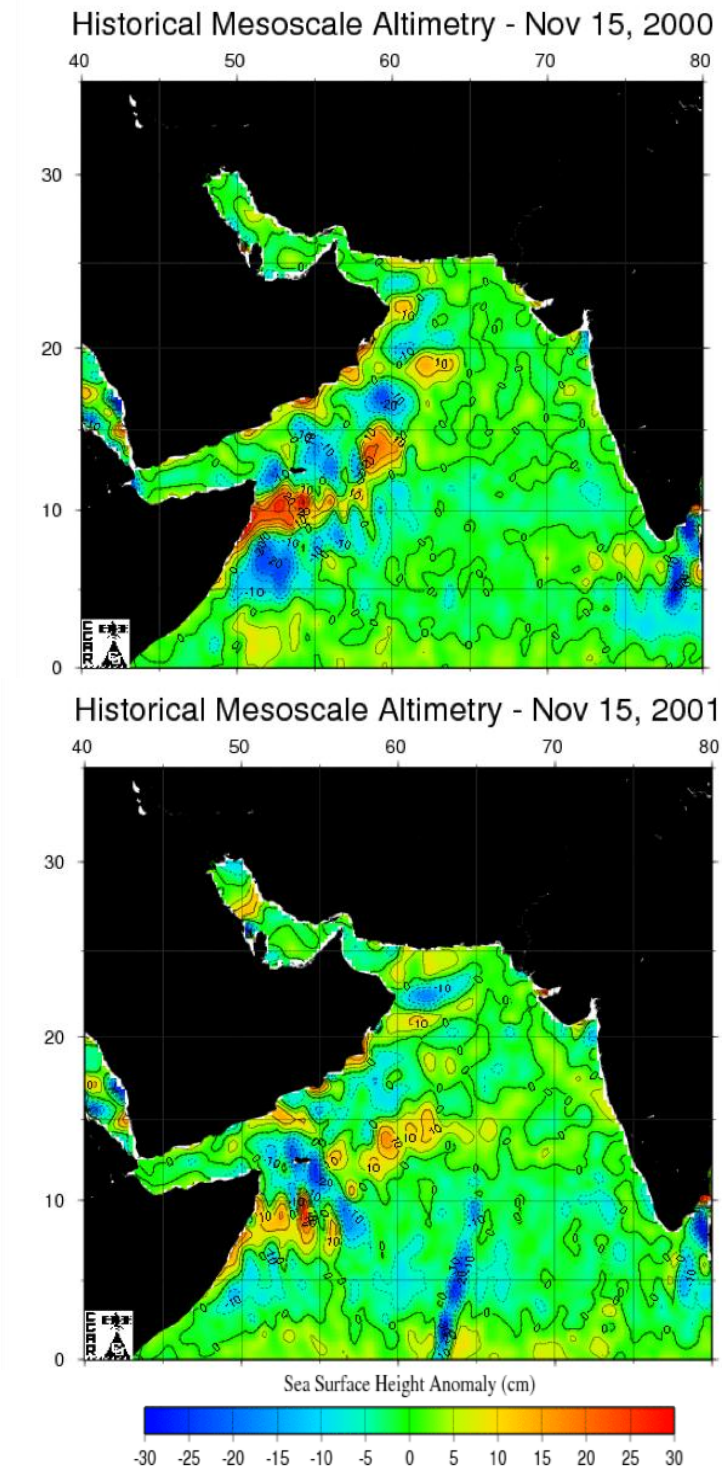

Figure A-11. Historical and real-time mesoscale altimetry maps for November 15, 2000-2009 (CCAR, 2009).

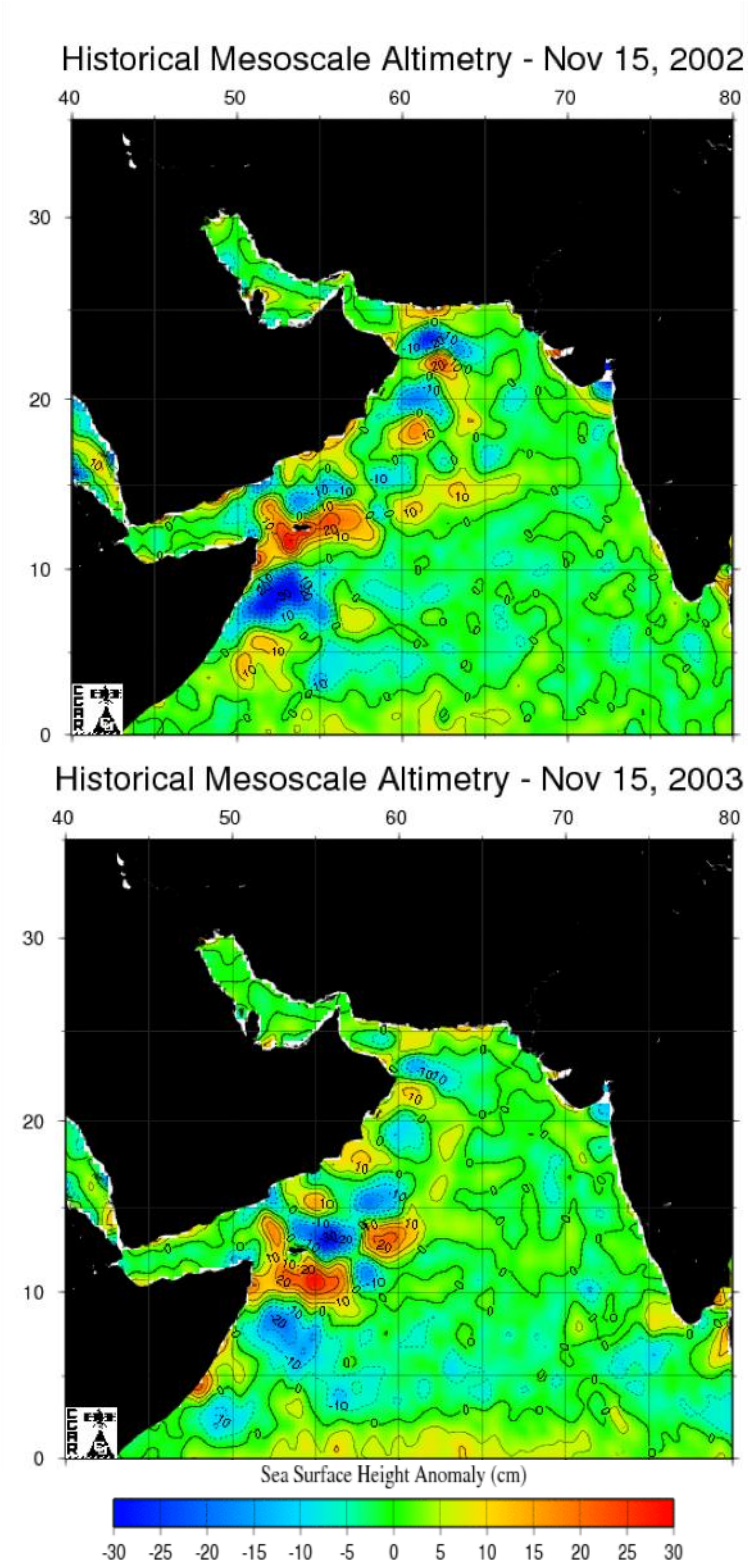

Figure A-11 continued.

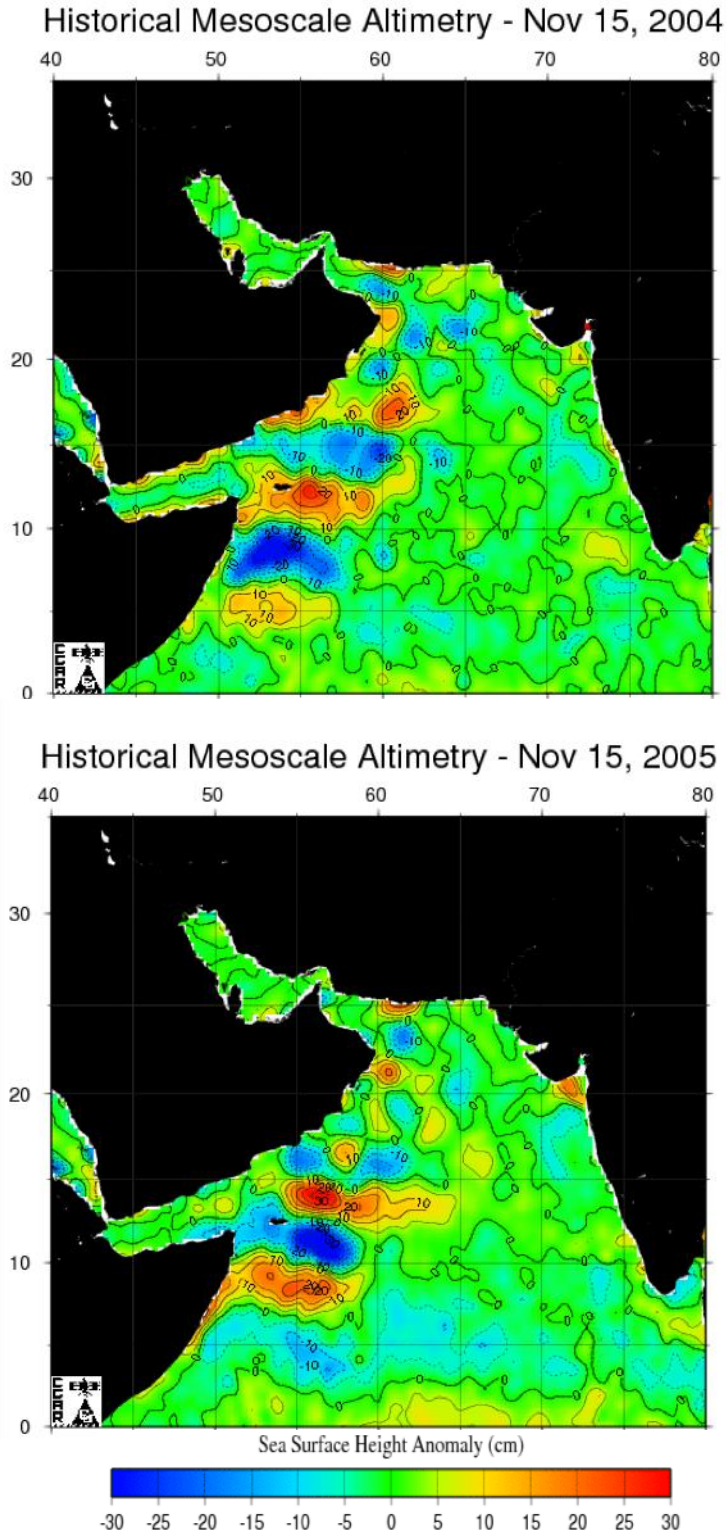

Figure A-11 continued.

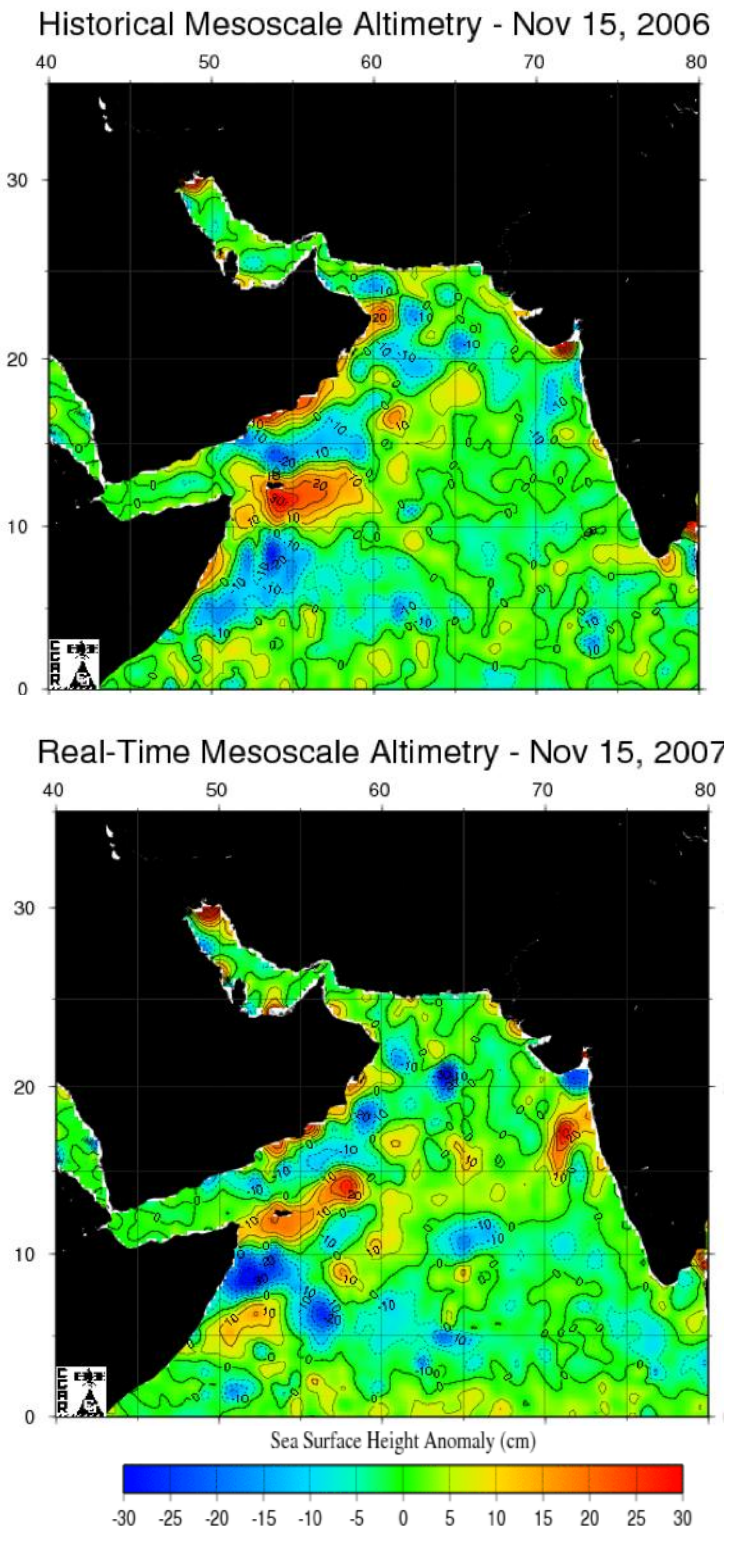

Figure A-11 continued.

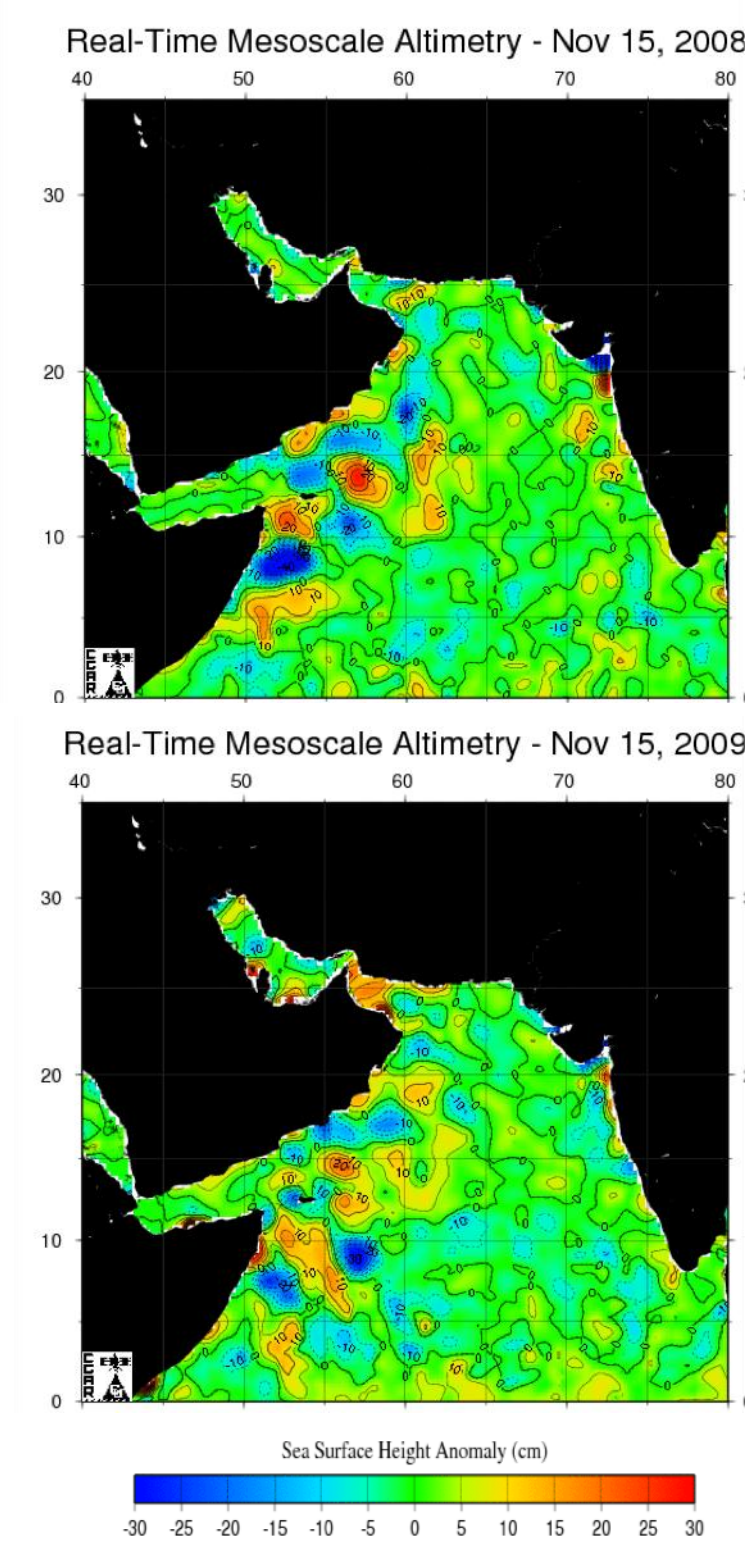

Figure A-11 continued.

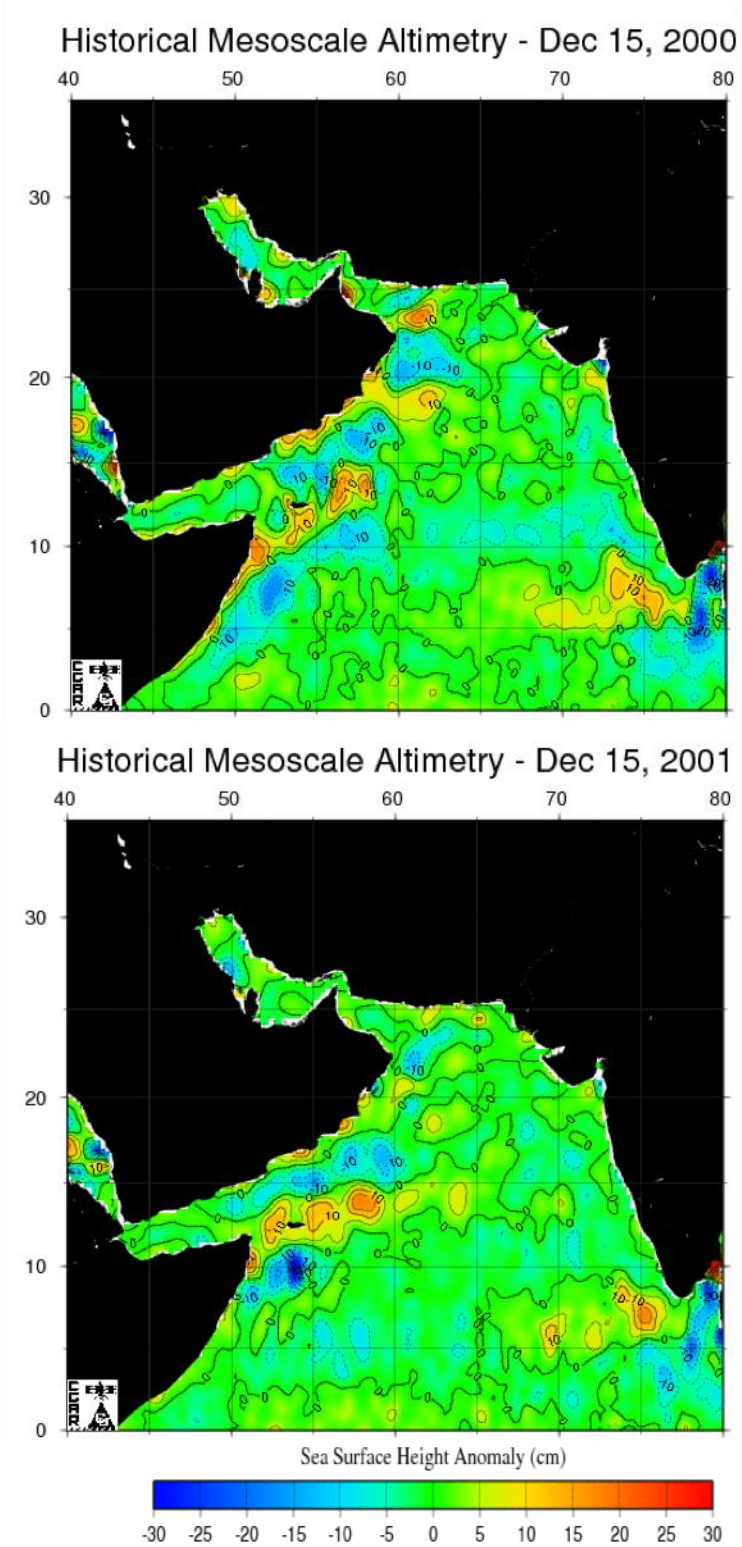

Figure A-12. Historical and real-time mesoscale altimetry maps for December 15, 2000-2009 (CCAR, 2009).

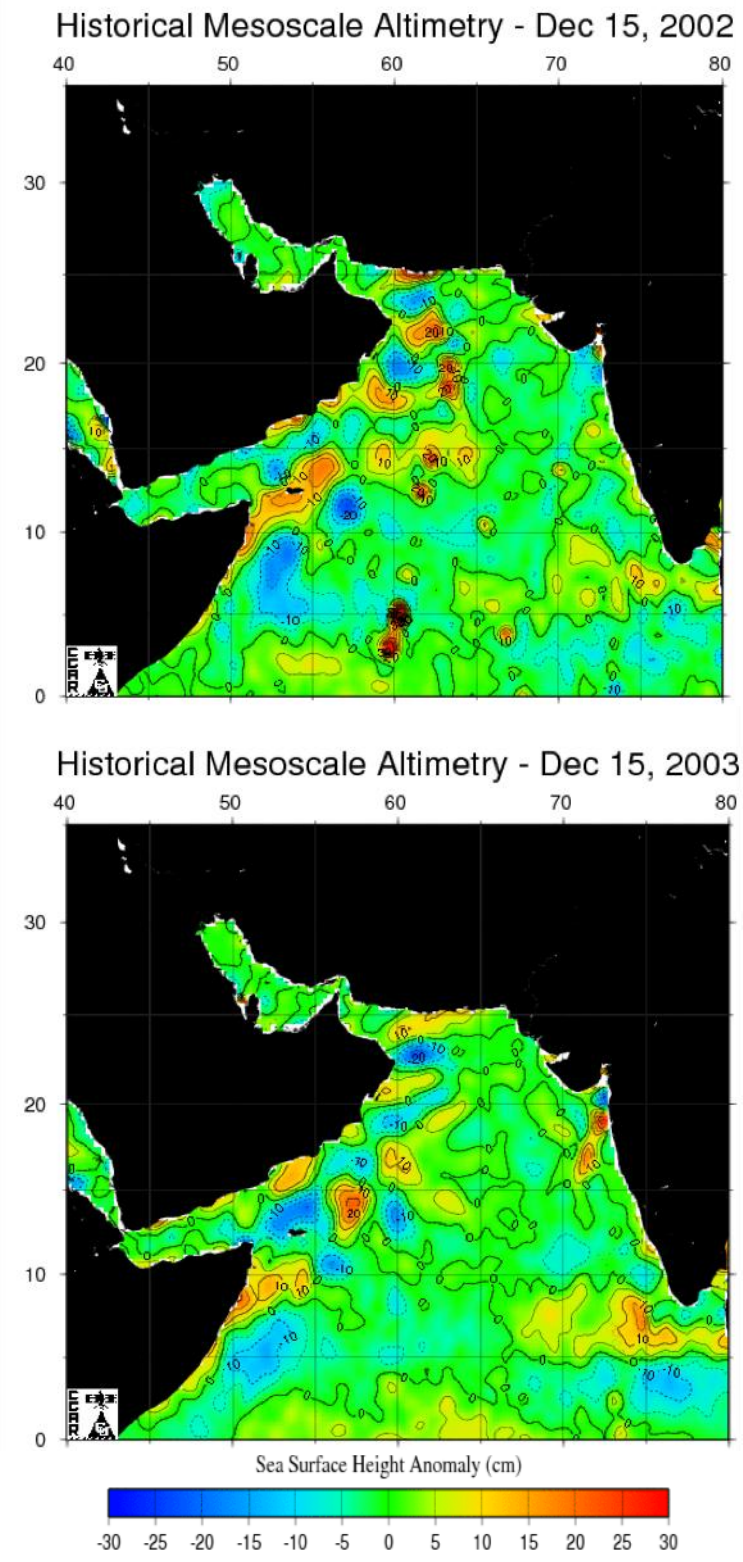

Figure A-12 continued.

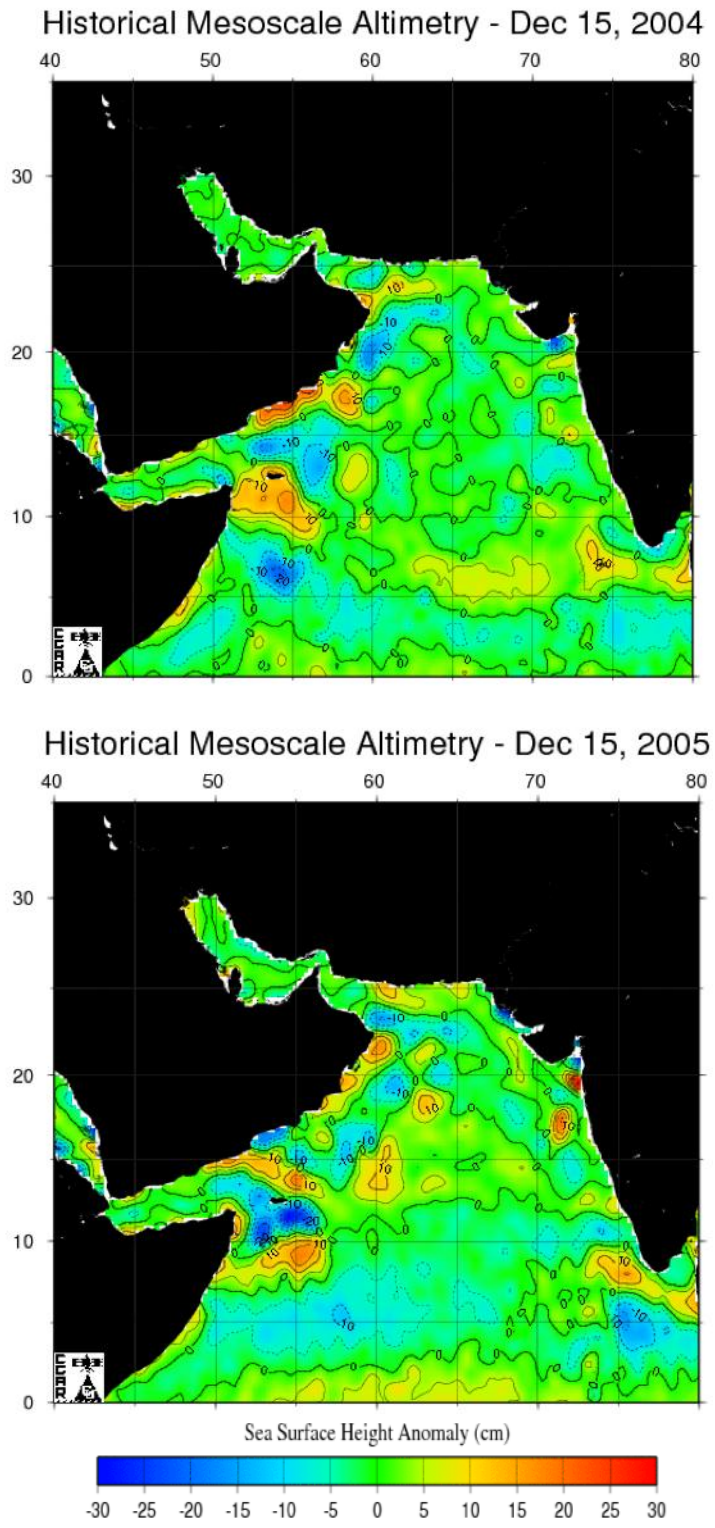

Figure A-12 continued.

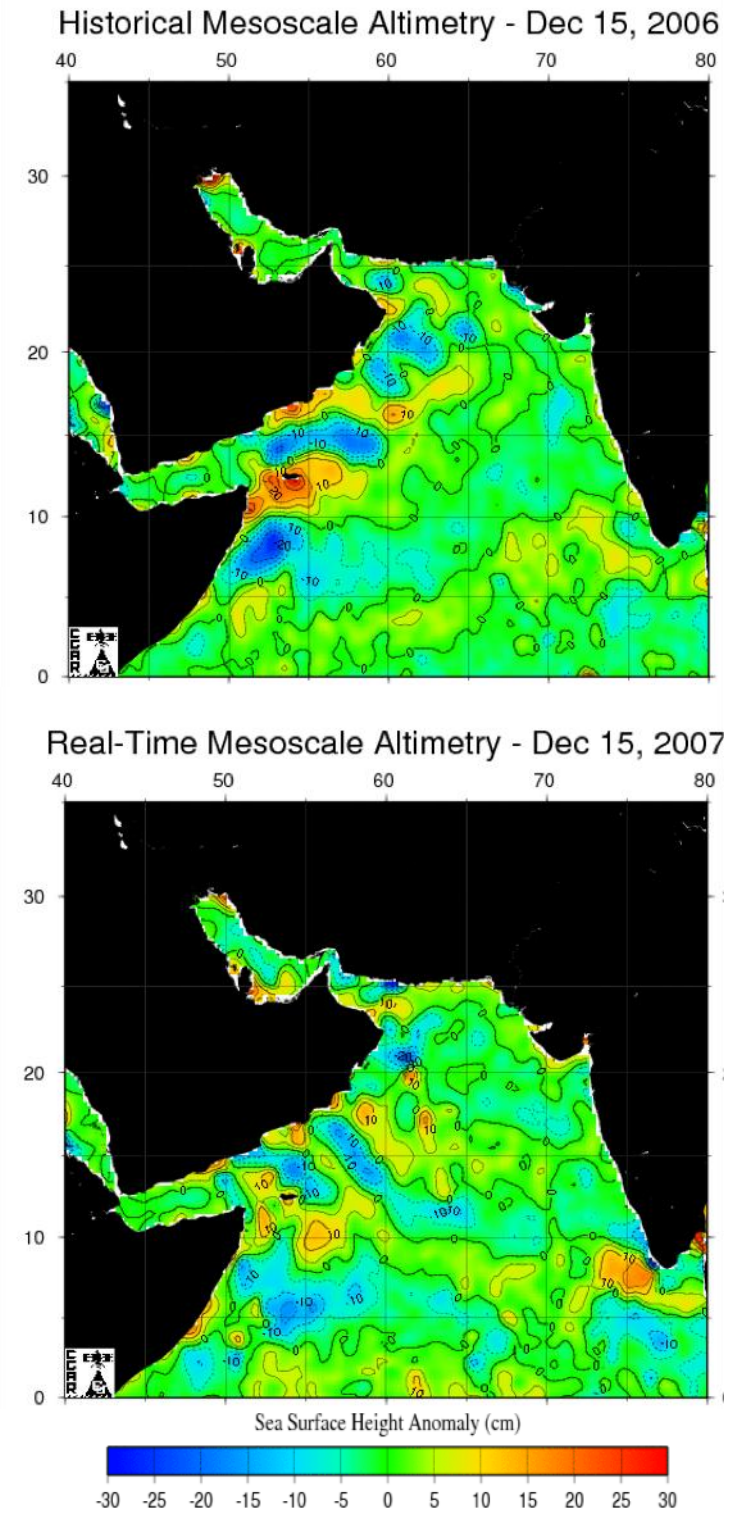

Figure A-12 continued.

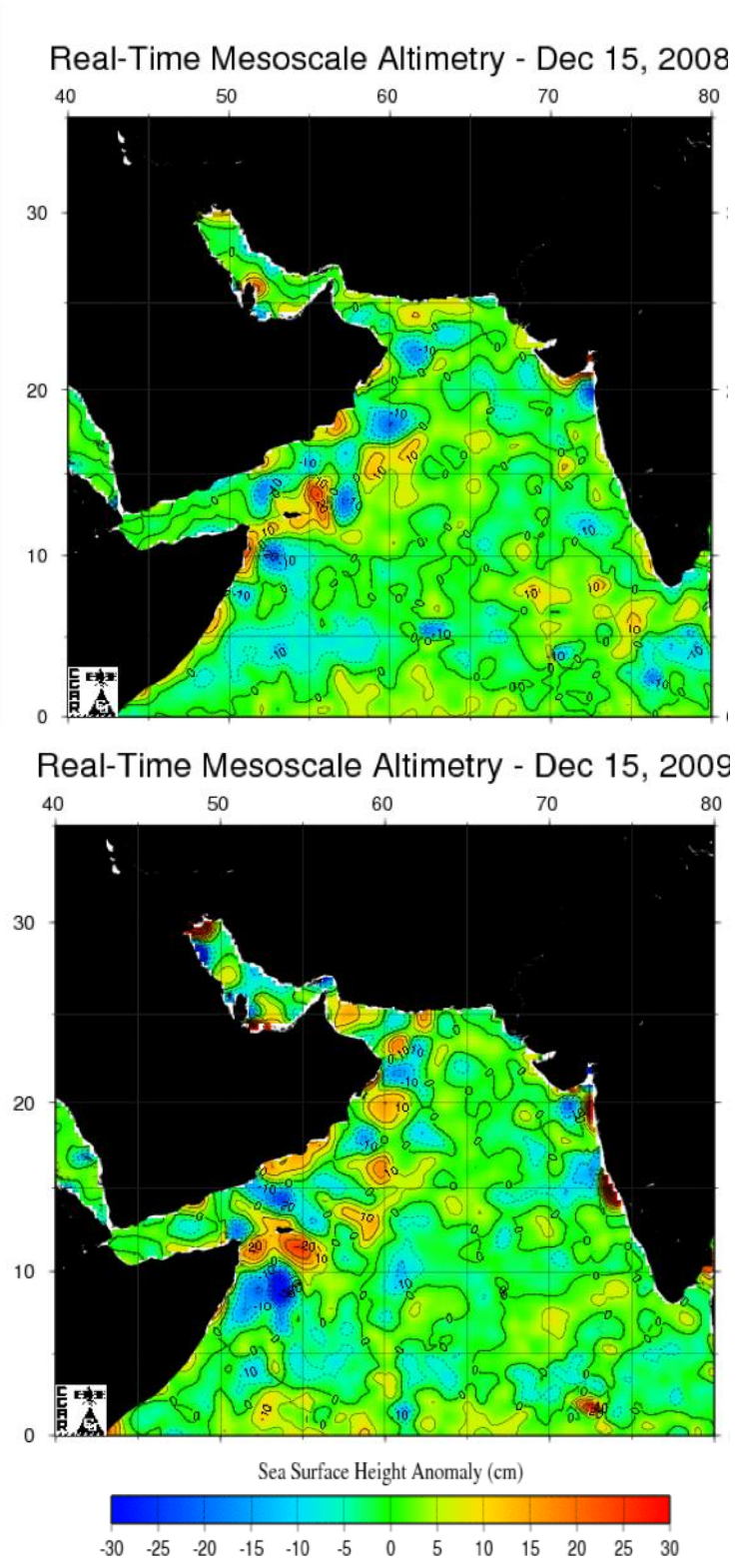

Figure A-12 continued.

APPENDIX B

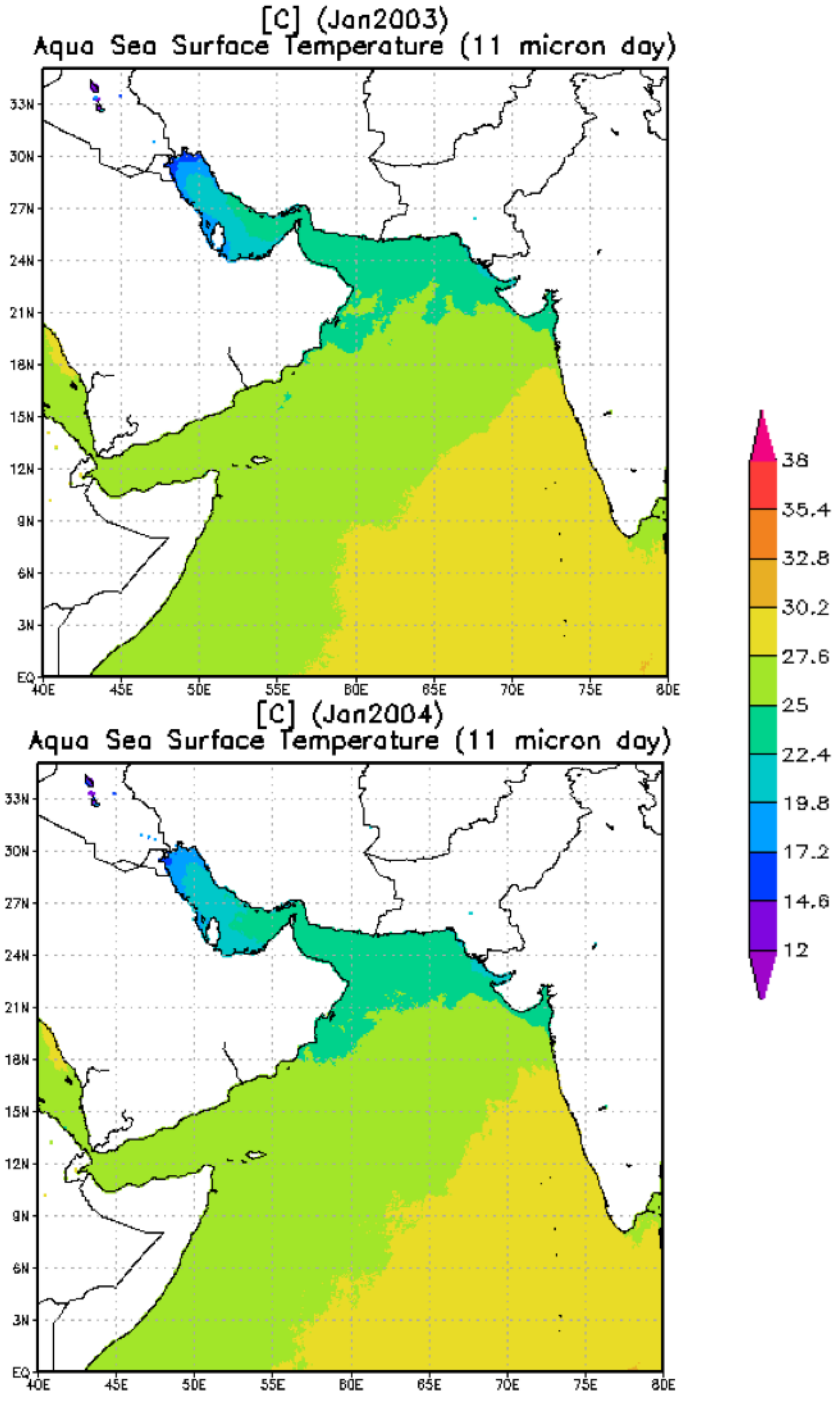

Figure B-1. January sea surface temperature maps generated by NASA's Giovanni (Kempler, 2011).

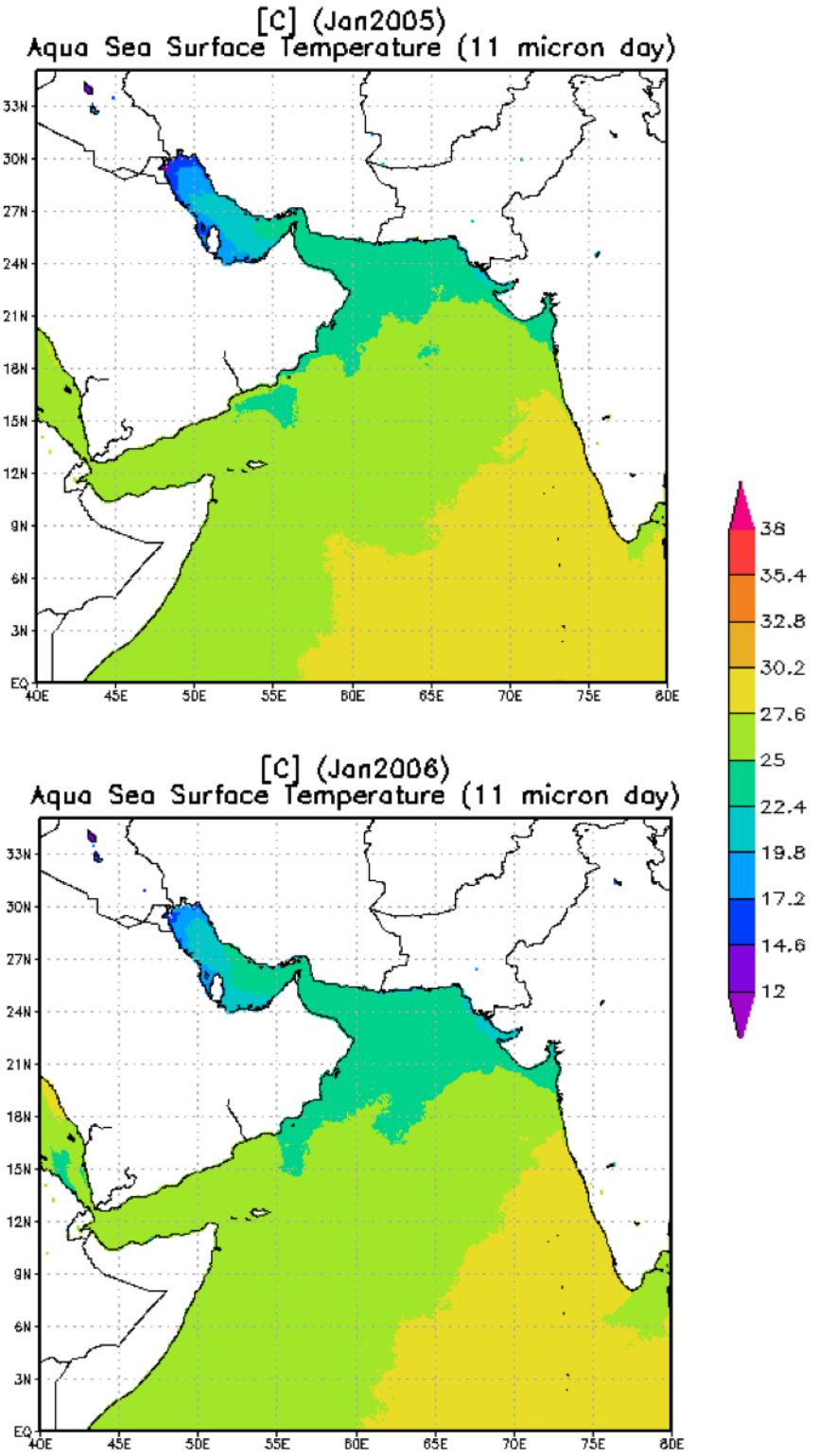

Figure B-1 continued.

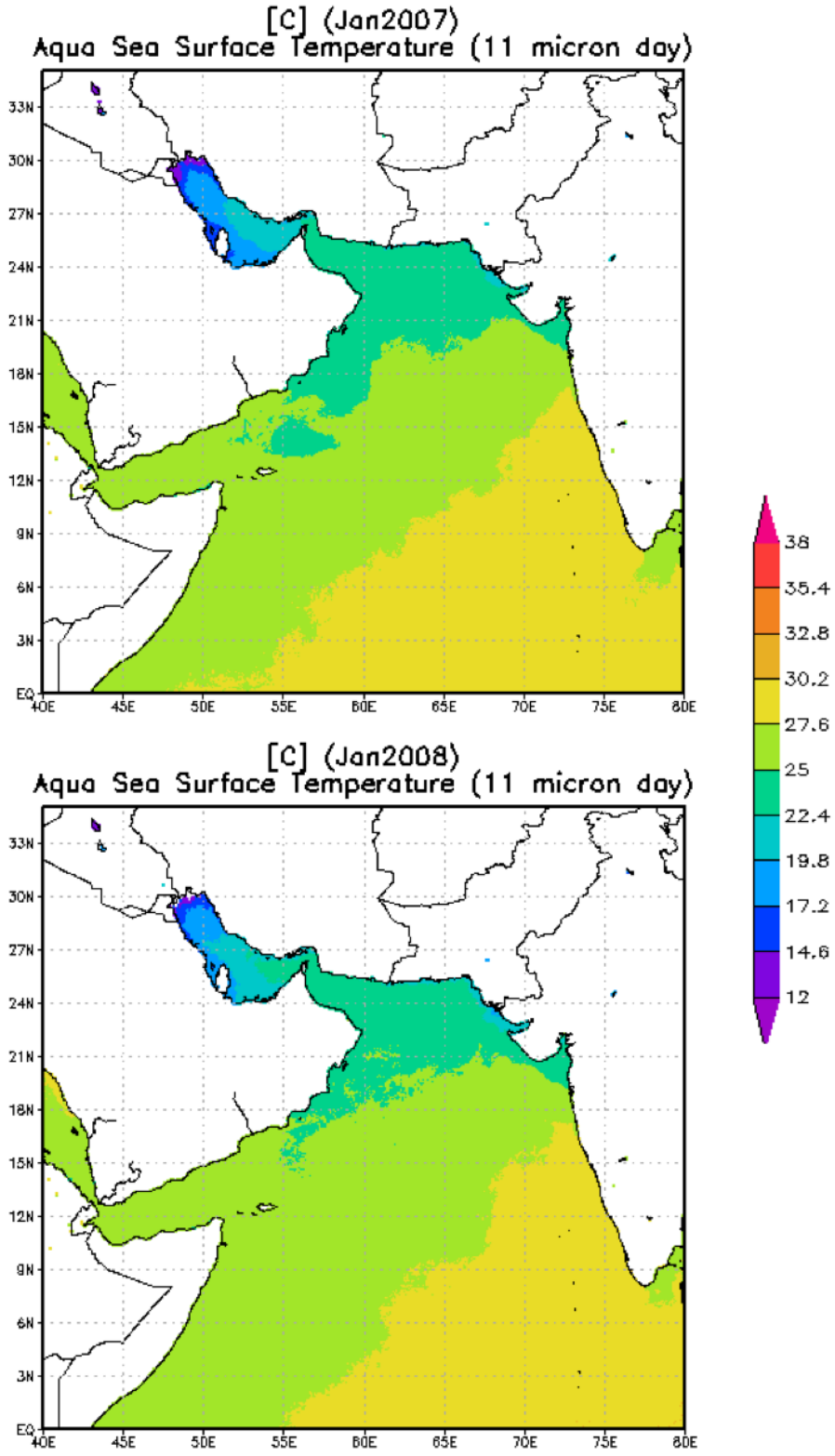

Figure B-1 continued.

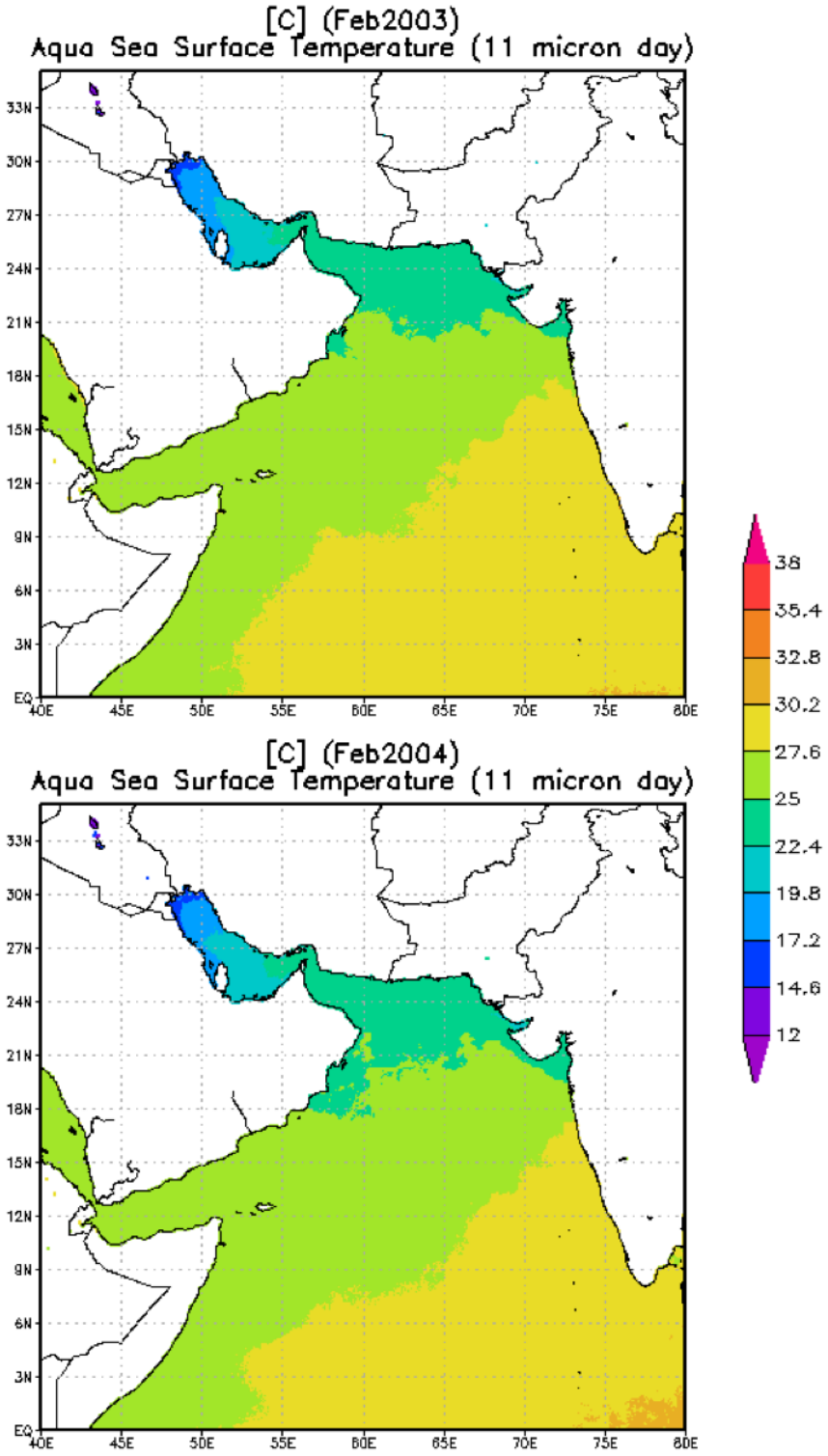

Figure B-2. February sea surface temperature maps generated by NASA's Giovanni (Kempler, 2011).

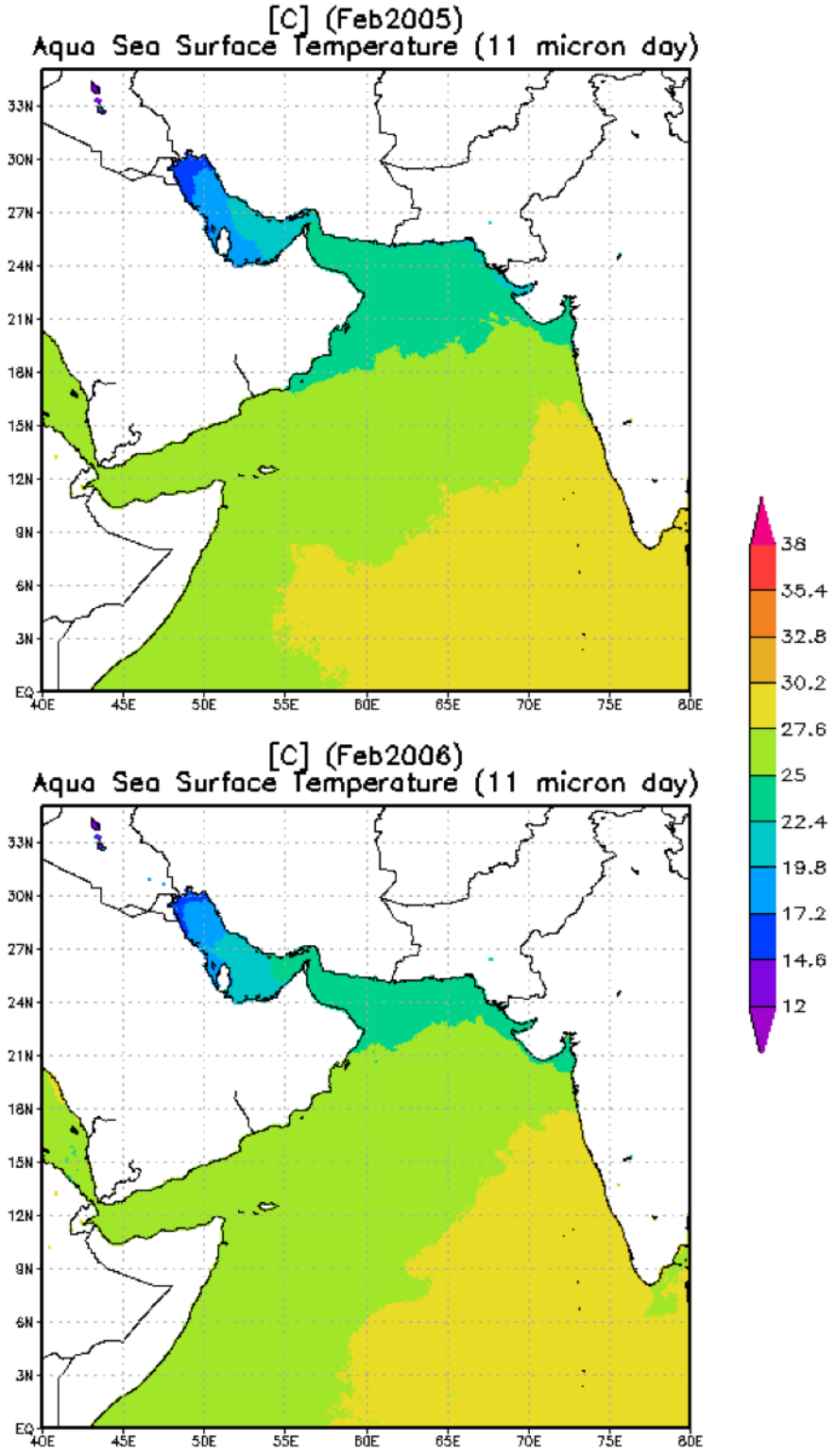

Figure B-2 continued.

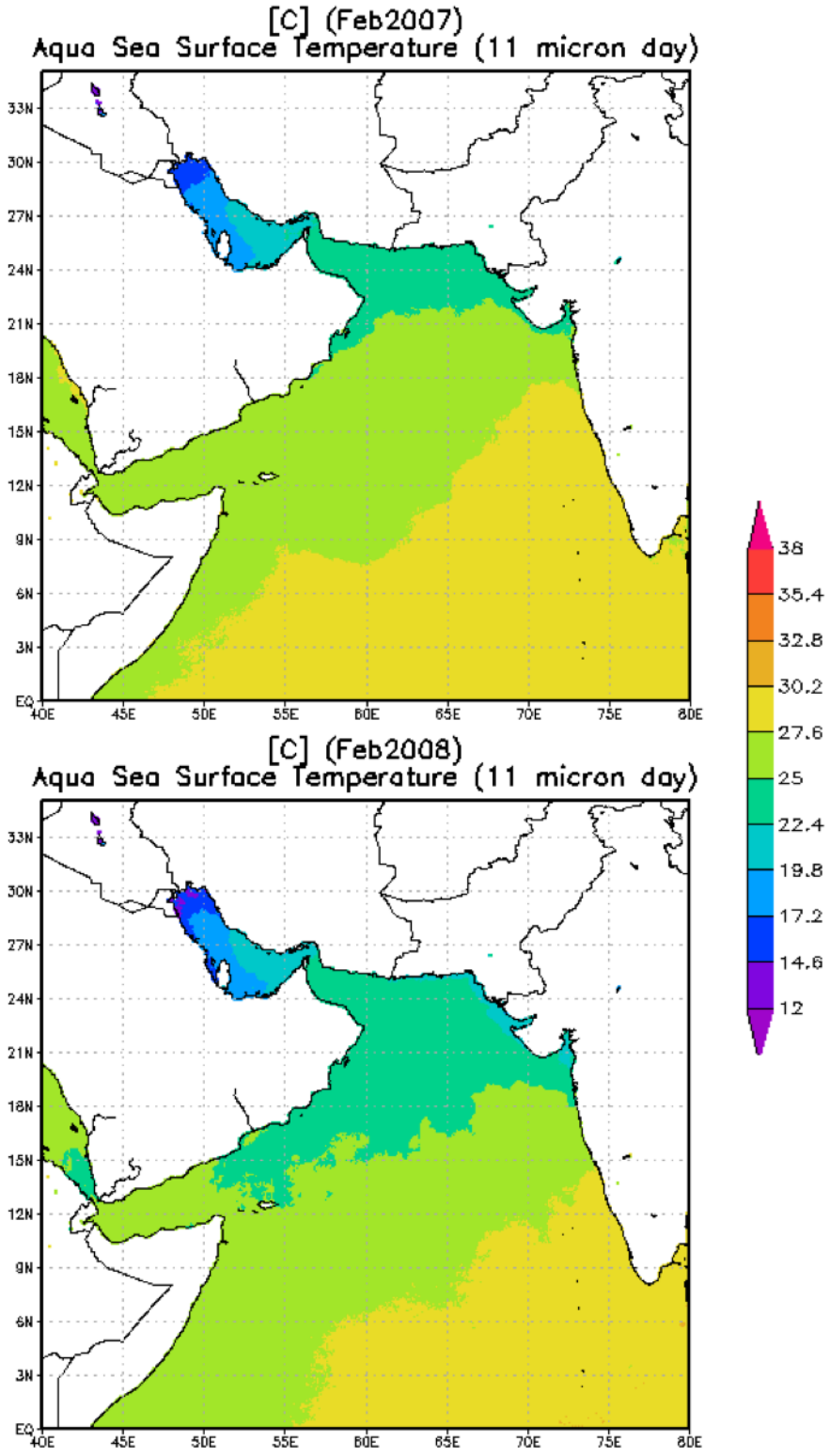

Figure B-2 continued.

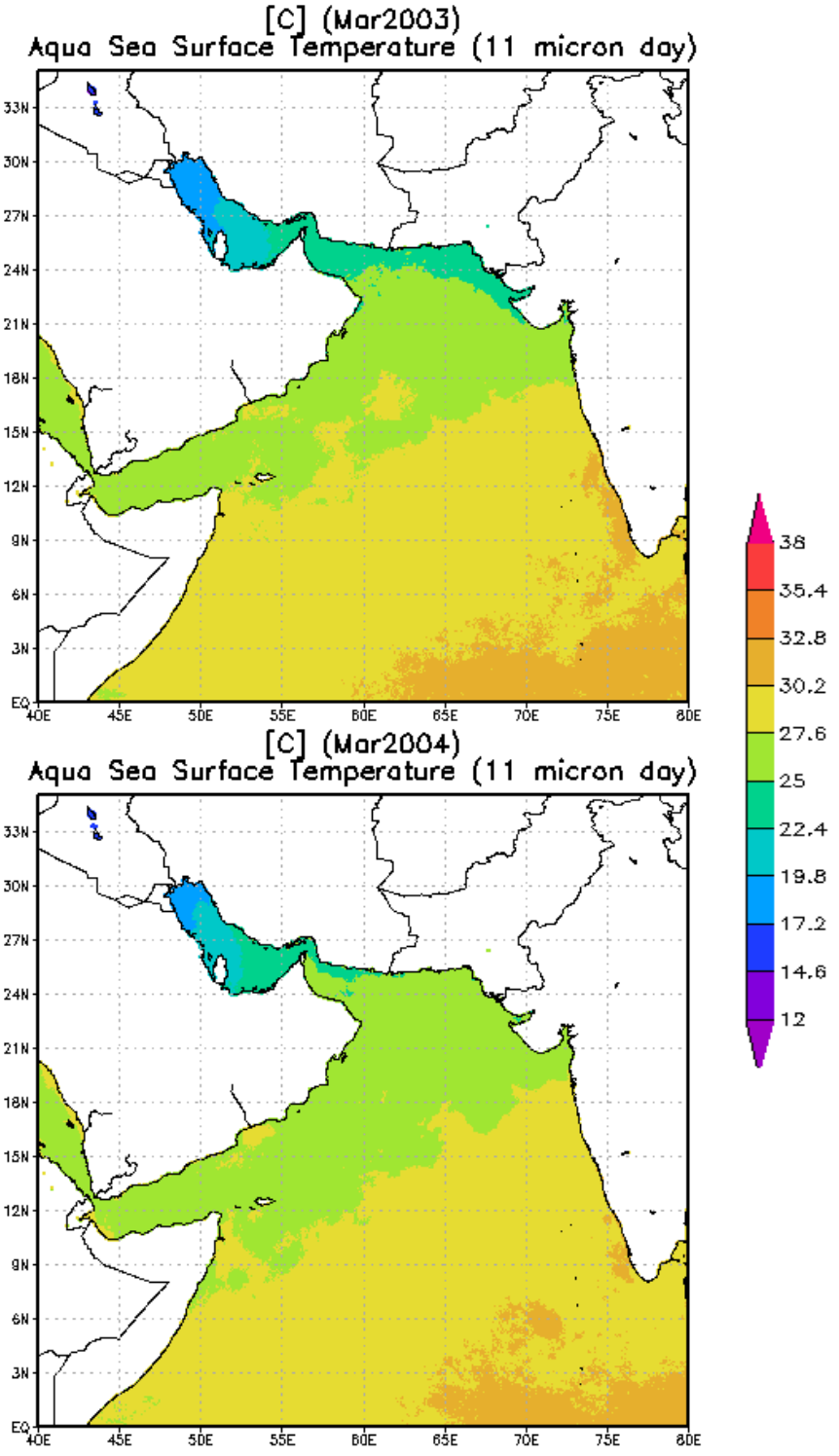

Figure B-3. March sea surface temperature maps generated by NASA's Giovanni (Kempler, 2011).

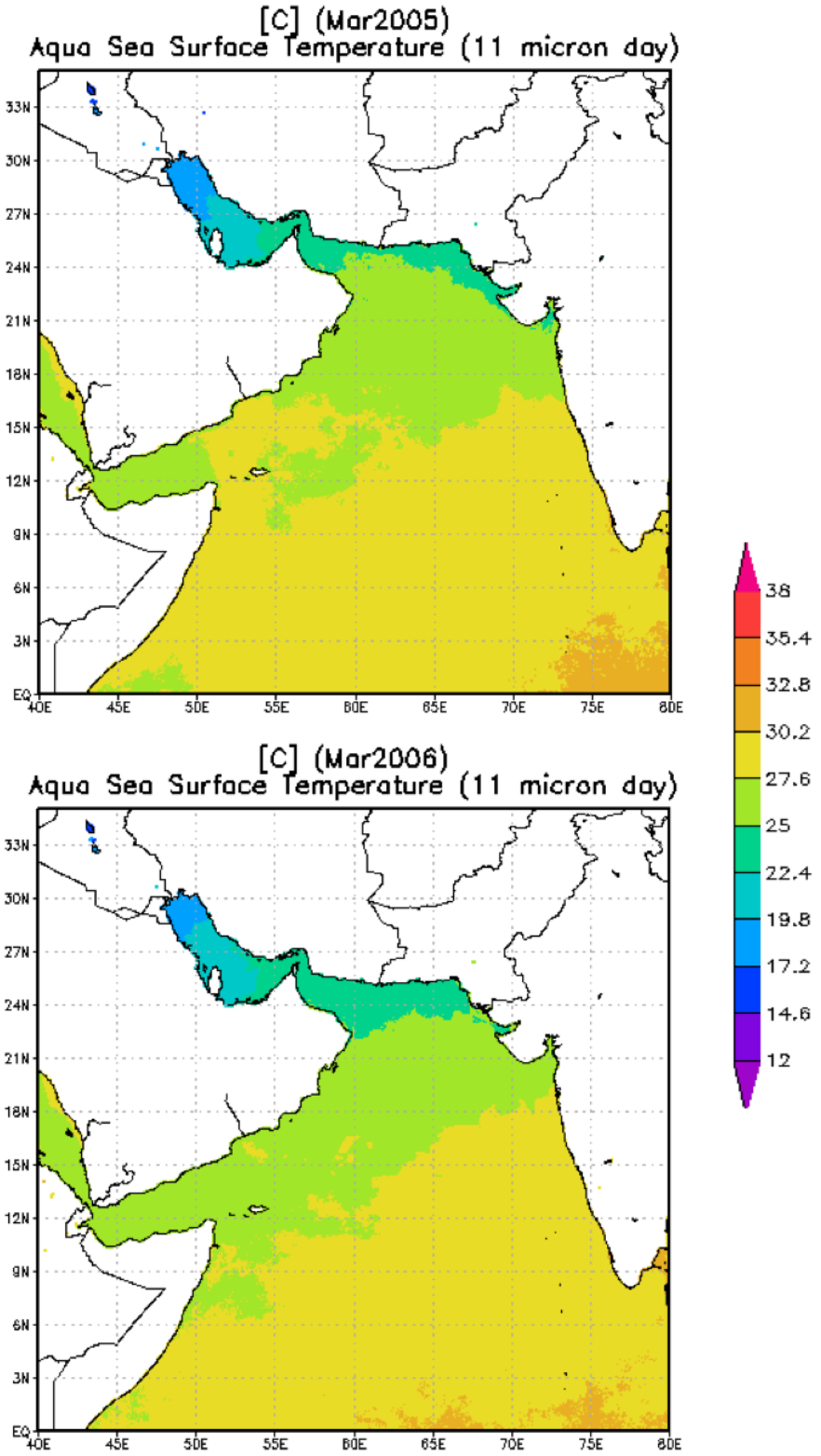

Figure B-3 continued.

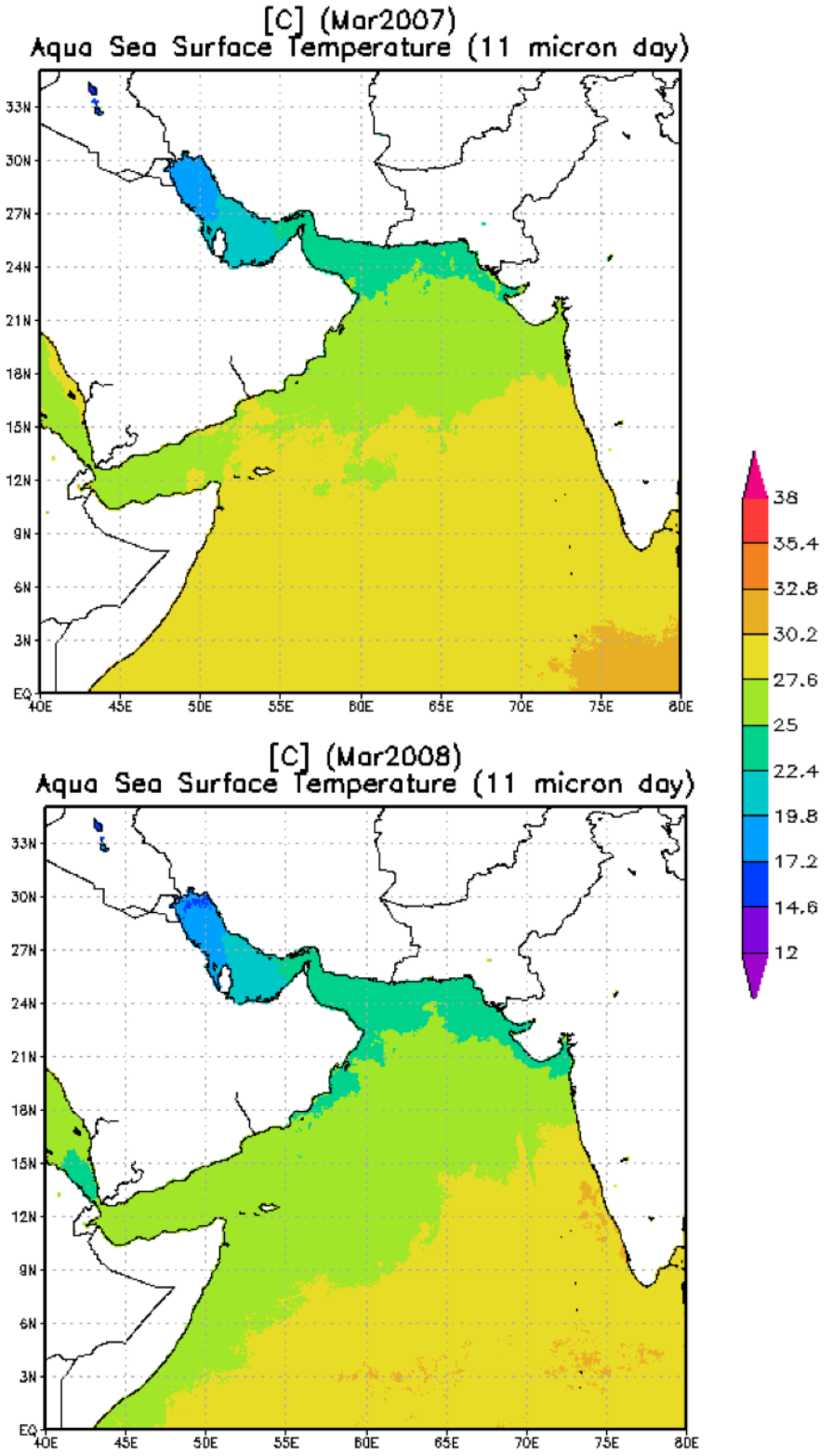

Figure B-3 continued.

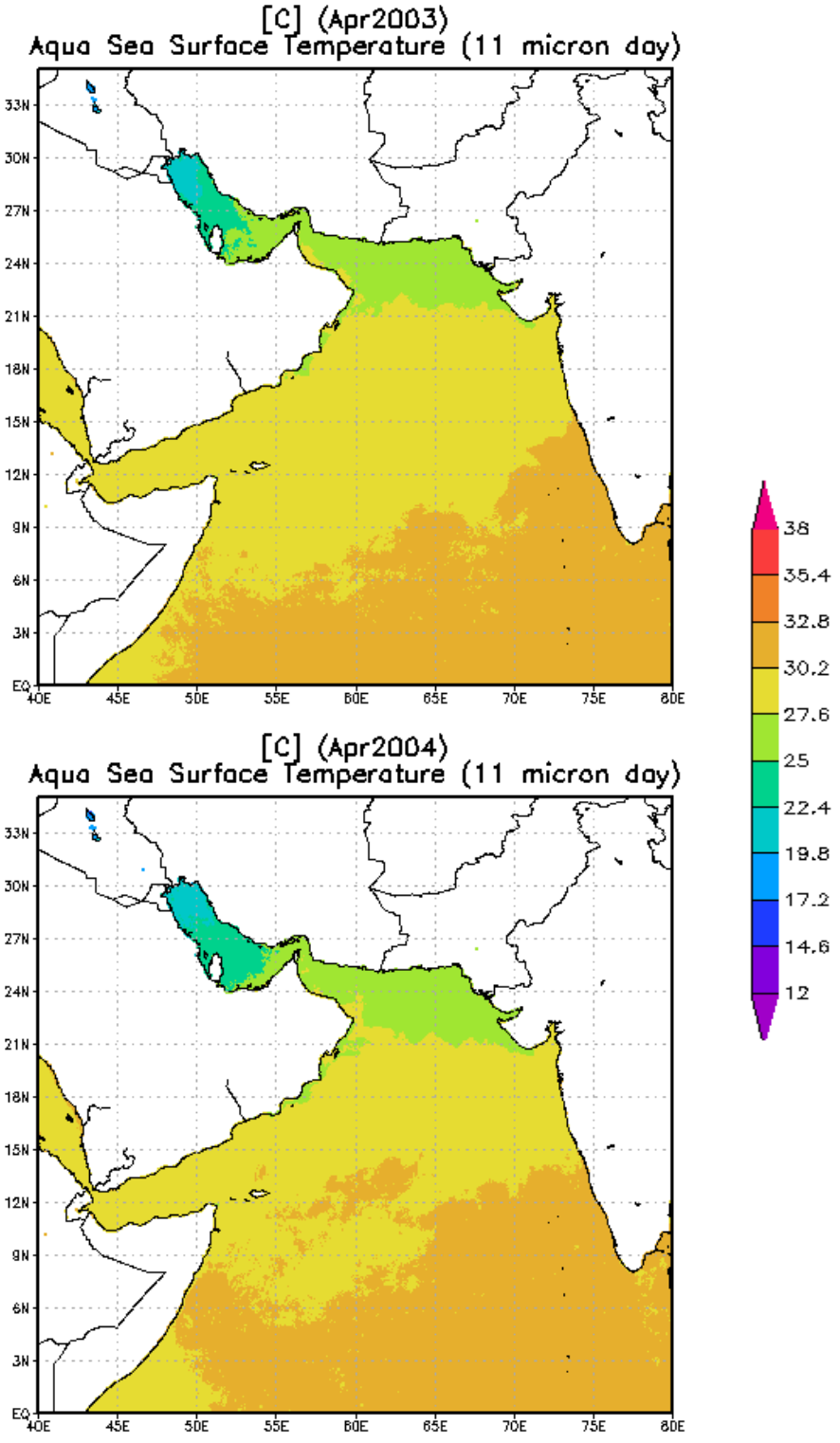

Figure B-4. April sea surface temperature maps generated by NASA's Giovanni (Kempler, 2011).

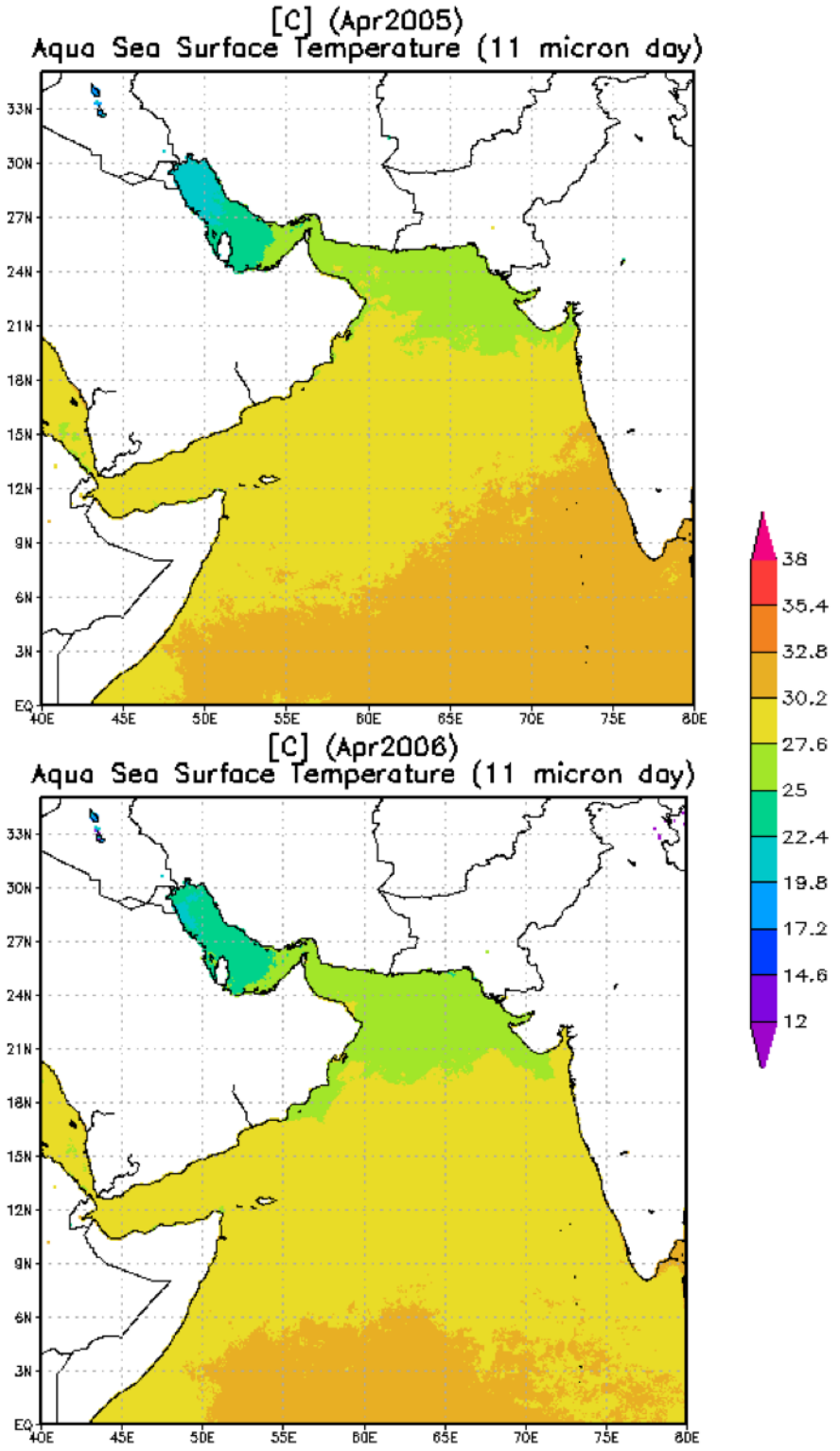

Figure B-4 continued.

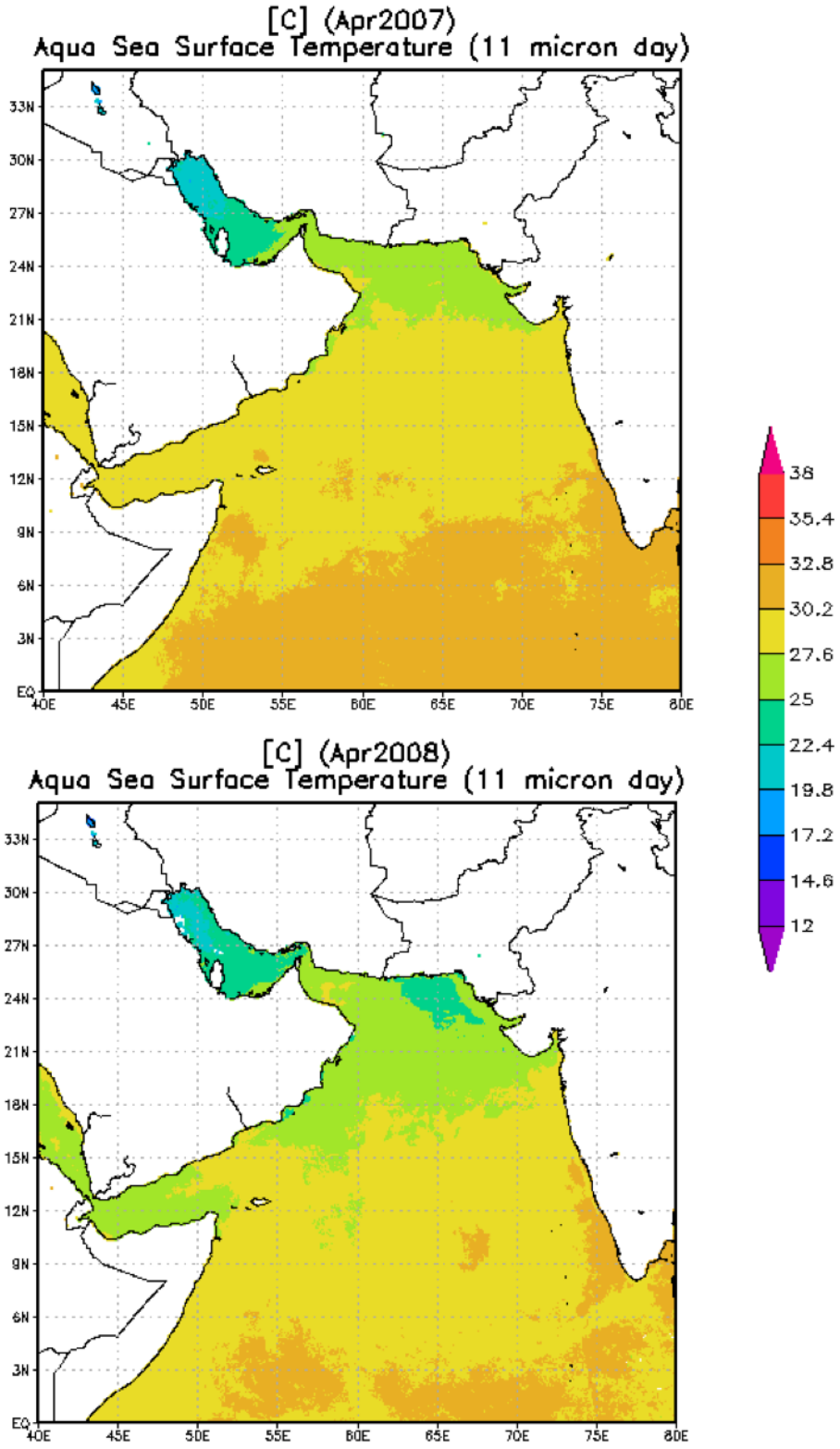

Figure B-4 continued.

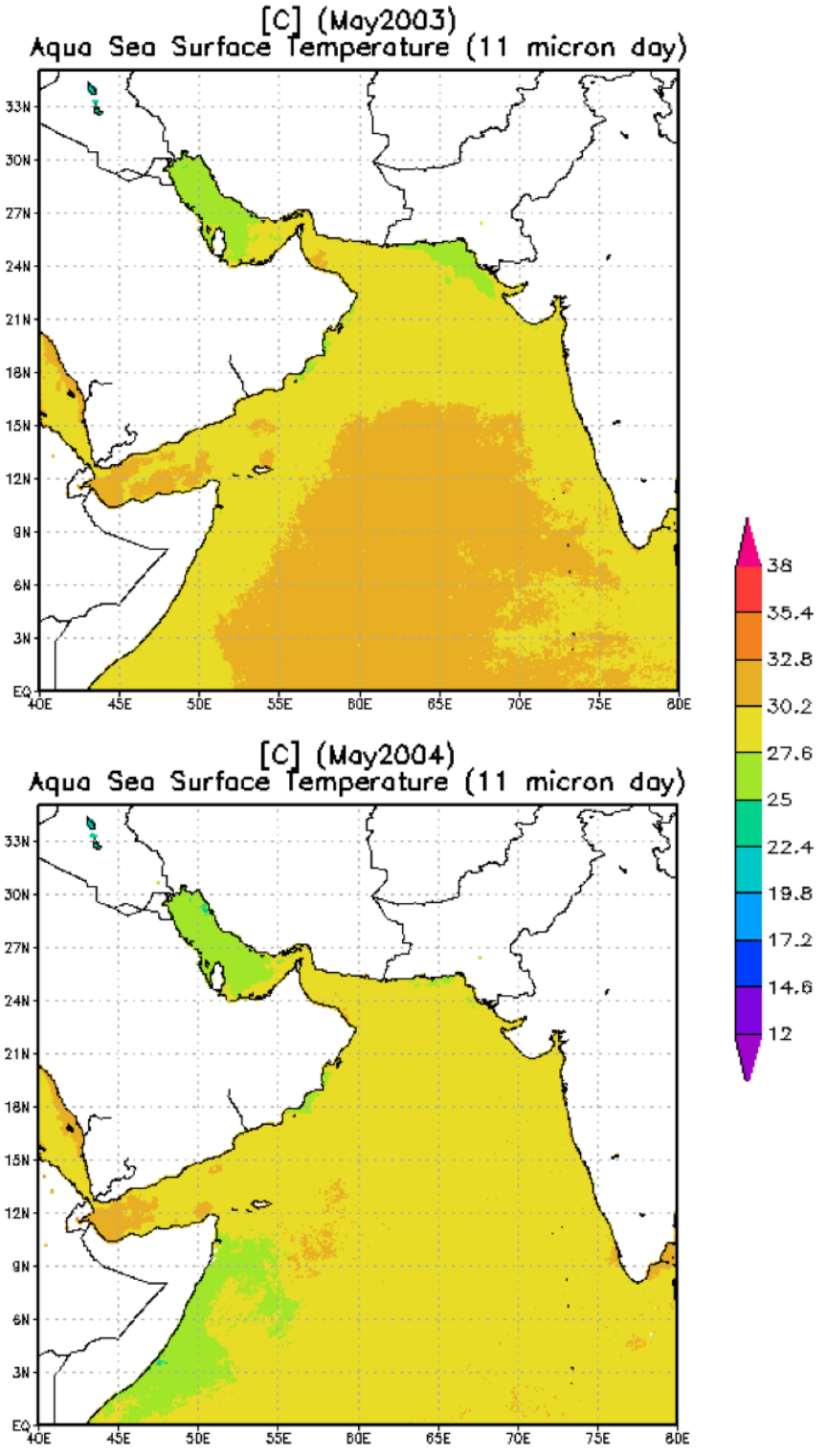

Figure B-5. May sea surface temperature maps generated by NASA's Giovanni (Kempler, 2011).

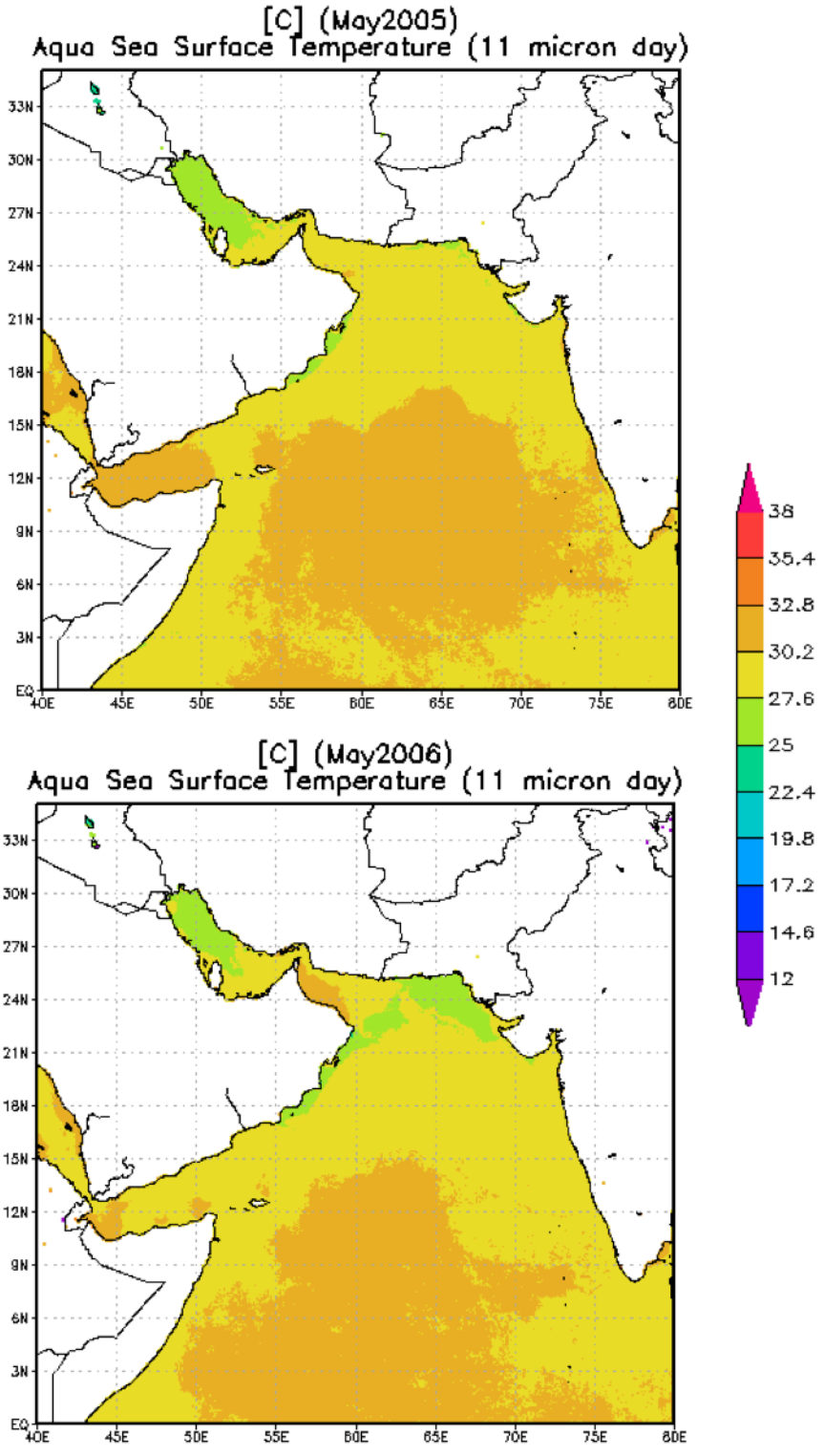

Figure B-5 continued.

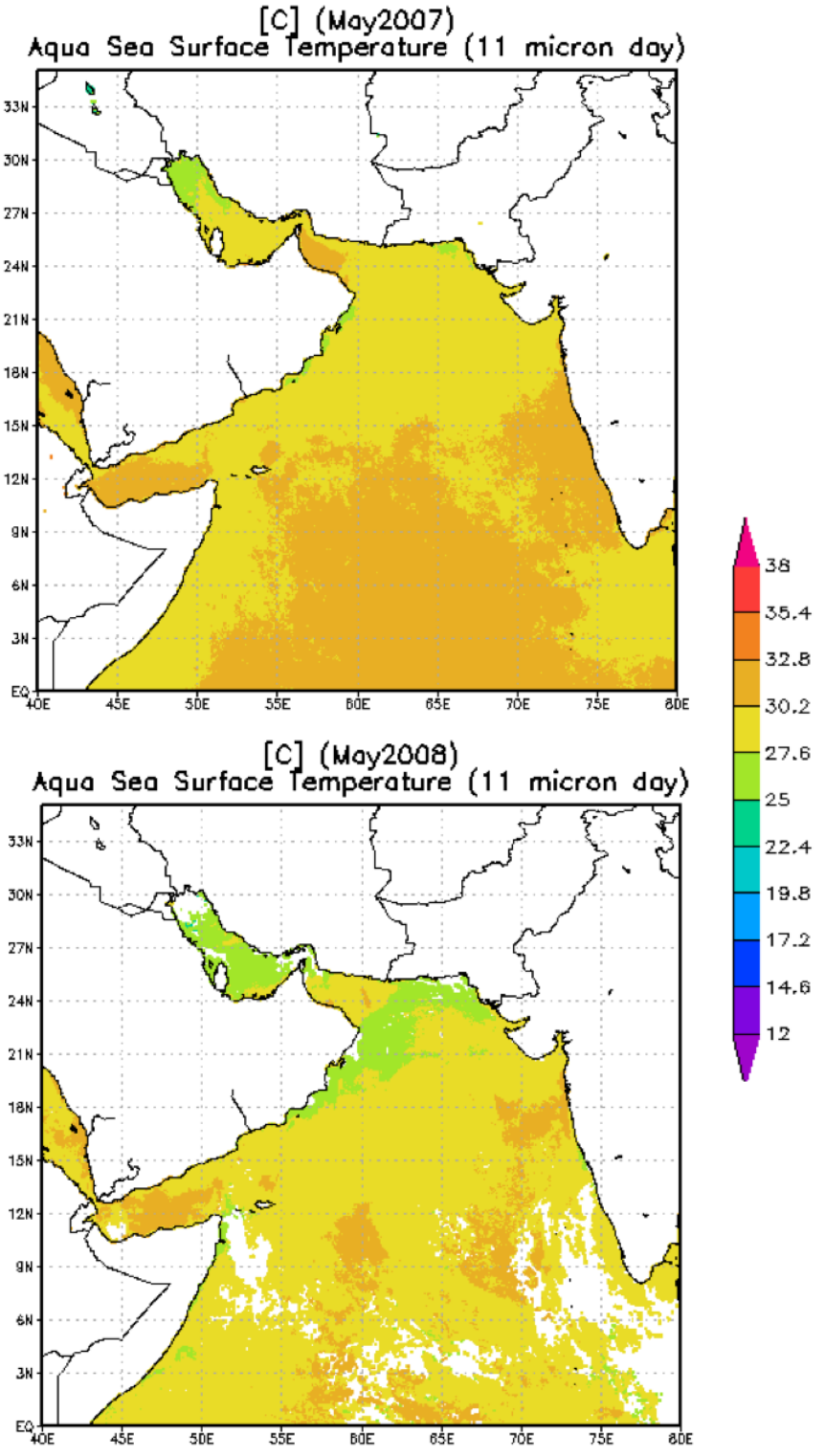

Figure B-5 continued.

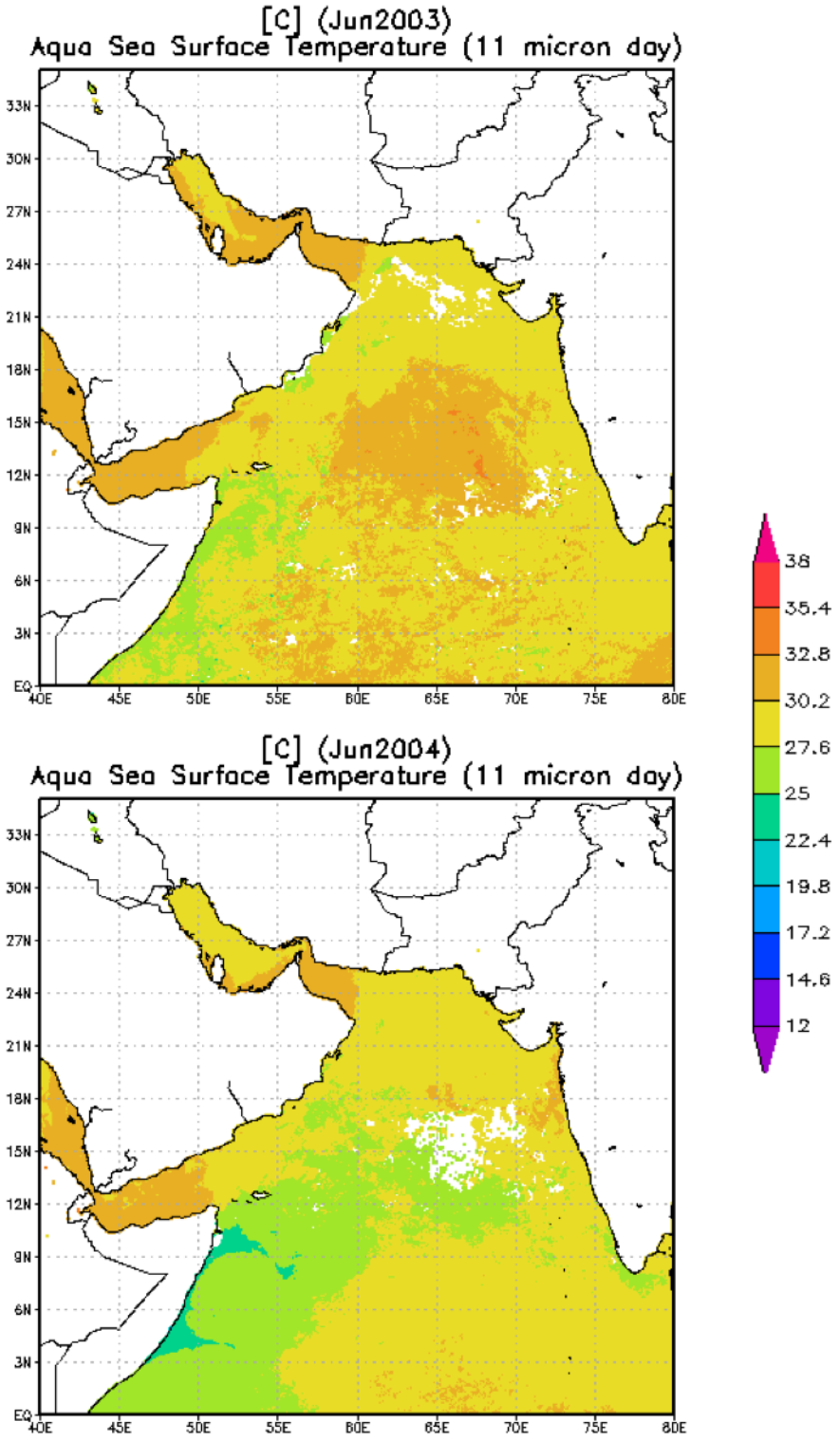

Figure B-6. June sea surface temperature maps generated by NASA's Giovanni (Kempler, 2011).

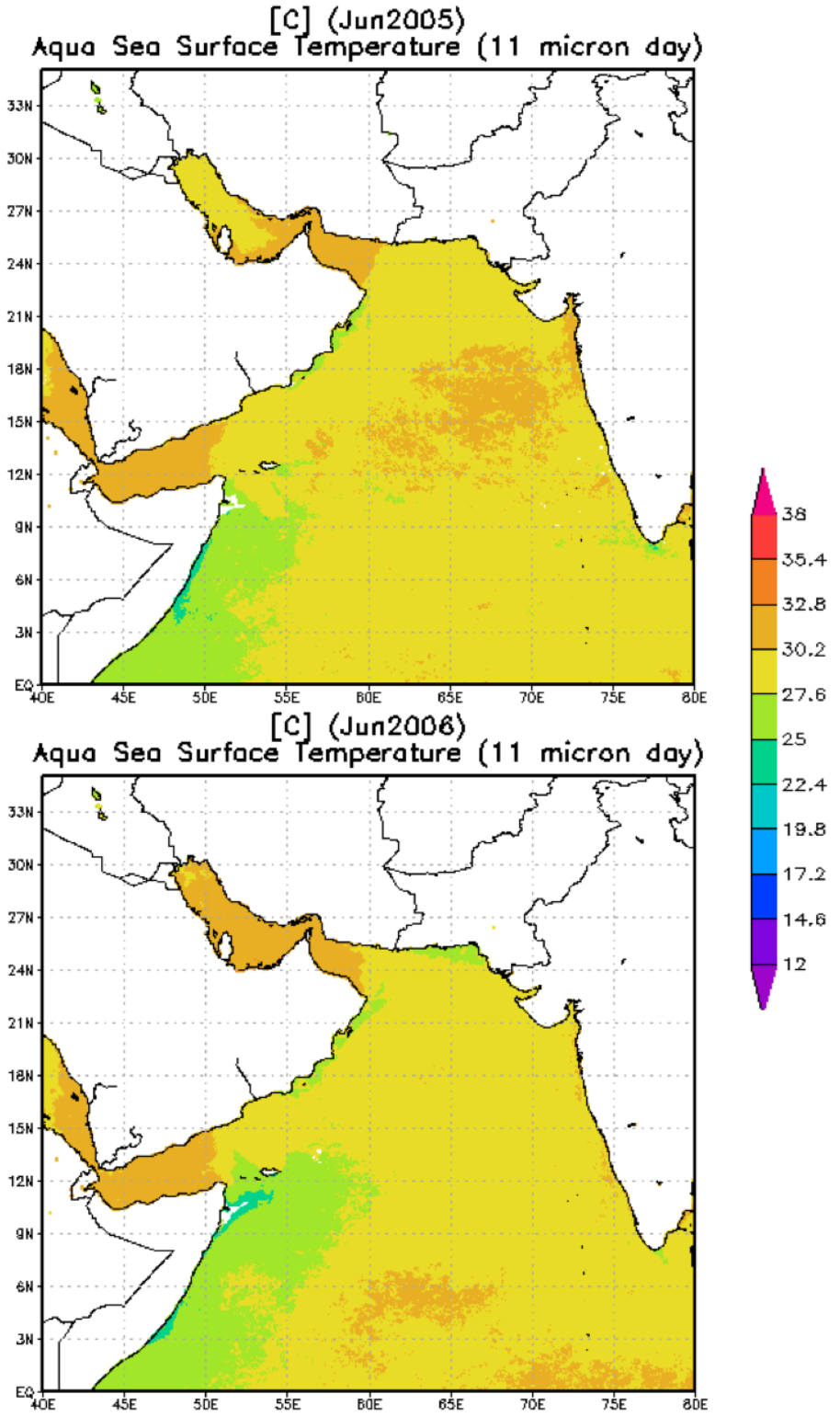

Figure B-6 continued.

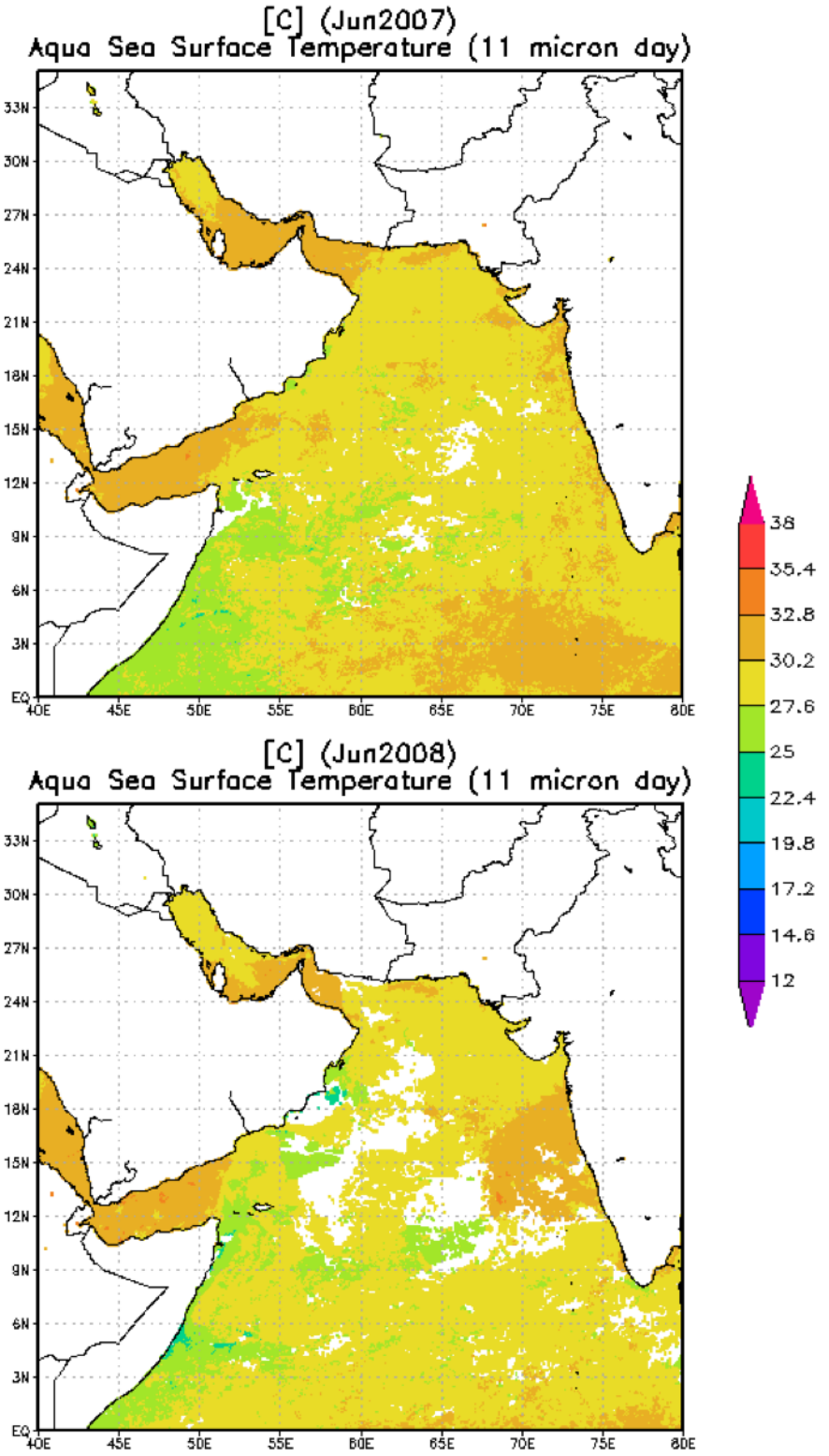

Figure B-6 continued.

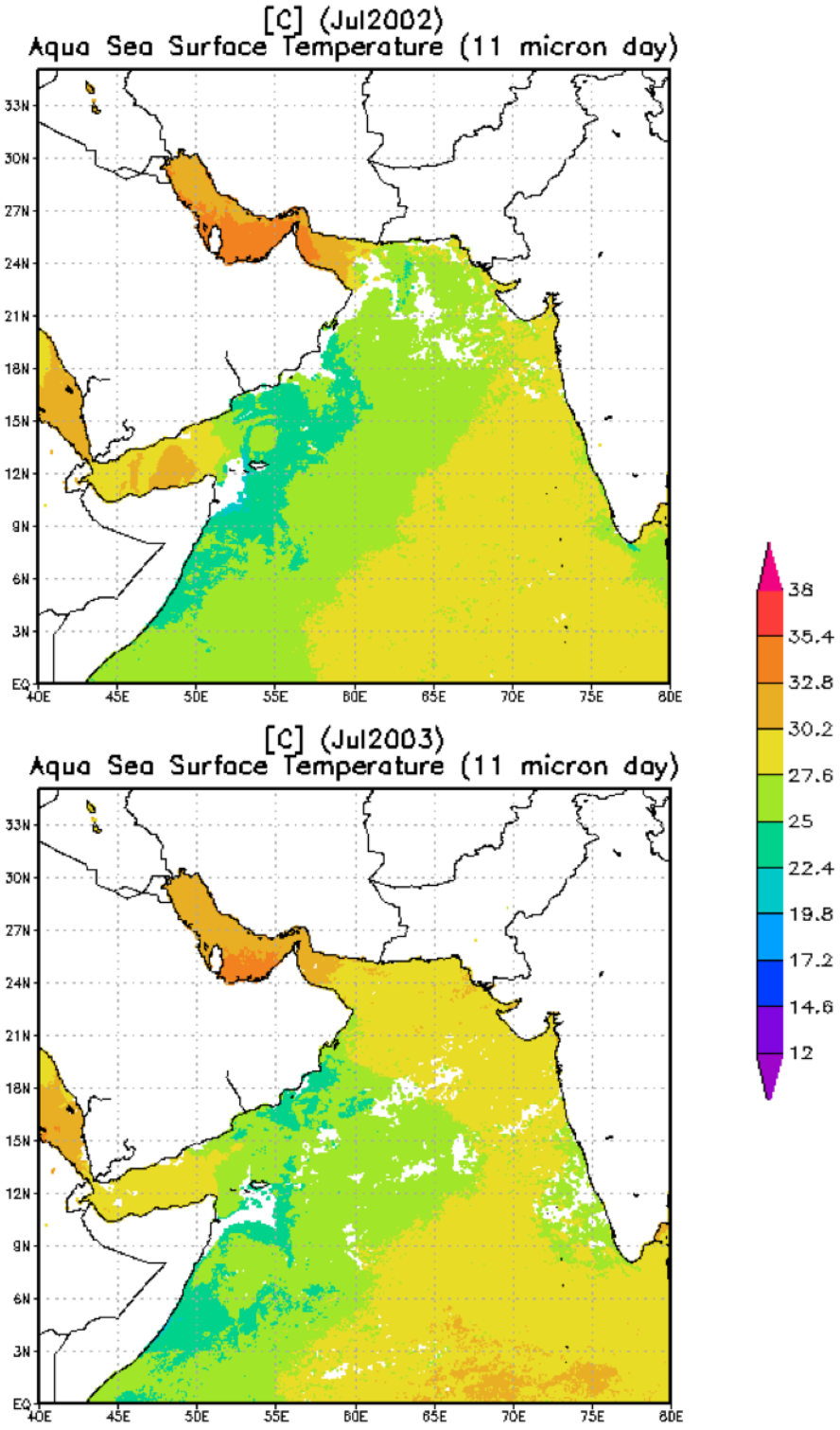

Figure B-7. July sea surface temperature maps generated by NASA's Giovanni (Kempler, 2011).

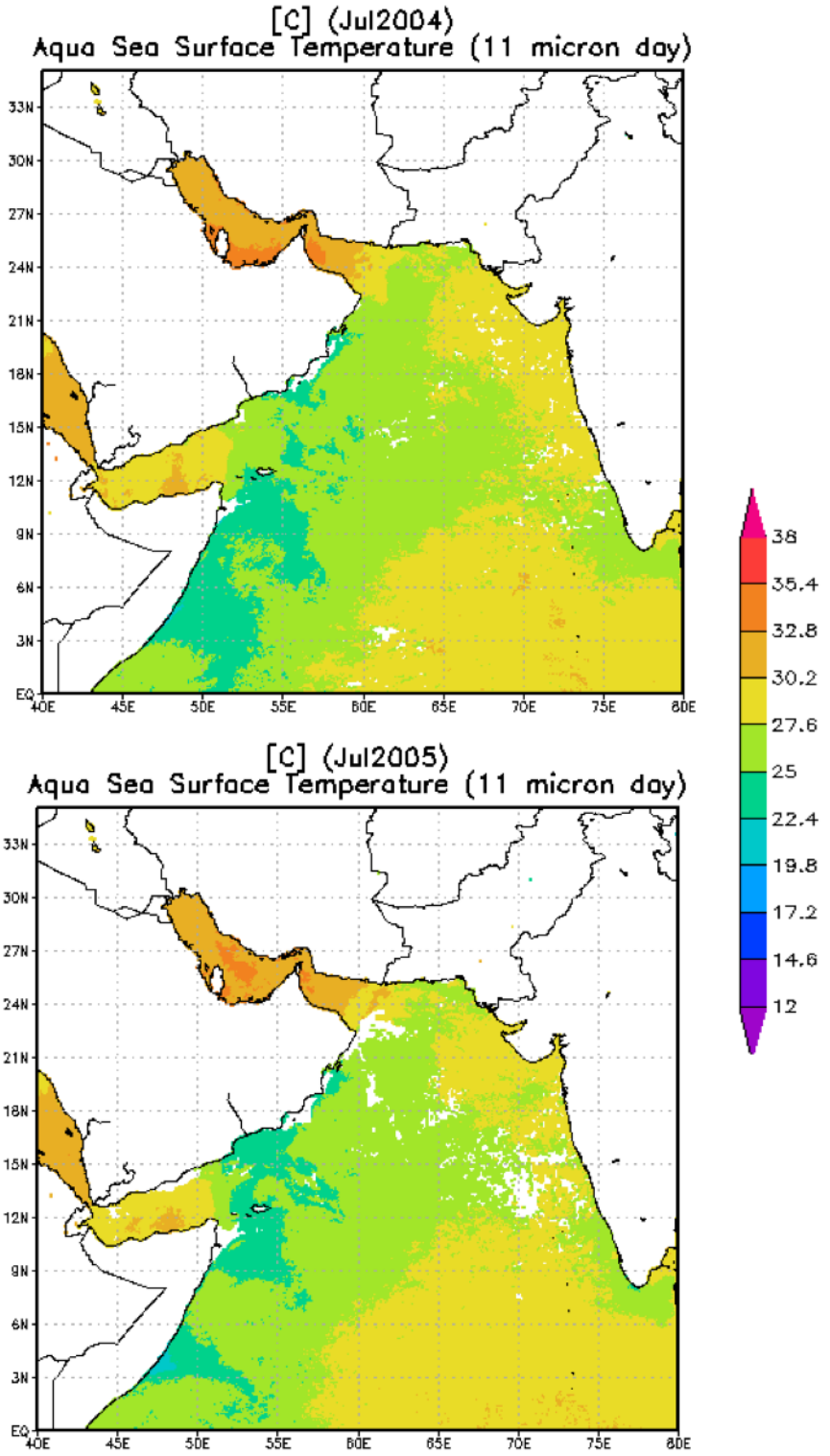

Figure B-7 continued.

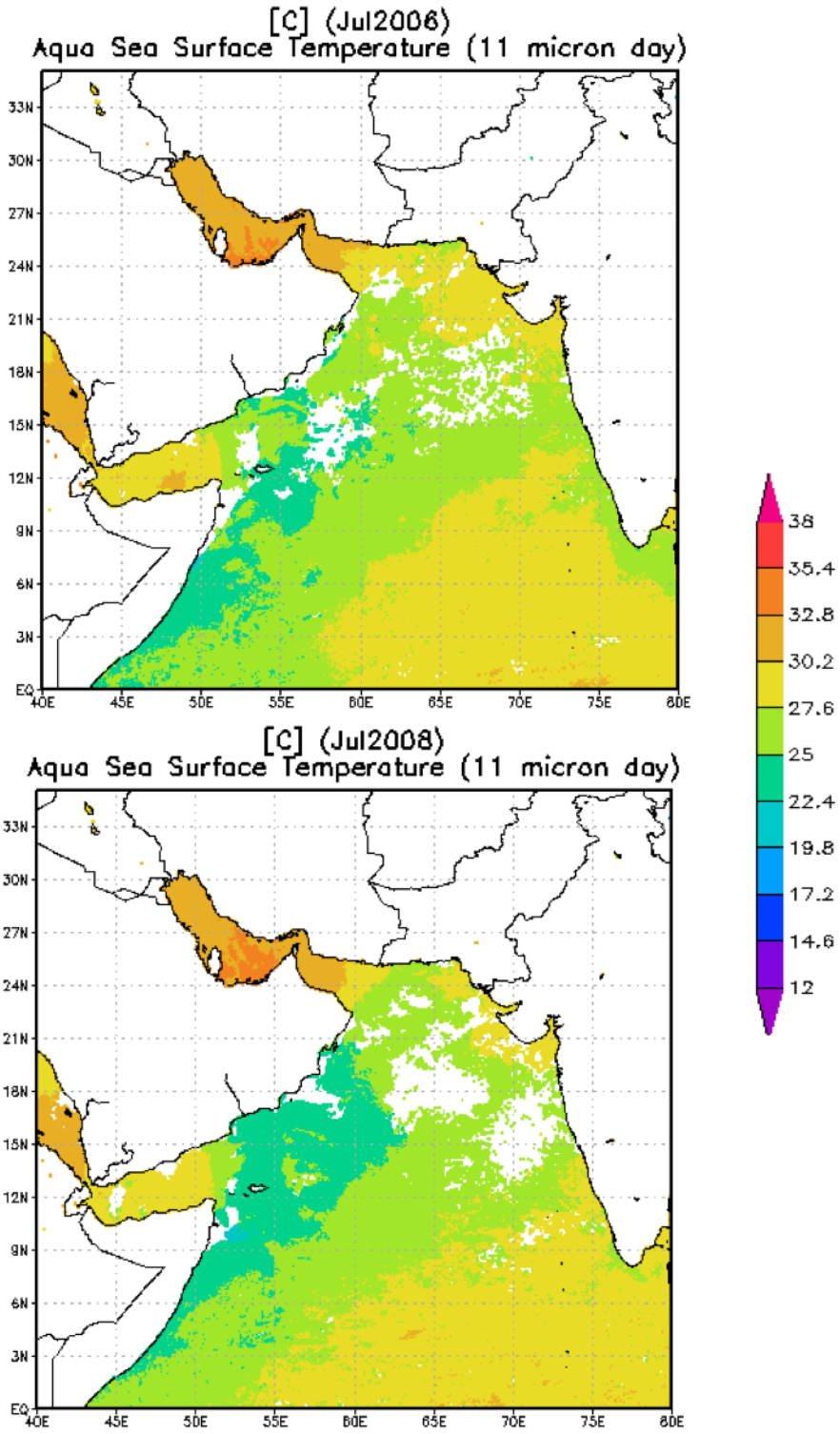

Figure B-7 continued.

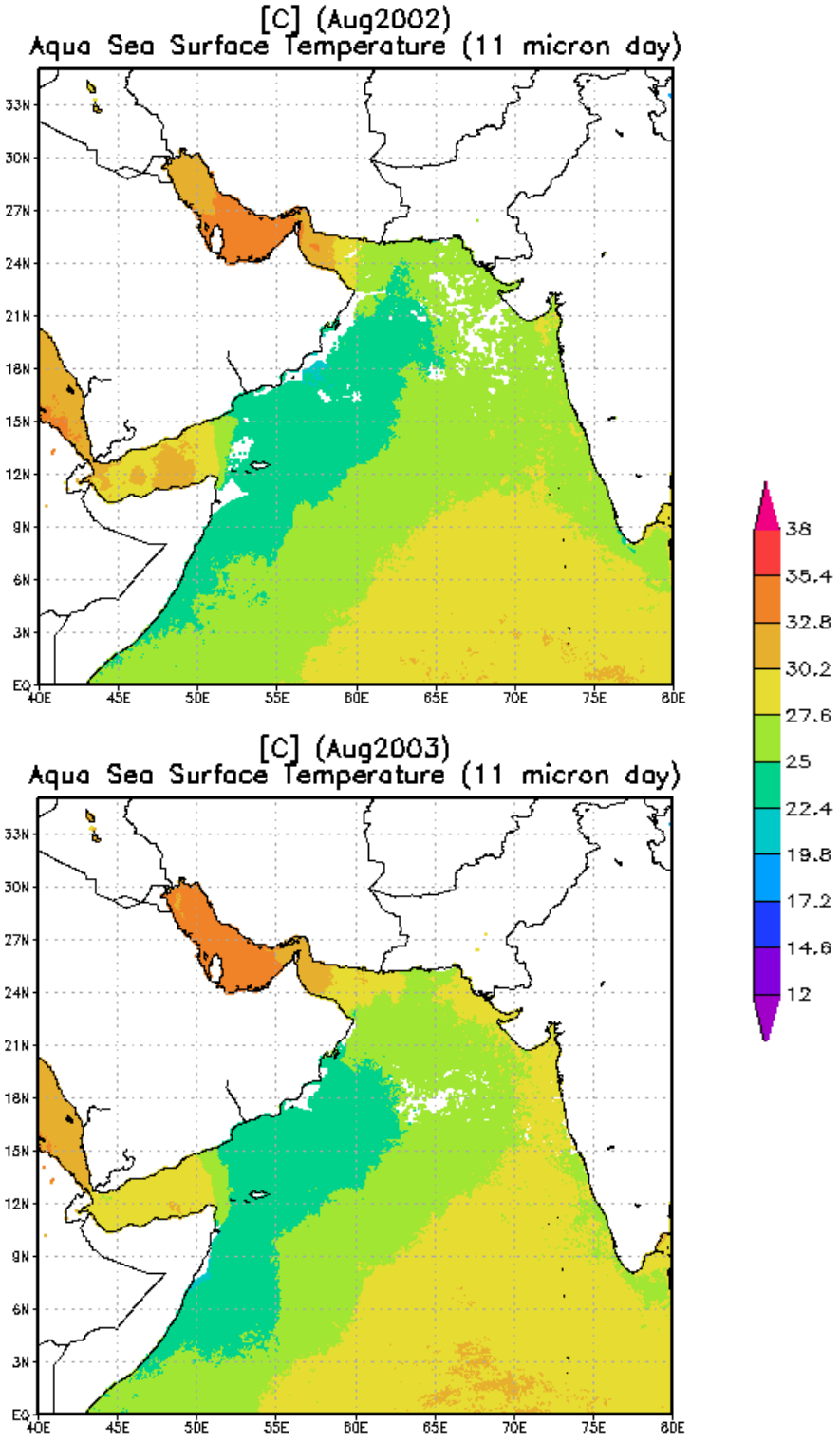

Figure B-8. August sea surface temperature maps generated by NASA's Giovanni (Kempler, 2011).

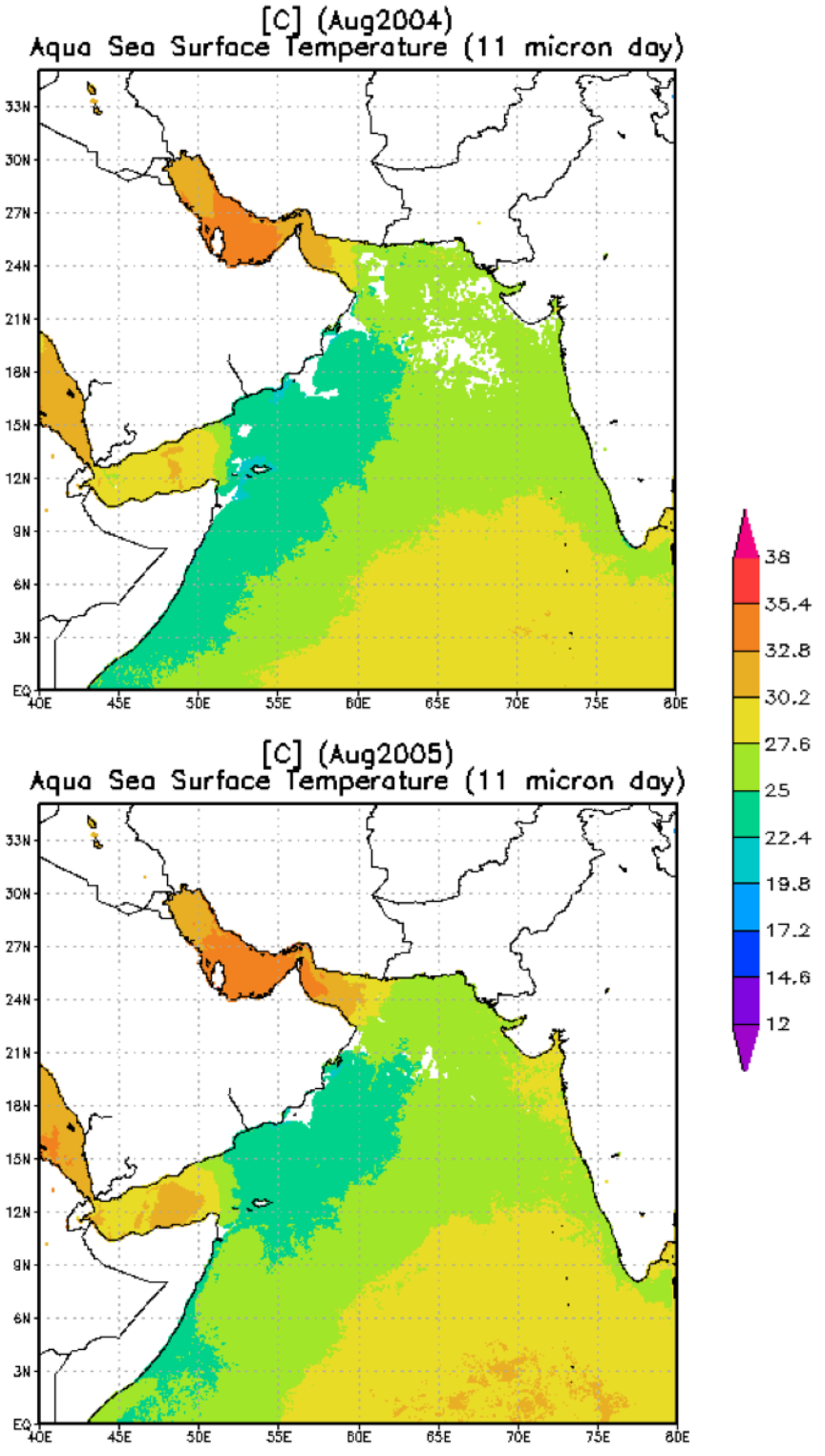

Figure B-8 continued.

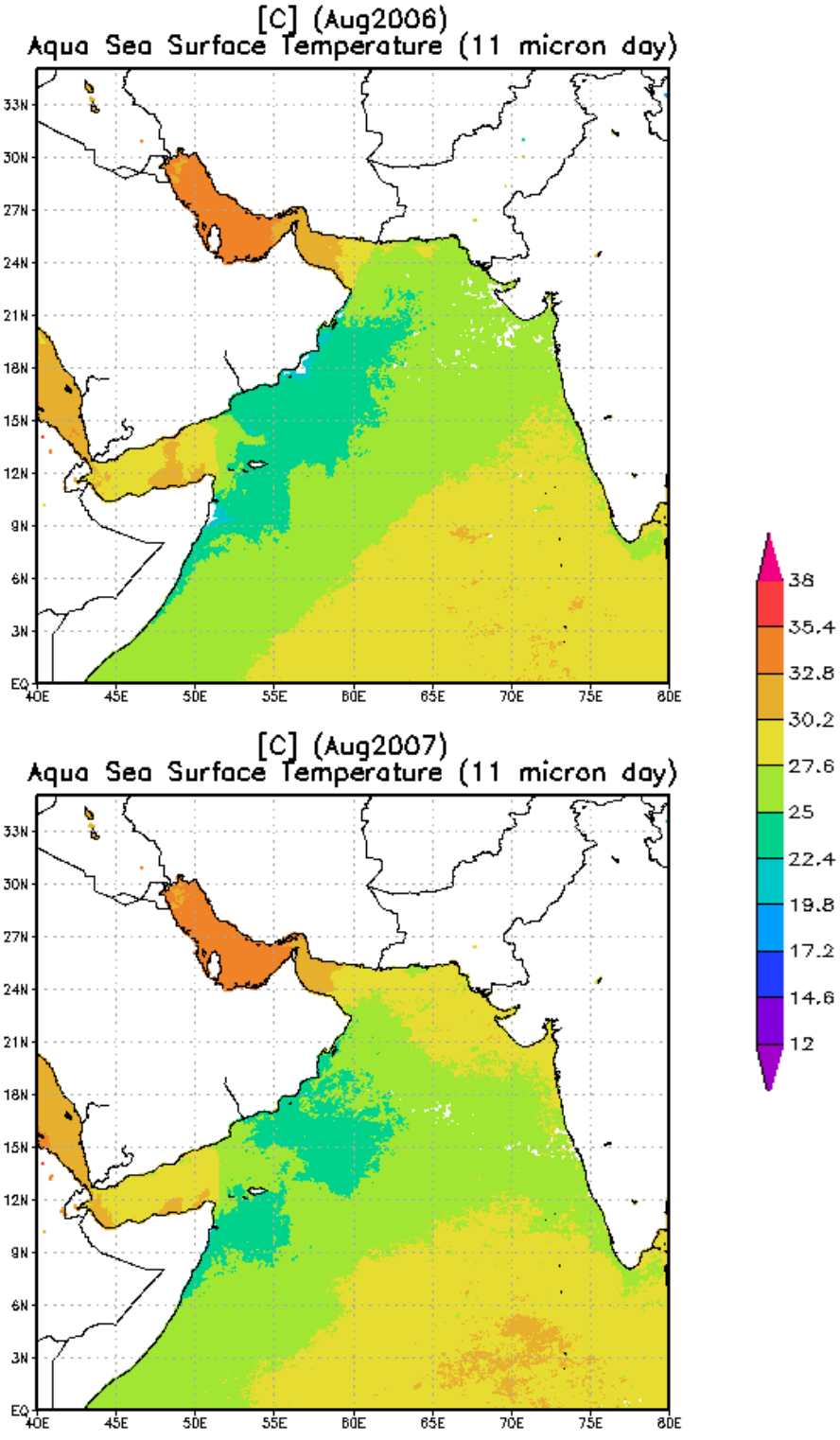

Figure B-8 continued.

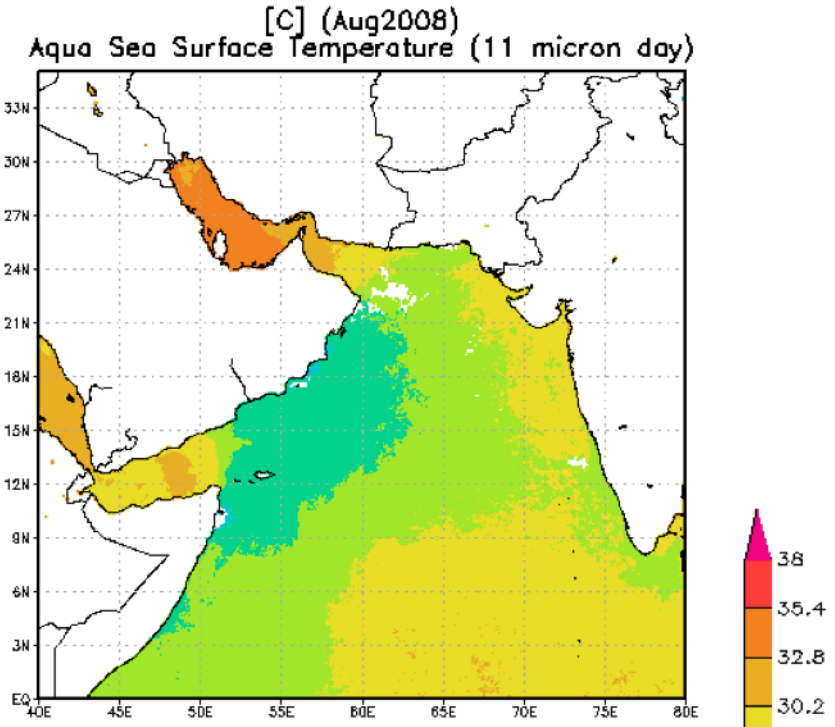

Figure B-8 continued.

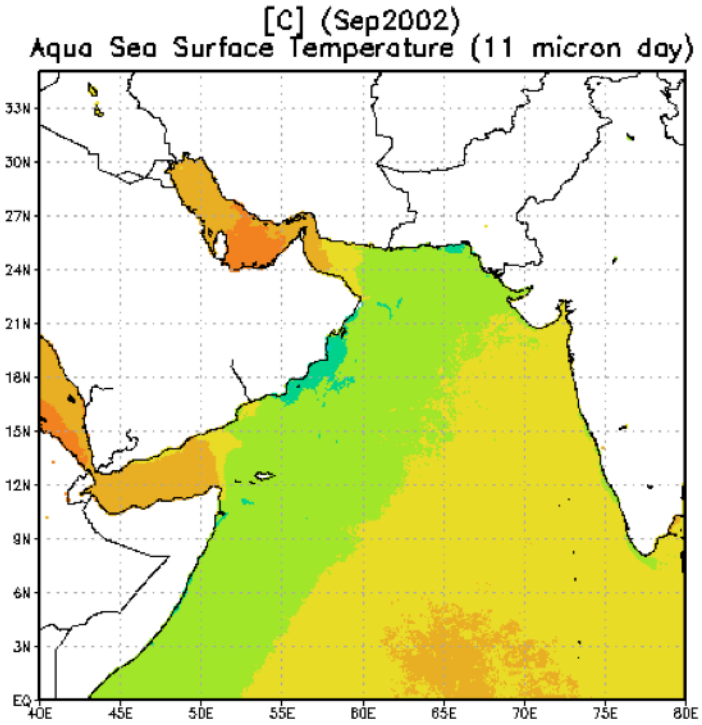

Figure B-9. September sea surface temperature maps generated by NASA's Giovanni (Kempler, 2011).

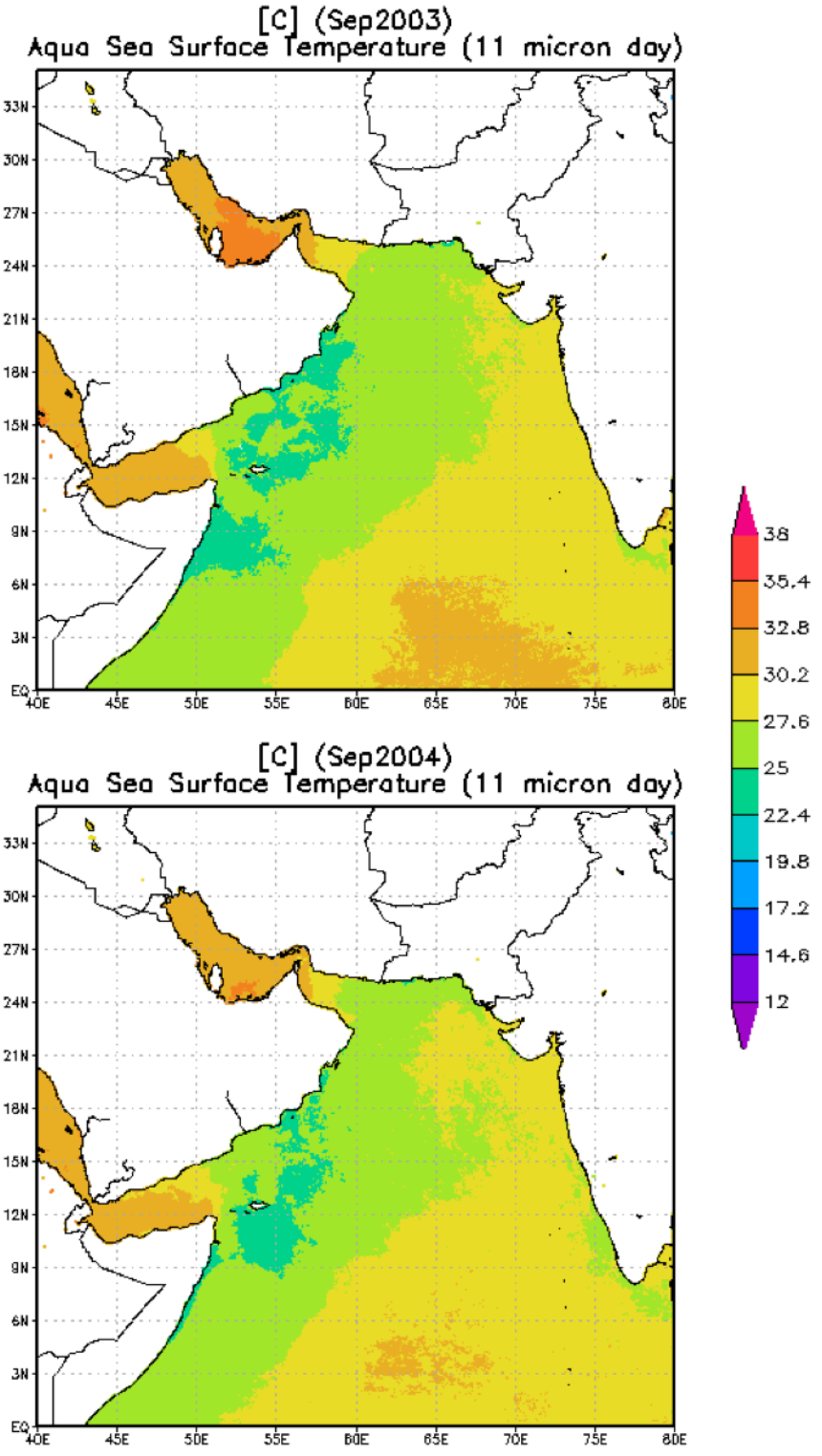

Figure B-9 continued.

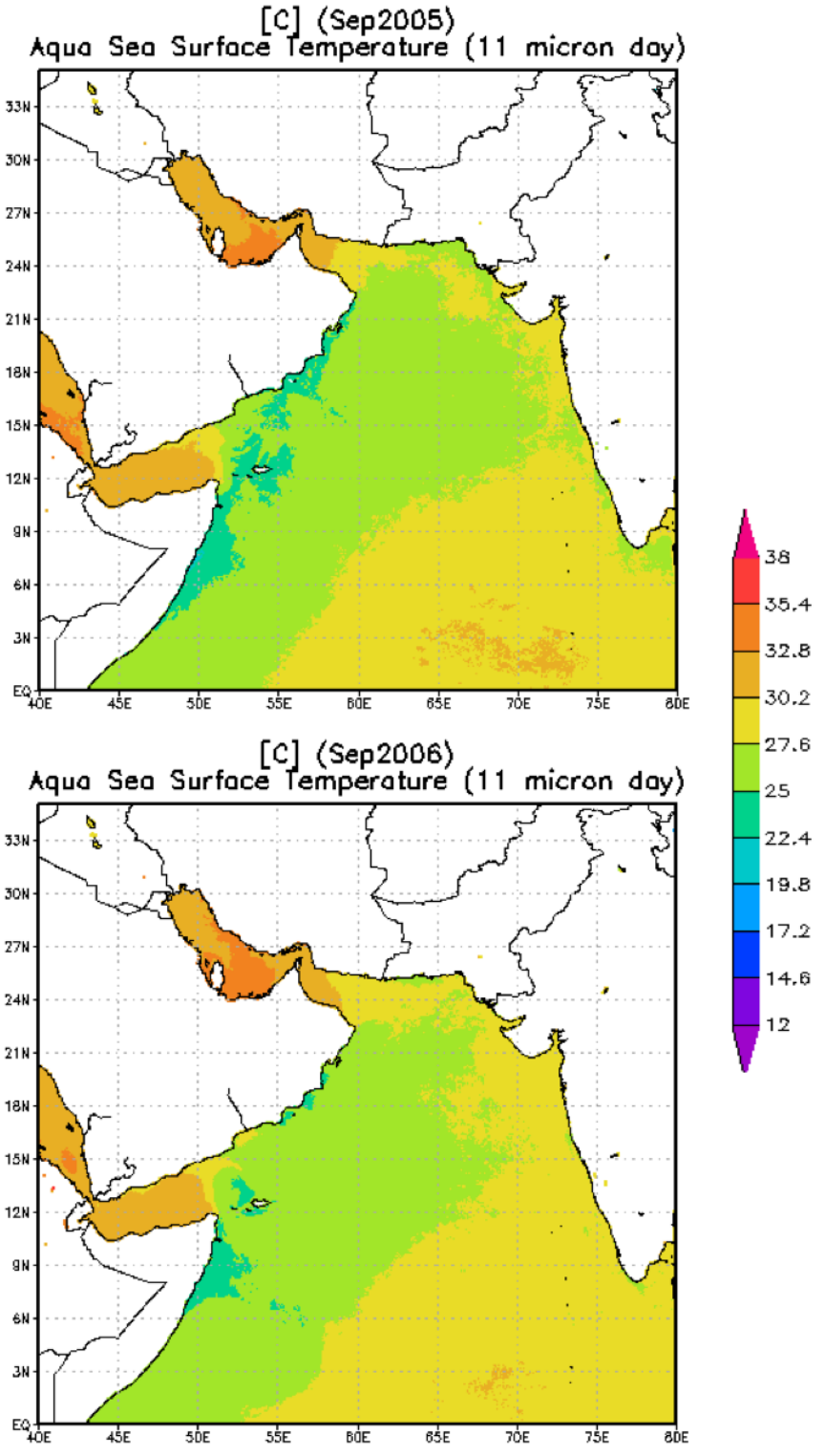

Figure B-9 continued.

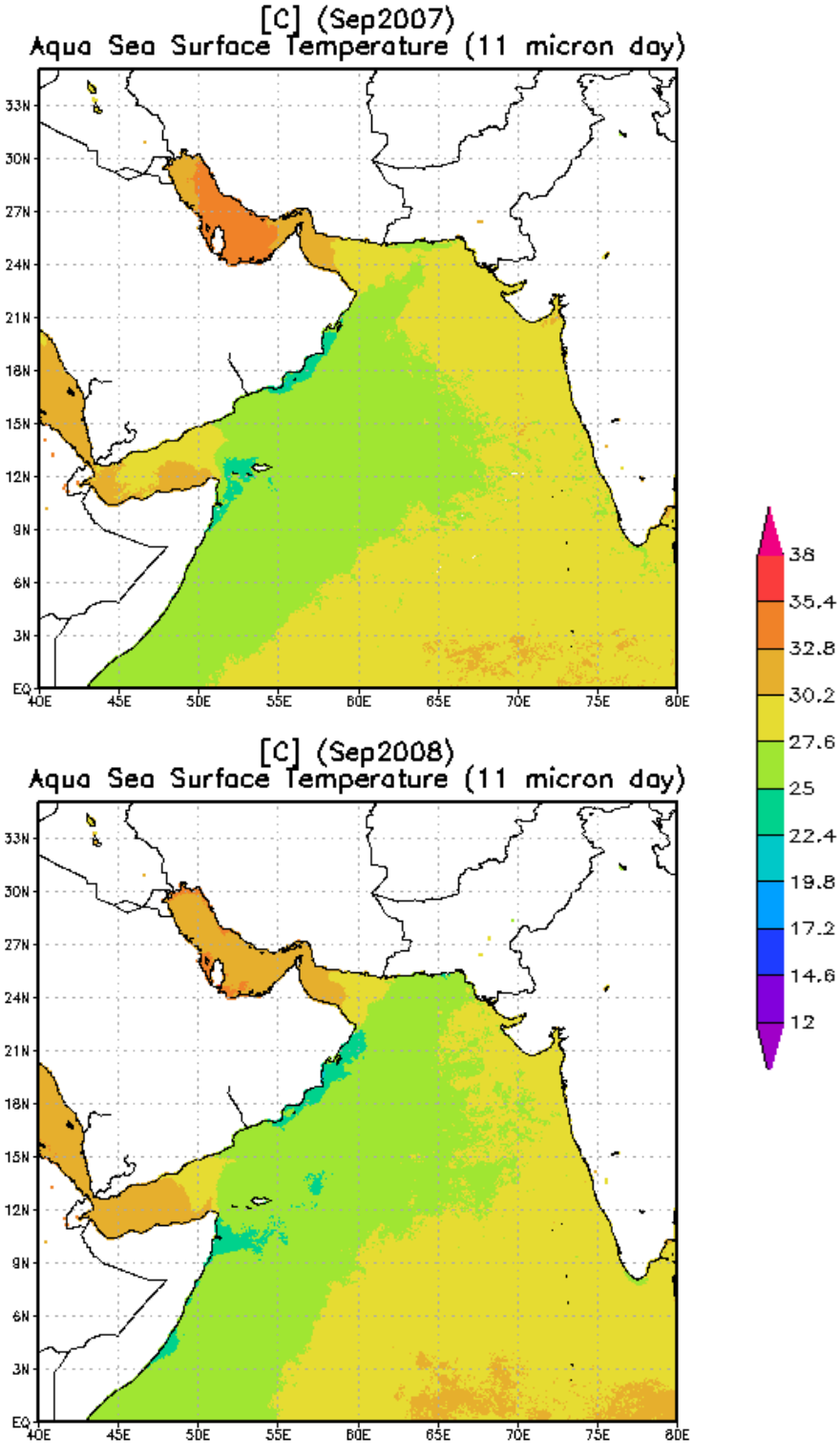

Figure B-9 continued.

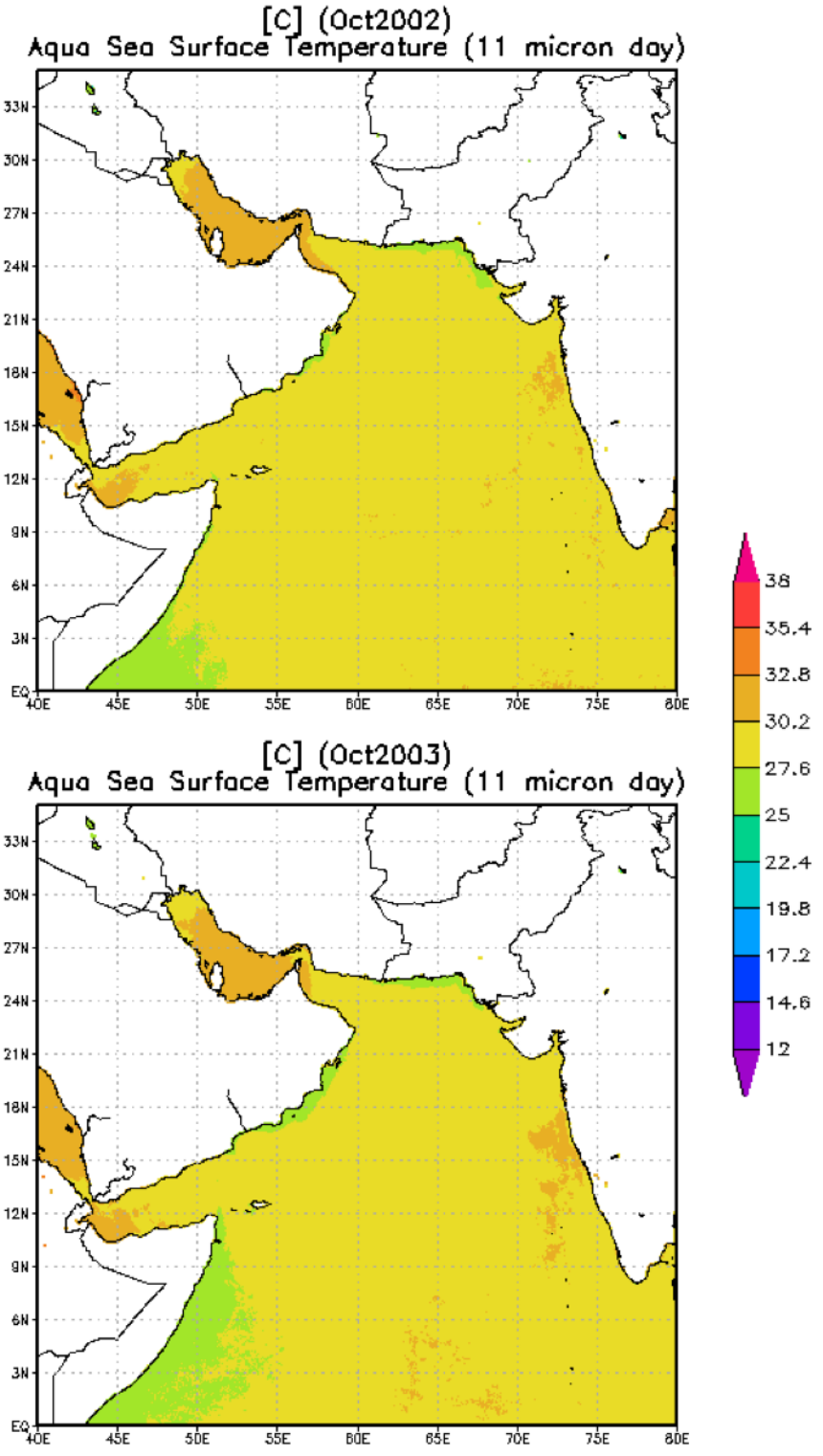

Figure B-10. October sea surface temperature maps generated by NASA's Giovanni (Kempler, 2011).

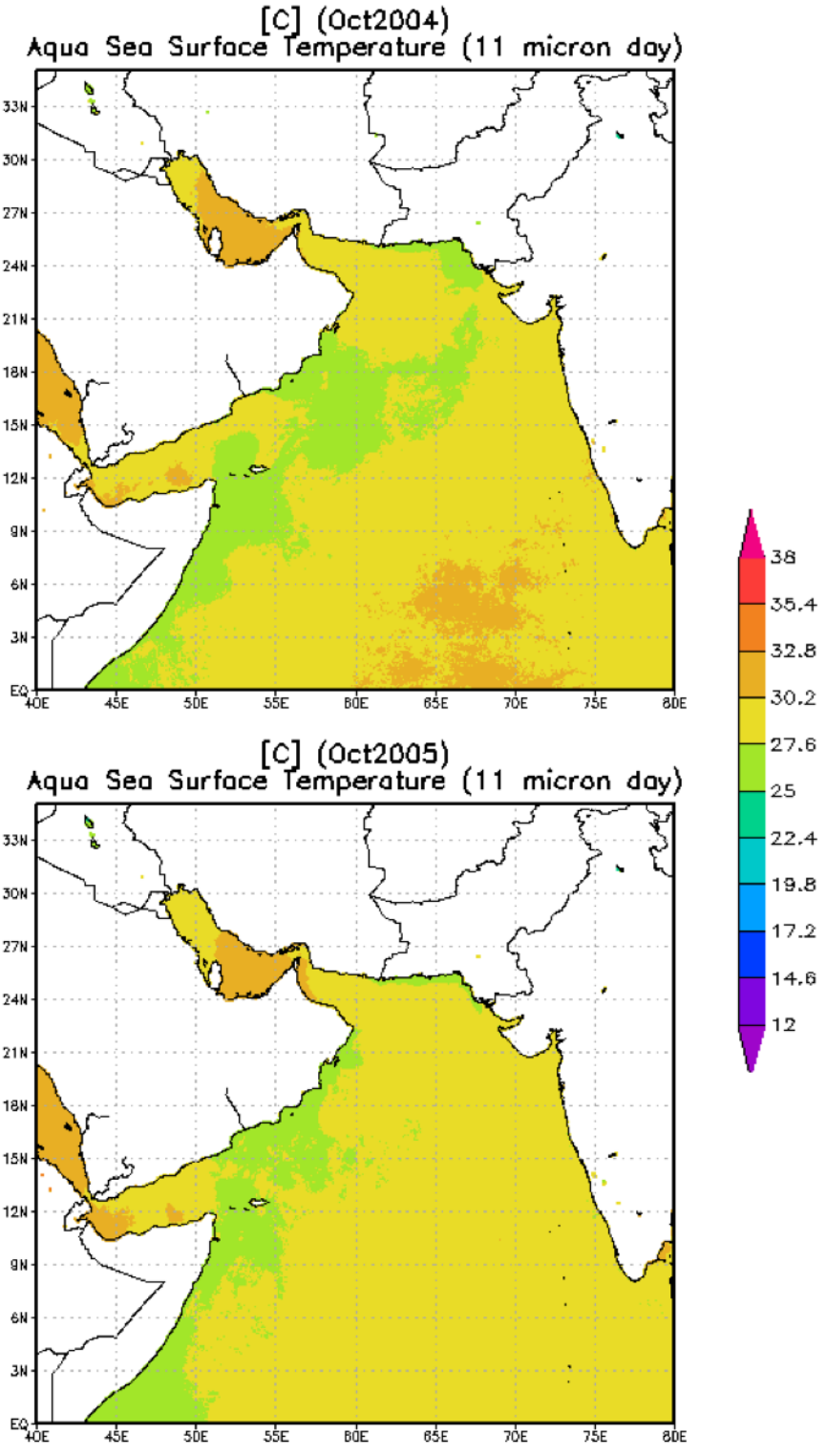

Figure B-10 continued.

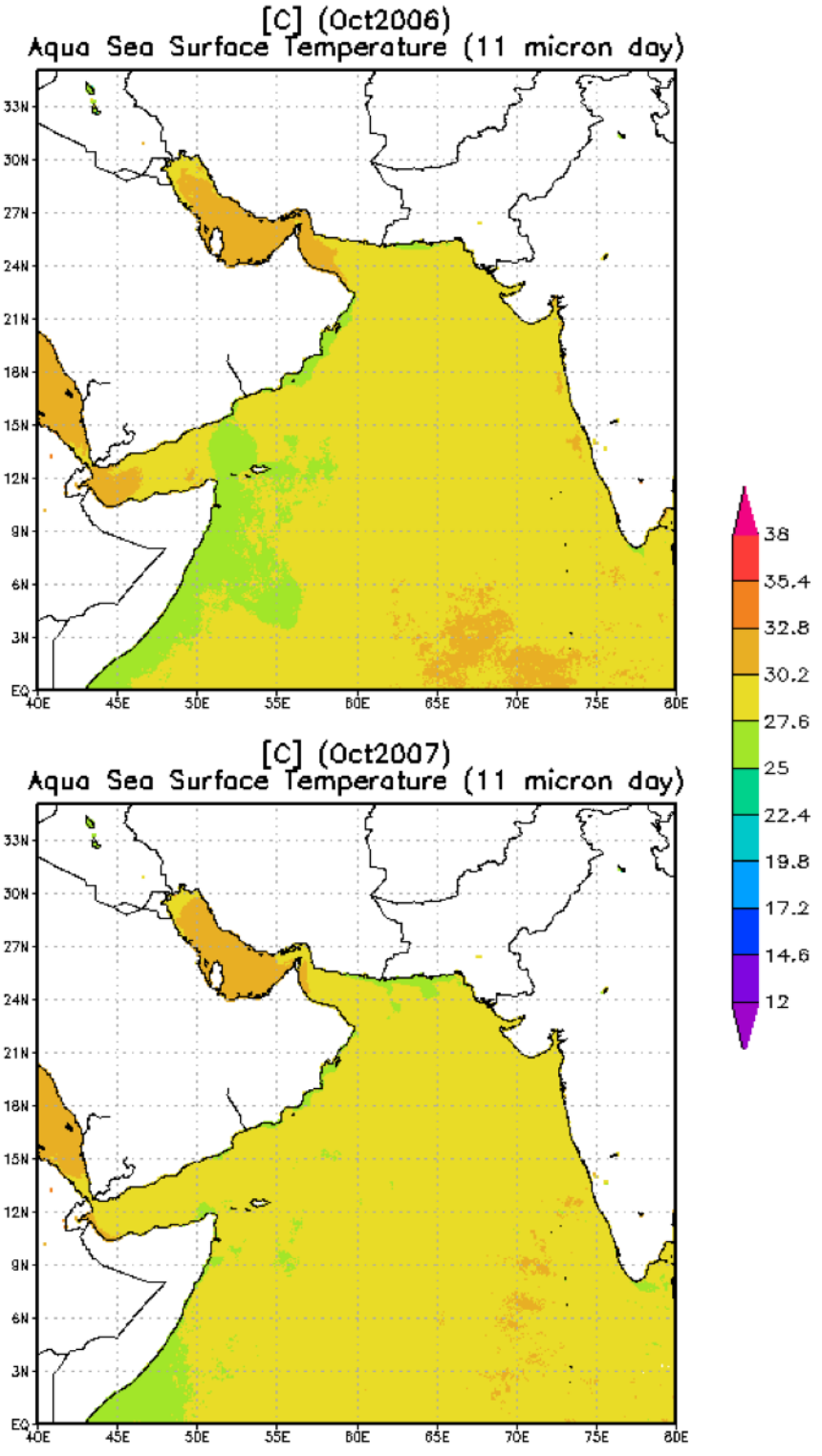

Figure B-10 continued.

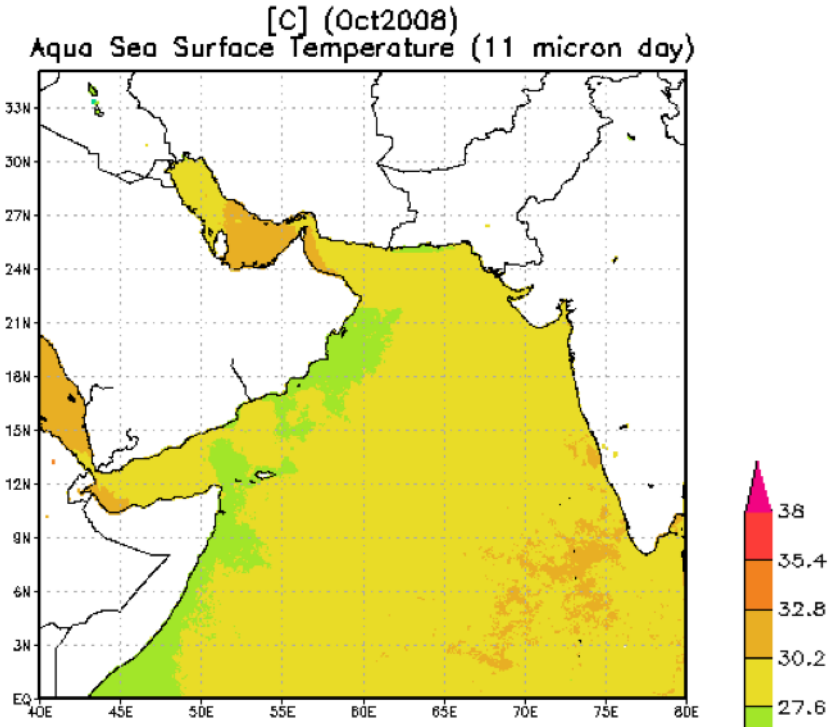

Figure B-10 continued.

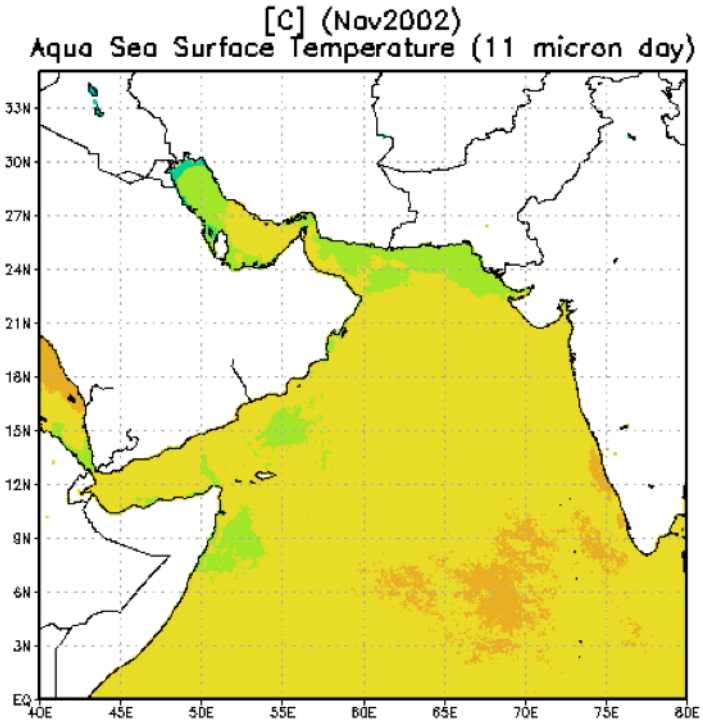

Figure B-11. November sea surface temperature maps generated by NASA's Giovanni (Kempler, 2011).

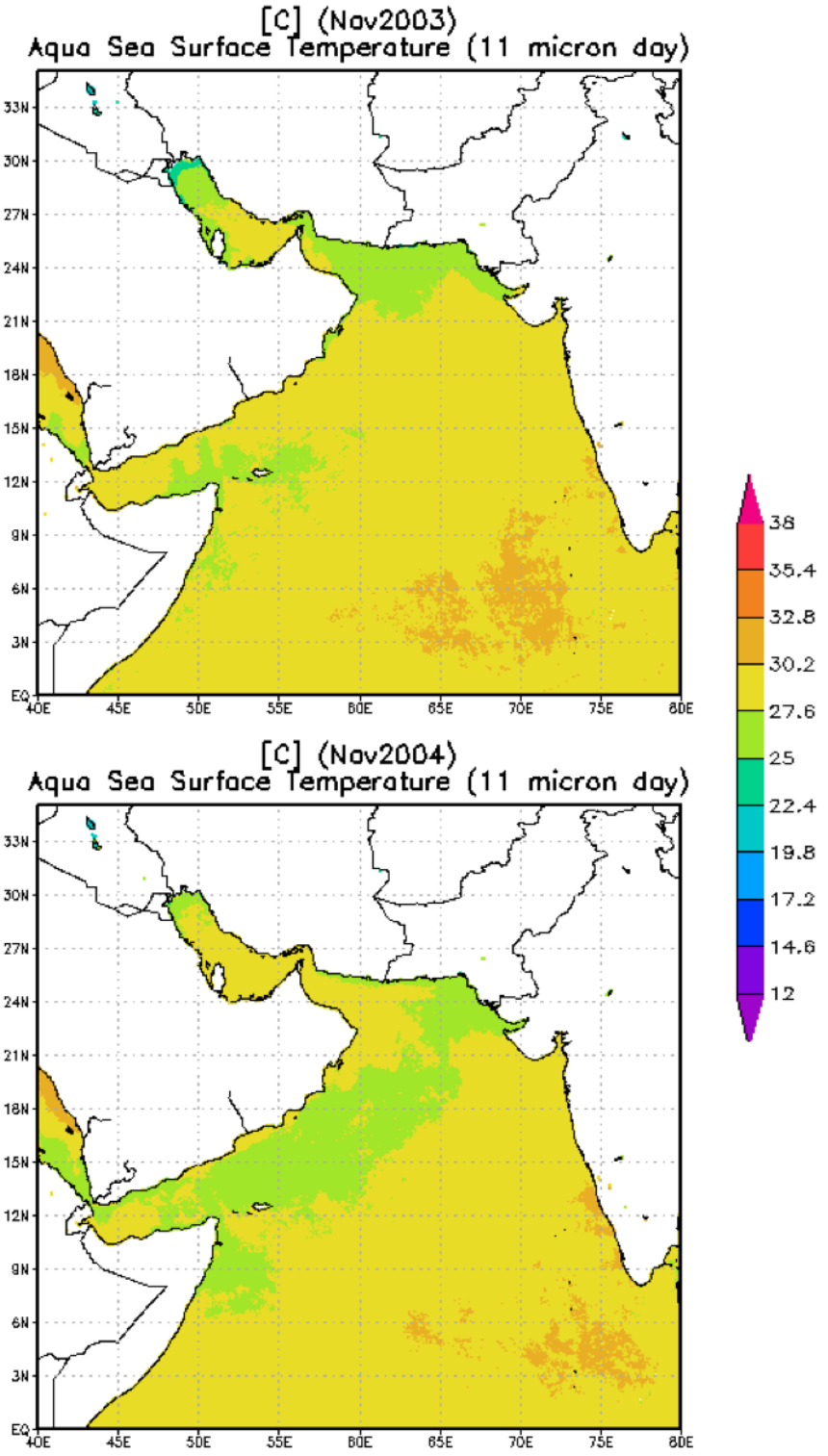

Figure B-11 continued.

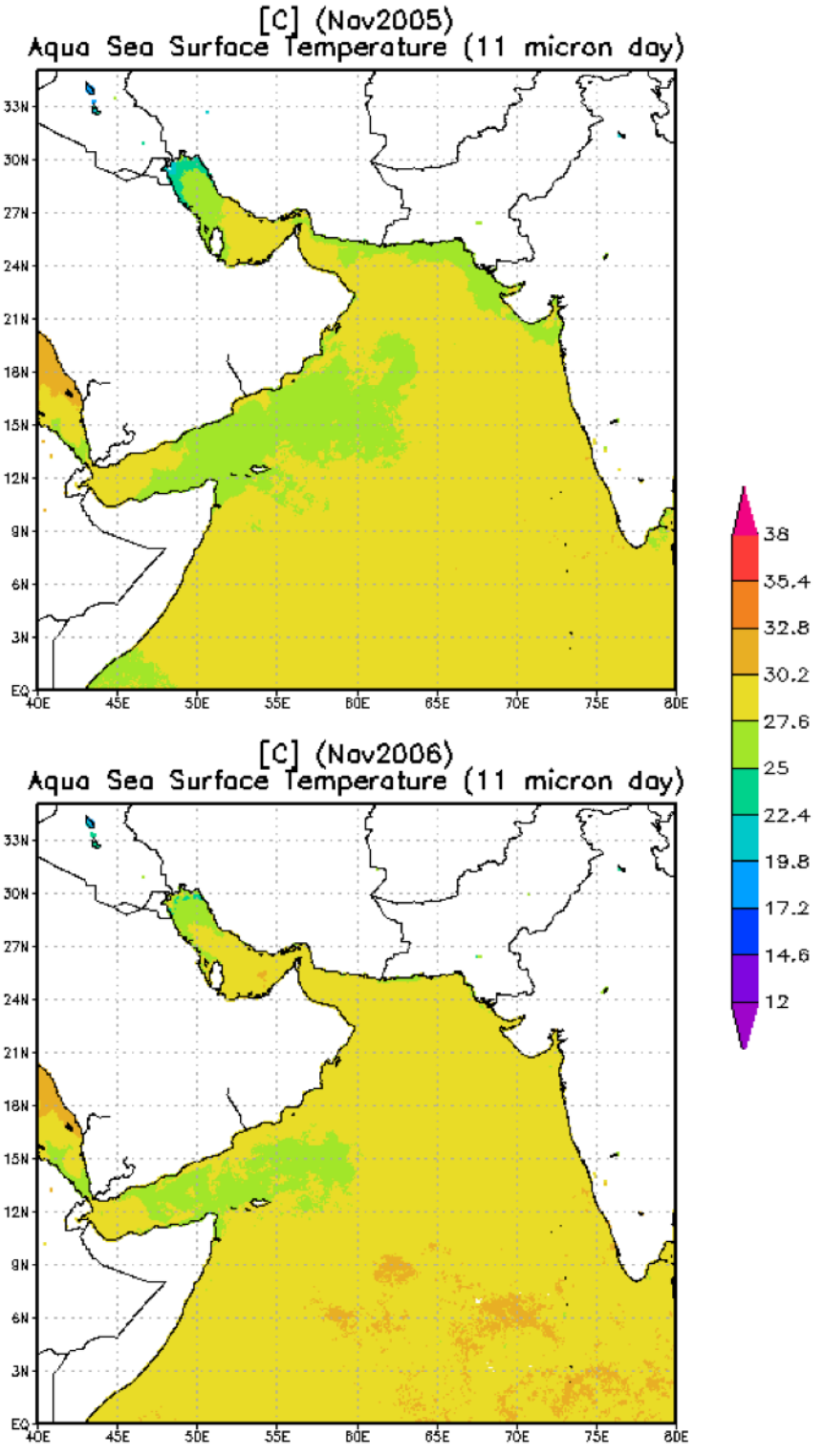

Figure B-11 continued.

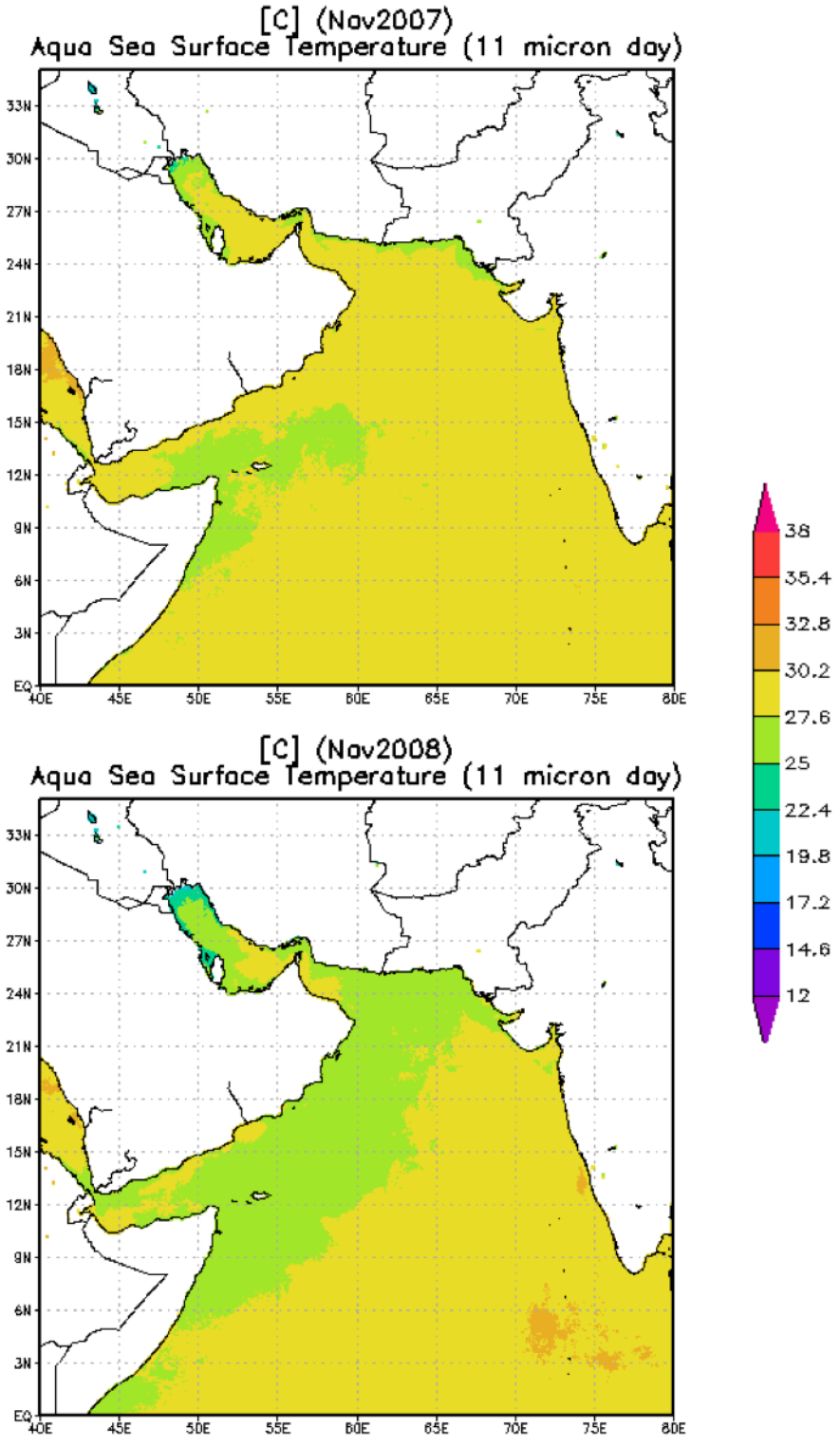

Figure B-11 continued.

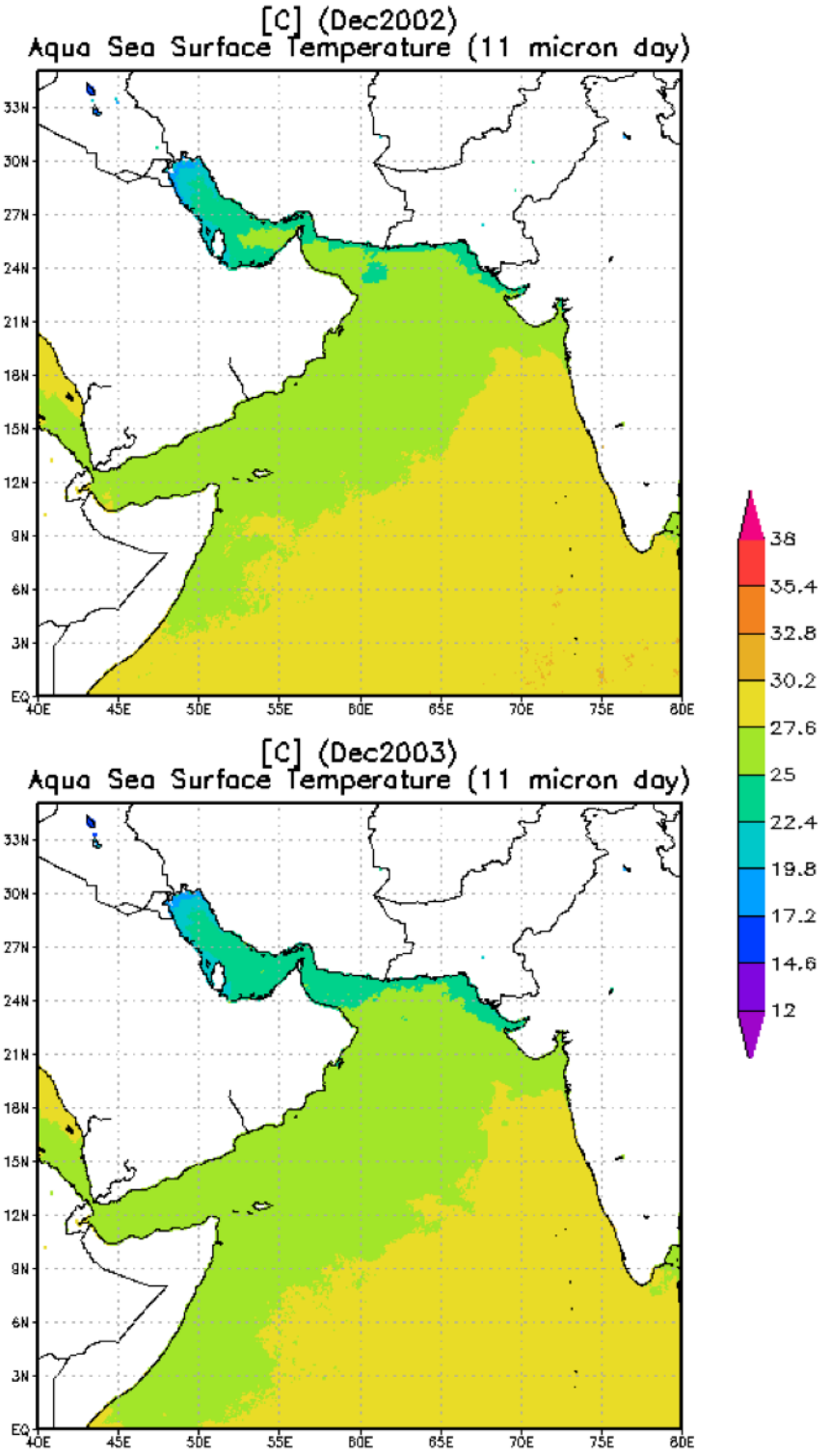

Figure B-12. December sea surface temperature maps generated by NASA's Giovanni (Kempler, 2011).

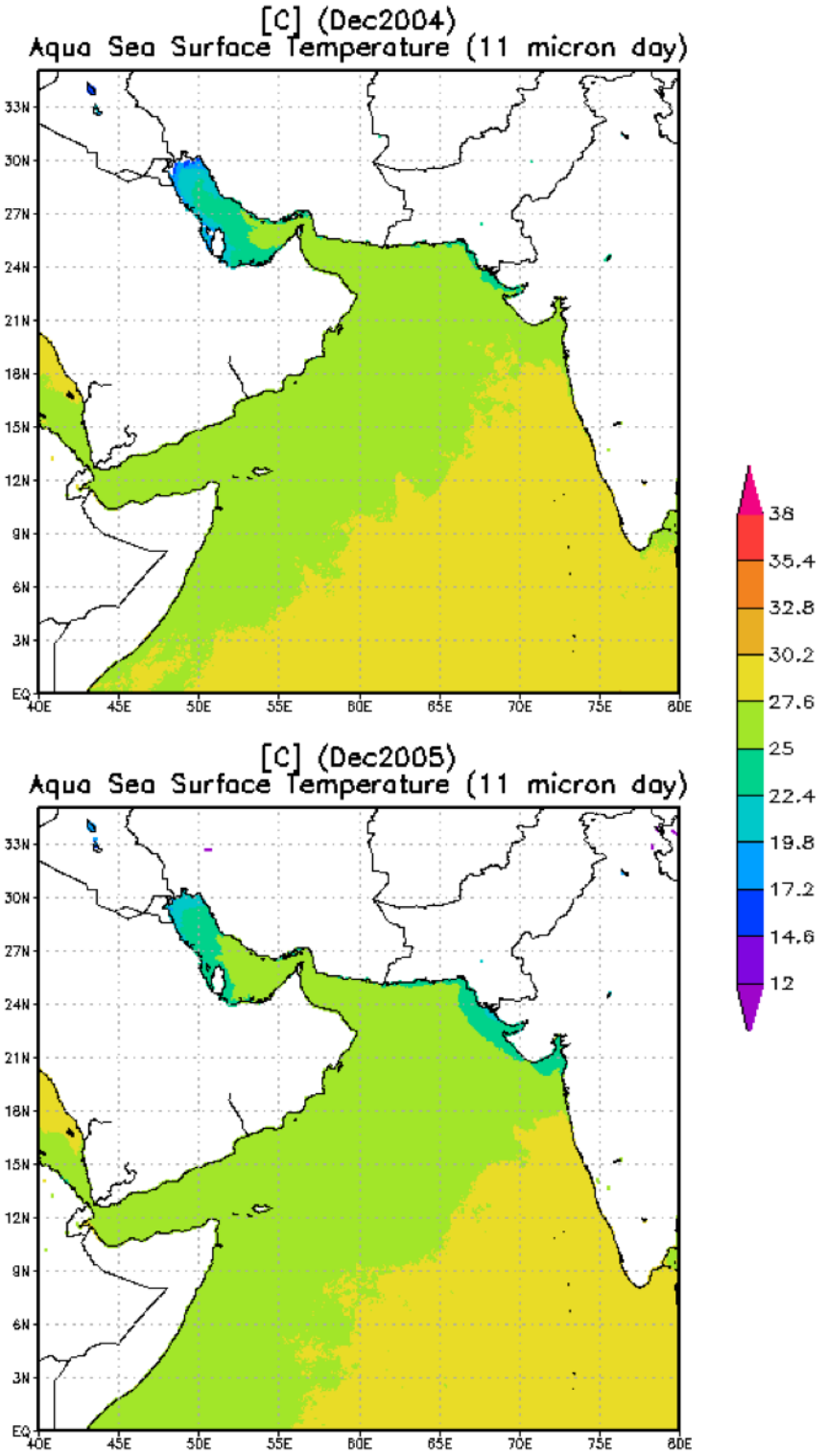

Figure B-12 continued.

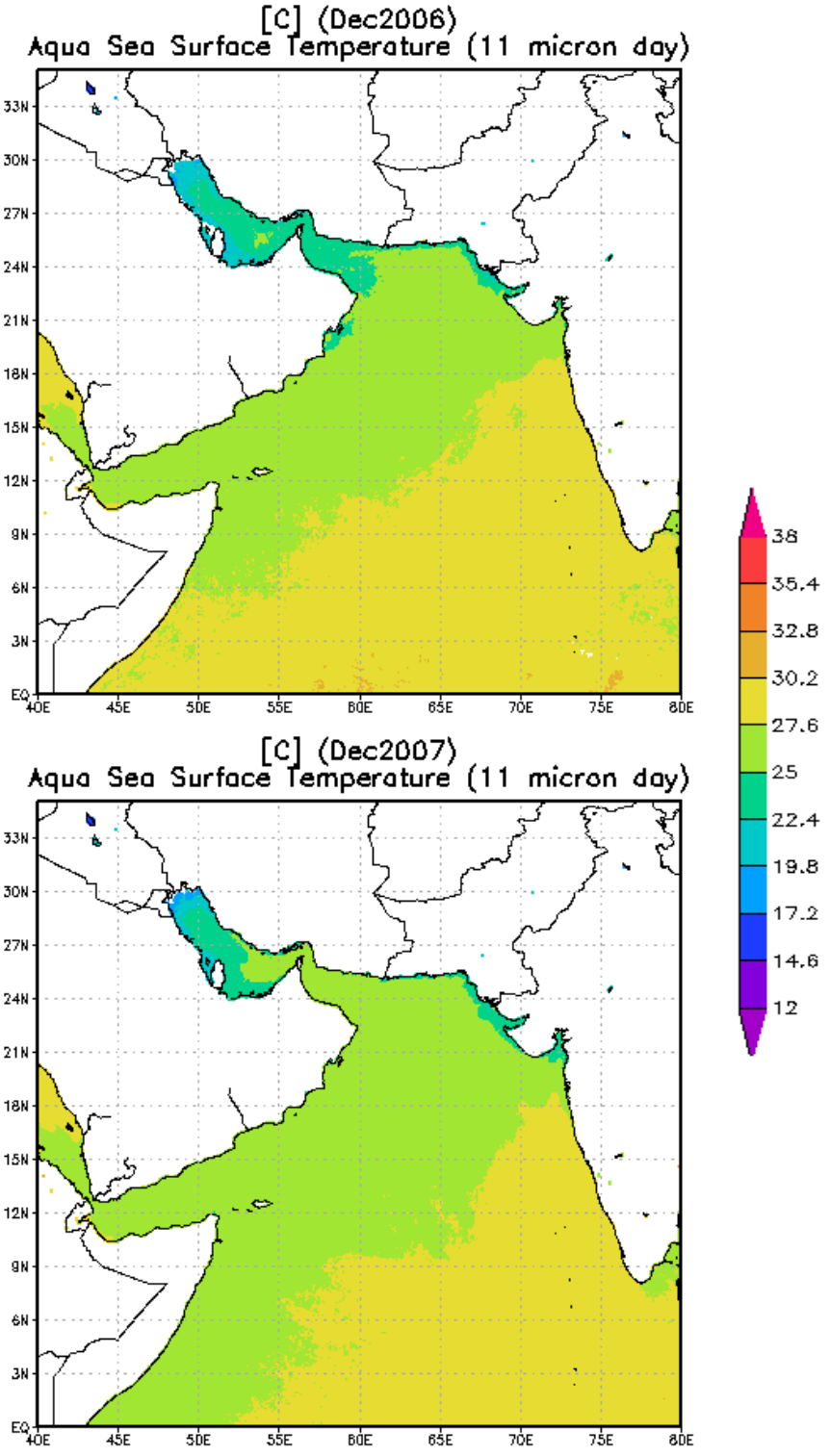

Figure B-12 continued.

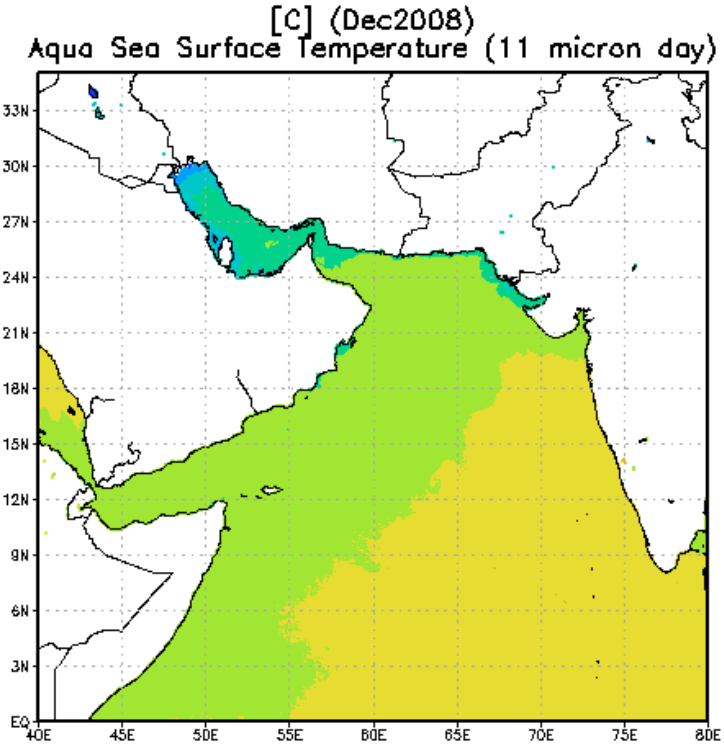

Figure B-12 continued.

APPENDIX C

Table C-1. Argo float distribution from Figure 7 for floats with a drifting depth of 1000m, 1500m or 2000m. Listed is the assigned float #, float ID, profile depth, drifting depth, the start date and the end date.

Argo Float Distribution with Drifting Depths of 1000, 1500 and 2000m					
Float # (Fig 8)	Float ID	Profile Depth (m)	Drifting Depth (m)	Start Date (from 1 JAN 2002)	End Date (through 31 DEC 2009)
1	1900156	1000	1000	6 MAR 2003	22 APR 2005
2	1900157	1000	1000	7 MAR 2003	18 DEC 2009
3	1900158	1000	1000	7 MAR 2003	16 MAY 2006
4	1900160	1000	1000	16 JUN 2003	30 AUG 2004
5	1900161	1000	1000	16 JUN 2003	11 OCT 2004
6	1900162	1000	1000	16 JUN 2003	17 JUN 2004
7	1900169	1000	1000	17 JUN 2003	10 OCT 2003
8	1900170	1000	1000	17 JUN 2003	23 JAN 2004
9	1900181	1000	1000	17 JUN 2003	2 MAY 2006
10	1900182	1000	1000	16 JUN 2003	30 MAR 2006
11	1900184	1000	1000	13 SEP 2003	2 JUL 2008
12	1900185	1000	1000	13 SEP 2003	20 FEB 2005
13	1900432	1200	1000	5 APR 2007	20 SEP 2007
14	1900435	1200	1000	5 APR 2007	9 AUG 2008
15	1900438	1200	1000	15 NOV 2008	4 APR 2009
16	1900439	1200	1000	4 MAY 2009	16 MAY 2009
17	1900443	1200	1000	5 MAY 2009	31 DEC 2009
18	2900103	1000	1000	11 SEP 2003	30 OCT 2006
19	2900105	2000	1000	10 SEP 2003	6 APR 2006
20	2900335	2000	1000	30 APR 2004	30 JAN 2005
21	2900336	2000	1000	27 APR 2004	25 FEB 2006
22	2900337	2000	1000	27 APR 2004	27 APR 2007
23	2900338	2000	1000	29 APR 2004	5 NOV 2006
24	2900339	2000	1000	4 MAY 2004	10 NOV 2006
25	2900340	2000	1000	1 MAY 2004	20 MAY 2004
26	2900341	2000	1000	1 MAY 2004	7 APR 2007
27	2900342	2000	1000	2 MAY 2004	17 NOV 2006
28	2900343	2000	1000	3 MAY 2004	11 AUG 2007
29	2900344	2000	1000	8 MAY 2004	10 OCT 2004
30	2900345	2000	1000	4 MAY 2004	20 SEP 2005
31	2900346	2000	1000	5 MAY 2004	5 DEC 2006
32	2900347	2000	1000	5 MAY 2004	24 JAN 2007
33	2900348	2000	1000	6 MAY 2004	11 NOV 2006
34	2900349	2000	1000	11 MAY 2004	26 FEB 2007
35	2900350	2000	1000	8 MAY 2004	31 AUG 2005
36	2900392	1000	1000	8 MAY 2004	31 DEC 2009
37	2900394	1000	1000	8 MAY 2004	28 MAR 2009
38	2900398	1000	1000	9 MAY 2004	20 SEP 2008
39	2900493	2000	1000	29 MAR 2005	6 AUG 2006
40	2900530	2000	1000	12 MAY 2005	23 DEC 2008
41	2900531	2000	1000	12 MAY 2005	6 AUG 2007
42	2900534	2000	1000	14 MAY 2005	13 APR 2006
43	2900552	2000	1000	1 SEP 2005	7 AUG 2008
44	2900553	2000	1000	6 SEP 2005	22 FEB 2009

Table C-1 continued.

Float # (Fig 8)	Float ID	Profile Depth (m)	Drifting Depth (m)	Start Date (from 1 JAN 2002)	End Date (through 31 DEC 2009)
45	2900554	2000	1000	6 SEP 2005	9 DEC 2008
46	2900555	2000	1000	6 SEP 2005	23 FEB 2009
47	2900556	2000	1000	11 SEP 2005	13 MAY 2009
48	2900557	2000	1000	16 SEP 2005	31 DEC 2009
49	2900558	2000	1000	5 SEP 2005	31 DEC 2009
50	2900559	2000	1000	16 SEP 2005	31 DEC 2009
51	2900560	2000	1000	16 SEP 2005	31 DEC 2009
52	2900561	2000	1000	16 SEP 2005	31 DEC 2009
53	2900562	2000	1000	8 SEP 2005	31 DEC 2009
54	2900563	2000	1000	9 SEP 2005	31 DEC 2009
55	2900564	2000	1000	16 SEP 2005	20 NOV 2006
56	2900565	2000	1000	16 SEP 2005	31 DEC 2009
57	2900567	2000	1000	16 SEP 2005	31 DEC 2009
58	2900570	2000	1000	16 SEP 2005	31 DEC 2009
59	2900621	1200	1000	14 JUN 2007	15 AUG 2008
60	2900622	1200	1000	14 JUN 2007	12 JUL 2007
61	2900623	1200	1000	14 JUN 2007	4 APR 2009
62	2900802	1200	1000	16 DEC 2007	1 JUN 2008
63	2900803	1200	1000	10 DEC 2007	12 FEB 2008
64	2900804	1200	1000	11 DEC 2007	20 JUN 2008
65	2900805	1200	1000	19 DEC 2007	9 APR 2008
66	2900808	1200	1000	9 JAN 2008	11 OCT 2008
67	2900810	1200	1000	11 JAN 2008	15 MAR 2008
68	2900811	1200	1000	11 JAN 2008	13 JUL 2008
69	2900826	1200	1000	12 JUL 2008	9 MAR 2009
70	2900827	1200	1000	12 JUL 2008	31 DEC 2008
71	2901084	2000	1000	14 AUG 2008	31 DEC 2009
72	2901085	2000	1000	7 AUG 2008	31 DEC 2009
73	2901086	2000	1000	8 AUG 2008	26 MAR 2009
74	2901087	2000	1000	12 AUG 2008	27 AUG 2009
75	2901090	2000	1000	26 AUG 2008	31 DEC 2009
76	2901094	2000	1000	1 FEB 2008	31 DEC 2009
77	2901095	2000	1000	29 JAN 2008	31 DEC 2009
78	2901096	2000	1000	31 JAN 2008	31 DEC 2009
79	2901097	2000	1000	29 JAN 2008	31 DEC 2009
80	2901105	1200	1000	11 NOV 2008	4 APR 2009
81	2901107	1200	1000	12 NOV 2008	31 DEC 2009
82	2901108	1200	1000	12 NOV 2008	31 DEC 2009
83	2901109	1200	1000	12 NOV 2008	5 APR 2009
84	2901111	1200	1000	8 DEC 2008	3 APR 2009
85	2901112	1200	1000	14 DEC 2008	30 DEC 2008
86	2901113	1200	1000	16 DEC 2008	26 FEB 2009
87	2901129	1200	1000	9 MAR 2009	31 DEC 2009
88	2901132	1200	1000	9 MAR 2009	31 DEC 2009
89	2901133	1200	1000	9 MAR 2009	31 DEC 2009
90	2901134	1200	1000	9 MAR 2009	18 DEC 2009
91	2901147	1200	1000	4 JUL 2009	25 AUG 2009
92	2901147	1200	1000	4 JUL 2009	31 DEC 2009
93	2901149	1200	1000	4 JUL 2009	31 DEC 2009
94	2901150	1200	1000	6 JUL 2009	31 DEC 2009
95	2901151	1200	1000	6 JUL 2009	31 DEC 2009

Table C-1 continued.

Float # (Fig 8)	Float ID	Profile Depth (m)	Drifting Depth (m)	Start Date (from 1 JAN 2002)	End Date (through 31 DEC 2009)
96	2901368	1200	1000	23 NOV 2009	31 DEC 2009
97	2901369	1200	1000	5 DEC 2009	31 DEC 2009
98	2901370	1200	1000	18 NOV 2009	31 DEC 2009
99	4900511	2000	1000	26 SEP 2005	28 MAY 2009
100	5900927	1000	1000	14 APR 2005	31 DEC 2009
101	1900369	2000	1500	11 MAY 2004	30 JUN 2004
102	1900370	2000	1500	11 MAY 2004	30 JUN 2004
103	1900371	2000	1500	12 MAY 2004	30 JUN 2008
104	1900372	2000	1500	12 MAY 2004	30 JUN 2008
105	1900373	2000	1500	12 MAY 2004	1 JAN 2005
106	1900374	2000	1500	12 MAY 2004	26 APR 2009
107	1900375	2000	1500	12 MAY 2004	28 OCT 2008
108	1900376	2000	1500	12 MAY 2004	1 FEB 2006
109	1900585	2000	1500	25 AUG 2005	31 DEC 2009
110	1900586	2000	1500	25 AUG 2005	31 DEC 2009
111	1900631	2000	1500	28 OCT 2005	7 MAR 2006
112	1900632	2000	1500	27 OCT 2005	9 JUN 2007
113	1900634	2000	1500	9 MAY 2006	30 DEC 2007
114	1901045	2000	2000	23 JUN 2009	23 DEC 2009
115	2900159	2000	2000	1 JAN 2002	16 FEB 2004
116	2900161	2000	2000	1 JAN 2002	8 DEC 2003
117	2900162	2000	2000	1 JAN 2002	26 JUN 2004
118	2900163	2000	2000	1 JAN 2002	14 OCT 2004
119	2900164	2000	2000	1 JAN 2002	28 JUN 2004
120	2900165	2000	2000	1 JAN 2002	21 MAY 2004
121	2900166	2000	2000	1 JAN 2002	26 MAR 2005
122	2900167	2000	2000	1 JAN 2002	3 JAN 2005
123	2900168	2000	2000	1 JAN 2002	28 OCT 2005
124	2900194	2000	2000	14 JUL 2002	19 APR 2005
125	2900229	2000	2000	25 OCT 2002	21 FEB 2005
126	2900230	2000	2000	13 JAN 2005	10 MAR 2006
127	2900256	2000	2000	1 JUN 2003	18 NOV 2003
128	2900257	2000	2000	2 JUN 2003	1 AUG 2003
129	2900258	2000	2000	2 JUN 2003	19 AUG 2004
130	2900259	2000	2000	30 MAY 2003	8 FEB 2005
131	2900260	2000	2000	30 MAY 2003	3 JUN 2004
132	2900261	2000	2000	14 JUN 2003	26 SEP 2004
133	2900262	2000	2000	15 JUN 2003	27 SEP 2004
134	2900263	2000	2000	11 JUN 2003	25 FEB 2004
135	2900264	2000	2000	12 JUN 2003	13 NOV 2004
136	2900275	2000	2000	31 MAY 2003	1 NOV 2003
137	2900276	2000	2000	31 MAY 2003	20 MAR 2004
138	2900758	2000	2000	3 AUG 2006	4 DEC 2009
139	2900769	2000	2000	14 MAR 2006	27 FEB 2009
140	2900770	2000	2000	15 MAR 2006	28 FEB 2009
141	2900771	2000	2000	21 MAR 2007	31 DEC 2009
142	2900773	2000	2000	21 MAR 2007	31 DEC 2009
143	2900774	2000	2000	18 MAR 2007	31 DEC 2009
144	2900776	2000	2000	1 APR 2007	31 DEC 2009
145	2900777	2000	2000	20 MAR 2007	31 DEC 2009
146	2900778	2000	2000	21 MAR 2007	26 OCT 2009

Table C-1 continued.

Float # (Fig 8)	Float ID	Profile Depth (m)	Drifting Depth (m)	Start Date (from 1 JAN 2002)	End Date (through 31 DEC 2009)
147	2900779	2000	2000	5 JUN 2007	8 OCT 2007
148	2900780	2000	2000	4 JUN 2007	31 DEC 2009
149	2900781	2000	2000	11 JUN 2007	31 DEC 2009
150	2900782	2000	2000	12 JUN 2007	31 DEC 2009
151	2900877	2000	2000	11 SEP 2007	31 DEC 2009
152	2900879	2000	2000	10 SEP 2007	31 DEC 2009
153	2900880	2000	2000	11 SEP 2007	31 DEC 2009
154	2900881	2000	2000	12 SEP 2007	31 DEC 2009
155	2901076	2000	2000	1 FEB 2008	31 DEC 2009
156	2901077	2000	2000	1 FEB 2008	17 NOV 2008
157	2901079	2000	2000	3 FEB 2008	31 DEC 2009
158	2901081	2000	2000	10 FEB 2008	31 DEC 2009

VITA

Name: Sarah A. Stryker

Address: Texas A&M, Eller O&M 3146
Department of Oceanography
College Station, TX 77843

Email Address: sstryker@ocean.tamu.edu

Education: B.S., Geophysics, The State University of New York at Fredonia, 2009

M.S., Oceanography, Texas A&M University, 2011